Anti-Localization in Oxide Heterostructures

Dissertation

zur Erlangung des akademischen Grades

Dr. rer. nat.

eingereicht an der
Mathematisch-Naturwissenschaftlich-Technischen Fakultät
der Universität Augsburg

von
Patrick Seiler

Augsburg, Juni 2018

Universität
Augsburg
University

Erstgutachter:	Prof. Dr. Thilo Kopp
Zweitgutachter:	Prof. Dr. Ulrich Eckern
Drittgutachter:	Prof. Dr. Piet Brouwer

Tag der mündlichen Prüfung: 05. Oktober 2018

Anti-Localization in Oxide Heterostructures

Patrick Seiler

Abstract

This thesis investigates the phenomenon of Anderson anti-localization in oxide heterostructures.

The strong spin–orbit coupling in many two-dimensional oxide materials appears in form of a weak anti-localization signature in magneto-transport. This signature depends significantly on microscopic details of the relevant spin relaxation mechanism, but has often been misinterpreted in the literature. This thesis clarifies the different microscopic pictures and selects suitable fitting formulas.

Beyond conventional weak anti-localization theory, which involves spin-$1/2$ particles, this thesis provides a closed form result for the magneto-transport of spin-$3/2$ states. This four-level system offers a generic model for a multiband weak anti-localization theory and identifies the coupling between Landau levels in the quintet and septet channel of the Cooperon as a key mechanism for the specific signature in magneto-transport.

Furthermore, weak anti-localization in oxide heterostructures is often obfuscated by the multiband Hall effect. A numerical analysis is developed that singles out the weak anti-localization contribution self-consistently. This analysis is successfully applied to data obtained from the $LaAlO_3/SrTiO_3$ heterostructure, identifying the spin structure at the Fermi surface and revealing an unexpected hole-like charge carrier.

The spin structure is also analyzed for magneto-transport data recently obtained from thin monolayers of $BaPbO_3$ on $SrTiO_3$. The so far undetected symplectic-metal–insulator transition is proposed for this structure and related materials, due to strong spin–orbit coupling, high charge carrier density, and single band behavior.

Contents

1 Introduction

Contents

1.1 Overview

Heterostructures of oxide materials are believed to be one of the building blocks of post semiconductor devices. Due to the tunability of several coupled degrees of freedom like charge, spin, orbital, and dimensionality, and even due to the impact of disorder, these materials inhibit rich physical behavior like magnetism, unconventional superconductivity, or topological spin structures. However, gaining a better understanding of these materials is still very challenging due to their complex nature. Even though the control during growth processes achieved a high level, the physical properties of many systems are still not very well understood. Many groups worldwide are trying to take oxide heterostructures to the next level.

Quite general concepts, which I will review in the first chapter, indicate that low-dimensional systems (that is, systems with only one or two effective spatial dimensions, like thin films or nanowires) cannot support a metallic state (that is, a state supporting electric transport at absolute zero temperature for arbitrary large samples). The reason is that mobile charge carriers are localized by any amount of disorder. This kind of low-dimensional electronic ground state, described in the late 1970s by the "Gang of Four"[1], is called an Anderson insulator and relates back to Anderson's ideas from the 1950s [1, 2].

Nevertheless, strong indications for a metallic state, as well as a metal–insulator transition, have actually been found in two-dimensional semiconductor devices during the 1990s, contradicting the theoretical proposal [3, 4]. This kind of metallic state seems to be driven by electron–electron interaction and might overcome the constraints of low-dimensionality and disorder, outruling the picture of single electrons drawn by the theoretical prediction of localization [1].

[1] Abrahams, Anderson, Licciardello, and Ramakrishnan (1979) [1].

There is a second fundamental type of metallic state in two spatial dimensions that has been predicted by theory and is understood in the framework of one-particle physics. This kind of metallic state is not driven by interaction, but by spin–orbit coupling: in combination with disorder, the relativistic effect of spin–orbit coupling results in the concept of anti-localization, the counterpart of the well-established Anderson localization. This mechanism lets the fermionic particle become mobile due to destructive interference in self-intersecting paths, which are enhanced by disorder. Due to the link to the symplectic symmetry of spin–orbit coupling, this metallic state is called a symplectic metal. Although the prediction of this state leads back to the 1980s [5], no experimental affirmation of the symplectic metal–insulator transition has been achieved so far, not even in well-controlled artificial lattices using ultracold atoms.

A major advantage of electronic systems in oxide materials—besides their strong confinement to two dimensions and the incorporated strong spin–orbit coupling—is a relatively high electron density, compared to the semiconductor quantum wells. This provides the possibility that the electron–electron interaction is well screened in oxide materials and allows the symplectic metallic state to emerge. On the other hand, oxide materials are also much more intriguing and more difficult to control. Magnetism, superconductivity, and multiband effects hinder an easy extraction of the symplectic state. In the search for a material that provides the symplectic metal state, all interference factors have to be understood quite well to come to a decisive conclusion.

The detailed understanding of Anderson anti-localization in low-dimensional oxide materials is the focus of this thesis. It is crucial to treat multiband effects and anti-localization on an equal footing, and I extend the current theories in several aspects: First, for the weakly disordered regime, I derive a closed form weak anti-localization formula for a multiband spin–orbit coupling. Secondly, I develop a self-consistent numerical analysis to single out the anti-localization contribution from the multiband Hall effect in magneto-transport data. Furthermore, I propose a sMIT, so far undetected in experiment, for the strongly disordered regime in a special kind of recently investigated oxide material.

The thesis is structured as follows:

- In **Chapter 1**, I give an introduction into Anderson localization. I briefly discuss the Anderson model, the concept of conductivity in different spatial dimensions, and Anderson metal–insulator transitions. Furthermore, I introduce the weak localization corrections, which can be calculated by considering maximally crossed diagrams within the Kubo linear response technique. Weak localization has been a great concept for experiments due to its sensitivity to an external magnetic field and its signature in the temperature dependent resistivity. This review is the starting point for the elaborations in this thesis.

- **Chapter 2** represents the theoretical core of this thesis. I review established theories for weak anti-localization and emphasize their distinctions in the microscopic picture, as well as in their magneto-transport signature, because these signatures have often been misinterpreted in the literature. I discuss not only the widely known Hikami–Larkin–Nagaoka-theory [6], which treats spin–orbit scatterers, but also the Iordanskii–Lyanda-Geller–Pikus-theory [7], which treats the spin–orbit coupling in terms of a spin dependent band splitting and has to be chosen as correct description for weak anti-localization in interfaces of heterostructures. I extend the established results with

calculations for anisotropic and cubic Rashba Hamiltonians as well as a multiband model by considering spin–orbit coupling for spin-$^3/_2$. This four-level system provides a generic model, which I employ to examine the impact of the multiband effect in the theory of weak anti-localization [8].

- **Chapter 3** focuses on the analysis of experimental magneto-transport data obtained in $LaAlO_3/SrTiO_3$ heterostructures, provided by experimental collaborators in Stuttgart[2], as well as novel structures based on barium oxides, provided by experimental collaborators in Augsburg[3]. In case of the $LaAlO_3/SrTiO_3$ heterostructure, the weak anti-localization signature is obfuscated by the multiband Hall effect. I develop a self-consistent data analysis that allows to single out the quantum correction. The results regarding the $LaAlO_3/SrTiO_3$ interface, including a three-fold winding spin structure at the Fermi surface, as well as an unexpected hole-like charge carrier, have been published in:

  Seiler et al., Phys. Rev. B **97** 075136 (2018) (Ref. [9]).

  Based on the first analysis of thin films of $BaPbO_3$ on $SrTiO_3$, I propose a detectable symplectic metal–insulator transition in this structure or related materials, due to strong spin–orbit coupling, high charge carrier density and single-band behavior [10].

- **Chapter 4** draws a conclusion of the results. I raise several further questions for future investigations, as well as recommendations for prospective experimental and theoretical projects regarding anti-localization in low-dimensional oxide materials.

The appendices contain additional detailed information:

- **Appendix A** includes calculations of the electric response in the disordered electronic system, like the Drude and Boltzmann conductivity. This appendix focuses on details that provide the basis of calculations in Chap. 2, like the emergence of the diffusion pole in the density–density correlation function.

- **Appendix B** contains mathematical details on the weak anti-localization evaluation for the spin-$^3/_2$ model in Chap. 2.

- **Appendix C** discusses details on the Hall effect and the self-consistent fitting routine used in the data analysis of Chap. 3. This routine allows to single out the WAL contribution from the multiband Hall effect.

- In **Appendix D**, further contributions to the conductivity are considered, namely quantum corrections due to electron–electron interaction and superconducting fluctuations, as well as the anomalous Hall effect. These contributions are addressed in the analysis of the experimental data in Chap. 3.

[2] Zabaleta, Wanke, and Mannhart, Max Planck Institute for Solid State Research Stuttgart.
[3] Meir and Hammerl, Chair of Experimental Physics 6, University of Augsburg.

1.2 Conductivity in the Different Spatial Dimensions

The conductance G of a bulk sample is classically described by Ohm's Law

$$G = \sigma \frac{A}{L}, \tag{1.1}$$

where A is the cross section of the sample, L its length and σ the material specific conductivity. In Drude's theory, the conductivity is given by

$$\sigma = \frac{ne^2\tau}{m} = ne\mu, \tag{1.2}$$

where n is the charge carrier density, e the elementary charge, τ the relaxation time, m the (effective) mass of the charge carriers, and μ the charge carrier mobility (see Sec. A.2). Working with the more elaborate Boltzmann transport theory, one ends up with the same formal expression, Eq. (1.2), but although all free electrons of the system contribute to the density n, only particles at the Fermi level participate in scattering processes and undergo local relaxation, thus τ actually is $\tau(\mathbf{k}_\mathrm{F})$ (see Sec. A.3). Apparently, the conductivity is finite as long as the electron density and mobility are finite. In this case, the system will respond with an electric current when an electric field is applied, and we refer to such a system as a metallic one, whereas it is insulating in the absence of electric current.

The electron density n in the Drude conductivity Eq. (1.2) is dependent on the space dimensions in which the electric current flows, and might be a three-, two-, or even one-dimensional property. Therefore, the conductivity (or specific conductance) σ and its inverse, the resistivity (or specific resistance) ρ, are given in units of

$$[\sigma] = \frac{1}{\Omega \mathrm{m}^{d-2}}, \tag{1.3}$$

$$[\rho] = \Omega \mathrm{m}^{d-2}. \tag{1.4}$$

Note that conductivity and resistivity depend on the dimension d of the considered system, but are length independent when d is fixed, as they are inherent material properties.

Conductance and resistance, however, depend on the length of a specific sample, because they are determined (in three dimensions) via Ohm's law. If we specify the appearing lengths in Eq. (1.1) in terms of a d-dimensional hypercube of length L (see Fig. 1.1), we find the strong dimensional dependence

$$G = \sigma L^{d-2}, \tag{1.5}$$

$$R = \frac{\rho}{L^{d-2}}, \tag{1.6}$$

and for the units of conductance and resistance

$$[G] = \frac{1}{\Omega}, \tag{1.7}$$

$$[R] = \Omega. \tag{1.8}$$

Therefore, conductance and resistance scale with the L, but are independent of d when L is fixed. This is also apparent in the conductance quantum, e^2/h, which carries the same units

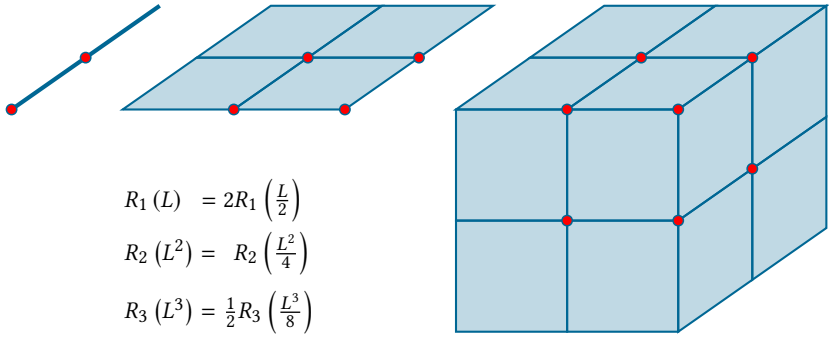

Figure 1.1: *Resistance for different dimensions and length scales.* For the following arguments, we keep the resistivity constant. If we measure the resistance over the full length of a one dimensional wire, and repeat the measurement by taking only half of this length, the value for the longer distance is twice the value of the shorter one. In a thin film, the larger plate and the smaller plate yields the same result for the resistance. In three dimensions, by measuring a cube, we cut out $1/8$ of the cube and find that the resistance value of the larger cube is only half of the value of the smaller cube.

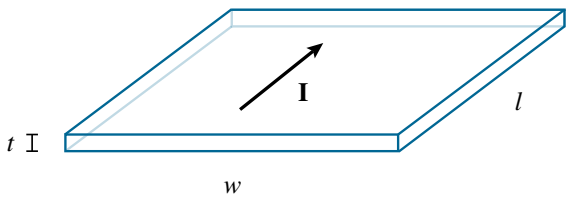

Figure 1.2: *Dimensions of a thin film.* In a thin film, we refer to thickness t, width w and length l, in respect to the direction of the electric current, **I**. These are used for the definition of the sheet resistance, R_{sh}.

independent of the dimensionality of the system. According to Eq. (1.6), for constant finite resistivity, the resistance decreases with system size in three dimensions. Therefore, we expect a sample to show better and better metallic behavior when we increase it in size. Instead, for a one-dimensional wire, the resistance increases with growing system size. The case of a two-dimensional sheet is the marginal case between a good and a poor macroscopic conductor: the resistance does not depend on the system size.

The special case of two spatial dimensions is in the focus of this thesis. In this case, resistivity and resistance are formally equivalent due to Eq. (1.6). For thin films, which can be considered to be effectively two-dimensional, the quantity of sheet resistance, R_{sh}, is a useful quantity for electric measurements. It is defined as the resistivity per thickness t, $R_{\mathrm{sh}} = \rho/t$, which gives $R = R_{\mathrm{sh}} l/w$ (see Fig. 1.2) and can be directly determined in a four-terminal measurement. R_{sh} carries the same units as the bulk resistance, Ω, but to distinguish between the two properties, for the sheet resistance the units Ohm-square, Ω□, or Ohm per square, Ω/□, are used likewise. The electron mobility μ in the Drude picture can now be defined using either the resistivity or the sheet resistance, $1/\mu = en_{3\mathrm{d}}\rho = en_{3\mathrm{d}}t\rho/t = en_{2\mathrm{d}}R_{\mathrm{sh}}$.[4]

[4] In Appendix C, we derive formulas for a multiband Hall effect in terms of the set $\{\rho, n\}$. To use the formulas for a two-dimensional system, one can easily replace the variables by $\{R_{\mathrm{sh}}, n_{2\mathrm{d}}\}$, and all formulas derived here are still valid.

1.3 A Short Theory of Anderson Localization

One central issue of condensed matter physics is the classification and description of macroscopic phases like (anti-)ferromagnetism, quantum or classical spin glasses, or superconductivity, in terms of a microscopic theory. In this framework it is also highly relevant to distinguish between a metal and an insulator, dependent on the response with an electric current at absolute zero temperature if an external electric field is applied (or, by the sensitivity of electronic states regarding a change of the boundary condition, called Thouless criterion [11]).

There are mainly three classes of insulators that have been discussed in course of time. The Bloch insulator is the one we know for the longest time [12]. The single electron states in a perfect crystal are organized in bands. If an energy gap lies between the highest occupied and the lowest empty band state, the system is insulating. Some finite energy excitation is necessary to lift a particle into the higher band, where it can contribute to a current. However, even in this example, there lies a much deeper subtlety, as topological terms in the Hamiltonian might result in topologically distinguishable band insulators. Some of them are insulating in the bulk only, but carry nonetheless edge states, which are robust against perturbations (see, e.g., Ref. [13]).

A second class of insulators are the Mott insulators [14]. In some transition metal oxides, for example, single electron band theory predicts electronic states at the Fermi energy, but the strong electron–electron interaction seems to suppress electronic transport in those systems completely. This kind of insulator can be understood by considering the Hubbard model, which describes transfer of electrons to neighboring sites but also treats local interaction [15]. To stay in the picture of an energy gap, a gap does not open between Bloch bands, but between Hubbard bands in Fock space.[5]

The third class is the Anderson insulator [2] and will be in focus on in this thesis. This insulator is driven by disorder: even in a non-interacting single particle picture, disorder introduces a random potential in which the charge carriers get localized. This phenomenon arises from self-interference of the single particle state. Electron–electron interaction, spin–orbit coupling, and topology have their distinct influence on the Anderson insulator.

In the following, we review some properties of the Anderson model, which describes the localization transition for strong disorder, before we examine quantum corrections to the conductivity, which are relevant for weak disorder.

1.3.1 The Anderson Model

In 1958, Anderson showed that for an electron wave, scattered by a static, but random potential, the diffusion process can be suppressed completely by interference of phase factors collected along distinct paths [2]. In this case, although a Bloch wave is delocalized in a perfect crystal, the state gets trapped in presence of disorder and no longer contributes to transport. The strength of disorder in a (three-dimensional) system can therefore control a metal–insulator transition, which is called the Anderson MIT.

[5] The "Hubbard bands" are not bands in the sense of (quasi-)particle excitations, as in metals and semiconductors, but in the sense of incoherent many-particle excitations. Only at the Fermi energy of two and three-dimensional systems, excitations of finite quasiparticle weight might exist in the metallic phase.

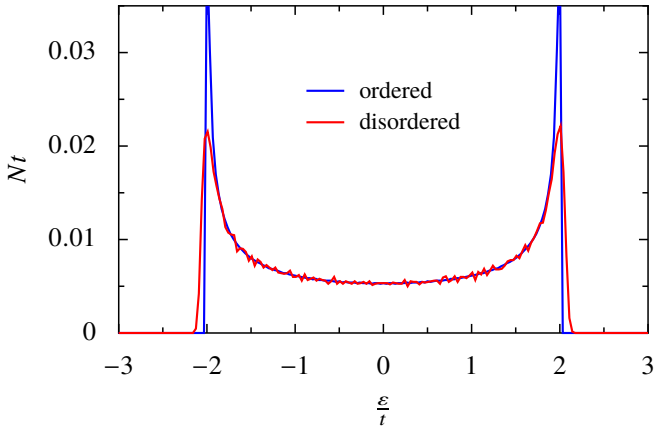

Figure 1.3: *Density of states for the one-dimensional Anderson model.* We show the disordered case with disorder strength $W/t = 0.25$ (red curve) in comparison with the ordered state, $W/t = 0$ (blue curve). The density of states N is very similar in both cases, despite the strong disorder potential.

For an analysis of disorder effects, Anderson has established a tight-binding model that includes random on-site potentials:

$$\mathcal{H} = W \sum_i \varepsilon_i c_i^\dagger c_i - t \sum_{\langle i,j \rangle} c_i^\dagger c_j, \tag{1.9}$$

where $c_i^\dagger$ (c_i) creates (annihilates) an electron on site i, t is the hopping amplitude between nearest neighbors, $|\varepsilon_i| \leq 0.5$ is a random number, and W is the strength of the disorder.

For $W = 0$, but $t \neq 0$, we obtain the limit of the ordinary tight-binding Hamiltonian and the eigenstates are classified as Bloch states, extended over the whole system. On the other hand, in the limit of $t = 0$, but $W \neq 0$, only the on-site energies remain and the electronic state collapses onto individual sites. A numerical analysis of the model given by Eq. (1.9) shows, that for dimension $d = \{1, 2\}$ all states of the system are localized for any finite value of W [11]. Only in the case $d = 3$, one finds a critical value w_c for the ratio $w = (W/t)$, distinguishing whether all states are localized for $w > w_c$, or extended states exist for $w < w_c$. Even for $w < w_c$, localized states still exist in the band edges and are separated from the extended states by the so-called mobility edge, a concept which has been introduced by Mott and which can be used to tune between metallic and insulating behavior [16, 17].

However, the localization argument is more involved. As an example, we implement via Eq. (1.9) a one-dimensional Anderson model on an atomic chain and compare the eigenvalues as well as the density of states with the case of vanishing disorder. We find that for small disorder, the eigenvalues ε are still distributed very similar in comparison to the ordered case and the density of states shows a slightly broadened band width (see Fig. 1.3). The states, however, become exponentially localized, $|\psi(\mathbf{r})|^2 \propto \exp(-|\mathbf{r}-\mathbf{r}_0|/\xi)$ [18] (see the exact solution for one dimension, Ref. [19]). Still, the localization length, ξ, might be large and a small sample with weak disorder might appear to provide a metallic state in an experiment.

Note that instead of crystal momentum, which is a good quantum number only in the translational invariant system, the eigenvalues can be classified by a boundary phase ϕ, which is defined for the hopping amplitude $t \exp(i\phi)$ between the two edges of the chain (see Fig. 1.4).

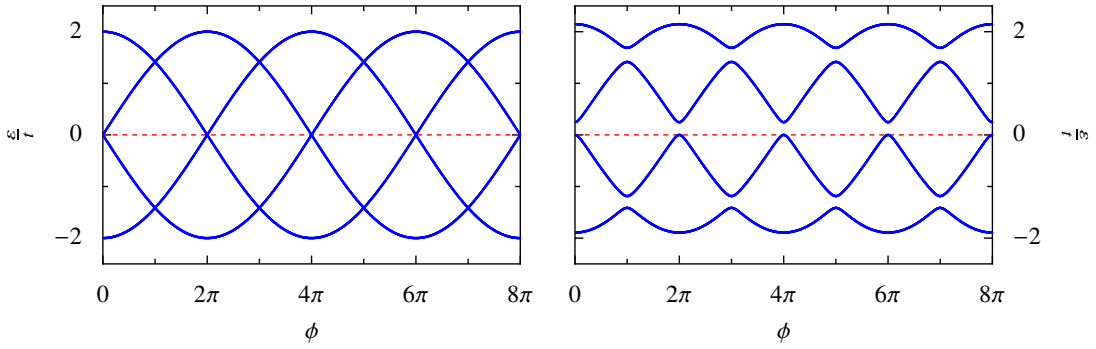

Figure 1.4: *Eigenvalues of an atomic chain with boundary twist.* We model a tight-binding chain with hopping parameter t and four sites. The chain is closed with hopping parameter $t\exp(i\phi)$ between its two edges. In the ordered state (left picture), the eigenvalues are 2π-periodic in the boundary phase ϕ. However, by following a "band" in ϕ-space, the periodicity of this "band" is $2\pi\times$(number of sites). In the disordered case (right picture) with on-site potential $\Delta/t = 0.5$ on only one atom in the chain, the "band" periodicity is only 2π and has lost the system size dependence.

This creates periodic boundary conditions for $\phi = 0$, and anti-periodic boundary conditions for $\phi = \pi$, and has been a tool for several numerical investigations on topological insulators [20]. In an ordered atomic chain with hopping parameter t, the system size L defines the momenta via $k = 2\pi n/L$ in the cosine band $\varepsilon_{\mathbf{k}} = -2t\cos(k)$ (lattice constant set to one). A boundary twist of $\Delta\phi = 2\pi$ leaves the eigenvalues invariant but shifts each state by an amount of $\Delta k = 2\pi/L$ in momentum space (see also Laughlin, Ref. [21]). In this case, the boundary phase translates into crystal momentum for the invariant system, and the Bloch states have a periodictiy of $2\pi L$, dependent on the full system size. In the disordered state, this picture changes. In one dimension, for an arbitrarily small on-site potential on only one site, the states loose any dependence of the system size and become 2π-periodic.

We already mentioned the importance of self-interference in the phenomenon of Anderson localization. For an illustration, we draw the following picture [16, 22]: Let a wave function spread from an origin $\mathbf{r}_0$. To calculate the probability P_A to find the particle at some location $\mathbf{r}_A$, we have to consider each possible path, denoted by i and with amplitude A_i. The amplitudes A_i are given by products of propagators along the path [23]. Together,

$$P_A = \sum_i |A_i|^2 + \sum_{i,j} A_i A_j^*, \tag{1.10}$$

where the latter term is the interference term. When this interference term averages to zero, the Boltzmann approach is valid, considering classical paths for the particle. However, for the special case when one particle wave is scattered in the closed loop of a self-intersecting path (see Fig. 1.5), the interference term is non-trivial, as long as the wave function scatters coherently. The closed path with amplitude A and its time reversal counterpart with amplitude A^{TR} now interfere constructively: in the coherent case, $A^{\mathrm{TR}} = A$, yielding

$$P_A^{\mathrm{qm}} = 4|A|^2, \tag{1.11}$$

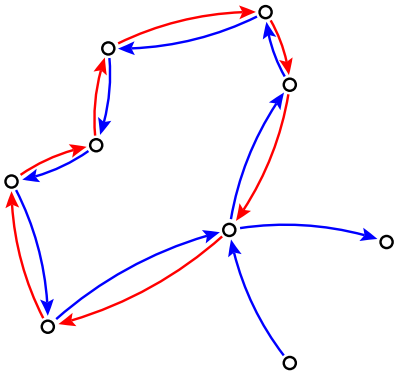

Figure 1.5: *Self-interference in a closed loop.* When the elastic scattering rate is much larger than the inelastic scattering rate, $1/\tau \gg 1/\tau_i$, self-intersecting paths become of importance. Interference between the path in one direction (blue) and its time reversal counterpart (red) results to an increased probability to be located in the loop.

whereas by neglecting the interference effects (in the non-coherent case), we find

$$P_A^{\mathrm{cl}} = 2|A|^2. \tag{1.12}$$

The probability for being located in the closed loop is enhanced by a factor of two: the quantum mechanical wave has a tendency to get trapped compared to classically moving particles.

1.3.2 Strong Disorder and Criticality

Nowadays, it is well accepted that the Anderson transition can be classified as a continuous phase transition, driven by disorder. However, the nature of the corresponding order parameter is still under debate, although it seems to be connected to the local density of states [18, 24].

In 1976, Wegner succeeded in describing the Anderson transition in analogy to magnetic phase transitions [25]. This implies a correlation length ξ (corresponding to the localization length on the insulating side of the transition), which diverges with critical exponent ν when the conductance G reaches the critical value, according to

$$\xi \propto |G - G_c|^{-\nu}\,. \tag{1.13}$$

In a seminal paper, Abrahams, Anderson, Licciardello, and Ramakrishnan (the "Gang of Four") established a scaling theory of localization [1] (see also Ref. [26]). The fundamental principle of this theory is that the dimensionless conductance,

$$g(L) = \frac{2\hbar}{e^2} G(L), \tag{1.14}$$

is a universal function of the system size L and is the only quantity that characterizes the phase transition. Using renormalization group techniques, a β-function can be defined that describes the change of the conductance with the system size,

$$\beta\big(g(L)\big) = \frac{\mathrm{d}\ln g(L)}{\mathrm{d}\ln L}. \tag{1.15}$$

The scaling theory claims that all finite size systems of the same universality class obey the same β-function, Eq. (1.15), only the microscopic details of a sample determine the exact position on the curve. When the system size is increased, the conductance begins to flow with the β-function. If the β-function is positive, the system is characterized as metallic due to a conductance that grows with system size and $g \propto L^{d-2}$ in the thermodynamic limit. If the

β-function is negative instead, the conductance flows to smaller values towards localization, $g \propto e^{-\alpha L}$. Where the β-function crosses zero, an unstable fixed point is found, marking a metal–insulator transition:

$$\begin{aligned} \beta(g) > 0: &\quad \text{metal,} \\ \beta(g) = 0: &\quad \text{metal–insulator transition,} \\ \beta(g) < 0: &\quad \text{insulator.} \end{aligned} \tag{1.16}$$

For the Drude case, Eq. (1.5) demands a β-function of the form

$$\beta^{\text{Drude}}(g) = d - 2. \tag{1.17}$$

For the weakly localized regime at large g, perturbation theory in $1/g$ results in corrections to the constant ohmic behavior that cause a reduction of the β-function for all three dimensions with decreasing conductance g (see Sec. 1.4). In case of strong disorder and small g, an expansion in g shows that the correction results in an increase of the β-function with increasing conductance. A continuous extrapolation between those two limits is valid, as long as the system size is finite [1].

In Fig. 1.6 we adapted the more elaborated four-loop order perturbation terms calculated by Wegner [5] (see also Ref. [18]), which is given by

$$\beta_{\text{o}}\left[g(L)\right] = \begin{cases} d - 2 - \frac{1}{\pi g} - \frac{3\zeta(3)}{4(\pi g)^4}, & g \gg 1 \\ \text{const} + \ln g, & g \ll 1 \end{cases}, \tag{1.18}$$

where $\zeta(n)$ is the Riemannian ζ-function. This four loop calculation is based on the field theoretical description of non-linear σ models [27, 28], which results in the same flow equation for the β-functions and therefore justifies the scaling approach of the "Gang of Four".[6]

Remarkably, in one and two spatial dimensions there is no true metallic behavior, because the β-function is always negative for any finite disorder strength. However, in three dimensions, the β-function crosses the zero line, resulting in an unstable fixed point at $g = g_{\text{c}}$, where the conductance becomes independent of all length scales. This marks the phase transition from metal to insulator: all systems with a macroscopic conductance $g < g_{\text{c}}$ are insulators, and all with $g > g_{\text{c}}$ are metals. Still, even if all states are localized in $d = 2$, the localization length can be arbitrarily large at finite temperature, and a sample might appear metallic in a transport experiment.

Near critical points, physical behavior can often be described with power laws. The exponents of the power laws are universal, meaning, independent of microscopic details, and define the different universality classes. To analyze the scaling behavior for the three-dimensional MIT, we linearize the β-function near the critical point. We follow the elaborations in Refs. [5, 16, 32, 33]. The linearized β-function is given by

$$\frac{\mathrm{d}\ln\left(\frac{g}{g_{\text{c}}}\right)}{\mathrm{d}\ln L} = s \ln\left(\frac{g}{g_{\text{c}}}\right), \tag{1.19}$$

[6] This loop expansion is performed for the small parameter $\hbar/\varepsilon_{\text{F}}\tau$. When the ladder diagrams are calculated for the conductivity (see Sec. A.4), one finds for the diffusion constant $D \propto \varepsilon_{\text{F}}\tau$, see Eq. (A.93) and Eq. (A.104). Diagrams involving crossed diagrams are of order $\hbar/\varepsilon_{\text{F}}\tau$ and correspond to a one-loop expansion. On class of these diagrams, the so-called maximally crossed diagrams, are treated explicitly in Sec. 1.4 and result in a Cooper pole and the phenomenon of weak localization. In the framework of the non-linear σ model for a system with dimension $d = 2 + \epsilon$, where ϵ is small, corrections for higher order in powers of $\hbar/\varepsilon_{\text{F}}\tau$ correspond to a higher number of loops in diagramatic perturbation theory [5, 18, 29–31].

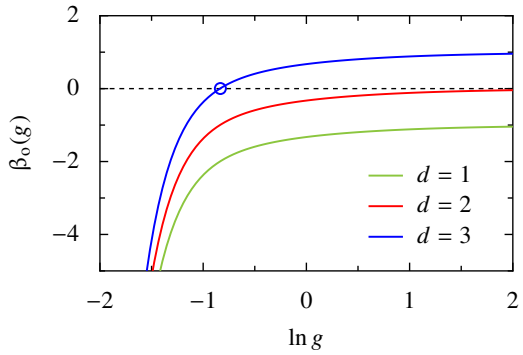

Figure 1.6: *Four-loop order β-function.* As calculated by Wegner [5], the β-function in $d = \{1, 2\}$ is always negative for any finite disorder strength, indicating no true metallic behavior. In $d = 3$, the β-function crosses the zero line, which marks a metal–insulator transition.

where s is the slope of the β-function at g_c. We integrate from a microscopic length scale L_{mic} to the length scale L, where the macroscopic regime begins. This yields

$$\int_{\ln g_{\text{mic}}}^{\ln g} \mathrm{d}\ln\left(\frac{g'}{g_c}\right) \frac{1}{\ln\left(\frac{g'}{g_c}\right)} = s \int_{\ln L_{\text{mic}}}^{\ln L} \mathrm{d}\ln L', \tag{1.20}$$

and finally

$$\left(\frac{L}{L_{\text{mic}}}\right)^s = \frac{\ln\left(\frac{g}{g_c}\right)}{\ln\left(\frac{g_{\text{mic}}}{g_c}\right)} \approx \frac{g - g_c}{g_{\text{mic}} - g_c}, \tag{1.21}$$

where the approximation is justified because in the vicinity of the critical point, the values of g are varying slowly. Therefore, on the macroscopic scale, g is a function of L^s.

We define the length scale ξ, as well as the control parameter η via

$$\xi \propto \left(\frac{g_c}{g_{\text{mic}} - g_c}\right)^\nu = \eta^{-\nu}, \tag{1.22}$$

where ξ is the localization length at the insulating side of the phase transition and η controls the microscopic conductance, which allows us to conclude

$$g(L) = g_c \left[1 - \left(\frac{L}{\xi}\right)^{\frac{1}{\nu}}\right]. \tag{1.23}$$

It is assumed that the conductance is a universal function of L/ξ at all length scales—which is the key assumption of the one-parameter scaling theory by the "Gang of Four". In comparison with Eq. (1.21), we identify

$$\nu = \frac{1}{s} \tag{1.24}$$

and the critical exponent of the localization length is given by the inverse slope of the β-function at the critical point. As Ohm's law requires

$$g \propto \left(\frac{L}{\xi}\right)^{d-2}, \tag{1.25}$$

we conclude for the conductivity from Eq. (1.5) to scale like

$$\sigma(L \to \infty) \propto \frac{1}{\xi^{d-2}} \propto \eta^{(d-2)\nu}. \tag{1.26}$$

The latter relation indicates that the conductivity for a macroscopic sample vanishes continuously when we approach the critical point in any dimension $d > 2$.

The four-loop order of the β-function is derived for dimensions $d = 2 + \epsilon$, where ϵ is small, but finite, to provide a critical point. The resulting critical exponent ν is estimated to be [5, 29–31]

$$\nu = \epsilon^{-1} - \tfrac{9}{4}\zeta(3)\,\epsilon^2 + O\left(\epsilon^3\right). \tag{1.27}$$

In disordered systems, the critical exponent should satisfy the condition $\nu \geq d/2$ [34].[7] Apparently, the ϵ-expansion provides no qualitative agreement with this criterion, as already pointed out by Wegner [5], and higher order terms are important.

Vollhardt and Wölfle derived an explicit value of $\nu = 1$ for $d = 3$ from a self-consistent theory of Anderson localization, where the maximally crossed diagrams are included to all orders [36, 37]; an even more elaborate self-consistent theory adjusted the value to $\nu = 1.5$ [38]. However, recent numerical work arrived at a precision where many different models and approaches agree on the $d = 3$ critical exponent and find $\nu \approx 1.57$ [39–42], thus the universality class of the Anderson transition seems to be settled [43].

Unfortunately, whereas the numerical efforts give a somehow complete picture of the Anderson metal–insulator transition in three dimensions, experimental findings for ν are not so easily accomplished, and there is still little evidence for this value in condensed matter systems (however, there is a recent report in Ref. [44]). However, setups using cold atomic gases are able to simulate the universality class of the Anderson transition. In their case, the critical behavior agrees with the observations of the numerical results [45].

In experiments, it is practicable to change the temperature T during the measurement instead of the length of the sample. A length scale corresponds to the inverse of an energy scale ε, and $T \propto \varepsilon \propto 1/L$, which is evident by taking units where $c = 1$, $k_\mathrm{B} = 1$, and $\hbar = 1$.[8] In this sense, cooling of a sample can reveal the same physical behavior as enlarging the system size, and a measurement done at a finite size sample at sufficiently low temperatures reveals the insulating or metallic character [46].

1.3.3 Criticality in the Symplectic Class

In the following, we expand the findings of the previous section to classes of different symmetry, classified by invariance under time reversal and spin rotation [47–49]. We use the notation of Ref. [18].

If time reversal symmetry is broken, Hamiltonians are simply given by hermitian matrices,

$$\mathcal{H} = \mathcal{H}^\dagger. \tag{1.28}$$

This set of matrices is invariant under unitary transformation, $\left(\mathcal{U}^\dagger\mathcal{H}\mathcal{U}\right)^\dagger = \mathcal{U}^\dagger\mathcal{H}\mathcal{U}$, and defines the unitary symmetry class [18].

If time reversal symmetry is preserved, we find $\mathcal{H} = \mathcal{T}\mathcal{H}\mathcal{T}^{-1}$, where $\mathcal{T}$ is the time inversion operator. By writing this operator in the form $\mathcal{T} = \mathcal{U}C$, where $\mathcal{U}$ is unitary and C is complex conjugation,

$$\mathcal{H} = \mathcal{U}C\mathcal{H}C^{-1}\mathcal{U}^{-1} = \mathcal{U}\left(\mathcal{H}^\dagger\right)^\mathrm{T}\mathcal{U}^{-1} = \mathcal{U}\mathcal{H}^\mathrm{T}\mathcal{U}^{-1}. \tag{1.29}$$

[7] Originally, this law has been formulated for the specific heat exponent α, which has to satisfy $\alpha = 2 - d\nu$ [35]. However, this criterion is also valid for Anderson localization, see Ref. [34].

[8] Aside this dimensional analysis, in the case of critical behavior, an additional dynamical exponent z has to be taken into account. See Eq. (1.37).

Twofold time reversal must leave the Hamiltonian unchanged, resulting in two realizations for $\mathcal{U}$. In the first case, this operator can be represented by the identity operator [18] and

$$\mathcal{H} = \mathcal{H}^{\mathrm{T}}, \tag{1.30}$$

which defines the set of real symmetric matrices. This set is invariant under orthogonal rotation, $\left(O^{\mathrm{T}}\mathcal{H}O\right)^{\mathrm{T}} = O^{\mathrm{T}}\mathcal{H}O$, and defines the orthogonal symmetry class [18]. In the second case, $\mathcal{U}$ can be represented as $\mathcal{U} = i\sigma_{\mathrm{y}}$ [18]. This corresponds to the time-reversal symmetric class where spin-rotation symmetry is broken, here

$$\mathcal{H} = \sigma_{\mathrm{y}}\mathcal{H}^{\mathrm{T}}\sigma_{\mathrm{y}}. \tag{1.31}$$

This set of Hamiltonians is invariant under a restricted set of unitary transformations $\mathcal{U}_{\mathrm{sp}}$, which conserve $\sigma_{\mathrm{y}} = \mathcal{U}_{\mathrm{sp}}\sigma_{\mathrm{y}}\mathcal{U}_{\mathrm{sp}}^{\mathrm{T}}$, so that $\sigma_{\mathrm{y}}\left(\mathcal{U}_{\mathrm{sp}}^{\dagger}\mathcal{H}\mathcal{U}_{\mathrm{sp}}\right)^{\mathrm{T}}\sigma_{\mathrm{y}} = \mathcal{U}_{\mathrm{sp}}^{\dagger}\mathcal{H}\mathcal{U}_{\mathrm{sp}}$. This defines the symplectic class, containing Hamiltonians with strong spin–orbit interactions [18].

For each of the three symmetry classes, orthogonal, unitary, and symplectic, distinct nonlinear σ models can be constructed [18], resulting in distinguished β-functions. In the last section, we have considered the β-function for the orthogonal case. In the unitary and symplectic case, the β-functions are given up to four loop order [5, 16, 18, 50] by

$$\beta_{\mathrm{u}}\left[g(L)\right] \approx (d-2) - \frac{1}{2\left(\pi g\right)^2} - \frac{3}{8\left(\pi g\right)^4}, \tag{1.32}$$

$$\beta_{\mathrm{sp}}\left[g(L)\right] \approx (d-2) + \frac{1}{2\pi g} - \frac{3\xi(3)}{64\left(\pi g\right)^4}. \tag{1.33}$$

Whereas in the unitary case, the β-function has the same qualitative shape as in the orthogonal case, there is a drastic change in the symplectic symmetry class (Fig. 1.7): the β-function for weak disorder increases for decreasing conductance, but finally changes the slope towards the localized regime. This results in a positive β-function in the two-dimensional, weakly disordered case, as well as a critical point indicating a transition from metallic to insulating behavior (sMIT). As this two-dimensional metallic state exists only in the symplectic case, we call this metal a symplectic metal.

We follow again the estimations in Eqs. (1.19)–(1.21). The critical behavior in the symplectic case is again covered by the slope s of the β-function at the fixed point. For $d > 2$, we can relate conductance and conductivity via Ohm's law and find a critical finite value for the conductance, as well as a vanishing conductivity at the critical point in analogy to Eq. (1.25) and Eq. (1.26). This defines the sMIT in $d = 3$. However, as $d = 2$ is the marginal dimension, we find that in the ohmic regime the conductance is no longer dependent on the length scale of the system and allows no such simple treatment. Actually, as we cannot formally distinguish between conductance and conductivity in $d = 2$, the conductivity will be given by a finite critical value.

How to characterize the metal–insulator transition then? In the vicinity of the critical point, we can use the finite size scaling directly [51]. We consider again Eqs. (1.19)–(1.21) with an upper integration limit of system size L,

$$\frac{\ln g(L) - \ln g_{\mathrm{c}}}{\ln g_{\mathrm{mic}} - \ln g_{\mathrm{c}}} = \left(\frac{L}{L_{\mathrm{mic}}}\right)^{1/\nu}, \tag{1.34}$$

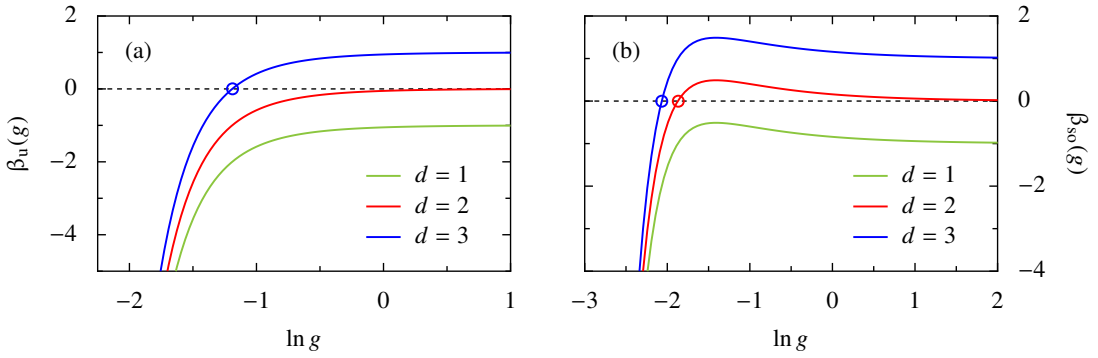

Figure 1.7: *Four-loop order β-functions for the unitary and symplectic class.* (a) The β-function of the unitary case is similar as in the orthogonal case. A metal–insulator transition occurs only for $d = 3$. (b) In the symplectic case, the β-function is enhanced for weak disorder, resulting in metallic behavior for two-dimensional systems (symplectic metal). For strong disorder, the fourth-order term of the loop expansion reduces the β-function and a metal–insulator transition occurs in $d = 2$, which is absent in the orthogonal and unitary symmetry class (symplectic metal–insulator transition, sMIT).

where g_{mic} and L_{mic} are microscopic properties. Assuming[9]

$$\ln g_{\text{mic}} - \ln g_{\text{c}} \approx \frac{g_{\text{mic}} - g_{\text{c}}}{g_{\text{c}}} \propto \frac{W_{\text{c}} - W_{\text{mic}}}{W_{\text{c}}} = w, \tag{1.35}$$

where W_{mic} is the microscopic disorder strength and w the disorder induced control parameter, we find

$$g(L) = g_{\text{c}} \exp\left[Aw\left(\frac{L^{1/\nu}}{L_{\text{mic}}}\right)\right], \tag{1.36}$$

where A is some constant.

In the vicinity of a quantum critical point, if $L \approx \infty$, but $T \neq 0$, the temperature behaves like an effective spatial dimension,

$$L_{\text{eff}} \propto T^{-1/z}, \tag{1.37}$$

where z is the dynamical exponent, and we find

$$g(T) = g_{\text{c}} \exp\left[Aw\left(\frac{T_{\text{mic}}}{T}\right)^{1/\nu z}\right]. \tag{1.38}$$

By changing the amount of disorder w through some control parameter, this kind of scaling behavior should be observable in an experiment. We show a plot of Eq. (1.38) in Fig. 1.8.

[9] We assume that for any finite system, the conductance will smoothly depend on the changing parameters. The change of the microscopic conductance translates into a change of the microscopic disorder strength. We assume the dependence to be linear in lowest order. This approximation is valid because near the critical point, the behavior should be determined by the critical exponents alone.

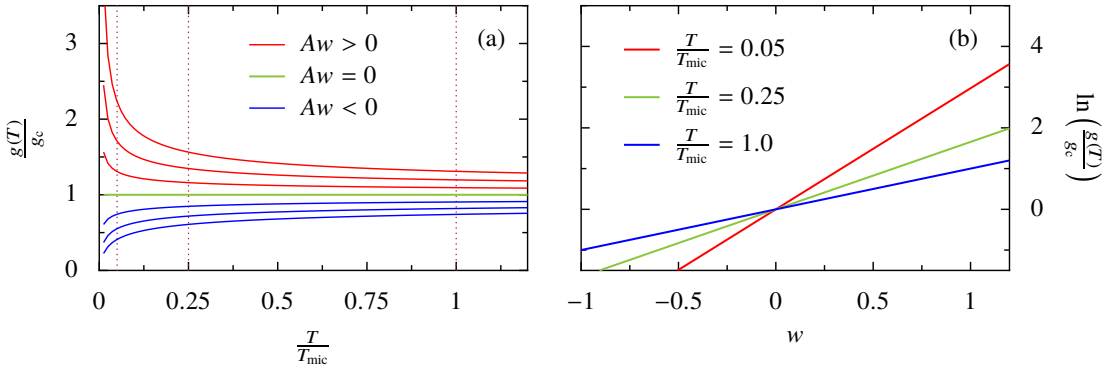

Figure 1.8: *Scaling behavior of the conductance.* (a) The temperature dependence of the conductance corresponding to Eq. (1.38). The dimensionless disorder parameter is given by Aw. For positive Aw, the system scales to a metallic state $g = \infty$, whereas for negative Aw, it scales towards an insulating state $g = 0$. The separatrix is given for $w = 0$, where the conductance is independent of the temperature scale. In this plot, $\nu z = 2.75$. (b) Logarithmic conductance as function of the disorder parameter. All lines meet in the critical point. The slope is given by $(T_{\text{mic}}/T)^{1/\nu z}$.

The universality of this symplectic Anderson transition has been studied in many numerical investigations, where symplectic versions of the Anderson model are analyzed. One example is the two-dimensional Ando model [52],

$$\mathcal{H} = W \sum_{i,\sigma} \varepsilon_i c^\dagger_{i\sigma} c_{i\sigma} + \sum_{\langle i,j\rangle\, \sigma\sigma'} V_{ij}(\sigma,\sigma') c^\dagger_{i\sigma} c_{j\sigma'}, \tag{1.39}$$

where the hopping elements $V_{ij}(\sigma,\sigma')$ are represented by a matrix in spin space with diagonal entries $(-t)$ and non-diagonal entries modeling spin–orbit coupling. The Ando model and other related models seem to converge against a critical exponent $\nu \approx 2.75$ [51, 53, 54].[10] Quite recently, it has been suggested that current technology is close to identifying the symplectic Anderson transition in a cold atom setup. Models for these experiments predict a critical exponent in these systems of $\nu = 2.67 \pm 0.14$ [58].

To close this section on the symplectic phase transition, we like to mention that the interplay between the Anderson transition and topology is still under debate. A topological term with $\mathbb{Z}_2$-symmetry in the σ models of the symplectic class apparently constrains localization [18]. An analysis by Fu and Kane showed that the topological symplectic non-linear σ model contains two distinct, but equivalent fixed points that describe a transition to a topologically trivial as well as a topologically non-trivial insulator [59]. Therefore, the critical (bulk) exponents are essentially the same at both possible transitions and both fixed points belong to the same symplectic universality class. Numerical work supports this prediction [60–62].[11] However, a

[10] Actually, it turned out that the conductance of a disordered system is not a self-averaging quantity and is dependent on the specific microscopic scattering potential in a sample. As the conductance distribution is becoming broad near the Anderson transition, the simple scaling law for the dimensionless conductance is not valid [55]. Instead, the distribution of the conductance and its mean value has to be studied [56, 57]. Therefore, for a numerical investigation, one takes an ensemble of many samples for each given disorder strength and tracks the scaling of the mean conductance.

[11] There seems to be still a discrepancy with the exponent found in the Kane-Mele model, where $\nu \approx 1.6$ instead of the value $\nu \approx 2.75$ found in Ref. [63].

difference in the critical behavior should be visible at the boundaries of the two-dimensional system, where topological states are expected [64, 65].

1.4 The Cooperon: Weak Localization Corrections

In the last section, we discussed the emergence of the Anderson MIT in the strongly disordered regime. In this section, we focus on the weakly disordered regime and consider a certain kind of diagrams with crossed impurity lines within Kubo's linear response theory. These diagrams result in a quantum correction of the order of e^2/h, which is added to the classical result for the Drude (or Boltzmann) conductivity. The effect of this quantum correction is called weak localization (WL).

In App. A, we give a review of the Kubo formalism, the derivation of the Boltzmann conductivity for a disordered electron gas, and the treatment of the diffusion pole in the density response. Here, we directly start with the evaluation of quantum corrections in the current–current correlation function. These play an important role for transport measurements in two-dimensional materials at low temperatures, especially when a magnetic field is applied. As we will see, magneto-transport is a basic technique to reveal physics regarding disorder, dimensionality, electron–electron interaction, superconductivity, and spin–orbit coupling.

Taking care of diagrams with crossed impurity lines is a complicated procedure. However, there exists one subset of diagrams that can be treated with relative ease: the maximally crossed diagrams, first considered by Langer and Neal in 1966 [66].

1.4.1 Maximally Crossed Diagrams

To describe the correction terms due to WL, we follow the scheme of Bergmann [67], who summarized the original publications by Hikami et al. [6], Altshuler et al. [68], and Maekawa and Fukuyama [69]. Further details about this calculation can be found in Refs. [23, 33, 70, 71]. To keep the formulas shorter, we introduce the notation

$$\int \frac{\mathrm{d}k^d}{(2\pi)^d} \equiv \int_{\mathbf{k}} \tag{1.40}$$

for a d-dimensional momentum integral.

The correction to the conductivity is given by the (zero external momentum) current–current response function,

$$\begin{aligned}\delta\sigma_{\alpha\beta}(\omega) = \frac{e^2}{\pi}\int_{-\infty}^{\infty}\mathrm{d}\omega' \frac{f(\hbar\omega'-\hbar\omega)-f(\hbar\omega')}{\hbar\omega}\int_{\mathbf{k}}\int_{\mathbf{k}'} v_\alpha(\mathbf{k})v_\beta(\mathbf{k}')\times \\ G^{\mathrm{ret}}(\mathbf{k},\omega')G^{\mathrm{adv}}(\mathbf{k},\omega'-\omega)C(\mathbf{k},\mathbf{k}',\omega,\omega')G^{\mathrm{ret}}(\mathbf{k}',\omega')G^{\mathrm{adv}}(\mathbf{k}',\omega'-\omega),\end{aligned} \tag{1.41}$$

where $G^{\mathrm{ret/adv}}$ are retarded and advanced Green's functions, f is the Fermi function, and each current vertex contributes a factor $e\hbar\mathbf{k}/m \equiv e\mathbf{v}$. For the scattering processes in the vertex $C(\mathbf{k},\mathbf{k}',\omega,\omega')$, we take into account diagrams with crossed impurity lines between retarded and advanced Green's functions. This crossing of impurity lines affects the order of a diagram in form of a small parameter $\hbar/p_\mathrm{F} l \propto \hbar/\varepsilon_\mathrm{F}\tau$, where p_F and ε_F are the Fermi momentum and Fermi energy, l is the mean free path, and τ the relaxation time. For $l \gg k_\mathrm{F}^{-1}$, which

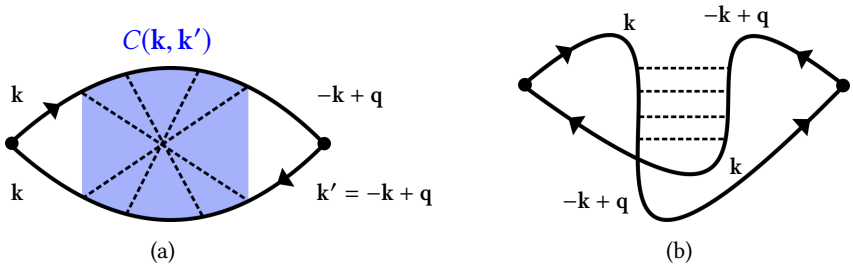

Figure 1.9: *Disentangling of maximally crossed diagrams.* Propagating electrons are represented as solid lines, the Cooperon as blue area, scattering at impurities as dashed lines, the current vertex as black circle. (a) WL corrections are calculated by evaluation of the maximally crossed diagrams. (b) The crossed diagrams can be disentangled by rearranging one of the propagator lines. The crossed diagrams appear to have a diffusion pole like structure for $\mathbf{q} \to 0$, but in the particle–particle channel. The amplitude for these diagrams is called the Cooperon and its scattering processes are characterized by the momentum relation $\mathbf{k} \sim -\mathbf{k}'$, rather than $\mathbf{k} \sim \mathbf{k}'$ as it is the case for the diffusion pole.

means that the mean free path is much larger that the average particle distance, this enables a well-behaved perturbation in quantum corrections to the conductivity [16].

A subset that yields the first order quantum correction contains the already mentioned maximally crossed diagrams.[12] These diagrams describe processes where lines, representing the scattering at some impurity, connects particle propagation (described by the retarded Green's function) with hole propagation (described by the advanced Green's function) in exactly reversed order, see Fig. 1.9 (a). This can be visualized with a particle that scatters at impurities located at $\mathbf{r}_1$, $\mathbf{r}_2$, $\mathbf{r}_3$, ... and interferes with its time-reversed partner, scattering at the impurities exactly in opposite order, at ..., $\mathbf{r}_3$, $\mathbf{r}_2$, $\mathbf{r}_1$. Therefore, the propagation can be visualized as a self-intersecting path, as depicted in Fig. 1.5.

Another visualization is given by a replacement of the advanced Green's function of momentum ($\mathbf{k}$) with a retarded Green's function with momentum ($-\mathbf{k}$) [70]. In the correlation function, this yields a disentangling of the maximally crossed diagrams and a rather simple scattering structure is revealed, which is given by a diffusion-like ladder in the particle–particle channel, see Fig. 1.9 (b). Therefore, this diffusion-like structure is described by a momentum transfer $\mathbf{q} = \mathbf{k} + \mathbf{k}'$, and the dominant processes are back scattering processes with $\mathbf{k}' \sim -\mathbf{k}$. This is a difference to the diffusive ladder in the current–current correlation function, where $\mathbf{k}' \sim \mathbf{k}$ (see Sec. A.4).[13] The diffusion-like pole structure in the particle–particle channel with two momenta $\mathbf{k}$ and $-\mathbf{k}$ reminds of Cooper pairs, and therefore $C(\mathbf{k}, \mathbf{k}', \omega, \omega')$ is called the Cooperon.

[12] There are still further diagrams that contribute to the same order, but are insensitive to small magnetic fields or temperature in comparison to the maximally crossed diagrams, whereas the maximally crossed diagrams contain the singular behavior in the low frequency, low momentum limit. See also Ref. [70], footnote on page 432.

[13] Note that the momentum transfer in the Cooperon is an internal momentum, over which has to be integrated, whereas the $\mathbf{q}$ in the diffusion calculation (Sec. A.4) is an external momentum.

Due to the importance of back-scattering processes, we replace $\mathbf{k}' = -\mathbf{k} + \mathbf{q}$ in the Green's function and linearize the kinetic energy near the Fermi energy

$$\xi_{\mathbf{k}'} = \frac{\hbar^2(\mathbf{k}')^2}{2m} = \frac{\hbar^2}{2m}(-\mathbf{k}+\mathbf{q})^2 \approx \xi_{\mathbf{k}} - \hbar \mathbf{v}_\mathrm{F}(\mathbf{k})\cdot\mathbf{q}. \tag{1.42}$$

Due to this simplification, the vertex depends only on $C(\mathbf{q},\omega)$ and we can split the two momentum integrals in Eq. (1.41) into integrals over $\mathbf{k}$ and $\mathbf{q}$. The velocities are set to be the Fermi velocities, which we assume further to be isotropic,

$$v_\alpha(\mathbf{k})v_\beta(\mathbf{k}') \approx -\delta_{\alpha\beta}v_\mathrm{F}^2. \tag{1.43}$$

By following the calculation steps for the diffusion pole, see Sec. A.4, Eq. (1.41) simplifies to

$$\delta\sigma_{\alpha\beta}(\omega) = \frac{e^2}{\pi}\int_{-\infty}^{\infty} \mathrm{d}\omega' \frac{f(\hbar\omega'-\hbar\omega)-f(\hbar\omega')}{\hbar\omega}\int_{\mathbf{q}} K(\mathbf{q},\omega)C(\mathbf{q},\omega), \tag{1.44}$$

where $K(\mathbf{q},\omega)$ denotes the $\mathbf{k}$-integral that is given by

$$\begin{aligned}
K(\mathbf{q},\omega) &= -\delta_{\alpha\beta}v_\mathrm{F}^2\int_{\mathbf{k}} G^{\mathrm{ret}}(\mathbf{k},\omega')G^{\mathrm{adv}}(\mathbf{k},\omega'-\omega)G^{\mathrm{ret}}(-\mathbf{k}+\mathbf{q},\omega')G^{\mathrm{adv}}(-\mathbf{k}+\mathbf{q},\omega'-\omega) \\
&= -\delta_{\alpha\beta}v_\mathrm{F}^2 N_\mathrm{F}\int \frac{\mathrm{dS}_d(\mathbf{k})}{\mathrm{S}_d(\mathbf{k})}\int_{-\infty}^{\infty}\mathrm{d}\xi_{\mathbf{k}} \frac{\hbar^4}{\left(\xi_{\mathbf{k}}-\hbar\omega'-\frac{i\hbar}{2\tau_0}\right)\left(\xi_{\mathbf{k}}-\hbar\omega'+\hbar\omega+\frac{i\hbar}{2\tau_0}\right)}\times \\
&\qquad \frac{1}{\left(\xi_{\mathbf{k}}-\hbar\mathbf{v}_\mathrm{F}\cdot\mathbf{q}-\hbar\omega'-\frac{i\hbar}{2\tau_0}\right)\left(\xi_{\mathbf{k}}-\hbar\mathbf{v}_\mathrm{F}\cdot\mathbf{q}-\hbar\omega'+\hbar\omega+\frac{i\hbar}{2\tau_0}\right)},
\end{aligned} \tag{1.45}$$

where S_d is the d-dimensional unit sphere and τ_0 is the elastic lifetime [67]. Closing the integral in either complex half plane yields the same result, and Eq. (1.45) simplifies to

$$\begin{aligned}
K(\mathbf{q},\omega) &= -\delta_{\alpha\beta}v_\mathrm{F}^2\frac{2\pi i N_\mathrm{F}}{d}\frac{\hbar^4}{\left(\hbar\omega+\frac{i\hbar}{\tau_0}\right)(\hbar\mathbf{v}_\mathrm{F}\cdot\mathbf{q})}\frac{-2(\hbar\mathbf{v}_\mathrm{F}\cdot\mathbf{q})}{\left(\hbar\omega+\frac{i\hbar}{\tau_0}\right)^2-(\hbar\mathbf{v}_\mathrm{F}\cdot\mathbf{q})^2} \\
&\approx \delta_{\alpha\beta}\frac{4\pi i v_\mathrm{F}^2 N_\mathrm{F}\hbar^4}{\left(\hbar\omega+\frac{i\hbar}{\tau_0}\right)^3 d} = -\delta_{\alpha\beta}\frac{4\pi v_\mathrm{F}^2 N_\mathrm{F}\hbar^4\left(\frac{\tau_0}{\hbar}\right)^3}{(1-i\omega\tau_0)^3 d} \approx -\delta_{\alpha\beta}\frac{4\pi v_\mathrm{F}^2 N_\mathrm{F}\hbar\tau_0^3}{d},
\end{aligned} \tag{1.46}$$

where for the latter step we assumed $\mathbf{v}_\mathrm{F}\cdot\mathbf{q} \ll 1/\tau_0$ (which is $lq \ll 1$ as the diffusive limit requests) and $\omega \ll 1/\tau_0$. By further using Eq. (A.74) and the diffusion constant in Eq. (A.93), $D = v_\mathrm{F}^2\tau_0/d$, the conductivity in the low frequency (and small momentum transfer) limit can then be expressed as

$$\delta\sigma_{\alpha\beta}(\omega\sim 0) = -\delta_{\alpha\beta}4e^2 N_\mathrm{F} D\tau_0^2\int_{\mathbf{q}} C(\mathbf{q},\omega). \tag{1.47}$$

For the calculation of the Cooperon amplitude $C(\mathbf{q},\omega)$ we follow the derivation of the diffusion ladder in Sec. A.4. One important difference is the higher order due to the crossed diagrams

that results in an additional prefactor C^0 in comparison to the diffusion vertex. The Dyson equation for the Cooperon is

$$C(\mathbf{q},\omega) = C^0 + C^0\Pi(\mathbf{q},\omega)C(\mathbf{q},\omega) \tag{1.48}$$

where Π denotes the particle–hole propagator. This yields

$$C(q) = \frac{C^0}{1 - C^0\Pi(q)}, \tag{1.49}$$

where, by using Eq. (A.31) for the elastic scattering rate,

$$C^0 = \Gamma^0 = \frac{n_i V^2}{\hbar^2} = \frac{1}{2\pi\hbar N_\mathrm{F}\tau_0}. \tag{1.50}$$

For Π, we find the same expression Eq. (A.92) as in the diffusion case, except that the hole propagator has changed into a particle propagator.

As final result for the Cooperon, we find

$$C(q,\omega) = \frac{1}{2\pi\hbar N_\mathrm{F}\tau_0}\frac{1}{Dq^2\tau_0 - i\omega\tau_0}, \tag{1.51}$$

The Cooperon shows for $\omega \to 0$ a diffusion-like pole for $\mathbf{q} = 0$, which expresses $\mathbf{k}' = -\mathbf{k}$.

In the following, we suppress the indices $\{\alpha, \beta\}$ and find for the quantum correction of the longitudinal conductivity

$$\delta\sigma(\omega \sim 0) = -\frac{4e^2 D\tau_0}{h}\int_\mathbf{q}\frac{1}{Dq^2\tau_0 - i\omega\tau_0}. \tag{1.52}$$

Eq. (1.52) is the main result of this section. In the following we determine the $\mathbf{q}$-integral. We do so by introducing a cutoff for the upper integration limit given by

$$q_\mathrm{max} = \frac{1}{\sqrt{D\tau_0}}, \tag{1.53}$$

which is related to the shortest diffusion step during one single collision time via inserting the diffusion constant, $q_\mathrm{max} \sim 1/l$. For the lower limit cutoff, we introduce an inelastic scattering time,

$$q_\mathrm{min} = \frac{1}{\sqrt{D\tau_\mathrm{i}}}, \tag{1.54}$$

which defines a length scale for the inelastic scattering, also known as the Thouless inelastic length, $L_\mathrm{i} = \sqrt{D\tau_\mathrm{i}}$ [46]. Due to the lower cutoff in $\mathbf{q}$, we can take safely the low frequency limit $\omega \to 0$, which simplifies the $\mathbf{q}$ integration. For $1/\tau_0 \gg \omega$, we find for the different spatial dimensions,

$$\delta\sigma \approx -\frac{e^2}{h}\times\begin{cases}\dfrac{2\nu_\mathrm{F}\tau_0}{\pi}\left(\sqrt{\dfrac{\tau_\mathrm{i}}{\tau_0}} - 1\right) & d = 1\\[2ex] \dfrac{1}{\pi}\ln\left(\dfrac{\tau_\mathrm{i}}{\tau_0}\right) & d = 2\\[2ex] \dfrac{2\sqrt{3}}{\pi^2\nu_\mathrm{F}\tau_0}\left(1 - \sqrt{\dfrac{\tau_0}{\tau_\mathrm{i}}}\right) & d = 3\end{cases}. \tag{1.55}$$

We like to emphasize several aspects:

- The ratio of elastic and inelastic life time is assumed to be much smaller than one, $\tau_0/\tau_i \ll 1$, therefore all corrections carry a negative sign and reduce the classical conductivity.
- All three expressions carry the same prefactor e^2/h, which indicates the quantum nature of the correction ($e^2/h \approx 1/25\,\mathrm{k\Omega}$). An increase of the inelastic scattering rate $\propto 1/\tau_i$ prevents the localization effect and the conductivity increases.
- Regarding the significance of the quantum corrections, we find a strong dimensional dependence in the elastic scattering rate. In three dimensions, if the elastic scattering rate is increasing, the quantum correction grows proportionally. In one-dimensional wires, instead, the correction actually becomes weaker with stronger elastic scattering rate. In the marginal two-dimensional case, the quantum correction increases with the logarithm of the elastic scattering rate. We like to stress at this point that this approximation is only in first order of the quantum corrections and can only show tendencies.[14]
- The inelastic scattering rate grows with temperature, and often a power law behavior is assumed, $1/\tau_i \propto T^p$ [46, 67], with p varying between 1 and 5 for different systems and mechanisms, but mostly $1 \leq p < 2$. For electron–electron interactions, logarithmic corrections have to be included: for very low temperatures, the electron–electron dephasing leads to $1/\tau_i \propto T\ln(T)$ in two dimensions [72, 73]. More recent publications find $1/\tau_i \propto T^2\ln(T)$ in the relatively high-temperature regime and $1/\tau_i \propto T$ in the low temperature regime for electron–electron interaction [74, 75].
- Instead of temperature dependence, we can study the change in the conductance if the system size L is enlarged. Instead of a inelastic scattering time, the finite size is introduced as a cutoff parameter for the integration. This leads to the replacement

$$\frac{1}{\tau_i} \to \frac{D}{L^2}, \tag{1.56}$$

and we connect also the elastic scattering time with some microscopic length scale l, so that

$$\frac{1}{\tau_0} \to \frac{D}{l^2}. \tag{1.57}$$

Then we find for the q-integral by further using $v_F\tau_0 = l$ [46, 76]

$$\delta\sigma \approx -\frac{e^2}{h} \times \begin{cases} \dfrac{2}{\pi}(L-l) & d=1 \\ \dfrac{2}{\pi}\ln\left(\dfrac{L}{l}\right) & d=2 \\ \dfrac{2}{\pi^2}\left(\dfrac{1}{l}-\dfrac{1}{L}\right) & d=3. \end{cases} \tag{1.58}$$

Whereas the negative contribution to the conductivity from WL grows with larger system size in one and two dimensions without limit, the amplitude in the three-dimensional case is bounded by the microscopic length l, $0 < |\delta\sigma| < 2e^2/h\pi l$.

[14] See the discussion in Section 1.3.2.

In the next section, we examine the WL correction in presence of a magnetic field. Because interference of time-reversed paths are all-dominant, the localization characteristics can be probed with a time-reversal breaking magnetic field.

1.4.2 Magneto-Conductivity

Weak localization has become an important tool for experimentalists. Especially the case of two spatial dimensions dragged a lot of attention, because a) the corrections to the Drude result are generally more important in the marginal dimension, and b) one can use the tool of a magnetic field perpendicular to the plane, which is not the case in one-dimensional systems (due to the missing transversal transport components) or three-dimensional systems (due to the rotational invariance) [67]. On account of the time-reversal breaking in a magnetic field, a wave in a self-intersecting path accumulates an additional phase due to the vector potential, which leads to a strong modification in the interference term: the propagating wave acquires a phase of $\Delta\phi = 2\Phi\, e/\hbar$ between a path and its time reversed, where Φ is the magnetic flux encircled by the path. This phase factor results in a decrease of the constructive interference and suppresses localization—an increasing magnetic field increases the conductance, leading to a positive magneto-conductivity and a negative magneto-resistivity.

In the following, we concentrate on WL for two-dimensional systems exposed to a perpendicular magnetic field B. This calculation follows Refs. [33, 67, 71]. We assume that the mean free path is smaller than the magnetic length,

$$l^2 < l_B^2 = \frac{\hbar}{2eB}, \tag{1.59}$$

and that the magneto-resistivity effects according to the Lorentz force can be neglected. In the presence of a magnetic field, time reversal symmetry is broken and it is convenient to change into a real space representation. Any path accumulates a path-dependent phase factor, which we can describe by

$$G^{\mathrm{ret}}(\mathbf{r},\mathbf{r}') = G^{\mathrm{ret}}(\mathbf{r}-\mathbf{r}')\exp\left[\frac{ie}{\hbar}\int_{\mathbf{r}}^{\mathbf{r}'} \mathrm{d}s A(s)\right]. \tag{1.60}$$

Note that due to the path dependence, the explicit translational invariance is broken. In the Cooperon,[15] the phase factor appears in the form

$$G^{\mathrm{adv}}(\mathbf{r},\mathbf{r}')G^{\mathrm{ret}}(\mathbf{r},\mathbf{r}') = G^{\mathrm{adv}}(\mathbf{r}-\mathbf{r}')G^{\mathrm{ret}}(\mathbf{r}-\mathbf{r}')\exp\left[\frac{2ie}{\hbar}\int_{\mathbf{r}}^{\mathbf{r}'} \mathrm{d}s A(s)\right]. \tag{1.61}$$

The equation in direct space and time for the Cooperon is given by

$$\left[\frac{\partial}{\partial t} + D\left(\nabla - \frac{2ie\mathbf{A}}{c}\right)^2\right] C(\mathbf{r},\mathbf{r}',t,t') = \frac{1}{2\pi\hbar N_{\mathrm{F}}\tau_0^2}\delta(\mathbf{r}-\mathbf{r}')\delta(t-t'), \tag{1.62}$$

which corresponds to a diffusive-like motion of the Cooperon.

[15] But not in the diffusion pole calculation!

Due to the small momentum transfer $\mathbf{q}$, $q^2 = (\mathbf{k} + \mathbf{k}')^2 \longrightarrow (\mathbf{q} + 2e\mathbf{A}/c)^2$, becomes quantized as in standard Landau level quantization,

$$q_n^2 = \frac{4eB}{\hbar}\left(n + \frac{1}{2}\right), \tag{1.63}$$

and for the Cooperon we find, similar to Eq. (1.51),

$$C(q_n, \omega) = \frac{1}{2\pi\hbar N_\mathrm{F}\tau_0}\frac{1}{Dq_n^2\tau_0 - i\omega\tau_0}. \tag{1.64}$$

The former $\mathbf{q}$ integral is replaced by a q_n summation. Again, we introduce the inelastic scattering time as lower cutoff, see Eq. (1.54), by setting the lower limit of the integration to zero, but replace $(-i\omega)$ in the integrand by $1/\tau_\mathrm{i}$, (see also the discussion in Ref. [67], section 3.3). Then we find for the magnetic field dependent correction

$$\begin{aligned}\delta\sigma(\omega = 0, B) &= -\frac{2e^2 D\tau_0}{\pi\hbar}\frac{eB}{\pi\hbar}\sum_{n=0}^{\frac{\hbar}{4eBD\tau_0}}\frac{1}{\frac{4eBD\tau_0}{\hbar}\left(n + \frac{1}{2}\right) + \frac{\tau_0}{\tau_\mathrm{i}}} \\ &= -\frac{e^2}{2\pi^2\hbar}\sum_{n=0}^{\frac{1}{\kappa\tau_0}}\frac{1}{n + \frac{1}{2} + \frac{1}{\kappa\tau_\mathrm{i}}}.\end{aligned} \tag{1.65}$$

where we defined

$$\kappa = \frac{4eBD}{\hbar}. \tag{1.66}$$

The sum can be expressed using the digamma or ψ-function,[16]

$$\psi\left(\frac{1}{2} + n\right) = -\gamma_\mathrm{EM} - 2\ln 2 + \sum_{k=1}^{n}\frac{1}{k - \frac{1}{2}}, \tag{1.67}$$

where γ_EM is the Euler-Mascheroni constant. The conductivity correction is therefore defined by a subtraction of ψ-functions, which finally results in [6, 26, 68]

$$\delta\sigma(\omega = 0, B) = -\frac{e^2}{\pi h}\left[\psi\left(\frac{1}{2} + \frac{B_\mathrm{o}}{B}\right) - \psi\left(\frac{1}{2} + \frac{B_\mathrm{i}}{B}\right)\right], \tag{1.68}$$

where

$$B_{\mathrm{i,o}} = \frac{\hbar}{4eD\tau_{\mathrm{i,0}}} \tag{1.69}$$

[16] The ψ-function is defined as logarithmic derivative of the gamma function, $\psi(x) = \frac{\mathrm{d}}{\mathrm{dx}}\ln\Gamma(x)$.

are characteristic magnetic fields, corresponding to the relaxation times for elastic (o) and inelastic (i) scattering. The equivalence of Eqs. (1.68) and (1.65) is shown below:

$$\begin{aligned}
\delta\sigma &= -\frac{e^2}{2\pi^2\hbar}\left(\sum_{k=1}^{\frac{1}{\kappa\tau_0}}\frac{1}{k-\frac{1}{2}} - \sum_{k=1}^{\frac{1}{\kappa\tau_\mathrm{i}}}\frac{1}{k-\frac{1}{2}}\right) \\
&= -\frac{e^2}{2\pi^2\hbar}\sum_{n=1+\frac{1}{\kappa\tau_\mathrm{i}}}^{\frac{1}{\kappa\tau_0}}\frac{1}{n-\frac{1}{2}} \\
&= -\frac{e^2}{2\pi^2\hbar}\sum_{n=0}^{\frac{1}{\kappa}\left(\frac{1}{\tau}-\frac{1}{\tau_\mathrm{i}}\right)-1}\frac{1}{n+\frac{1}{2}+\frac{1}{\kappa\tau_\mathrm{i}}} \\
&\approx -\frac{e^2}{2\pi^2\hbar}\sum_{n=0}^{\frac{1}{\kappa\tau_0}}\frac{1}{n+\frac{1}{2}+\frac{1}{\kappa\tau_\mathrm{i}}},
\end{aligned} \tag{1.70}$$

where in the last step we assumed $\tau_\mathrm{i}/\tau_0 \gg 1$ and $1/\kappa\tau_0 \gg 1$.

For very large arguments in the ψ-function (meaning $B \to 0$), the latter can be expanded into a generalized Puiseux series [77],

$$\psi\left(\frac{1}{2}+x\right) = \ln(x) + \frac{1}{24x^2} + O\left(\frac{1}{x^4}\right) \tag{1.71}$$

and

$$\delta\sigma(B\to 0) = -\frac{e^2}{\pi h}\ln\left(\frac{\tau_\mathrm{i}}{\tau_0}\right), \tag{1.72}$$

in agreement with Eq. (1.55).

Figure 1.10 shows a plot of the magneto-conductivity, defined as

$$\Delta\sigma = \sigma(B) - \sigma(0) = \delta\sigma(B) - \delta\sigma(0), \tag{1.73}$$

which results in

$$\Delta\sigma = -\frac{e^2}{\pi h}\left[\psi\left(\frac{1}{2}+\frac{B_\mathrm{o}}{B}\right) - \psi\left(\frac{1}{2}+\frac{B_\mathrm{i}}{B}\right) - \ln\left(\frac{B_\mathrm{o}}{B}\right) + \ln\left(\frac{B_\mathrm{i}}{B}\right)\right]. \tag{1.74}$$

By using the abbreviated notation

$$\Psi\left(\frac{1}{x}\right) = \psi\left(\frac{1}{2}+\frac{1}{x}\right) - \ln\left(\frac{1}{x}\right), \tag{1.75}$$

we find the more compact form

$$\Delta\sigma = -\frac{e^2}{\pi h}\left[\Psi\left(\frac{B_\mathrm{o}}{B}\right) - \Psi\left(\frac{B_\mathrm{i}}{B}\right)\right]. \tag{1.76}$$

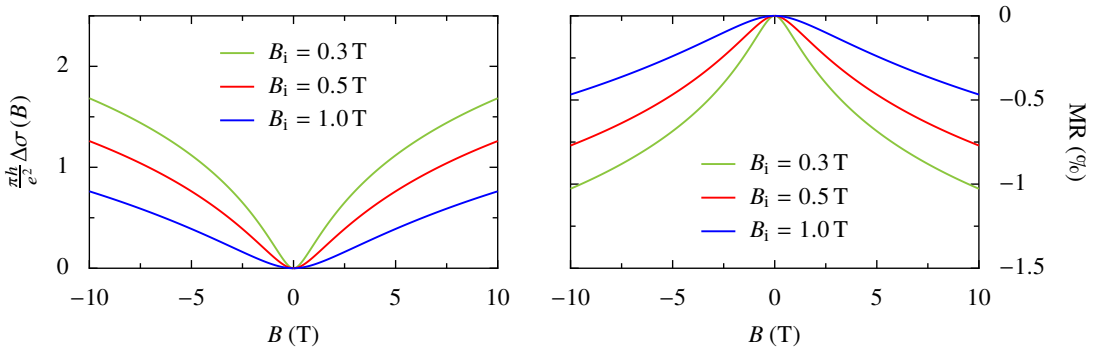

Figure 1.10: *Positive magneto-conductivity/Negative magneto-resistivity due to weak localization.* A magnetic field perpendicular to a two-dimensional plane suppresses the interference effect of WL. The magneto-conductivity increases with the magnetic field B and is smaller in amplitude for increasing inelastic scattering, represented by the effective inelastic scattering field B_i. The scattering field $B_o \sim \infty$ is assumed to be very large in this plot. For the magneto-resistivity (MR) plot, the sheet resistance is chosen to be 500 Ω.

In small magnetic fields, the magneto-conductivity near $B = 0$ evolves as

$$\Delta\sigma(B \sim 0) = \frac{e^2}{\pi h}\frac{B^2}{24}\left(\frac{1}{B_i^2} - \frac{1}{B_o^2}\right) \tag{1.77}$$

and is therefore analytic in the magnetic field. Note that $B_o \gg B_i$.

For very large magnetic fields, as well as $B \sim B_o \gg B_i$, the ψ-function saturates [78, 79],

$$\psi\left(\frac{1}{2}\right) = -\gamma_{EM} - \ln(4), \tag{1.78}$$

$$\psi\left(\frac{3}{2}\right) = 2 - \gamma_{EM} - \ln(4). \tag{1.79}$$

In this large field case,

$$\Delta\sigma = -\frac{e^2}{\pi h}\left[2 - \ln\left(\frac{B}{B_i}\right)\right], \tag{1.80}$$

and the logarithmic term dominates, causing a steady increasing magneto-conductivity without saturation.

Often the strong scattering regime is considered, where $B_o \gg B$. This is a stronger version of Eq. (1.59) because for $d = 2$, $B_o \gg B$ translates into $l_B \gg l$ and we find an even simpler expression for the magneto-conductivity,

$$\Delta\sigma = \frac{e^2}{\pi h}\Psi\left(\frac{B_i}{B}\right). \tag{1.81}$$

An increasing magnetic field suppresses localization and results in a higher magneto-conductivity. Increasing the inelastic scattering (by increasing temperature) weakens the effect.

1.4.3 Finite Size in the Third Spatial Dimension

To close this section, we discuss the issue of a finite thickness t in a realistic sample. A thin film is rarely strictly two-dimensional with only one quantum number in the perpendicular spatial direction. Still, if the quantization in z-direction creates a large gap between excitation levels, a low-dimensional picture often is legitimate. In the case of WL, we characterize a system as two-dimensional if the diffusion time between the boundary surfaces is small compared to the inelastic life time of the electrons. In vanishing magnetic field this is expressed by $t^2 \ll D\tau_\mathrm{i}$; in the presence of a magnetic field we take the smaller value, either τ_i or the magnetic time $1/\kappa$, which results in $t^2 \ll \hbar/4eB$ for large fields [67]. For a field with 15 T the constraint for the thickness is therefore $t \ll 3\,\mathrm{nm}$.

However, a quantization in z-direction can be taken directly into account in the calculation of the WL correction. The value for q^2 in Eq. (1.63) has to be replaced by $q^2 \to q_\mathrm{xy}^2 + q_\mathrm{z}^2$, where q_z is an integer multiple of π/t. The denominator in the derivation of Eq. (1.70) is then given by

$$n + \frac{1}{2} + \frac{B_\mathrm{i,o}}{B} + n^2 \frac{\hbar\pi^2}{4eBt^2} \tag{1.82}$$

and a sum over all values n has to be taken, where we define the effective finite size field

$$B_\mathrm{th} = \frac{\hbar\pi^2}{4et^2}, \tag{1.83}$$

which only depends on the thickness t,

$$B_\mathrm{th}\,(\mathrm{T}) \approx \frac{1624}{[t\,(\mathrm{nm})]^2} \tag{1.84}$$

for a thickness measured in nanometers and the field measured in Tesla. The result for two dimensions has to be altered when B_th is sufficiently small and becomes of the order of the inelastic field B_i. In the limit $B_\mathrm{o} \gg B$, we find

$$\Delta\sigma = \frac{e^2}{\pi h} \sum_{n=0}^{\infty} \Psi\left(\frac{B_\mathrm{i} + n^2 B_\mathrm{th}}{B}\right). \tag{1.85}$$

For larger values of n, the contributions become small and are negligible. The dimensional effect is most important for small n (or very strong magnetic fields), see Fig. 1.11. The limit $t \to \infty$ results in the magneto-conductivity for three dimensions and becomes independent of the alignment of the magnetic field [70].

The thickness that still allows a two-dimensional treatment can be estimated by

$$B_\mathrm{i} \approx B_\mathrm{th}(B). \tag{1.86}$$

Then we find

$$\begin{aligned} B_\mathrm{i} = 1.0\,\mathrm{T} &\quad\to\quad t_{d=2} \approx 40\,\mathrm{nm}, \\ B_\mathrm{i} = 0.1\,\mathrm{T} &\quad\to\quad t_{d=2} \approx 130\,\mathrm{nm}, \\ B_\mathrm{i} = 0.01\,\mathrm{T} &\quad\to\quad t_{d=2} \approx 400\,\mathrm{nm}. \end{aligned} \tag{1.87}$$

The samples we study in Chap. 3 feature very small values for $B_\mathrm{i} < 0.05$, thus these samples are considered to be two-dimensional in the frame of WL.

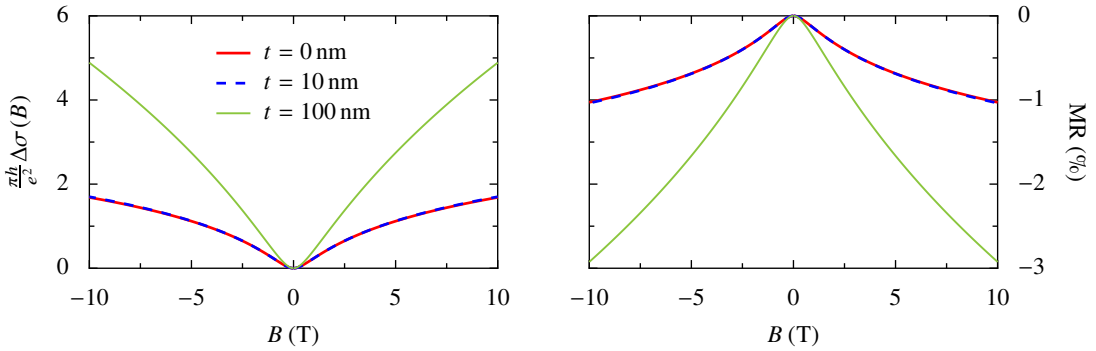

Figure 1.11: *Effect of finite size on weak localization.* For these plots, the effective fields are chosen to be $B_\mathrm{i} = 0.3\,\mathrm{T}$, $B_\mathrm{o} \sim \infty$. Finite size of a sample into the third spatial direction requires to sum over all quantum numbers in z-direction for the Cooperon momentum. For the chosen parameters, even a thickness of 10 nm does not differ considerably from the exact two-dimensional response. For the magneto-resistivity (MR) plot, the sheet resistance is chosen to be 500 Ω.

Summary of Chapter 1

In the first chapter, I discussed Ohm's law that connects the Drude conductivity with the conductance in the different spatial dimensions. A one-dimensional, infinite system is an electric insulator, whereas a three-dimensional system in the thermodynamic limit is a metal. The two-dimensional case is the marginal one, located on the border between metal and insulator. Disorder drives each of these systems in direction of an electric insulator, thus the two-dimensional system becomes insulating for an arbitrary amount of disorder. For the weakly disordered two-dimensional case, I reviewed the computation of the first order quantum correction to the conductivity. This predecessor of Anderson localization is called weak localization and can be detected via magnetic field, where it manifests itself in a negative magneto-resistivity. The three-dimensional case, however, exhibits a metal–insulator transition to the Anderson insulator, controlled by the amount of disorder. This transition can be described by a continuous phase transition where the conductivity vanishes at the critical point, obeying a power law.

A combination of disorder and spin–orbit coupling, however, drives the systems into the metallic direction instead. In the two-dimensional case, this results immediately in a metallic state (called a symplectic metal) for an arbitrary amount of disorder, thus a symplectic metal–insulator transition emerges when the disorder becomes stronger. The critical point—only existent in two dimensions when spin–orbit coupling is important—is characterized by a critical finite conductivity. In Chap. 2, we will discuss the localization correction for the case when spin–orbit coupling is important. This manifests itself in the phenomenon of weak anti-localization.

2 The Role of Spin–Orbit Coupling in Weak Anti-Localization

Contents

In the last section of Chap. 1, we discussed the first disorder generated quantum correction to the conductivity of an electron system. The consideration of the maximally crossed diagrams in the Kubo approach revealed the concept of WL, a self-interference effect of the charge carriers that reduces the conductivity with disorder strength. In this chapter, we add the electron spin to this picture.

Whereas the Schrödinger equation provides three quantum numbers for the spatial distribution of a particle, the covariance of the Dirac equation in four-dimensional space–time enforces the concept of spin. However, like space–time, spin and orbitals are not independent degrees of freedom, but intertwined in a relativistic theory and only separated into orbital and spin quantum numbers in the rest frame. The first relativistic correction of the Schrödinger equation results in a term inversely proportional to c^2,

$$\mathcal{H}_{\mathrm{so}} = \frac{\hbar}{4m^2c^2}(\mathbf{p}\times\boldsymbol{\sigma})\cdot\nabla V, \tag{2.1}$$

where m is the electron mass, $\mathbf{p}$ the momentum, V an electric potential and $\boldsymbol{\sigma}$ the vector of Pauli matrices. The spin–orbit coupling becomes strong for velocities near the (vacuum) speed of light c, but it is only a small correction in most atomic systems [80]. The Hamiltonian

Eq. (2.1) describes the spin–orbit coupling in the presence of an electric field **E**, induced by the gradient of an atomic potential V. In an itinerant electron system, if an electron propagates through a periodic potential with a momentum **p**, its spin is affected by the effective magnetic field that is created in its rest frame. This spin–orbit coupling is the driving force behind the concept of spin-transport, topological insulators and, as we will discuss in this chapter, Anderson anti-localization.

When spin–orbit coupling is strong, the spin of a moving particle is locked to its momentum quantum number. Comparing self-intersecting paths and their time reversed counterparts (Fig. 1.5), the half-integer spin contributes an extra phase to the interference, resulting in the opposed effect of weak anti-localization (WAL). Comparing the spin–orbit coupled case with the simple arguments in Eqs. (1.10)–(1.12) for the self-intersecting path, for spin-$1/2$ particles we find that $A^{\mathrm{TR}} = -A$ and the probability $P_A^{\mathrm{qm}} = 2|A|^2 - 2|A|^2 = 0$ for staying in the loop is quantum mechanically reduced. Magnetic fields, exactly as in the WL case, suppress the spin-dependent phase contribution. Magneto-transport provides a viable experimental tool for the determination of spin–orbit strengths.

In the following, we discuss relevant spin–orbit mechanisms for low-dimensional itinerant electron systems like two-dimensional semiconductor quantum wells and oxide heterostructures. We review two different approaches to include spin–orbit coupling into the crossed diagram calculation. First, we discuss spin–orbit scattering events that take place at impurities like heavy ions. This is the so called HLN-theory of WAL, named after their developer Hikami, Larkin, and Nagaoka [6]. In the second part we discuss spin–orbit splitting in the band structure, where the spin of the conduction electrons is locked at the Fermi surface. This is the so called ILP-theory of WAL, named after Iordanskii, Lyanda-Geller, and Pikus [7]. Although the qualitative results of both theories are similar, they differ in several details and most of all, in the physical picture:

- The HLN approach considers Elliott–Yafet spin relaxation in the scattering process, namely a spin flip during a scattering event. For this relaxation mechanism, the spin of the scattered electron is no longer conserved and spin-up and spin-down channels of the Cooperon are intermixed.

- The ILP approach considers the D'yakonov–Perel' spin relaxation. Non-diagonal entries in the Hamiltonian's spin space cause a mixing of spins during the propagation of a particle. In combination with spin-independent momentum scattering, the different spin channels of the Cooperon are intermixed. Rashba and Dresselhaus effects are typical examples for this kind of spin-splitting and play a prominent role in oxide structures.

In this chapter, we expand the ILP-theory to two scenarios that have not been discussed so far in the current literature. These scenarios are motivated by the two-dimensional electron gas at the $LaAlO_3/SrTiO_3$ heterostructure. Experimental and theoretical investiagtions, discussed in more detail in Chap. 3, have revealed a multiband picture with an extraordinary spin structure. We discuss the ILP-theory for an anisotropic Rashba Hamiltonian, which has been suggested as an effective Hamiltonian for one of the involved spin-split bands. Beyond that, we take a first step towards a multiband WAL theory by considering spin–orbit coupling for the four levels of a spin-$3/2$ model. We will compare the different theories presented here with experimental data from two-dimensional electronic systems in oxides in Chap. 3.

2.1 Hikami–Larkin–Nagaoka Theory

2.1.1 Spin–Orbit Scatterers

Even in systems that are invariant under inversion of space (and time), the Elliott–Yafet relaxation mechanism [81, 82] takes place and mixes different spin projections. If we consider the Bloch state $|\psi\rangle_{\mathbf{k}\uparrow}$, its time reversed counterpart is given by

$$\mathcal{T}\,|\psi\rangle_{\mathbf{k}\uparrow} = |\psi\rangle^{*}_{-\mathbf{k}\downarrow}\,, \tag{2.2}$$

where $\mathcal{T}$ is the time inversion operator and the latter state is known as the Kramer's partner of the first. Respecting spatial inversion symmetry, we find two degenerate Bloch states with opposite spin but equal momentum,

$$\mathcal{I}\mathcal{T}\,|\psi\rangle_{\mathbf{k}\uparrow} = |\psi\rangle^{*}_{\mathbf{k}\downarrow}\,, \tag{2.3}$$

where $\mathcal{I}$ is the spatial inversion operator. However, the lattice ions might introduce a spin–orbit potential as a relativistic effect via

$$V_{\mathrm{so}} = \frac{\hbar}{4m^2c^2}\,(\nabla V_{\mathrm{c}} \times \mathbf{p}) \cdot \boldsymbol{\sigma}, \tag{2.4}$$

where V_{c} is the periodic crystal lattice potential. The spin–orbit potential V_{so} features the same symmetry properties as the lattice potential and respects time reversal as well as spatial inversion symmetry.

However, bands that are separated by a small energy gap γ allow for a mixing of spin-up and spin-down states with spin–orbit coupling matrix element λ between those bands. The Bloch states for the hybridized bands have an effective spin projection [81, 83]

$$\left|\tilde{\uparrow}\right\rangle_{\mathbf{k}} = a_{\mathbf{k}}\,|\uparrow\rangle + b_{\mathbf{k}}\,|\downarrow\rangle\,, \tag{2.5}$$

$$\left|\tilde{\downarrow}\right\rangle_{\mathbf{k}} = a^{*}_{-\mathbf{k}}\,|\downarrow\rangle - b^{*}_{-\mathbf{k}}\,|\uparrow\rangle\,, \tag{2.6}$$

where ${}^{|b|}/_{|a|} \approx {}^{\lambda}/_{\gamma}$. The Bloch states Eq. (2.5) and Eq. (2.6) are still degenerate, as the second wave function is the inversion and time symmetric partner of the first one. Typically, $|a| \lesssim 1$ and $|b| \ll 1$, allowing the Bloch states still to be considered meaningfully as spin-up and spin-down states [84].

Without scattering processes, these spin states are still stable eigenstates of the system. Elliott pointed out that the lattice induced spin–orbit coupling in combination with a spin-independent momentum scattering process provides a spin-relaxation mechanism [81]. In first-order of perturbation theory, the spin–orbit relaxation rate is given by

$$\frac{1}{\tau_{\mathrm{so,\,EY}}} \approx \left(\frac{\lambda}{\gamma}\right)^{2} \frac{1}{\tau_0}, \tag{2.7}$$

therefore the spin relaxation rate is proportional to the elastic scattering rate. Yafet contributed that the spin–orbit coupling of the lattice ions is affected by phonons, introducing an additional coupling of the spin-up and spin-down states [82], which again in combination with the Elliott mechanism results in spin relaxation. Rather general, the spin relaxation time has to be treated according to the specific momentum scattering mechanism; also a heavy impurity induces a

spin-flip channel on its own due to the strong core potential [84]. All these different processes are similar in respect to the instant of spin relaxation at the scattering event, and can be summarized in the Elliott–Yafet relaxation, Eq. (2.7).

In the following, we simplify the picture by introducing an effective scattering potential (from here we mainly follow the arguments of Ref. [67]),

$$V(\mathbf{k},\mathbf{k}') = V_\mathrm{o} + iV_\mathrm{so}\left(\hat{\mathbf{k}}\times\hat{\mathbf{k}}'\right)\cdot\boldsymbol{\sigma} + J\mathbf{S}\cdot\boldsymbol{\sigma} \tag{2.8}$$

where $V_\mathrm{so} \propto V_\mathrm{o}$ and for the spin relaxation we find for the component in i direction (see also Eq. (A.31) and Eq. (A.77) for the scattering rates),

$$\frac{\hbar}{\tau_0} = 2\pi n_\mathrm{imp} N_\mathrm{F} V_\mathrm{o}^2, \tag{2.9}$$

$$\frac{\hbar}{\tau_\mathrm{so}^i} = 2\pi n_\mathrm{imp} N_\mathrm{F} |V_\mathrm{so}|^2 \overline{\left(\hat{\mathbf{k}}\times\hat{\mathbf{k}}'\right)_i^2} \tag{2.10}$$

$$\frac{\hbar}{\tau_\mathrm{m}^i} = 2\pi n_\mathrm{imp} N_\mathrm{F} J^2 \langle S_i\rangle^2, \tag{2.11}$$

where n_imp is the impurity density and the bar denotes angle averaging.

The first theory of WAL has been put forward in the paper by Hikami, Larkin, and Nagaoka [6], where an analytic form of the general magneto-conductivity for orthogonal (non-magnetic), unitary (magnetic) and symplectic (spin–orbit) scattering processes has been derived. Referring to the Cooperon calculation in the particle–particle channel (see Sec. 1.4), the Dyson equation is formulated as

$$C_{\alpha\beta,\gamma\delta} = C^0_{\alpha\beta,\gamma\delta} + \sum_{\mu,\nu} C^0_{\alpha\mu,\gamma\nu}\Pi_{\mu\nu}C_{\mu\beta,\nu\delta}, \tag{2.12}$$

$$C^0_{\alpha\beta,\gamma\delta} = \frac{1}{2\pi N_\mathrm{F}\hbar}\left[\frac{\delta_{\alpha\beta}\delta_{\gamma\delta}}{\tau_0} - \sum_i \frac{\sigma^i_{\alpha\beta}\sigma^i_{\gamma\delta}}{\tau^i_\mathrm{so}} + \sum_i \frac{\sigma^i_{\alpha\beta}\sigma^i_{\gamma\delta}}{\tau^i_\mathrm{m}}\right], \tag{2.13}$$

$$\Pi_{\mu\nu} = \Pi, \tag{2.14}$$

where the pair of spins $(\alpha\beta)$ denotes the spin along one propagating line, see Fig. 2.1. The particle–hole propagator Π is identical to the expression calculated in the diffusion process Eq. (A.86). Note that the scattering potentials enter the Cooperon equation quadratically, resulting in different signs for the different contributions—whereas the elastic and magnetic scattering produce a positive sign, the spin–orbit scattering produces a negative one.

At the current vertex of the response functions, charge and spin have to be conserved, therefore the spin of the electron entering and leaving the current vertex is identical. For the ladder diagrams, this corresponds to the case $\alpha = \delta$ as well as $\gamma = \beta$ in Fig. 2.1 (a). This defines a triplet condition at the vertices, T_v. Using Fierz identities [33], we find for this vertex condition

$$\delta_{\alpha\delta}\delta_{\beta\gamma} = \frac{1}{2}\delta_{\alpha\beta}\delta_{\gamma\delta} + \frac{1}{2}\sigma_{\alpha\beta}\sigma_{\gamma\delta} \equiv T_\mathrm{v}, \tag{2.15}$$

and for a singlet condition S_v (which is not realized at the vertex),

$$\sigma_{\alpha\delta}\sigma_{\beta\gamma} = \frac{3}{2}\delta_{\alpha\beta}\delta_{\gamma\delta} - \frac{1}{2}\sigma_{\alpha\beta}\sigma_{\gamma\delta} \equiv S_\mathrm{v}. \tag{2.16}$$

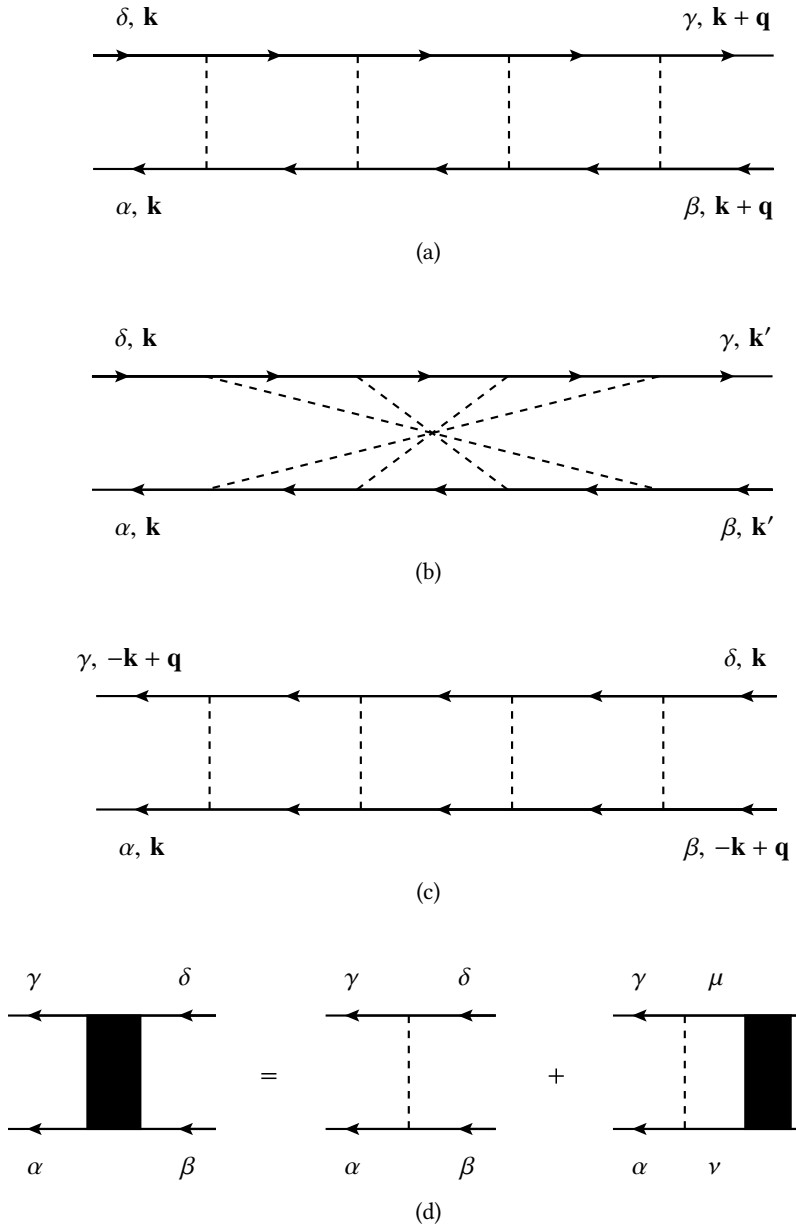

Figure 2.1: *Spin dependent version of maximally crossed diagrams.* (a) Under consideration of spin–orbit coupling, the spin quantum number is no longer conserved during the propagation of particles. Only the triplet of electron and hole at a vertex ($\alpha = \delta$, $\gamma = \beta$) contributes to the diffusion ladder. (b) The triplet of electron–hole pairs ($\alpha = \delta$, $\gamma = \beta$) is also the only contribution to the maximally crossed diagrams. (c) Turning around one propagator line, the Cooperon is reformulated as a spin dependent ladder, where not only the triplet, but also the singlet channel contributes to the particle–particle channel (because still $\alpha = \delta$, $\gamma = \beta$, but not necessarily $\alpha = \gamma$ and $\beta = \delta$). (d) Dyson equation for the particle–particle representation of the Cooperon. The dashed line is a single scattering event involving a possible spin flip.

Referring to the spin indices during propagation, $(\alpha\beta)$ and $(\gamma\delta)$, the required case for the diffusion ladder can be decomposed into triplet T_d and singlet S_d contributions before and after entering the scattering process:[1]

$$\delta_{\alpha\beta}\delta_{\gamma\delta} \equiv T_\mathrm{d}, \tag{2.17}$$

$$\sigma_{\alpha\beta}\sigma_{\gamma\delta} \equiv S_\mathrm{d}. \tag{2.18}$$

The first case refers to no spin flip for the completed propagation, whereas the second relation refers to different realizations of a net spin flip of both Green's functions. The necessary condition, Eq. (2.15), can therefore be expressed as

$$\delta_{\alpha\delta}\delta_{\beta\gamma} = \frac{1}{2}\left(S_\mathrm{d} + T_\mathrm{d}\right). \tag{2.19}$$

The analogon for the Cooperon ladder is achieved by reversal of one of the propagator lines, which negates the antisymmetric contribution, $\sigma_{\alpha\beta} \longrightarrow -\sigma_{\alpha\beta}$. Then the necessary vertex condition Eq. (2.15) is represented by

$$\delta_{\alpha\delta}\delta_{\beta\gamma} = \frac{1}{2}\left(-S_\mathrm{c} + T_\mathrm{c}\right). \tag{2.20}$$

The triplet channel of the Cooperon contributes three parts to the quantum correction, the singlet only one [33]. Without spin–orbit coupling, all contributions are equal and one triplet contribution is canceled by the singlet contribution, leaving two contributions, as expected for the two spin projections. We will use this argument in later calculations, but in the following, we compute the finite components of the Cooperon by keeping track of the spin indices directly.

We follow the calculation for the case of isotropic spin–orbit scattering (as well as no magnetic scattering),

$$\frac{1}{\tau_\mathrm{so}^i} = \frac{1}{3}\frac{1}{\tau_\mathrm{so}}, \tag{2.21}$$

but show the more general formula in the end. We introduce the notation (+) for the spin-up and (−) for the spin-down projection explicitly. The only finite elements are given by[2]

$$C^0_{++,++} = C^0_{--,--} = \frac{1}{2\pi N_\mathrm{F}\hbar}\left(\frac{1}{\tau_0} - \frac{1}{3\tau_\mathrm{so}}\right) \tag{2.22}$$

$$C^0_{+-,-+} = C^0_{-+,+-} = -\frac{1}{2\pi N_\mathrm{F}\hbar}\frac{2}{3\tau_\mathrm{so}} \tag{2.23}$$

$$C^0_{++,--} = C^0_{--,++} = \frac{1}{2\pi N_\mathrm{F}\hbar}\left(\frac{1}{\tau_0} + \frac{1}{3\tau_\mathrm{so}}\right). \tag{2.24}$$

We find for the conductivity in two spatial dimensions

$$\begin{aligned}\delta\sigma(\omega) &= -2e^2 N_\mathrm{F} D\tau^2 \sum_{\alpha\beta}\int_0^{q_\mathrm{max}} \frac{\mathrm{d}^2 q}{(2\pi)^2} C_{\alpha\beta,\beta\alpha} \\ &= -2e^2 N_\mathrm{F} D\tau^2 \int_0^{q_\mathrm{max}} \frac{\mathrm{d}^2 q}{(2\pi)^2}\left(C_{++,++} + C_{--,--} + C_{+-,-+} + C_{-+,+-}\right),\end{aligned} \tag{2.25}$$

[1] Note that this assignment to singlet and triplet states is not consistent in the literature.

[2] Note that the contribution of the spin–orbit relaxation in Eq. (2.22) and Eq. (2.24) have their origin in the σ_z matrix, whereas in Eq. (2.23) the origin is in the σ_x and σ_y matrices.

where the relaxation time is given by

$$\frac{1}{\tau} = \frac{1}{\tau_0} + \frac{1}{\tau_{\mathrm{so}}}. \tag{2.26}$$

Note that the expression of the Green's functions appearing on the left- and right-hand-side of the Cooperon in Eq. (1.41) have to change accordingly. However, only those terms contribute where the spins entering and leaving the Cooperon are identical. As the energy is degenerate for both spin projections, the expression for these integral leads the same result as shown in Eq. (1.46).

The Dyson equation yields for the triplet channel,

$$\begin{aligned} C_{++,++} = C_{--,--} &= \frac{C^0_{++,++}}{1 - C^0_{++,++}\Pi} \\ &= \frac{1}{2\pi N_{\mathrm{F}}\hbar\tau} \frac{1}{Dq^2\tau - i\omega\tau + \frac{4}{3}\frac{\tau}{\tau_{\mathrm{so}}}} \end{aligned} \tag{2.27}$$

and for the singlet channel,

$$\begin{aligned} C_{+-,-+} = C_{-+,+-} &= \frac{C^0_{+-,-+}(1 - C^0_{++,--}\Pi) + C^0_{++,--}C^0_{+-,-+}\Pi}{|1 - C^0_{++,--}\Pi|^2 - |\Pi|^2 (C^0_{+-,-+})^2} \\ &= \frac{1}{4\pi N_{\mathrm{F}}\hbar\tau} \left(\frac{1}{Dq^2\tau - i\omega\tau + \frac{4}{3}\frac{\tau}{\tau_{\mathrm{so}}}} - \frac{1}{Dq^2\tau - i\omega\tau} \right) \frac{2}{3}\frac{\tau}{\tau_{\mathrm{so}}}. \end{aligned} \tag{2.28}$$

If we insert Eq. (2.27) into Eq. (2.25) for the case $1/\tau_{\mathrm{so}} = 0$, we find the earlier result Eq. (1.52). However, in Eq. (2.27) we find that the Cooper pole is shifted by the spin–orbit scattering rate. Equation (2.28) enters the conductivity as an additional contribution that has no analogon in the former Cooperon calculation. For $1/\tau_{\mathrm{so}} = 0$, this term becomes zero.

Considering the magnetic scattering relaxation rate, Eq. (2.11), we find

$$C^0_{\alpha\beta,\gamma\delta} = \frac{1}{2\pi N_{\mathrm{F}}\hbar} \left[\frac{\delta_{\alpha\beta}\delta_{\gamma\delta}}{\tau_0} + \sum_i \left(\frac{1}{\tau^i_{\mathrm{m}}} - \frac{1}{\tau^i_{\mathrm{so}}} \right) \sigma^i_{\alpha\beta}\sigma^i_{\gamma\delta} \right]. \tag{2.29}$$

The scattering rate $1/\tau$ in Eqs. (2.27)–(2.28) has to be replaced in this case by

$$\frac{1}{\tau} = \frac{1}{\tau_0} + \frac{1}{\tau_{\mathrm{so}}} + \frac{1}{\tau_{\mathrm{m}}}. \tag{2.30}$$

Note that the magnetic and spin–orbit scattering rates shift the diffusion-like pole in the denominator of Eqs. (2.27)–(2.28). In the end of the calculation it is valid to approximate the scattering rate by $\tau \approx \tau_0$, because elastic scattering is assumed to be dominant in the diffusive regime.

We consider a magnetic field and replace the momentum integration by a summation over effective Landau levels, following the computation procedure described in Sec. 1.4.2. This calculation yields the quantum correction in the conductance,

$$\delta\sigma(B) = -\frac{e^2}{\pi h} \left[\psi\left(\frac{1}{2} + \frac{B_1}{B}\right) - \psi\left(\frac{1}{2} + \frac{B_2}{B}\right) + \frac{1}{2}\psi\left(\frac{1}{2} + \frac{B_3}{B}\right) - \frac{1}{2}\psi\left(\frac{1}{2} + \frac{B_4}{B}\right) \right], \tag{2.31}$$

where

$$B_1 = B_\mathrm{o} + B_\mathrm{so}^\mathrm{x} + B_\mathrm{so}^\mathrm{y} + B_\mathrm{so}^\mathrm{z} + B_\mathrm{m}^\mathrm{x} + B_\mathrm{m}^\mathrm{y} + B_\mathrm{m}^\mathrm{z}, \tag{2.32}$$

$$B_2 = 2B_\mathrm{so}^\mathrm{x} + 2B_\mathrm{so}^\mathrm{z} + 2B_\mathrm{m}^\mathrm{x} + B_\mathrm{i}, \tag{2.33}$$

$$B_3 = 4B_\mathrm{m}^\mathrm{x} + 2B_\mathrm{m}^\mathrm{z} + B_\mathrm{i}, \tag{2.34}$$

$$B_4 = 4B_\mathrm{so}^\mathrm{x} + 2B_\mathrm{m}^\mathrm{z} + B_\mathrm{i}. \tag{2.35}$$

The effective magnetic fields are defined by a generalized version of Eq. (1.69), thus for the spin–orbit coupling, τ_so, and the magnetic scattering, τ_m, the effective fields are given by

$$B_{\mathrm{so,m}} = \frac{\hbar}{4eD\tau_{\mathrm{so,m}}}. \tag{2.36}$$

We discuss three different cases:

- *Orthogonal case:* $B_\mathrm{so} = B_\mathrm{m} = 0$. In this case, the last two terms in Eq. (2.31) cancel out each other and Eq. (1.68) is recovered, describing WL.

- *Unitary case:* $B_\mathrm{so} = 0$, $B_\mathrm{m} \neq 0$. As we already expect from the β-functions (see Sec. 1.3.3), in the unitary case we see no qualitative change in comparison to the orthogonal case. The magnetic scattering field, B_m, operates similarly as the inelastic magnetic field, B_i, and B_m can effectively be absorbed into B_i.

- *Symplectic case:* $B_\mathrm{so} \neq 0$, $B_\mathrm{m} = 0$. In the symplectic case, the change is rather significant. For $B_\mathrm{so} \gg B_\mathrm{i}$, the inelastic field is ineffective in B_2, but not in B_3, where it enters via the ψ-function in a term with the opposite sign in Eq. (2.31). In the limit of vanishing magnetic field, we use Eq. (1.71) for Eq. (2.31) and reveal for the temperature dependent conductivity

  $$\delta\sigma(T) \approx \frac{e^2}{2\pi h} \ln\left(\frac{\tau_\mathrm{i}}{\tau_\mathrm{so}}\right), \tag{2.37}$$

  which yields a positive contribution to the conductivity for decreasing temperature, in contrast to Eqs. (1.55) and (1.72).

In the following, we discuss the symplectic case. We assume $B_\mathrm{m} = 0$ and $B_\mathrm{o} \gg B_\mathrm{i}$, B_so. Furthermore, we set $B_\mathrm{so}^\mathrm{z} = 0$, $2B_\mathrm{so}^\mathrm{x} = B_\mathrm{so}$. The dependence of the magneto-conductivity on the effective spin–orbit field is shown in Fig. 2.2. For the small magnetic field expansion, Eq. (1.71), we find the two distinct cases

$$B_\mathrm{i} \gg B_\mathrm{so}: \qquad \Delta\sigma(B \sim 0) \approx \frac{e^2}{\pi h} \frac{B^2}{24B_\mathrm{i}^2}, \tag{2.38}$$

$$B_\mathrm{i} \ll B_\mathrm{so}: \qquad \Delta\sigma(B \sim 0) \approx \frac{e^2}{\pi h} \frac{B^2}{48} \left(\frac{9}{4B_\mathrm{so}^2} - \frac{1}{B_\mathrm{i}^2}\right). \tag{2.39}$$

The first case, $B_\mathrm{i} \gg B_\mathrm{so}$ yields WL where the magneto-conductivity is positive. In the second case, $B_\mathrm{i} \ll B_\mathrm{so}$, the inelastic scattering field causes a negative magneto-conductivity. For large magnetic fields, Eq. (2.46) does not saturate, similar to the WL case.

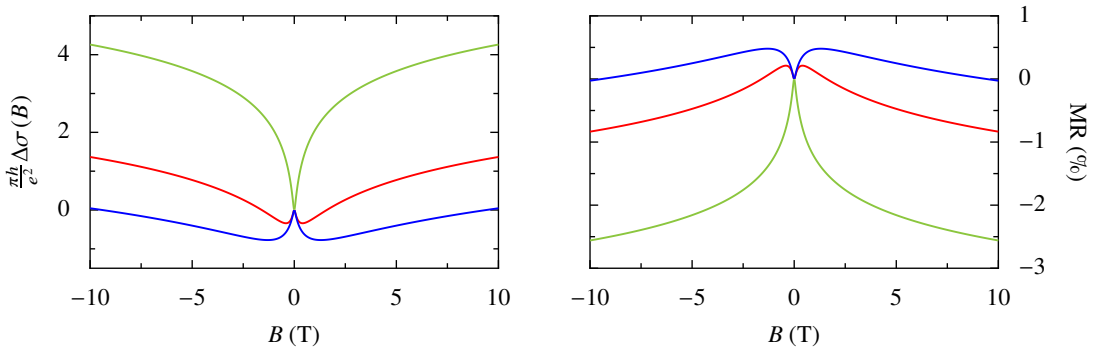

Figure 2.2: *Magneto-conductivity and magneto-resistivity (MR) for spin–orbit scattering events.* Dominant spin–orbit scattering events results in a negative magneto-conductivity, as the destructive interference in self-intersecting paths is suppressed. The stronger the effective spin–orbit field, B_{so}, the stronger the amplitude of the negative magneto-conductivity. Values of the spin–orbit fields in this plot are $B_{\mathrm{so}} = 0\,\mathrm{T}$ (green curve), $B_{\mathrm{so}} = 0.1\,\mathrm{T}$ (red curve), $B_{\mathrm{so}} = 0.3\,\mathrm{T}$ (blue curve), and the inelastic scattering field is $B_{\mathrm{i}} = 0.02\,\mathrm{T}$ for all pictures. For the MR plot the sheet resistance is chosen to be $500\,\Omega$.

Let us discuss the symplectic case for vanishing magnetic field in more detail. Then we find

$$\delta\sigma(B \to 0) = -\frac{e^2}{2\pi h} \ln\left(\frac{B_{\mathrm{o}}^2 B_{\mathrm{i}}}{(2B_{\mathrm{so}} + B_{\mathrm{i}})^2 (4B_{\mathrm{so}} + B_{\mathrm{i}})}\right). \tag{2.40}$$

For the case $B_{\mathrm{i}} \gg B_{\mathrm{so}}$, we reproduce the orthogonal case

$$\delta\sigma(B \to 0) = -\frac{e^2}{\pi h} \ln\left(\frac{B_{\mathrm{o}}}{B_{\mathrm{i}}}\right), \tag{2.41}$$

and by assuming a temperature dependence of the form $B_{\mathrm{i}} = aT^{\alpha}$,

$$\delta\sigma(T) = \frac{\alpha e^2}{\pi h} \ln\left(\frac{T}{T_{\mathrm{o}}}\right), \tag{2.42}$$

where the elastic scattering defines a temperature scale

$$T_{\mathrm{o}} = \left(\frac{B_{\mathrm{o}}}{a}\right)^{\frac{1}{\alpha}}. \tag{2.43}$$

The correction Eq. (2.42) is always negative, as $T < T_{\mathrm{o}}$ by precondition. The conductivity decreases with temperature, indicating an insulating ground state. For $B_{\mathrm{i}} \ll B_{\mathrm{so}}$, however, we find

$$\delta\sigma(B \to 0) = -\frac{e^2}{2\pi h} \ln\left(\frac{B_{\mathrm{o}}^2 B_{\mathrm{i}}}{2B_{\mathrm{so}}^3}\right) = -\frac{\alpha e^2}{2\pi h} \ln\left(\frac{T}{T_{\mathrm{so}}}\right), \tag{2.44}$$

where the spin–orbit scattering defines the temperature scale in interplay with the elastic scattering,

$$T_{\mathrm{so}} = \left(\frac{2B_{\mathrm{so}}^3}{aB_{\mathrm{o}}^2}\right)^{\frac{1}{\alpha}}. \tag{2.45}$$

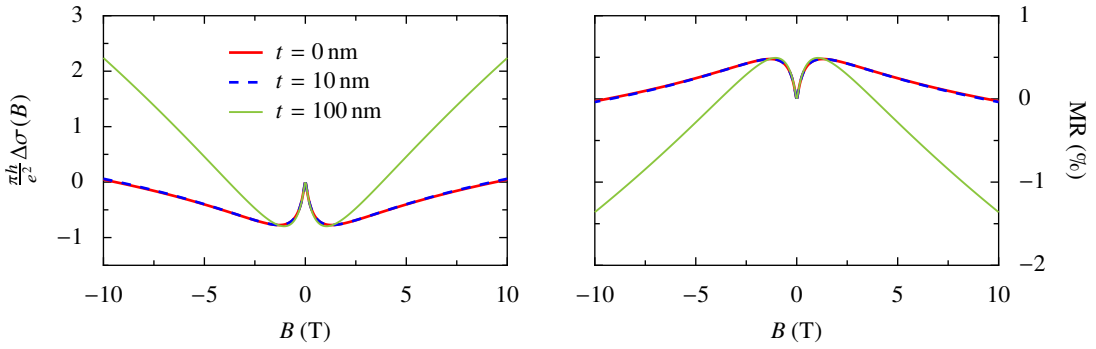

Figure 2.3: *Effect of finite size on the weak anti-localization.* Here, t is the thickness of the film. For these plots, the effective fields are chosen to be $B_\mathrm{i} = 0.02\,\mathrm{T}$, $B_\mathrm{so} = 0.3\,\mathrm{T}$, $B_\mathrm{o} \sim \infty$. The effect becomes important for $B_\mathrm{so} \approx B_\mathrm{th}$. For the magneto-resistivity (MR) plot the sheet resistance is chosen to be $500\,\Omega$.

Note that the sign of the correction Eq. (2.44) is negative for $T > T_\mathrm{so}$ and positive for $T < T_\mathrm{so}$. The correction is increasing logarithmically with decreasing temperature in both cases, indicating a metallic ground state.

Using Eq. (1.75), we write for the magneto-conductivity in the diffusive limit, $B_\mathrm{o} \gg B_\mathrm{so}$, and for spin–orbit scattering only ($B_\mathrm{m} = 0$), where we set $B_\mathrm{so}^\mathrm{x} = B_\mathrm{so}^\mathrm{y}$,

$$\Delta\sigma(B) = \frac{e^2}{\pi h}\left[\Psi\left(\frac{2B_\mathrm{so}^\mathrm{x} + 2B_\mathrm{so}^\mathrm{z} + B_\mathrm{i}}{B}\right) + \frac{1}{2}\Psi\left(\frac{4B_\mathrm{so}^\mathrm{x} + B_\mathrm{i}}{B}\right) - \frac{1}{2}\Psi\left(\frac{B_\mathrm{i}}{B}\right)\right]. \tag{2.46}$$

The HLN-formula has provided a well accepted explanation for the negative magneto-resistivity found in silicon-MOS and cesiated silicon surfaces by Kawaguchi et al. [85–87]. Typical values for B_so have been reported by Bergman for thin films of aluminum with a thickness of 9 nm, where $B_\mathrm{so} \approx 0.01\,\mathrm{T}$. After a coverage of 0.25 atomic layers of gold, this value has been increased to $B_\mathrm{so} \approx 0.42\,\mathrm{T}$ [88].

For the finite size effect, the general considerations in Sec. 1.4.3 hold. In this case we have to compare the finite size field B_th with the spin–orbit scattering field B_so. Results for different film thickness are shown in Fig. 2.3.

2.1.2 Cooperon for Zeeman Splitting

Whereas the aforementioned samples of Kawaguchi et al. have shown no significant behavior for a magnetic field applied parallel to the surface, measurements on copper films performed by Komori et al. [89, 90] revealed a finite parallel magneto-resistivity. In HLN-theory, the orbital motion of the charge carriers is affected by the magnetic field perpendicular to the plane, and so there is no explanation for a parallel field effect in the experimental data. Maekawa and Fukuyama [69] suggested that Zeeman splitting, in combination with spin–orbit scattering, plays a major role in the magneto-transport of these systems. By considering a Zeeman term in the Hamiltonian,

$$\mathcal{H} = \frac{\hbar^2\mathbf{k}^2}{2m} + \frac{g_\mathrm{L}}{2}\mu_\mathrm{B}\mathbf{B}\cdot\boldsymbol{\sigma}, \tag{2.47}$$

bands are split into their spin-up and spin-down components with an energy gap $|g_\mathrm{L}\mu_\mathrm{B}B|$, where g_L is the Landé factor. This splitting is rotational invariant, and the dispersion in the

Green's functions of the spin-up and spin-down channels is altered also in case of a parallel magnetic field, leading to a modified result in the evaluation of the Cooperon equation. In the following, we sketch the calculation for the magneto-conductivity correction with included Zeeman field.

The Zeeman term enters the Green's functions and causes a direct magnetic field and spin dependency,

$$G_\nu^{\mathrm{ret/adv}}(\mathbf{k},\omega) = \frac{\hbar}{\hbar\omega - \left(\dfrac{\hbar^2\mathbf{k}^2}{2m} + \dfrac{\nu g_\mathrm{L}\mu_\mathrm{B}B}{2}\right) \pm \dfrac{i\hbar}{2\tau_0}}, \tag{2.48}$$

where $\nu = \pm 1$ denotes the spin projection. Note that in the calculation of the residuum the spin splitting cancels for equal spin projections in both Green's functions, but the full Zeeman gap remains in case of different spin projections, see Eq. (A.67). The Dyson equation is given by

$$C_{\alpha\beta,\gamma\delta} = C^0_{\alpha\beta,\gamma\delta} + \sum_{\mu,\nu} C^0_{\alpha\mu,\gamma\nu}\Pi_{\mu\nu}C_{\mu\beta,\nu\delta}, \tag{2.49}$$

$$C^0_{\alpha\beta,\gamma\delta} = \frac{1}{2\pi N_\mathrm{F}\hbar}\left[\frac{\delta_{\alpha\beta}\delta_{\gamma\delta}}{\tau_0} - \sum_i \frac{\sigma^i_{\alpha\beta}\sigma^i_{\gamma\delta}}{\tau^i_\mathrm{so}}\right], \tag{2.50}$$

$$\Pi_{\mu\nu}(\mathbf{q},\omega) = \int_{\mathbf{k}} G_\nu^{\mathrm{ret}}\left(\mathbf{k}+\frac{\mathbf{q}}{2},\omega\right) G_\mu^{\mathrm{adv}}\left(\mathbf{k}-\frac{\mathbf{q}}{2},\omega\right). \tag{2.51}$$

For the spin dependent particle–hole propagator,

$$C_0\Pi_{\nu,\nu} = 1 + i\omega\tau - Dq^2\tau, \tag{2.52}$$

$$C_0\Pi_{\nu,-\nu} = 1 + i\omega\tau - Dq^2\tau + \nu i g_\mathrm{L}\mu_\mathrm{B}B\tau, \tag{2.53}$$

and for the Cooperon (in the isotropic case, Eq. (2.21), and for $\tau_0 \approx \tau \ll \tau_\mathrm{so}$)

$$C_{++,++} = C_{--,--} = \frac{1}{2\pi N_\mathrm{F}\hbar\tau}\frac{1}{Dq^2\tau - i\omega\tau + \frac{4\tau}{3\tau_\mathrm{so}}} \tag{2.54}$$

as well as

$$C_{+-,-+} = C_{-+,+-} = \\ = \frac{1}{4\pi N_\mathrm{F}\hbar\tau\sqrt{1-\gamma_\perp}}\left(\frac{1}{Dq^2\tau - i\omega\tau + \frac{2\tau}{\tau_\mathrm{so}}\left(1+\sqrt{1-\gamma_\perp}\right)} - \frac{1}{Dq^2\tau - i\omega\tau + \frac{2\tau}{\tau_\mathrm{so}}\left(1-\sqrt{1-\gamma_\perp}\right)}\right), \tag{2.55}$$

where

$$\gamma_\perp = \gamma_\perp(B) = \left(\frac{g_\mathrm{L}\mu_\mathrm{B}}{4eD}\frac{B}{2B^\mathrm{x}_\mathrm{so}}\right)^2 \tag{2.56}$$

is a Zeeman normalization factor. Apparently, the Zeeman splitting enters the singlet contribution, Eq. (2.55), whereas the triplet contribution, Eq. (2.54), is not altered.

The result for the magneto-conductivity in perpendicular magnetic field is structural similar to the HLN result. For the non-isotropic case (but $\tau_{\mathrm{so}}^{x} = \tau_{\mathrm{so}}^{y}$) the final result is given by (note that $\gamma_\perp = 0$ for $B = 0$)

$$\Delta\sigma_\perp(B) = \frac{e^2}{\pi h}\left\{\Psi\left(\frac{2B_{\mathrm{so}}^{\mathrm{x}} + 2B_{\mathrm{so}}^{\mathrm{z}} + B_{\mathrm{i}}}{B}\right) + \frac{1}{2}\ln\left(\frac{4B_{\mathrm{so}}^{\mathrm{x}} + B_{\mathrm{i}}}{B_{\mathrm{i}}}\right) + \frac{1}{2\sqrt{1-\gamma_\perp}}\left[\psi\left(\frac{1}{2} + \frac{2B_{\mathrm{so}}^{\mathrm{x}}\left(1+\sqrt{1-\gamma_\perp}\right) + B_{\mathrm{i}}}{B}\right) - \psi\left(\frac{1}{2} + \frac{2B_{\mathrm{so}}^{\mathrm{x}}\left(1-\sqrt{1-\gamma_\perp}\right) + B_{\mathrm{i}}}{B}\right)\right]\right\}. \tag{2.57}$$

If the Zeeman term is neglected via $g_{\mathrm{L}} \to 0$, the HLN result, Eq. (2.46), is recovered.

The Zeeman term in the Green's functions also affects the transport in the diffusion-like pole if the magnetic field is restricted to be exclusively in plane, where it has no direct influence on the Cooperon ladder. Again, the spin flip information only enters the singlet channel through a prefactor, leaving the triplet channel unchanged. For a parallel magnetic field, the magneto-conductivity is negative and decreases quadratically for weak fields before it saturates for higher fields. It is given by

$$\Delta\sigma_\parallel(B) = \frac{e^2}{\pi\hbar}\left[\frac{1}{2\sqrt{1-\gamma_\parallel}}\ln\left(\frac{B_{\mathrm{i}} + \left(B_{\mathrm{so}}^{\mathrm{x}} + B_{\mathrm{so}}^{\mathrm{z}}\right)\left(1+\sqrt{1-\gamma_\parallel}\right)}{B_{\mathrm{i}} + \left(B_{\mathrm{so}}^{\mathrm{x}} + B_{\mathrm{so}}^{\mathrm{z}}\right)\left(1-\sqrt{1-\gamma_\parallel}\right)}\right) - \frac{1}{2}\ln\left(1 + \frac{2B_{\mathrm{so}}^{\mathrm{x}} + 2B_{\mathrm{so}}^{\mathrm{z}}}{B_{\mathrm{i}}}\right)\right], \tag{2.58}$$

where the second term ensures the vanishing of the magneto-conductivity in zero field and

$$\gamma_\parallel = \left(\frac{g_{\mathrm{L}}\mu_{\mathrm{B}}}{4eD}\frac{B}{B_{\mathrm{so}}^{\mathrm{x}} + B_{\mathrm{so}}^{\mathrm{z}}}\right)^2. \tag{2.59}$$

In the limit $g_{\mathrm{L}} \to 0$, which closes the band spin splitting, the parallel magneto-conductivity vanishes. Magneto-transport is shown in Fig. 2.4.

2.1.3 Disputable Scattering Mechanism

In the final formulas for the magneto-conductivity, we used isotropic scattering explicitly. This is legitimate when the states of the conduction electrons still have a three-dimensional character, whereas transport is to be considered two-dimensional [69].

However, in a strict two-dimensional xy-plane, HLN have emphasized that only the z-component[3] of the spin–orbit scattering rate enters as a relevant scattering mechanism [6]. In this case, the Elliott–Yafet mechanism demands $1/\tau_{\mathrm{so,z}} \propto |\mathbf{k}\times\mathbf{k}'|_{\mathrm{z}}^2$, whereas the scattering rates $1/\tau_{\mathrm{so,x}} = 0$ and $1/\tau_{\mathrm{so,y}} = 0$. This causes in both the HLN as well as in the Maekawa–Fukuyama result that the spin–orbit scattering contributions in form of $B_{\mathrm{so}}^{\mathrm{x}}$ and $B_{\mathrm{so}}^{\mathrm{y}}$ vanish. As exactly these effective fields create the WAL structure in Eq. (2.31) and Eq. (2.57), we find no qualitative signature of spin–orbit coupling in the magneto-conductivity.

[3] The index in the scattering rate should not be confused with a scattering direction. It originates from the scattering potential which is proportional to $i(\mathbf{k}\times\mathbf{k}')\cdot\boldsymbol{\sigma}$, where $\boldsymbol{\sigma}$ is the vector of Pauli matrices, and therefore labels the spin channel of the scattering mechanism, which is the σ_{z} channel for transport in xy-plane.

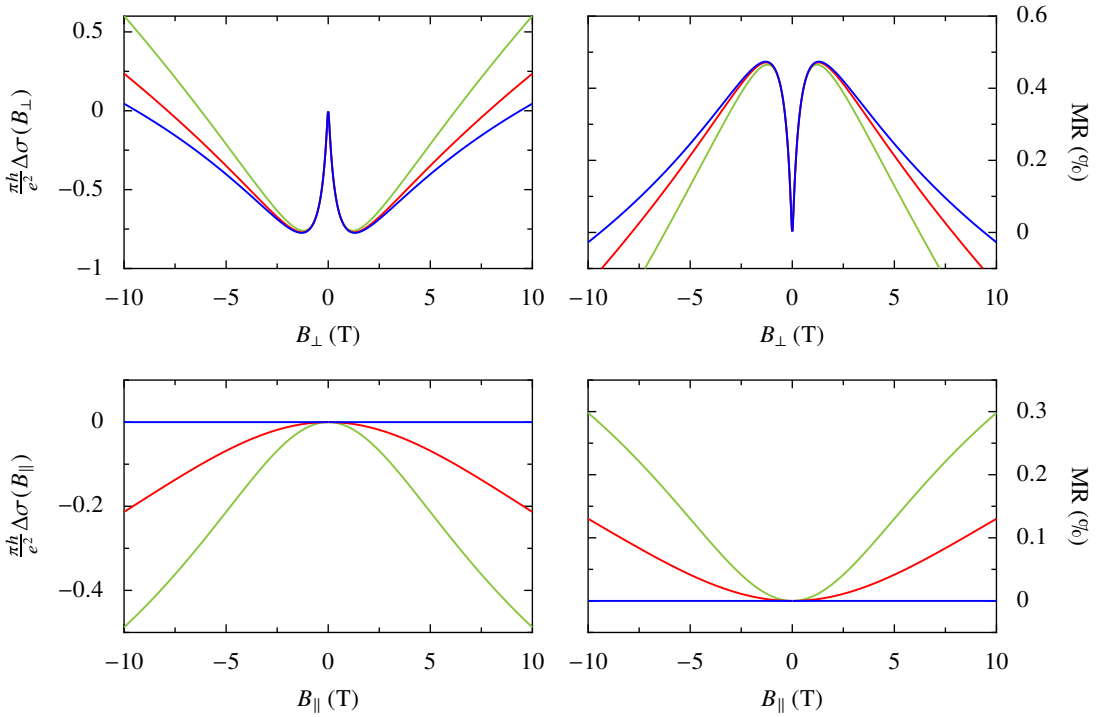

Figure 2.4: *Magneto-conductivity and magneto-resistivity (MR) in the Maekawa–Fukuyama formalism.* Response in magnetic field components perpendicular and parallel to the two-dimensional electron system. The value for the g_L factor is chosen to be $g_\mathrm{L}/D = 0\,\mathrm{s/cm^2}$ (blue), $g_\mathrm{L}/D = 0.05\,\mathrm{s/cm^2}$ (red), and $g_\mathrm{L}/D = 0.1\,\mathrm{s/cm^2}$ (green). The effective fields for all plots are $B_\mathrm{i} = 0.02\,\mathrm{T}$, $B_\mathrm{so} = 0.3\,\mathrm{T}$; the zero field resistivity is $\rho(0) = 500\,\Omega$.

We conclude that the Elliott–Yafet mechanism cannot describe a negative magneto-conductivity in strictly two-dimensional systems. It might be applicable to use these theories for thin metallic films and electron liquids in semiconductor quantum wells, but electronic states in oxide heterostructures are often considered to be well confined in the perpendicular direction. Any recognizable WAL structure in an experimental signal (given by positive magneto-resistivity for low magnetic fields, as well as negative magneto-resistivity for higher fields) should follow from a theory treating the D'yakonov–Perel' spin relaxation instead [91]. We introduce this scattering mechanism in the following sections, but give a short prospect on how this mechanism has been treated within HLN-theory.

Altshuler, Aronov, Larkin and Khmel'nitskii (often referred to as AALKh) [22] incorporated a dispersiv spin–orbit splitting in the band structure into the localization theory. They used a D'yakonov–Perel' spin relaxation rate in the effective fields by taking $B_\mathrm{so}^\mathrm{z} = 0$ explicitly and consequently $2B_\mathrm{so}^\mathrm{x} = B_\mathrm{so}$ [92]. Although it cannot be justified from a microscopic view, this procedure transfered the D'yakonov–Perel' mechanism, connected to a in-plane Bloch vector [22, 93, 94], into the HLN-theory.

If we follow these arguments, the Maekawa–Fukuyama formulas simplify into

$$\Delta\sigma_{\perp}(B) = \frac{e^2}{\pi h}\left\{\Psi\left(\frac{B_{\mathrm{so}}+B_{\mathrm{i}}}{B}\right)+\frac{1}{2}\ln\left(\frac{2B_{\mathrm{so}}+B_{\mathrm{i}}}{B_{\mathrm{i}}}\right)\right.$$
$$\left.+\frac{1}{2\sqrt{1-\gamma_{\perp}}}\left[\psi\left(\frac{1}{2}+\frac{B_{\mathrm{so}}\left(1+\sqrt{1-\gamma_{\perp}}\right)+B_{\mathrm{i}}}{B}\right)-\psi\left(\frac{1}{2}+\frac{B_{\mathrm{so}}\left(1-\sqrt{1-\gamma_{\perp}}\right)+B_{\mathrm{i}}}{B}\right)\right]\right\}. \tag{2.60}$$

$$\Delta\sigma_{\parallel}(B) = \frac{e^2}{\pi\hbar}\left[\frac{1}{2\sqrt{1-\gamma_{\parallel}}}\ln\left(\frac{B_{\mathrm{i}}+\frac{B_{\mathrm{so}}}{2}\left(1+\sqrt{1-\gamma_{\parallel}}\right)}{B_{\mathrm{i}}+\frac{B_{\mathrm{so}}}{2}\left(1-\sqrt{1-\gamma_{\parallel}}\right)}\right)-\frac{1}{2}\ln\left(1+\frac{B_{\mathrm{so}}}{B_{\mathrm{i}}}\right)\right], \tag{2.61}$$

where

$$\gamma_{\perp} = \gamma_{\perp}(B) = \left(\frac{g_{\mathrm{L}}\mu_{\mathrm{B}}}{4eD}\frac{B}{B_{\mathrm{so}}}\right)^2, \tag{2.62}$$

$$\gamma_{\parallel} = \left(\frac{g_{\mathrm{L}}\mu_{\mathrm{B}}}{2eD}\frac{B}{B_{\mathrm{so}}}\right)^2, \tag{2.63}$$

and the HLN formula for $g_{\mathrm{L}} \to 0$ is given by

$$\Delta\sigma(B) = \frac{e^2}{\pi h}\left[\Psi\left(\frac{B_{\mathrm{so}}+B_{\mathrm{i}}}{B}\right)+\frac{1}{2}\Psi\left(\frac{2B_{\mathrm{so}}+B_{\mathrm{i}}}{B}\right)-\frac{1}{2}\Psi\left(\frac{B_{\mathrm{i}}}{B}\right)\right]. \tag{2.64}$$

These formulas have actually resulted in reasonable fits for the data on GaAs/AlGaAs heterostructures [92]. The same approach has successfully been used by several groups for the analysis of magneto-transport on heterostructures of $LaAlO_3/SrTiO_3$ [95–97]. As D'yakonov–Perel' relaxation is still treated via the scattering processes in perturbation theory in a Elliott–Yafet like mechanism, this approach can only produce agreement for small magnetic fields $B < B_{\mathrm{so}}$. However, we will find in upcoming sections that the typical spin–orbit coupling in two dimensional systems introduces an additional term in the magneto-conductivity, which is dominant for fields $B \gtrsim B_{\mathrm{so}}$, but not captured in HLN-theory. We review the microscopic theory for D'yakonov–Perel' spin relaxation in the following sections.

2.2 Dispersive Spin–Orbit Splitting: Model Hamiltonians

2.2.1 Dresselhaus and Rashba Spin–Orbit Coupling

To construct relevant Hamiltonians with incorporated spin–orbit coupling on a very general level, we employ symmetry considerations. For example, under time reversal we find that

$$\mathbf{p} \to -\mathbf{p}, \tag{2.65}$$
$$\boldsymbol{\sigma} \to -\boldsymbol{\sigma}, \tag{2.66}$$
$$\nabla V \to \nabla V, \tag{2.67}$$

therefore the spin–orbit coupling Hamiltonian Eq. (2.1) preserves time reversal symmetry, and eigenenergies $\varepsilon_{\mathbf{k}}$ of the Hamiltonian follow the relation

$$\varepsilon_{\mathbf{k}\uparrow} = \varepsilon_{-\mathbf{k}\downarrow}. \tag{2.68}$$

Those degenerate states are known as Kramer's pairs.

Another symmetry concern in solids is the presence or absence of spatial inversion symmetry. In many crystals, spatial inversion is preserved and one finds the stronger condition (in addition to time reversal symmetry)

$$\varepsilon_{\mathbf{k}\uparrow} = \varepsilon_{\mathbf{k}\downarrow} = \varepsilon_{-\mathbf{k}\downarrow} = \varepsilon_{-\mathbf{k}\uparrow}, \tag{2.69}$$

which signifies perfect spin degeneracy of eigenstates (nonetheless, as discussed in Sec. 2.1.1, nearby bands might result in spin mixing).

If the spatial inversion symmetry is broken in a crystal by a non-symmetric unit cell or by confinement potentials, the upper relation, Eq. (2.69), no longer holds, and the spin degeneracy is lifted. A term in the Hamiltonian that keeps time reversal symmetry but violates spatial inversion is odd in momentum $\mathbf{k}$ as well as in $\boldsymbol{\sigma}$. As for a spin-1/2 particle we expect the Pauli matrices only to appear linearly in a one-particle description, a spin–orbit term in the Hamiltonian can only appear in the form [80]

$$\mathcal{H}_{\mathrm{so}} = \hbar\boldsymbol{\Omega}(\mathbf{k}) \cdot \boldsymbol{\sigma}, \tag{2.70}$$

where the Bloch vector $\boldsymbol{\Omega}(\mathbf{k})$ is an odd function in $\mathbf{k}$. Throughout the thesis, we use the following representation of the Pauli matrices and corresponding normalized eigenvectors:

$$\sigma_{\mathrm{x}} = \begin{pmatrix} 0 & 1 \\ 1 & 0 \end{pmatrix}, \quad v_+ = \frac{1}{\sqrt{2}}\begin{pmatrix} 1 \\ 1 \end{pmatrix}, \quad v_- = \frac{1}{\sqrt{2}}\begin{pmatrix} -1 \\ 1 \end{pmatrix}, \tag{2.71}$$

$$\sigma_{\mathrm{y}} = \begin{pmatrix} 0 & -i \\ i & 0 \end{pmatrix}, \quad v_+ = \frac{1}{\sqrt{2}}\begin{pmatrix} -i \\ 1 \end{pmatrix}, \quad v_- = \frac{1}{\sqrt{2}}\begin{pmatrix} i \\ 1 \end{pmatrix}, \tag{2.72}$$

$$\sigma_{\mathrm{z}} = \begin{pmatrix} 1 & 0 \\ 0 & -1 \end{pmatrix}, \quad v_+ = \begin{pmatrix} 1 \\ 0 \end{pmatrix}, \quad v_- = \begin{pmatrix} 0 \\ 1 \end{pmatrix}. \tag{2.73}$$

We will discuss two kinds of broken spatial inversion symmetry. First, the symmetry can be broken by lack of an inversion center in the unit cell (broken bulk inversion symmetry). This can be realized in a three-dimensional material like the zinc-blende structured GaAs and results in Dresselhaus spin–orbit coupling. Secondly, the inversion symmetry can be broken explicitly by external fields (like an electric field) or induced by an interface, which results in Bychkov–Rashba spin–orbit coupling (broken structure inversion symmetry).

Dresselhaus spin–orbit coupling

For three-dimensional materials with broken bulk inversion symmetry, the spin splitting in the conduction electron bands is proportional to the momentum cubed in lowest order [80, 98, 99],

$$\boldsymbol{\Omega}_{\mathrm{D}}(\mathbf{k}) = 2\gamma_{\mathrm{D}} \begin{pmatrix} k_{\mathrm{x}}\left(k_{\mathrm{y}}^2 - k_{\mathrm{z}}^2\right) \\ k_{\mathrm{y}}\left(k_{\mathrm{z}}^2 - k_{\mathrm{x}}^2\right) \\ k_{\mathrm{z}}\left(k_{\mathrm{x}}^2 - k_{\mathrm{y}}^2\right) \end{pmatrix}. \tag{2.74}$$

This kind of spin–orbit coupling is known as the Dresselhaus effect. In two-dimensional systems, the Dresselhaus term transfers into descendents linear as well as cubic in momentum [80]

$$\mathcal{H}_{\mathrm{D}} = \hbar\boldsymbol{\Omega}_{\mathrm{D}}(\mathbf{k}) \cdot \boldsymbol{\sigma} = \beta_{\mathrm{D}}\left(-k_{\mathrm{x}}\sigma_{\mathrm{x}} + k_{\mathrm{y}}\sigma_{\mathrm{y}}\right) + \gamma_{\mathrm{D}}\left(k_{\mathrm{x}}k_{\mathrm{y}}^2\sigma_{\mathrm{x}} - k_{\mathrm{x}}^2k_{\mathrm{y}}\sigma_{\mathrm{y}}\right), \tag{2.75}$$

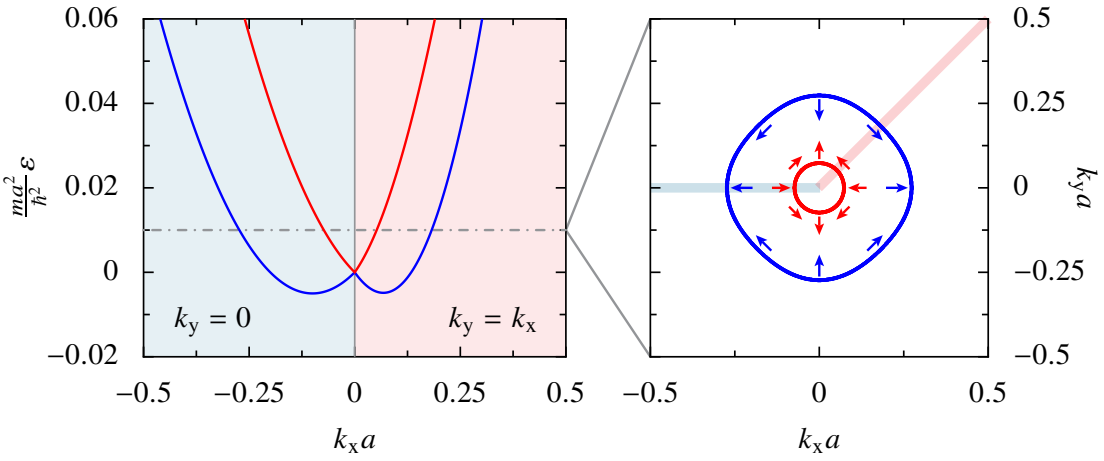

Figure 2.5: *Bands and Fermi surface of an electron gas with Dresselhaus spin–orbit coupling.* The strength of the spin–orbit coupling is chosen to be $\beta_D = 0.1\,\hbar^2/am$, where a is the lattice constant and m is the effective electron mass, and $\gamma_D = 0.3\,\hbar^2 a/m$. If the spin quantization axis is traced around the Fermi surface, the spin winding number is found to be $w = -1$ for both bands.

where $\beta_D = \gamma_D \langle k_z^2 \rangle$, and $\langle k_z^2 \rangle$ is the averaged squared wave vector in z-direction perpendicular to the two-dimensional plane, which is constant. Using

$$k_x = k \cos\phi, \tag{2.76}$$
$$k_y = k \sin\phi \tag{2.77}$$

and $\tan\phi = {}^{k_y}/_{k_x}$, as well as $k^2 = k_x^2 + k_y^2$, the effective spin–orbit field can be expressed in terms of harmonics of the angle ϕ defined in the momentum plane [7, 100, 101],

$$\begin{aligned} \Omega_D &= \gamma_D \left[\left(k \langle k_z^2 \rangle - \frac{k^3}{4} \right) \begin{pmatrix} -\cos\phi \\ \sin\phi \end{pmatrix} - \frac{k^3}{4} \begin{pmatrix} \cos(3\phi) \\ \sin(3\phi) \end{pmatrix} \right] \\ &\equiv \Omega_{D1} \begin{pmatrix} -\cos\phi \\ \sin\phi \end{pmatrix} - \Omega_{D3} \begin{pmatrix} \cos(3\phi) \\ \sin(3\phi) \end{pmatrix}. \end{aligned} \tag{2.78}$$

If either first or third harmonic of the spin–orbit coupling is dominant, the spin–orbit splitting is isotropic. In combination, however, the splitting is given by

$$|\Omega_D| = \sqrt{(\Omega_{D1})^2 + (\Omega_{D3})^2 + 2\Omega_{D1}\Omega_{D3}\cos(4\phi)}. \tag{2.79}$$

For $\Omega_{D1} = \Omega_{D3} \equiv \Omega_D$, the splitting becomes

$$|\Omega_D| = 4\Omega_D \cos(2\phi) \tag{2.80}$$

and results in degenerate points at the Fermi surface. The spin structure for a free electron gas with Dresselhaus spin–orbit coupling and kinetic energy $\xi_k = \hbar^2 k^2/2m$ is shown in Fig. 2.5. The plotted spin structure of the spin–orbit split eigenvalues represents the spin expectation value along the quantization axis, which is given by the momentum dependent effective field of the Bloch vector.

The general eigenvectors, defined in a spin space projected to the z-axis, are given by

$$v_+ = \frac{1}{\sqrt{2}} \begin{pmatrix} \dfrac{-\Omega_{D1}\cos\phi - \Omega_{D3}\cos(3\phi) + i\Omega_{D1}\sin\phi - i\Omega_{D3}\sin(3\phi)}{|\mathbf{\Omega}_D|} \\ 1 \end{pmatrix}, \tag{2.81}$$

$$v_- = \frac{1}{\sqrt{2}} \begin{pmatrix} -\dfrac{-\Omega_{D1}\cos\phi - \Omega_{D3}\cos(3\phi) + i\Omega_{D1}\sin\phi - i\Omega_{D3}\sin(3\phi)}{|\mathbf{\Omega}_D|} \\ 1 \end{pmatrix}, \tag{2.82}$$

Due to the cubic momentum splitting in energy, the spin structure contains first as well as third harmonics. The non-degenerate Fermi surface can be characterized by a spin winding number w, which we define as the ratio of

$$w = \frac{\phi_S}{\phi_F}, \tag{2.83}$$

where ϕ_F represents the angle enclosed when the Fermi surface is traced around the Γ point and ϕ_S is the angle the spin quantization axis rotates during this tracking. As both angles are multiples of 2π, the winding number is an integer. The character of the spin winding for the Dresselhaus Hamiltonian changes dependent on the filling:

- $|\Omega_{D1}| > |\Omega_{D3}|$ for $k_F < \sqrt{2\langle k_z^2\rangle}$: Single spin winding, $w = -1$,
- $|\Omega_{D1}| = |\Omega_{D3}|$ for $k_F = \sqrt{2\langle k_z^2\rangle}$: No spin winding; perfect anisotropy,
- $|\Omega_{D1}| < |\Omega_{D3}|$ for $k_F > \sqrt{2\langle k_z^2\rangle}$: Triple spin winding. $w = +3$.

The first case is the most realistic case in a narrow quantum well, due to large values of $\langle k_z^2\rangle$ [80]. However, the third harmonic might dominate the Fermi surface for high fillings, see Fig. 2.6. For a three-dimensional Dresselhaus splitting, due to

$$\sin^3(\phi) = \frac{3}{4}\sin(\phi) - \frac{1}{4}\sin(3\phi), \tag{2.84}$$

$$\cos^3(\phi) = \frac{3}{4}\cos(\phi) + \frac{1}{4}\cos(3\phi), \tag{2.85}$$

the third harmonic again is only a smaller modulation of the larger first harmonic.

Rashba spin–orbit coupling

Another kind of spin–orbit interaction is the Rashba coupling Ω_R [102] (see also the recent reviews, Refs. [103, 104]), caused by a broken structure inversion symmetry (for example by applying an external electric field perpendicular to the plane) [105]. This breaks the symmetry between the z and −z direction [99]. For the Rashba spin–orbit coupling, the Hamiltonian has a linear momentum dependence [80]

$$\mathcal{H}_{R1} = \alpha_{R1}(\boldsymbol{\sigma}\times\mathbf{k})\cdot\hat{\mathbf{z}} \tag{2.86}$$

$$= \alpha_{R1}\left(\sigma_x k_y - \sigma_y k_x\right). \tag{2.87}$$

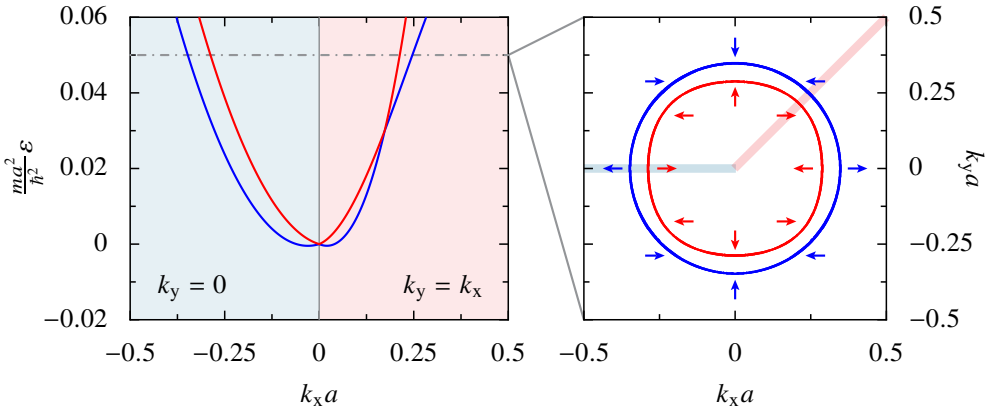

Figure 2.6: *Bands and Fermi surface of an electron gas with strong cubic Dresselhaus spin–orbit contribution.* The strength of the spin–orbit coupling is chosen to be $\beta_D = 0.03\,\hbar^2/am$ and $\gamma_D = 1.0\,\hbar^2 a/m$ in this picture. The spin winding number is $w = +3$ for the surfaces of both bands. For intermediate filling, a node appears at the Fermi surface and the spin winding number is no longer a meaningful quantity at this node.

Thus the propagation in x-direction is connected to the y-component Pauli matrix and vice versa. The effective spin–orbit field in this case is given by [100, 101]

$$\Omega_{R1} = \Omega_{R1} \begin{pmatrix} \sin\phi \\ -\cos\phi \end{pmatrix}, \tag{2.88}$$

where $\Omega_{R1} = \alpha_R k$ and α_R usually is propotional to a uniform electrical field E. The eigenvalues of the above Hamiltonian are given by

$$\varepsilon_\pm = \pm\alpha_{R1} k \tag{2.89}$$

and the eigenvectors, written in z-axis representation, are given by

$$v_+ = \frac{1}{\sqrt{2}} \begin{pmatrix} \sin\phi + i\cos\phi \\ 1 \end{pmatrix}, \qquad v_- = \frac{1}{\sqrt{2}} \begin{pmatrix} -\sin\phi - i\cos\phi \\ 1 \end{pmatrix}, \tag{2.90}$$

which are for $\phi = 0$ and $\phi = \pi/2$ identical with the eigenvectors of the y and x Pauli matrices, respectively. The spin structure at the Fermi surface is shown in Fig. 2.7.

For a Rashba as well as Dresselhaus spin–orbit splitting, the quantization axis for the three dimensional spin always lies within the interface xy-plane and is connected to a non-trivial winding number for each band. For Rashba spin–orbit coupling, the winding number is $w = +1$ for both Fermi surfaces. For linear Dresselhaus spin–orbit coupling, the winding number is $w = -1$ for both Fermi surfaces. For the cubic Dresselhaus effect, the spin winding number is $w = +3$ for each Fermi surface. As result, we always find an even winding number for the complete system.

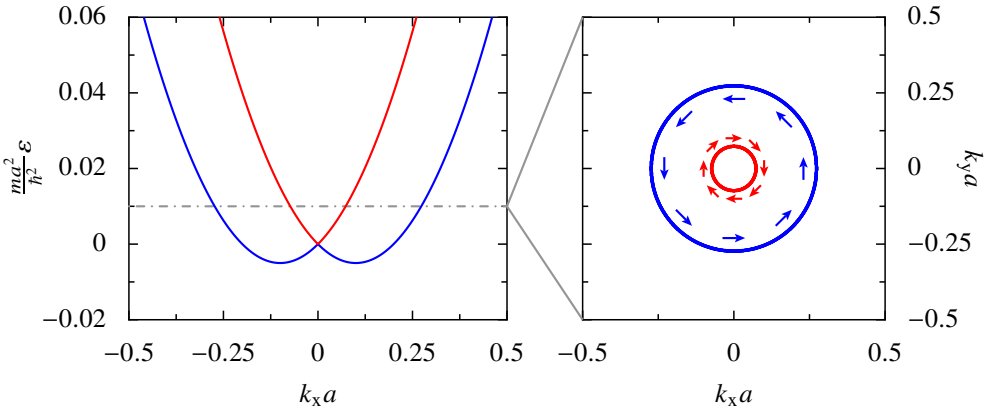

Figure 2.7: *Bands and Fermi surface of an electron gas with Rashba spin–orbit coupling.* The strength of the spin–orbit coupling is chosen to be $\alpha_R = 0.1\,\hbar^2/am$ in this picture. The spin winding number is $w = +1$ for the Fermi surfaces of both bands.

2.2.2 Cubic and Anisotropic Rashba Spin–Orbit Effect

In a multiband system, the particular spin structure at the Fermi surface strongly depends on the specific hybridization of the bands (see Sec. 3.1.2). Furthermore, for semiconductors as well as for oxide heterostructures, it has been shown that the observed spin–orbit couplings are often better understood in terms of a mixture of multiband and atomic spin–orbit coupling effects [106, 107]. In the following, we introduce two effective Hamiltonians that are extensions of the Rashba Hamiltonian, and which will be discussed later for the WAL theory of $LaAlO_3/SrTiO_3$ in Chap. 3: First, a cubic Rashba effect with triple spin winding (providing an effective model for the higher band pair of the $LaAlO_3/SrTiO_3$ six-band model) and secondly, an anisotropic Rashba spin–orbit coupling, where single and triple winding are of equal importance (providing an effective model for the middle band pair of the $LaAlO_3/SrTiO_3$ six-band model).

First, we discuss the cubic Rashba Hamiltonian,

$$\mathcal{H}_{R3} = \alpha_{R3}\left[k_y\left(3k_x^2 - k_y^2\right)\sigma_x + k_x\left(3k_y^2 - k_x^2\right)\sigma_y\right]. \tag{2.91}$$

Using $\hbar\Omega_{R3} = \alpha_{R3}k^3$, the corresponding Bloch vector contains only third harmonic contributions [108]

$$\mathbf{\Omega}_{R3}(\mathbf{k}) = \Omega_{R3}\begin{pmatrix}\sin(3\phi)\\ -\cos(3\phi)\end{pmatrix}, \tag{2.92}$$

describing a spin winding number $w = +3$ at the Fermi surface. The normalized eigenstates are given by

$$v_+ = \frac{1}{\sqrt{2}}\begin{pmatrix}\sin(3\phi) + i\cos(3\phi)\\ 1\end{pmatrix}, \qquad v_- = \frac{1}{\sqrt{2}}\begin{pmatrix}-\sin(3\phi) - i\cos(3\phi)\\ 1\end{pmatrix}. \tag{2.93}$$

The cubic Rashba effect results in an energy gap of

$$\varepsilon_\pm = \pm\alpha_{3R}\sqrt{\left(k_x^2 + k_y^2\right)^3}, \tag{2.94}$$

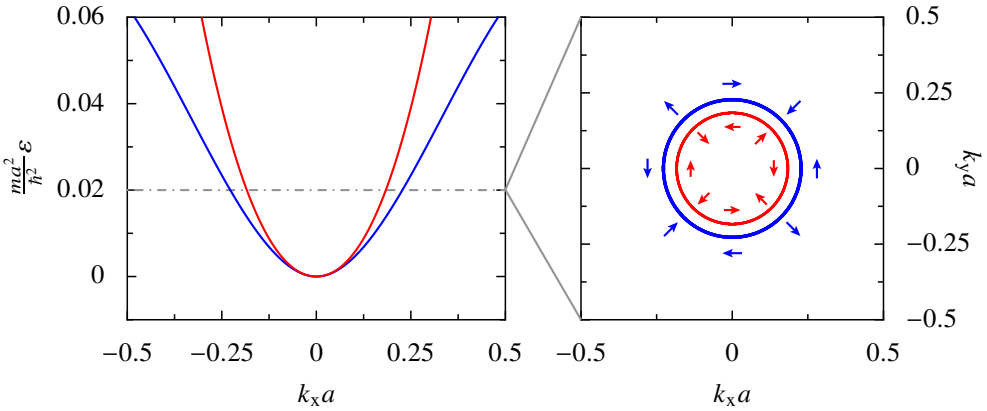

Figure 2.8: *Bands and Fermi surface of an electron gas with cubic Rashba spin–orbit coupling.* The strength of the spin–orbit coupling is chosen to be $\alpha_{3R} = 0.5\,\hbar^2 a/m$, where a is the lattice constant and m the effective electron mass. The spin winding number is $w = +3$ for the surfaces of both bands.

the dispersion is depicted in Fig. 2.8.

The anisotropic Rashba description has been proposed in Ref. [109]:

$$\mathcal{H}_{\mathrm{R1=R3}} = \alpha_{\mathrm{R}} \left(k_{\mathrm{y}}^2 - k_{\mathrm{x}}^2\right) (\boldsymbol{\sigma} \times \mathbf{k}) \cdot \hat{\mathbf{z}} \tag{2.95}$$

$$= \alpha_{\mathrm{R}} \left(k_{\mathrm{y}}^2 - k_{\mathrm{x}}^2\right) \left(\sigma_{\mathrm{x}} k_{\mathrm{y}} - k_{\mathrm{x}} \sigma_{\mathrm{y}}\right). \tag{2.96}$$

Expressed in terms of the Bloch vector, the band pair is characterized by

$$\Omega_{\mathrm{R1=R3}}(\mathbf{k}) = \frac{\alpha_{\mathrm{R}}}{\hbar} k^3 \left(\sin^2\phi - \cos^2\phi\right) \begin{pmatrix} \sin\phi \\ -\cos\phi \end{pmatrix} \tag{2.97}$$

$$= \Omega_{\mathrm{R}} \left[\begin{pmatrix} \sin\phi \\ \cos\phi \end{pmatrix} + \begin{pmatrix} -\sin(3\phi) \\ \cos(3\phi) \end{pmatrix} \right]. \tag{2.98}$$

It has a similar structure than the Dresselhaus Hamiltonian, but the contributions from first and third harmonic are of the same size for all fillings. We find for the Hamiltonian the energy splitting

$$\varepsilon_{\pm} = \pm 2\Omega_{\mathrm{R}} \cos(2\phi), \tag{2.99}$$

and for the normalized eigenstates

$$v_{+} = \frac{1}{\sqrt{2}} \begin{pmatrix} +\frac{1}{2\cos(2\phi)} \left[i\cos\phi + i\cos(3\phi) - \sin\phi + \sin(3\phi)\right] \\ 1 \end{pmatrix}, \tag{2.100}$$

$$v_{-} = \frac{1}{\sqrt{2}} \begin{pmatrix} -\frac{1}{2\cos(2\phi)} \left[i\cos\phi + i\cos(3\phi) - \sin\phi + \sin(3\phi)\right] \\ 1 \end{pmatrix}. \tag{2.101}$$

The spin structure at the Fermi surface is shown in Fig. 2.9. This Hamiltonian contains a degeneracy at the Fermi surface for all fillings, and the spin winding number is not a meaningful quantity. Note that this splitting (but not the eigenvectors) is completely analogous to the Dresselhaus splitting with equal first and third contribution.

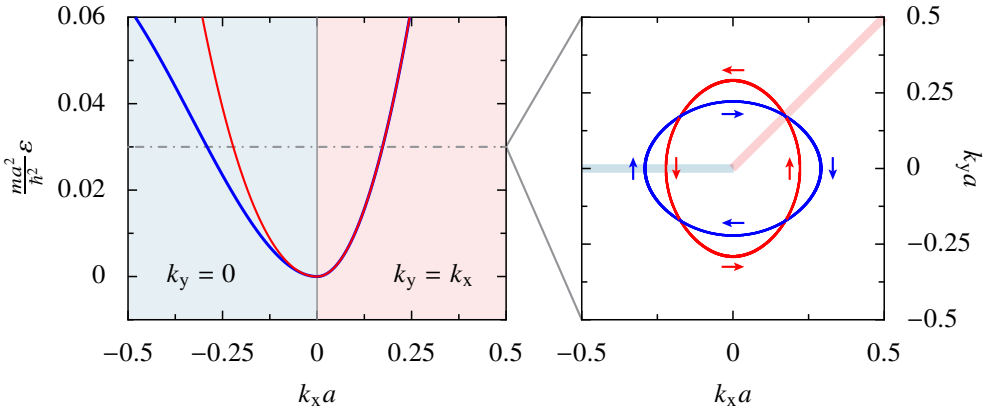

Figure 2.9: *Bands and Fermi surface of an electron gas with Rashba spin–orbit coupling.* The strength of the spin–orbit coupling is chosen to be $\alpha_R = 0.5\,\hbar^2 a/m$ in this picture. The spin winding number is +1 for the Fermi surfaces of both bands.

2.3 Iordanskii–Lyanda-Geller–Pikus Theory

In Sec. 2.1, we discussed the HLN-theory of WAL. Although some attempts have been made to extend the microscopic picture involved in this theory, the HLN calculation is clearly based on the Elliott–Yafet mechanism of spin relaxation. This mechanism takes place even when spatial inversion symmetry is not explicitly broken, and the Elliott–Yafet spin relaxation time is proportional to the elastic scattering time, $\tau_{so} \propto \tau_0$, see Eq. (2.7). This relaxation mechanism does not allow for a WAL signature for magneto-transport in a strongly confined two-dimensional system, but might still be relevant for thin films.

Next, we discussed several model Hamiltonians with broken spatial inversion symmetry in Sec. 2.2. In these systems, D'yakonov–Perel' spin relaxation [22, 93, 110] takes place. This relaxation mechanism is expected to be relevant for crystal inversion symmetry broken semiconductors as well as structure inversion symmetry broken heterostructures or quantum wells due to the asymmetric confining potentials [84].

The spin splitting is given by the amplitude of the Bloch vector, $2|\boldsymbol{\Omega}(\mathbf{k})| = 2\Omega$. The Bloch vector acts as an effective magnetic field for each spin projection and can be interpreted in terms of a Larmor frequency [84], causing spin precession. In a perfect crystal, the electron spins would be distributed according to Ω, but momentum scattering events (under the condition $\Omega\tau_0 \ll 1$) cause a scattering rate of [83]

$$\frac{1}{\tau_{soc}^{DP}} \approx \Omega^2 \tau_0, \tag{2.102}$$

leading to a spin relaxation time that is inverse proportional to the elastic scattering time. A scattering process changes direction and frequency of the precession. Therefore the spin phases are randomized between collisions, whereas in the Elliott–Yafet mechanism, the spin looses phase information at the collision [84].

2.3.1 Cooperon for Dispersive Spin–Orbit Splitting

In 1994, Iordanskii, Lyanda-Geller and Pikus (ILP) proposed a treatment of the maximally crossed diagrams where the spin–orbit coupling is taken into account via D'yakonov–Perel'

spin relaxation [7]. In the following, we review the calculations by following Refs. [7, 100, 101]. The Hamiltonian is given by

$$\mathcal{H} = \frac{\hbar^2 \mathbf{k}^2}{2m} + \hbar \boldsymbol{\sigma} \cdot \boldsymbol{\Omega}(\mathbf{k}), \tag{2.103}$$

where $\boldsymbol{\sigma}$ is the two-dimensional vector of Pauli matrices for x-,y-direction[4] and $\boldsymbol{\Omega}$ represents the corresponding Bloch vector (see Sec. 2.2 for different cases like Dresselhaus or Rashba Hamiltonians). This theory has gone beyond the scattering approach of the HLN-theory and Maekawa–Fukuyama-theory and has been succesfully used to describe magneto-transport data in GaAs/Al_xGa_{1-x}As quantum wells [111]. In the following, we keep both, the conventional Rashba and Dresselhaus effect in the Bloch vector,

$$\boldsymbol{\Omega}(\mathbf{k}) = \Omega_{\mathrm{R1}}(\mathbf{k}) \begin{pmatrix} \sin\phi \\ -\cos\phi \end{pmatrix} + \Omega_{\mathrm{D1}}(\mathbf{k}) \begin{pmatrix} -\cos\phi \\ \sin\phi \end{pmatrix} - \Omega_{\mathrm{D3}}(\mathbf{k}) \begin{pmatrix} \cos(3\phi) \\ \sin(3\phi) \end{pmatrix}. \tag{2.104}$$

However, until the particular structure of the Bloch vector becomes important, we simply separate the first and the third harmonics of the Bloch vector,

$$\boldsymbol{\Omega} = \boldsymbol{\Omega}_1 + \boldsymbol{\Omega}_3. \tag{2.105}$$

The aim is to solve the expression Eq. (1.41) for the conductivity by using the Hamiltonian (2.103). We will find that an analytical result is still possible if it is assumed that the scattering rate $1/\tau_0$ is large in comparison with the spin–orbit splitting and $v_{\mathrm{F}}q$. Then these terms can be neglected in the Green's functions to the left- and right-hand side of the Cooperon [see Eq. (1.46)] and we are left with

$$\delta\sigma(\omega \to 0) = -2e^2 N_{\mathrm{F}} D \tau^2 \sum_{\alpha\beta} \int_{\mathbf{q}} C_{\alpha\beta\beta\alpha}(\mathbf{q}). \tag{2.106}$$

The Cooperon[5] is found by evaluation of the Dyson equation,

$$\begin{aligned} C_{\alpha\gamma\beta\delta}(\mathbf{k}, \mathbf{k}', \mathbf{q}) = {} & \frac{n_{\mathrm{imp}} \left| V_{\mathbf{k},\mathbf{k}'} \right|^2}{\hbar^2} \delta_{\alpha\beta}\delta_{\gamma\delta} \\ & + \frac{n_{\mathrm{imp}}}{\hbar^2} \int \frac{\mathrm{d}^2 g}{(2\pi)^2} \sum_{\nu,\mu} V_{\mathbf{k},\mathbf{g}} V_{-\mathbf{k},-\mathbf{g}} G^{\mathrm{ret}}_{\alpha\nu}(\omega, \mathbf{g}) G^{\mathrm{adv}}_{\gamma\mu}(\omega, -\mathbf{g}+\mathbf{q}) C_{\nu\mu\beta\delta}(\mathbf{g}, \mathbf{k}', \mathbf{q}), \end{aligned} \tag{2.107}$$

which involves scattering processes with $\Delta\mathbf{k} = 2\mathbf{k}_{\mathrm{F}}$ for small $\mathbf{q} \approx 0$ (see also Fig. 2.10).

We incorporate the inelastic scattering rate directly into the Green's functions (see the discussion of the integral cutoffs in Eq. (1.65) and Eq. (1.54), respectively), which are defined in a 2×2 spin space each,

$$G^{\mathrm{ret/adv}}(\mathbf{k}, \omega) = \frac{\hbar}{\hbar\omega - [\xi_{\mathbf{k}} + \hbar\boldsymbol{\sigma} \cdot \boldsymbol{\Omega}(\mathbf{k})] \pm \frac{i\hbar}{2}\left(\frac{1}{\tau_0} + \frac{1}{\tau_{\mathrm{i}}}\right)}, \tag{2.108}$$

where τ_{i} is the inelastic life time.

[4] A Zeeman term would be characterized by a z-component of the $\boldsymbol{\sigma}$ vector and magnetic field dependent $\boldsymbol{\Omega}$.
[5] Note that the ILP-theory uses a different assignment of the involved spin pairs than HLN-theory.

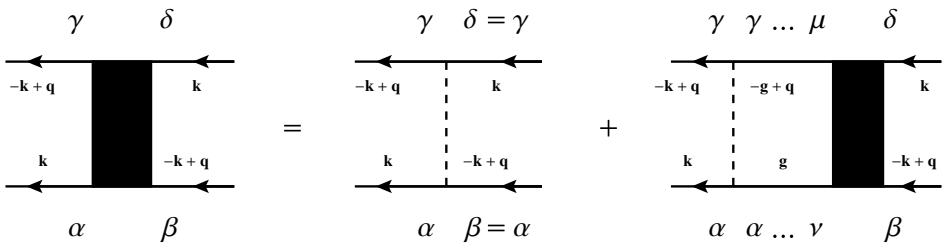

Figure 2.10: *Dyson equation for the D'yakonov–Perel' spin relaxation in the Cooperon.* The Cooperon involves scattering processes that conserve the spin projection. However, the spin splitting in the Hamiltonian acts as effective field and leads to a D'yakonov–Perel' spin relaxation process during the propagation of the particles (denoted by "..."). This allows the mixing of spin states even for orthogonal scattering.

The product of advanced and retarded Green's function is an object in a 4×4 spin-product space, which is also the case for the Cooperon. However, note that two indices of the Cooperon are inert in Eq. (2.107), explicitly β and δ. The four scattering channels will result in spin singlet and spin triplet contributions, similar to the HLN calculation.

Also note that the scattering process matrix elements $V_{\mathbf{k},\mathbf{k}'}$ are—contrary to the approach of HLN-theory—diagonal in spin space. We will find in the following that the Bloch vector will appear in the particle–hole propagator $\Pi_{\alpha\beta}$ in a similar functioning than the spin–orbit scattering in the HLN calculation.

If we assume that the spin–orbit splitting is small in comparison with the kinetic energy,

$$\hbar\boldsymbol{\sigma} \cdot \boldsymbol{\Omega}(\mathbf{g}) \ll \xi_{\mathbf{g}}, \tag{2.109}$$

we can convert the momentum integral into polar representation and transform the radial part $\varepsilon(\mathbf{g}) \approx \xi_{\mathbf{g}} - \mu$ into an energy integral over $\xi_{\mathbf{g}}$ (see the discussion of the integral limits in Eqs. (A.64)–(A.67)). Furthermore, we assume that the scattering potential $V_{\mathbf{k},\mathbf{k}'}$ only depends on the scattering angle and on the absolute value of the momentum transfer. Then we find the Cooperon matrix by considering the Dyson equation,

$$\begin{aligned} C_{\mathbf{k},\mathbf{k}'}(\mathbf{q}) = {} & \frac{n_{\mathrm{imp}} \left|V_{\mathbf{k},\mathbf{k}'}\right|^2}{\hbar^2} + \frac{n_{\mathrm{imp}} N_{\mathrm{F}}}{\hbar^2} \int \frac{\mathrm{d}\phi}{2\pi} \int \mathrm{d}\xi_{\mathbf{g}} \left|V_{\mathbf{k},\mathbf{g}}\right|^2 \\ & \times \frac{\hbar}{\xi_{\mathbf{g}+\mathbf{q}} - \hbar\omega + \hbar\boldsymbol{\sigma} \cdot \boldsymbol{\Omega}(\mathbf{g}) - \frac{i\hbar}{2}\left(\frac{1}{\tau_0} + \frac{1}{\tau_{\mathrm{i}}}\right)} \frac{\hbar}{\xi_{\mathbf{g}} - \hbar\omega + \hbar\boldsymbol{\rho} \cdot \boldsymbol{\Omega}(-\mathbf{g}+\mathbf{q}) + \frac{i\hbar}{2}\left(\frac{1}{\tau_0} + \frac{1}{\tau_{\mathrm{i}}}\right)} C_{\mathbf{g},\mathbf{k}'}(\mathbf{q}), \end{aligned} \tag{2.110}$$

where $\boldsymbol{\sigma}$ acts on the first pair of spin indices, α and ν, and $\boldsymbol{\rho}$ acts on the second pair of spin indices, γ and μ.

By using the explicit form of the dispersion $\xi_{\mathbf{g}+\mathbf{q}}$, Eq. (1.42), the latter expression allows to use the residue theorem[6] and

$$\begin{aligned} C_{\mathbf{k},\mathbf{k}'}(\mathbf{q}) = & \frac{n_{\mathrm{imp}} \left|V_{\mathbf{k},\mathbf{k}'}\right|^2}{\hbar^2} \\ & + \frac{2\pi N_{\mathrm{F}} n_{\mathrm{imp}} \tau_0}{\hbar} \int \frac{\mathrm{d}\phi}{2\pi} \frac{\left|V_{\mathbf{k},\mathbf{g}}\right|^2 C_{\mathbf{g},\mathbf{k}'}(\mathbf{q})}{\frac{\tau_0}{i\hbar}\left[-\hbar v_{\mathbf{g}} \cdot \mathbf{q} - \hbar\boldsymbol{\sigma} \cdot \boldsymbol{\Omega}(\mathbf{g}) + \hbar\boldsymbol{\rho} \cdot \boldsymbol{\Omega}(-\mathbf{g}+\mathbf{q}) + \frac{i\hbar}{\tau_0} + \frac{i\hbar}{\tau_{\mathrm{i}}}\right]}, \end{aligned} \tag{2.111}$$

where we have neglected terms of order $\mathbf{q}^2 \ll \mathbf{k}_{\mathrm{F}} \cdot \mathbf{q}$. The velocity $\mathbf{v}_{\mathbf{g}}$ is the Fermi velocity[7] in the direction of $\mathbf{g}$. Also the Bloch vectors $\boldsymbol{\Omega}$ are given here by their Fermi surface values, evaluated in the direction of the momentum in their argument.

Because $\mathbf{q}$ is small we use that the spin–orbit term is the anti-symmetric in momentum and

$$\boldsymbol{\sigma} \cdot \boldsymbol{\Omega}(\mathbf{g}) - \boldsymbol{\rho} \cdot \boldsymbol{\Omega}(-\mathbf{g}+\mathbf{q}) \approx (\boldsymbol{\sigma}+\boldsymbol{\rho}) \cdot \boldsymbol{\Omega}(\mathbf{g}). \tag{2.112}$$

We expand the denominator of Eq. (2.111) in the small terms containing $\mathbf{q}$ and $\boldsymbol{\Omega}$[8]

$$\begin{aligned} & \frac{1}{1 + i\tau_0 \mathbf{v}_{\mathbf{g}} \cdot \mathbf{q} + i\tau_0 (\boldsymbol{\sigma}+\boldsymbol{\rho}) \cdot \boldsymbol{\Omega}(\mathbf{g}) + \frac{\tau_0}{\tau_{\mathrm{i}}}} \\ & \approx 1 - i\tau_0 \mathbf{v}_{\mathbf{g}} \cdot \mathbf{q} - i\tau_0 (\boldsymbol{\sigma}+\boldsymbol{\rho}) \cdot \boldsymbol{\Omega} - \frac{\tau_0}{\tau_{\mathrm{i}}} \\ & - \tau_0^2 \left(\mathbf{v}_{\mathbf{g}} \cdot \mathbf{q}\right)^2 - 2\tau_0^2 \left(\mathbf{v}_{\mathbf{g}} \cdot \mathbf{q}\right)(\boldsymbol{\sigma}+\boldsymbol{\rho}) \cdot \boldsymbol{\Omega} - \tau_0^2 \left[(\boldsymbol{\sigma}+\boldsymbol{\rho}) \cdot \boldsymbol{\Omega}\right]^2, \end{aligned} \tag{2.113}$$

where we have neglected higher order terms in the inelastic scattering rate.

The lowest order of the expansion Eq. (2.113), which is linear in the Bloch vector, contains only first and third harmonics. The relaxation times, expressed in terms of those harmonics, are

$$\frac{1}{\tau_n} = \int \mathrm{d}\phi W(\phi) \left[1 - \cos(n\phi)\right] \tag{2.114}$$

where $n = \{1, 3\}$ and $W(\phi)$ is the probability for scattering by an angle ϕ. When W is angle independent, the elastic scattering rate is revealed,

$$\frac{1}{\tau_0} = \int \mathrm{d}\phi W(\phi). \tag{2.115}$$

Note that the case of τ_1 corresponds to the Boltzmann transport time τ_{tr}, see Eq. (A.77).

[6] Note that each Green's function carries two linear independent poles due to the spin structure, and in more detail, $\xi_{\mathbf{g}+\mathbf{q}}$ has to be replaced by $\sigma_0 \xi_{\mathbf{g}+\mathbf{q}}$ and $\xi_{\mathbf{g}}$ with $\rho_0 \xi_{\mathbf{g}}$. Under the assumption of small spin–orbit coupling, these two poles are approximately at the same energy, and the result of the integration is the same in both cases. The $\xi_{\mathbf{g}}$ part of the energy cancels when the integral is evaluated. The two independent contributions from the residue theorem are then again collected by using a matrix notation. However, the small non-diagonal entries in the matrices are kept and have to be diagonalized in the following calculation. This results in spin singlet and spin triplet contributions to the Cooperon. Therefore, for small spin–orbit coupling, the approximations are justified.

[7] Again, the whole matrix has to be replaced by its Fermi surface value. This is only justified for small spin–orbit splitting.

[8] The terms $-\tau_0^2 (\boldsymbol{\Omega} \cdot \boldsymbol{\sigma})^2 - \tau_0^2 (\boldsymbol{\Omega} \cdot \boldsymbol{\rho})^2$ are often omitted in the literature.

In the following, we consider the homogenous Cooperon equation. By identifying

$$W(\phi) = \frac{n_{\mathrm{imp}} N_{\mathrm{F}} \left|V_{\mathrm{k,k'}}\right|^2}{\hbar}, \tag{2.116}$$

the homogenous Cooperon equation becomes

$$C_{\mathrm{k,k'}} = \lambda \tau_0 \int \mathrm{d}\phi W(\mathrm{g,k'}) C_{\mathrm{g,k'}}, \tag{2.117}$$

where λ is the eigenvalue of of the Cooperon. Splitting the Cooperon into its harmonics,

$$C^{(n)}_{\mathrm{k,k'}} = C^{(n)} \cos\left[n\left(\phi_{\mathrm{k}} - \phi_{\mathrm{k'}}\right)\right], \tag{2.118}$$

we find for the zero-component the equation

$$C^{(0)}_{\mathrm{k,k'}} = \lambda_0 \tau_0 \int \mathrm{d}\phi W(\mathrm{g,k'}) C^{(0)}_{\mathrm{g,k'}} = \lambda_0 C^{(0)}, \tag{2.119}$$

which gives $\lambda_0 = 1$, as $C^{(0)}_{\mathrm{g,k'}} = C^{(0)}$ has no angular dependence. For the higher harmonics of the Cooperon, we find by inserting Eq. (2.114) and Eq. (2.115),

$$C^{(n)}_{\mathrm{k,k'}} = \tau_0 \int \mathrm{d}\phi W(\mathrm{g,k'}) \lambda_n C^{(n)}_{\mathrm{g,k'}} = \lambda_n \left(1 - \frac{\tau_0}{\tau_n}\right) C^{(n)}, \tag{2.120}$$

and the eigenvalues are therefore given by

$$\lambda_n = \left(1 - \frac{\tau_0}{\tau_n}\right)^{-1}. \tag{2.121}$$

In comparison with the zero-harmonic $C^{(0)}$, the higher harmonics of the Cooperon are small, because they appear in connection with terms containing the small momentum $\mathbf{q}$ or the Bloch vector $\boldsymbol{\Omega}$.

As the Cooperon equation contains terms up to the cubic harmonic, we substitute

$$C_{\mathrm{g,k'}}(\mathbf{q}) \approx C^{(0)}_{\mathrm{g,k'}} + C^{(1)}_{\mathrm{g,k'}} + C^{(3)}_{\mathrm{g,k'}} \tag{2.122}$$

in Eq. (2.111). The first and third harmonic of the homogenous Cooperon equation can then be compared with the eigenvalue equation, Eq. (2.120),

$$\begin{aligned} C^{(1)}_{\mathrm{k,k'}} &= \tau_0 \int \mathrm{d}\phi W(\mathrm{g,k'}) \left\{ C^{(1)}_{\mathrm{g,k'}} - i\tau_0 \left[\left(\mathbf{v}_{\mathrm{g}} \cdot \mathbf{q}\right) + \left(\boldsymbol{\sigma} + \boldsymbol{\rho}\right) \cdot \boldsymbol{\Omega}_1(\mathbf{g}) \right] C^{(0)}_{\mathrm{g,k'}} \right\} \\ &= \tau_0 \int \mathrm{d}\phi W(\mathrm{g,k'}) \left\{ \frac{\tau_1}{\tau_1 - \tau_0} \right\} C^{(1)}_{\mathrm{g,k'}}, \end{aligned} \tag{2.123}$$

$$\begin{aligned} C^{(3)}_{\mathrm{k,k'}} &= \tau_0 \int \mathrm{d}\phi W(\mathrm{g,k'}) \left\{ C^{(3)}_{\mathrm{g,k'}} - i\tau_0 \left(\boldsymbol{\sigma} + \boldsymbol{\rho}\right) \cdot \boldsymbol{\Omega}_3(\mathbf{g}) C^{(0)}_{\mathrm{g,k'}} \right\} \\ &= \tau_0 \int \mathrm{d}\phi W(\mathrm{g,k'}) \left\{ \frac{\tau_3}{\tau_3 - \tau_0} \right\} C^{(3)}_{\mathrm{g,k'}}. \end{aligned} \tag{2.124}$$

This allows to identify the Cooperon amplitude on the right-hand side of Eq. (2.111) in first order with the zero-harmonic only:

$$C^{(1)}_{\mathrm{g},\mathbf{k}'} = -i\,(\tau_1 - \tau_0)\left[\left(\mathbf{v}_\mathrm{g}\cdot\mathbf{q}\right) + (\boldsymbol{\sigma}+\boldsymbol{\rho})\cdot\Omega_1(\mathrm{g})\right] C^{(0)}_{\mathrm{g},\mathbf{k}'}, \tag{2.125}$$

$$C^{(3)}_{\mathrm{g},\mathbf{k}'} = -i\,(\tau_3 - \tau_0)\left[(\boldsymbol{\sigma}+\boldsymbol{\rho})\cdot\Omega_3(\mathrm{g})\right] C^{(0)}_{\mathrm{g},\mathbf{k}'}. \tag{2.126}$$

This is the crucial step in the ILP computation because the full Cooperon, containing all higher harmonics, is now approximated in terms of the zero harmonic Cooperon, which is angle independent and simplifies the integration enormously. We return to the inhomogenous equation and use Eq. (2.122) combined with Eq. (2.125) and Eq. (2.126), as well as Eq. (2.111). In combination with the expansion Eq. (2.113), we find the following inhomogeneous equation to solve for the Cooperon:

$$\begin{aligned} C_{\mathbf{k},\mathbf{k}'}(\mathbf{q}) = {} & \frac{n_\mathrm{imp}\left|V_{\mathbf{k},\mathbf{k}'}\right|^2}{\hbar^2} \\ & + \frac{2\pi N_\mathrm{F} n_\mathrm{imp}\tau_0}{\hbar}\int\frac{\mathrm{d}\phi}{2\pi}\left|V_{\mathrm{g},\mathbf{k}'}\right|^2\Big\{\quad 1 - \frac{\tau_0}{\tau_\mathrm{i}} - i\tau_1\left(\mathbf{v}_\mathrm{g}\cdot\mathbf{q}\right) - i\,(\boldsymbol{\sigma}+\boldsymbol{\rho})\cdot(\tau_1\Omega_1 + \tau_3\Omega_3) \\ & \qquad - \tau_0\tau_1\left[\left(\mathbf{v}_\mathrm{g}\cdot\mathbf{q}\right) + (\boldsymbol{\sigma}+\boldsymbol{\rho})\cdot\Omega_1\right]^2 \\ & \qquad -\tau_0\tau_3\left[(\boldsymbol{\sigma}+\boldsymbol{\rho})\cdot\Omega_3\right]^2 \quad\Big\} C^{(0)}_{\mathrm{g},\mathbf{k}'}, \end{aligned} \tag{2.127}$$

where several terms vanish with the full 2π integration due to the proportionality $\propto \cos(\phi)$, $\sin(\phi)$, $\cos(3\phi)$, $\sin(3\phi)$, or products of these orthogonal expressions. Also note the angular dependence $\mathbf{v}_\mathrm{g}\cdot\mathbf{q} \propto \cos\left(\phi_\mathrm{g} - \phi_\mathbf{q}\right)$. The remaining finite expressions in the curly brackets in Eq. (2.127), under consideration of Eq. (2.104), show the following angle dependence:

$$\begin{aligned} & 1 - \frac{\tau_0}{\tau_\mathrm{i}} - \tau_0\tau_1 v_\mathrm{F}^2 q^2\cos^2\left(\phi - \phi_\mathbf{q}\right) - 2\tau_0\tau_1\left(\sigma_\mathrm{x}+\rho_\mathrm{x}\right)\left(\sigma_\mathrm{y}+\rho_\mathrm{y}\right)\Omega_{\mathrm{D}1}\Omega_{\mathrm{R}1} \\ & - 2\tau_0\tau_1 v_\mathrm{F} q\cos\left(\phi - \phi_\mathbf{q}\right) \\ & \qquad \times\left[\left(\sigma_\mathrm{x}+\rho_\mathrm{x}\right)\left(-\cos\phi\Omega_{\mathrm{D}1} + \sin\phi\Omega_1^\mathrm{R}\right) + \left(\sigma_\mathrm{y}+\rho_\mathrm{y}\right)\left(\sin\phi\Omega_{\mathrm{D}1} - \cos\phi\Omega_{\mathrm{R}1}\right)\right] \\ & - 2\tau_0\tau_1\left(1+\sigma_\mathrm{x}\rho_\mathrm{x}\right)\left[\cos^2(\phi)\left(\Omega_{\mathrm{D}1}\right)^2 + \sin^2(\phi)\left(\Omega_{\mathrm{R}1}\right)^2\right] \\ & - 2\tau_0\tau_1\left(1+\sigma_\mathrm{y}\rho_\mathrm{y}\right)\left[\sin^2(\phi)\left(\Omega_{\mathrm{D}1}\right)^2 + \cos^2(\phi)\left(\Omega_{\mathrm{R}1}\right)^2\right] \\ & - 2\tau_0\tau_3\left(\Omega_{\mathrm{D}3}\right)^2\left[\cos^2(3\phi)\left(1+\sigma_\mathrm{x}\rho_\mathrm{x}\right) + \sin^2(3\phi)\left(1+\sigma_\mathrm{y}\rho_\mathrm{y}\right)\right]. \end{aligned} \tag{2.128}$$

The integration can now be performed, because the zero component of the Cooperon carries no explicit angular dependence. The term containing the $\cos\left(\phi - \phi_\mathbf{q}\right)$ part has to be taken with care. This term contributes differently in two distinguished cases:

$$\phi_\mathbf{q} = 0 \rightarrow \cos\left(\phi - \phi_\mathbf{q}\right) = \cos\phi, \tag{2.129}$$

$$\phi_\mathbf{q} = \frac{\pi}{2} \rightarrow \cos\left(\phi - \phi_\mathbf{q}\right) = \sin\phi. \tag{2.130}$$

The first case, Eq. (2.129), corresponds to $q = q_x$, the second case, Eq. (2.130), to $q = q_y$. After angular integration, and by using the explicit form of the elastic scattering rate Eq. (A.31), we find for the Dyson equation Eq. (1.49)

$$C_{\alpha\gamma\beta\delta} = \frac{\delta_{\alpha\gamma}\delta_{\beta\delta}}{2\pi\hbar N_F \tau_0} + L_{\alpha\nu\gamma\mu} C_{\nu\mu\beta\delta}, \tag{2.131}$$

where L is the integrated form of Eq. (2.128). This allows us to write

$$\left(\delta_{\alpha\nu}\delta_{\gamma\mu} - L_{\alpha\nu\gamma\mu}\right) C_{\nu\mu\beta\delta} = \frac{\delta_{\alpha\gamma}\delta_{\beta\delta}}{2\pi\hbar N_F \tau_0}, \tag{2.132}$$

$$\mathcal{L}_{\alpha\nu\gamma\mu} C_{\nu\mu\beta\delta} = \frac{\delta_{\alpha\gamma}\delta_{\beta\delta}}{2\pi\hbar N_F \tau_0^2}, \tag{2.133}$$

which is in compact notation,

$$\mathcal{L} C = \frac{\mathbf{1}}{2\pi\hbar N_F \tau_0^2} \tag{2.134}$$

where[9]

$$\begin{aligned}\mathcal{L} = \frac{1}{\tau_i} + \frac{v_F^2 \tau_1}{2} q^2 + \tau_1 \nu_F \left[(\sigma_x + \rho_x)\left(-\Omega_{D1} q_x + \Omega_{R1} q_y\right) + \left(\sigma_y + \rho_y\right)\left(\Omega_{D1} q_y - \Omega_{R1} q_x\right)\right] \\ + 2\tau_1 \left(\sigma_x + \rho_x\right)\left(\sigma_y + \rho_y\right)\Omega_{D1}\Omega_{R1} + \left(2 + \sigma_x\rho_x + \sigma_y\rho_y\right)\left(\tau_1 \Omega_{R1+D1}^2 + \tau_3 \Omega_{D3}^2\right).\end{aligned} \tag{2.135}$$

Note that Ω_{R1+D1} contains contributions from both, the Rashba and the Dresselhaus effect.

We represent $\mathcal{L}$ in its eigenbasis,

$$\mathcal{L}(n) = \sum_{r=1}^{4} \psi_{r,n} E_{r,n} \psi_{r,n}^*, \tag{2.136}$$

where $\psi_{r,n}$ are the normalized eigenvectors of $\mathcal{L}$:

$$\mathcal{L}\psi_{r,n} = E_{r,n}\psi_{r,n}. \tag{2.137}$$

Due to the operator identity Eq. (2.134), the Cooperon also has a diagonal structure in the eigenbasis of $\mathcal{L}$, where the entries are inverse eigenvalues of $\mathcal{L}$. Not specifying the spin indices for now, the solution for Eq. (2.134) can be written as

$$C_{\alpha\gamma\beta\delta}(n) = \frac{1}{2\pi\hbar N_F \tau_0^2} \sum_{r=1}^{4} \psi_{r,n}(\alpha,\gamma) \frac{1}{E_{r,n}} \psi_{r,n}^*(\beta,\delta). \tag{2.138}$$

Note that the spin indices are of different order in comparison with the $\mathcal{L}$ operator. In the $\mathcal{L}$ operator, the first two indices refer to the spin indices in the retarded Green's functions (before and after the scattering vertex), and the latter two indices refer to the spin indices in the advanced Green's function. In the Cooperon, Eq. (2.138), the first two indices are related to the

[9] Note that in Refs. [7, 100, 101] in the mixed term proportional to $\Omega_{D1}\Omega_{R1}$ in this step of the calculation there are several terms omitted. However, they are needed to derive the final result, which is again correctly shown in all articles.

spin pair entering the scattering vertex (in the retarded as well as advanced Green's function), and the second pair refers to the leaving spin pair (see Fig. 2.10). To return from the (arbitrary) particle–particle propagator to the actual current response with maximally crossed diagrams, the conserved spin at the current vertex for the Cooperon restricts the components to fulfill $\gamma = \beta$ and $\delta = \alpha$, and thus the latter eigenstate has interchanged spin indices in comparison to the first:

$$C_{\alpha\beta\beta\alpha}(n) = \frac{1}{2\pi\hbar N_\mathrm{F}\tau_0^2}\sum_{r=1}^{4}\psi_{r,n}(\alpha,\beta)\frac{1}{E_{r,n}}\psi^*_{r,n}(\beta,\alpha). \tag{2.139}$$

The eigenfunctions $\psi_{r,n}(\alpha,\beta)$ are defined in spin space. We choose the basis with eigenfunctions $\psi^0_{r,n}(\alpha,\beta)$ that are antisymmetric in the spin indices, which corresponds to a spin singlet with total momentum $J = 0$, and eigenfunctions $\psi^m_{r,n}(\alpha,\beta)$ that are symmetric in spin indices, which corresponds to a triplet state with total quantum number $J = 1$ and $J_\mathrm{z} = -1, 0, 1$. We find, similar to Eq. (2.20),

$$2\pi\hbar N_\mathrm{F}\tau_0^2\sum_{\alpha,\beta,n}C_{\alpha\beta\beta\alpha}(n) = \sum_{n=0}^{n_\mathrm{max}}\left(-\frac{1}{E_0(n)} + \sum_{m=-1}^{1}\frac{1}{E_m(n)}\right). \tag{2.140}$$

Whereas the triplet channel gives three positive contributions to the magneto-conductivity, the singlet channel gives a negative one. When spin relaxation mechanisms are small, the negative contribution cancels one of the positive contributions, and the spinless case is revealed with a factor of two. However, a finite spin–orbit relaxation reduces only the contribution from the triplet channel, because there is no spin relaxation involved in the singlet channel. We identify the two-dimensional diffusion constant via Eq. (A.93) and find for the spin independent singlet part

$$\mathcal{L}^\mathrm{s} = Dq^2 + \frac{1}{\tau_\mathrm{i}}. \tag{2.141}$$

Regarding the triplet channel, the quantities $\sigma/2$ and $\rho/2$ each define a spin-1/2 algebra. We define the total spin operator, which is symmetric in both spin operators,

$$\mathbf{J} = \frac{(\boldsymbol{\sigma} + \boldsymbol{\rho})}{2}, \tag{2.142}$$

$$J_\pm = \frac{J_x \pm iJ_y}{\sqrt{2}}, \tag{2.143}$$

and we use the notation

$$q_\pm = q_\mathrm{x} \pm iq_\mathrm{y}. \tag{2.144}$$

Note that we use the normalized ladder operators $J_\pm$ here. The triplet state can be expressed as a single spin system with total spin-1. This allows us to write for the triplet state $J^2 = J_\mathrm{x}^2 + J_\mathrm{y}^2 + J_\mathrm{z}^2$ with eigenvalue $j(j+1) = 2$ and

$$\begin{aligned}\mathcal{L}^\mathrm{t} = \frac{1}{\tau_\mathrm{i}} + Dq^2 + 2\sqrt{D\tau_1}\left[-\Omega_\mathrm{D1}\left(J_+q_+ + J_-q_-\right) + i\Omega_\mathrm{R1}\left(J_+q_- - J_-q_+\right)\right] \\ - 4i\Omega_\mathrm{D1}\Omega_\mathrm{R1}\tau_1\left(J_+^2 - J_-^2\right) + 2\left(\tau_1\Omega^2_\mathrm{R1+D1} + \tau_3\Omega^2_\mathrm{D3}\right)\left(2 - J_\mathrm{z}^2\right).\end{aligned} \tag{2.145}$$

In a magnetic field, the momentum operator becomes quantized with the following relations:

$$q_+ = \sqrt{\frac{\kappa}{D}} a, \tag{2.146}$$

$$q_- = \sqrt{\frac{\kappa}{D}} a^\dagger, \tag{2.147}$$

$$q^2 = \frac{\kappa}{2D} \left\{a, a^\dagger\right\} = \frac{\kappa}{2D} \left(a a^\dagger + a^\dagger a\right), \tag{2.148}$$

where $\{\cdot, \cdot\}$ denotes the anti-commutator and $\kappa = {}^{4eBD}/_{\hbar}$ has been defined in Eq. (1.66). The operators a and $a^\dagger$ increase and decrease Landau level n and have the non-zero matrix elements

$$\langle n-1| a |n\rangle = \langle n| a^\dagger |n-1\rangle = \sqrt{n} \tag{2.149}$$

$$\langle n| \left\{a, a^\dagger\right\} |n\rangle = n + \frac{1}{2}. \tag{2.150}$$

The magneto-conductivity is then given by

$$\Delta\sigma = \frac{e^2\kappa}{2\pi h} \sum_{n=0}^{n_{\max}} \left(-\frac{1}{E_0(n)} + \sum_{m=0,\pm1} \frac{1}{E_m(n)} \right). \tag{2.151}$$

The eigenvalue of the singlet channel can be identified directly,

$$\frac{L_0(n)}{\kappa} = n + \frac{1}{2} + \frac{B_\mathrm{i}}{B}, \tag{2.152}$$

which corresponds to the contribution in the spinless case, except for the different diffusion constant involved in κ.

The triplet state $\mathcal{L}$ operator in magnetic field is given by

$$\begin{aligned} \mathcal{L}^\mathrm{t} = \frac{1}{\tau_\mathrm{i}} + \kappa \left\{a, a^\dagger\right\} + 2\sqrt{\kappa\tau_1} \left[-\Omega_{\mathrm{D}1} \left(J_+ a + J_- a^\dagger\right) + i\Omega_{\mathrm{R}1} \left(J_+ a^\dagger - J_- a\right) \right] \\ - 4i\Omega_{\mathrm{D}1}\Omega_{\mathrm{R}1}\tau_1 \left(J_+^2 - J_-^2\right) + 2\left(\tau_1 \Omega_{\mathrm{R1+D1}}^2 + \tau_3 \Omega_{\mathrm{D}3}^2\right) \left(2 - J_z^2\right). \end{aligned} \tag{2.153}$$

In comparison with the singlet contribution, the triplet contains not only Landau level expressions, but the spin–orbit coupling introduces a coupling of different Landau levels in combination with a spin flip. It is apparent that only the first harmonic of the spin–orbit coupling induces a Landau level coupling, whereas the third harmonic only results in a splitting of the Landau level in Eq. (2.153) due to the different eigenvalues of J_z.[10] There is no simple (analytical) treatment to find the eigenvalues of Eq. (2.153). In general, this operator has to be diagonalized numerically [100]. However, there exist special cases where a closed form solution can be achieved.

[10] This is the reason why by neglecting the first harmonics, which are typical for two-dimensional systems, the qualitative result of the HLN calculation is recovered.

2.3.2 Dresselhaus Spin–Orbit Coupling

If either $\Omega_{R1} = 0$ or $\Omega_{D1} = 0$, the $\mathcal{L}$ operator can be treated analytically [7]. In this section, we assume a pure Dresselhaus spin–orbit coupling as described by Eq. (2.78) ($\Omega_{R1} = 0$) and skip the index "D". The $\mathcal{L}$ operator for the triplet state becomes

$$\mathcal{L}^{t} = \frac{1}{\tau_i} + \kappa \left\{a, a^\dagger\right\} - 2\Omega_1\sqrt{\kappa\tau_1}\left(J_+ a + J_- a^\dagger\right) + 2\left(\tau_1\Omega_1^2 + \tau_3\Omega_3^2\right)\left(2 - J_z^2\right). \tag{2.154}$$

We define the D'yakonov–Perel' spin–orbit scattering rates in analogy to Eq. (2.102),

$$\frac{1}{\tau_{so}} = 2\left(\Omega_1^2\tau_1 + \Omega_3^2\tau_3\right), \tag{2.155}$$

$$\frac{1}{\tau'_{so}} = 2\Omega_1^2\tau_1, \tag{2.156}$$

and the corresponding effective magnetic fields,

$$\frac{B_{so}}{B} = \frac{1}{\kappa\tau_{so}}, \tag{2.157}$$

$$\frac{B'_{so}}{B} = \frac{1}{\kappa\tau'_{so}}, \tag{2.158}$$

as well as the inelastic field,

$$\frac{B_i}{B} = \frac{1}{\kappa\tau_i}. \tag{2.159}$$

Then the $\mathcal{L}$ operator can be written in the form

$$\frac{\mathcal{L}^{t}}{\kappa} = \left\{a, a^\dagger\right\} + \frac{B_i}{B} - \sqrt{\frac{2B'_{so}}{B}}\left(J_+ a + J_- a^\dagger\right) + \frac{B_{so}}{B}\left(2 - J_z^2\right), \tag{2.160}$$

which becomes a 3×3 block matrix structure in the product space of eigenfunctions of the operator $\left\{a, a^\dagger\right\}$ with the eigenfunctions of J_z with quantum numbers $S_z = \{1, 0, -1\}$. This corresponds to Landau levels with quantum number n, which are split with the spin projection in z-direction. Each Landau-level $\{n, S_z = 0\}$ is intermixed with the Landau-level $\{n-1, S_z = 1\}$ as well as $\{n+1, S_z = -1\}$. The Landau levels with $S_z = \pm 1$, however, are only connected to one other Landau level each. Therefore the matrix block diagonalizes in a 3×3 structure.[11] Note that in the general case, with both, Rashba and Dresselhaus contributions, this block decomposition is not possible because both processes, for example increasing of a Landau level by lowering and enhancing the J_z quantum number, have to be considered. For $n > 0$ we find for the Dresselhaus case:

$$\frac{\mathcal{L}^{(n)}}{\kappa} = \begin{pmatrix} (n-1) + \frac{1}{2} + \frac{B_i + B_{so}}{B} & -\sqrt{\frac{2nB'_{so}}{B}} & 0 \\ -\sqrt{\frac{2nB'_{so}}{B}} & n + \frac{1}{2} + \frac{B_i + 2B_{so}}{B} & -\sqrt{\frac{2(n+1)B'_{so}}{B}} \\ 0 & -\sqrt{\frac{2(n+1)B'_{so}}{B}} & (n+1) + \frac{1}{2} + \frac{B_i + B_{so}}{B} \end{pmatrix}, \tag{2.161}$$

[11] In the case where only the third harmonic of the spin–orbit interaction is considered, the result are simply disconnected Landau levels, which are split due to the magnetic quantum number S_z. This reduces to the HLN case.

where only the single winding B'_{so} term mixes different Landau levels.

To solve the sum of inverse eigenvalues in Eq. (2.151), we use

$$\sum_m \frac{1}{E_m} = \sum_m \frac{|\mathcal{L}_{mm}|}{|\mathcal{L}|}, \tag{2.162}$$

where $|\cdot|$ denotes the determinant and $\mathcal{L}_{mm}$ are the minors of the matrix $\mathcal{L}$, which are derived by removing rows and columns of one diagonal element (see Ref. [112]).[12] The determinant of Eq. (2.161) is given by

$$\left|\frac{\mathcal{L}^{(n)}}{\kappa}\right| = \left(a_n + \frac{B_{\mathrm{so}}}{B}\right) a_{n-1}a_{n+1} - 2\frac{B'_{\mathrm{so}}}{B}\left[(2n+1)a_n - 1\right], \tag{2.163}$$

where we define

$$a_n = n + \frac{1}{2} + \frac{B_{\mathrm{i}} + B_{\mathrm{so}}}{B}, \tag{2.164}$$

and the sum over the minors of diagonal elements is

$$\sum_m \left|\frac{\mathcal{L}^{(n)}_{mm}}{\kappa}\right| = 3a_n^2 + 2a_n\frac{B_{\mathrm{so}}}{B} - 1 - 2(2n+1)\frac{B'_{\mathrm{so}}}{B}. \tag{2.165}$$

In addition we have to consider the triplet term $n = 0$ with the reduced matrices (see Fig. 2.11)

$$\frac{\mathcal{L}^{(1)}}{\kappa} = \begin{pmatrix} \frac{1}{2} + \frac{B_{\mathrm{i}}+2B_{\mathrm{so}}}{B} & -\sqrt{\frac{2B'_{\mathrm{so}}}{B}} \\ -\sqrt{\frac{2B'_{\mathrm{so}}}{B}} & 1 + \frac{1}{2} + \frac{B_{\mathrm{i}}+B_{\mathrm{so}}}{B} \end{pmatrix}, \qquad \frac{\mathcal{L}^{(0)}}{\kappa} = \left(\frac{1}{2} + \frac{B_{\mathrm{i}}+B_{\mathrm{so}}}{B}\right). \tag{2.166}$$

We find for the sum over inverse triplet eigenvalues

$$\sum_{n,m} \frac{\kappa}{E_m(n)} = \frac{1}{a_0} + \frac{2a_0 + 1 + \frac{B_{\mathrm{so}}}{B}}{a_1\left(a_0 + \frac{B_{\mathrm{so}}}{B}\right) - 2\frac{B'_{\mathrm{so}}}{B}} + \sum_{n=1}^{n_{\max}} \left(\frac{3a_n^2 + 2a_n\frac{B_{\mathrm{so}}}{B} - 1 - 2(2n+1)\frac{B'_{\mathrm{so}}}{B}}{\left(a_n + \frac{B_{\mathrm{so}}}{B}\right)a_{n-1}a_{n+1} - 2\frac{B'_{\mathrm{so}}}{B}\left[(2n+1)a_n - 1\right]} \right). \tag{2.167}$$

The discussion above has been concerned with the triplet part. For the singlet part, we find only one eigenvalue and consider the sum

$$\sum_{n=0}^{n_{\max}} \frac{1}{n + \frac{1}{2} + \frac{B_{\mathrm{i}}}{B}} \approx \psi\left(\frac{1}{2} + \frac{B_{\mathrm{o}}}{B}\right) - \psi\left(\frac{1}{2} + \frac{B_{\mathrm{i}}}{B}\right) \tag{2.168}$$

$$\approx \ln\left(\frac{B_{\mathrm{o}}}{B}\right) - \psi\left(\frac{1}{2} + \frac{B_{\mathrm{i}}}{B}\right), \tag{2.169}$$

where we assumed B_{o} to be very large, as discussed in Eq. (1.70).

[12] The sum over inverse eigenvalues of a symmetric $n \times n$ matrix is given by the negative ratio of coefficients of the linear and constant term of the characteristic polynomial. The constant term is given by the determinant. The linear coefficient is given by the sum of determinants of matrices that are created by replacing one diagonal element by (-1) and the entries in the corresponding rows and columns with 0 [112].

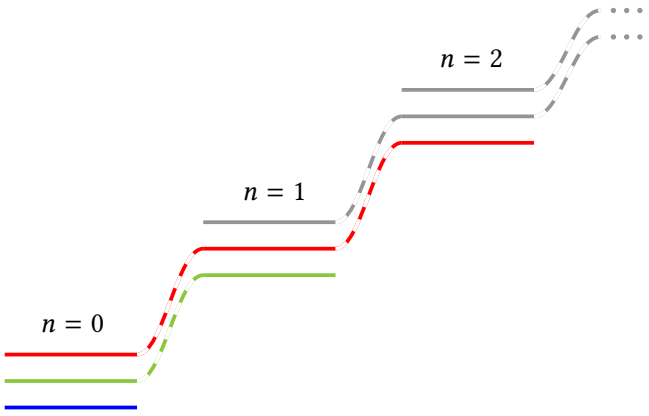

Figure 2.11: *Effective Landau level splitting.* Each effective Landau level is split in three sub-levels with magnetic quantum numbers $\{-1, 0, 1\}$. The linear Dresselhaus contribution couples these different Landau sub-levels for different magnetic quantum numbers. Except for the two lowest sub-levels, three sub-levels are coupled at a time.

Joining the calculated parts, we find the final formula[13] for the Cooperon quantum correction in a magnetic field for the case of a Dresselhaus-like spin–orbit coupling:

$$\begin{aligned}\delta\sigma(B) = -\frac{e^2}{2\pi h}\Bigg[&\frac{1}{a_0} + \frac{2a_0 + 1 + \frac{B_{\mathrm{so}}}{B}}{a_1\left(a_0 + \frac{B_{\mathrm{so}}}{B}\right) - 2\frac{B'_{\mathrm{so}}}{B}} \\ &+ \sum_{n=1}^{n_{\max}} \frac{3a_n^2 + 2a_n\frac{B_{\mathrm{so}}}{B} - 1 - 2(2n+1)\frac{B'_{\mathrm{so}}}{B}}{\left(a_n + \frac{B_{\mathrm{so}}}{B}\right)a_{n-1}a_{n+1} - 2\frac{B'_{\mathrm{so}}}{B}\left[(2n+1)a_n - 1\right]} \\ &+ \psi\left(\frac{1}{2} + \frac{B_{\mathrm{i}}}{B}\right) + 2\ln\left(\frac{B_{\mathrm{tr}}}{B}\right) - \sum_{n=1}^{\infty}\frac{3}{n} + 3\gamma_{\mathrm{EM}}\Bigg],\end{aligned} \tag{2.170}$$

where we used the Euler–Mascheroni constant,

$$\gamma_{\mathrm{EM}} = \lim_{n\to\infty}\left(\sum_{k=1}^{n}\frac{1}{k} - \ln n\right), \tag{2.171}$$

and the transport field is given by

$$B_{\mathrm{tr}} = \frac{\hbar}{4eD\tau_1}, \tag{2.172}$$

which is assumed to be large. Note that the cutoff in the sum is magnetic field dependent and determined by the transport field $n_{\max} = {}^{B_{\mathrm{tr}}}/_{B}$. We show the magneto-transport for different ratios of ${}^{B'_{\mathrm{so}}}/_{B_{\mathrm{so}}}$ in Fig. 2.12. A comparison of the ILP-theory and the HLN-theory is plotted in Fig. 2.13. Even if the response for solely single or triple spin winding shows a qualitatively similar behavior, the single winding contribution yields a much more pronounced magnetic field dependence.

[13] Note that the sum starts with 1, not 0. This is correctly shown in the original paper Ref. [7], but not in the review, Ref. [101].

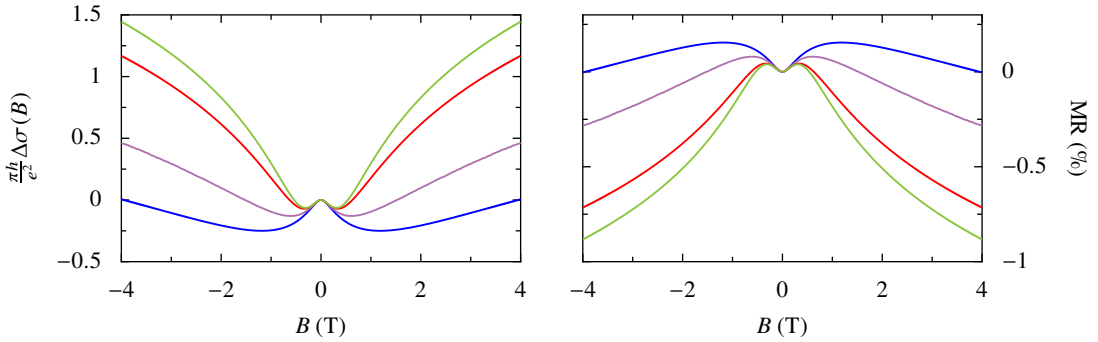

Figure 2.12: *Magneto-transport for linear and cubic Dresselhaus spin–orbit coupling.* In these plots, the effective fields are chosen to be $B_\mathrm{i} = 0.08\,\mathrm{T}$, $B_\mathrm{so} = 0.3\,\mathrm{T}$, $B_\mathrm{tr} \sim \infty$. The zero magnetic field resistivity for the magneto-resistivity (MR) plot is chosen to be 500 Ω. The case $B'_\mathrm{so}/B_\mathrm{so} = 0$ corresponds to the purely cubic spin–orbit coupling of a quasi three dimensional Dresselhaus case (blue curve); $B'_\mathrm{so}/B_\mathrm{so} = 1$ corresponds to the purely linear spin–orbit splitting (green curve). In between, the cases of $B'_\mathrm{so}/B_\mathrm{so} = 0.5$ (violet curve) and $B'_\mathrm{so}/B_\mathrm{so} = 0.9$ (red curve) are shown.

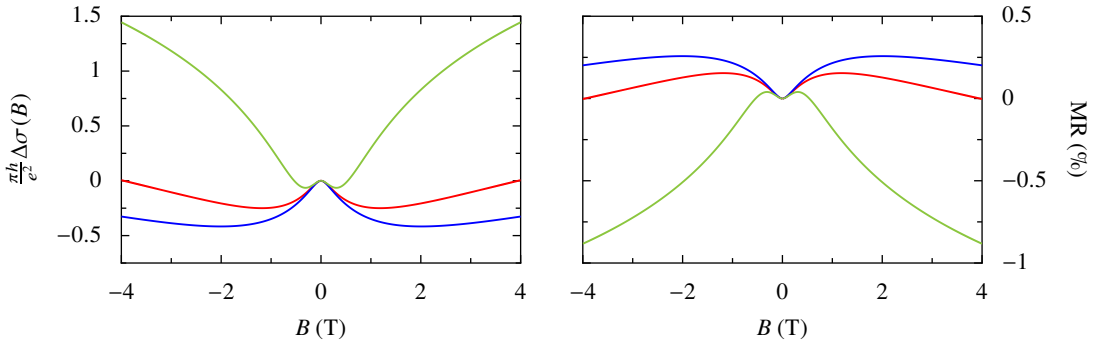

Figure 2.13: *Magneto-transport in ILP-theory for the two limiting cases:* $B'_\mathrm{so}/B_\mathrm{so} = 0$ *(red line) and* $B'_\mathrm{so}/B_\mathrm{so} = 1$ *(green line).* In these plots, the effective fields are chosen to be $B_\mathrm{i} = 0.08\,\mathrm{T}$, $B_\mathrm{so} = 0.3\,\mathrm{T}$, $B_\mathrm{tr} \sim \infty$. The zero magnetic field resistivity for the magneto-resistivity (MR) plot is chosen to be 500 Ω. The case $B'_\mathrm{so}/B_\mathrm{so} = 0$ corresponds to the solely triple spin winding. $B'_\mathrm{so}/B_\mathrm{so} = 1$ corresponds to the solely single spin winding, which is a more realistic scenario in quasi two-dimensional systems. Although the signals are similar for small external magnetic fields, the curve for the single spin winding shows a much stronger dependence on the magnetic field. Whereas the HLN-theory in D'yakonov–Perel' approximation gives identical results to the red curve, the result for the isotropic scattering HLN-theory is different for the same parameters (blue curve).

In a narrow quantum well, $\langle k_z^2 \rangle$ can become quite large, which means $\Omega_1 \gg \Omega_3$ for realistic Dresselhaus interaction. By considering small angle scattering, we find

$$1 - \cos n\phi \approx \frac{n^2\phi^2}{2} \tag{2.173}$$

and $\tau_1 = 9\tau_3$. However, when the scattering does not depend on the angle, $\tau_1 \approx \tau_3$. Therefore the ratio τ_1/τ_3 is restricted,

$$1 < \frac{\tau_1}{\tau_3} < 9. \tag{2.174}$$

In realistic cases $B'_{\mathrm{so}} \sim B_{\mathrm{so}}$, which signifies that the cubic contribution $\Omega_3^2\tau_3 \sim 0$ does not play a major role [7]. The ILP-theory has been successfully used to explain magneto-transport data and provided considerably better fits to experimental curves than HLN-theory [101, 111].

Even if the expression Eq. (2.170) uses the exact (inverse) eigenvalues of the $\mathcal{L}$ operator, it still contains a sum over all effective Landau levels, which has to be treated numerically. It is the term containing the single winding contribution, B'_{so}, that causes the difference in comparison to the HLN formula: by neglecting this term, ILP showed that the HLN result is recovered, but with slightly different characteristic fields.[14] In the following, we derive this kind of HLN result by keeping only the $1/\tau_{\mathrm{so}}$ relaxation. First, we find

$$\begin{aligned}\delta\sigma(B) = -\frac{e^2}{2\pi h}\Bigg[&\frac{1}{a_0} + \frac{2a_0 + 1 + \frac{B_{\mathrm{so}}}{B}}{a_1\left(a_0 + \frac{B_{\mathrm{so}}}{B}\right)} + \sum_{n=1}^{n_{\max}} \frac{3a_n^2 + 2a_n\frac{B_{\mathrm{so}}}{B} - 1}{\left(a_n + \frac{B_{\mathrm{so}}}{B}\right)a_{n-1}a_{n+1}} \\ &+\psi\left(\frac{1}{2} + \frac{B_{\mathrm{i}}}{B}\right) + 2\ln\left(\frac{B_{\mathrm{tr}}}{B}\right) - \sum_{n=1}^{\infty}\frac{3}{n} + 3\gamma_{\mathrm{EM}}\Bigg].\end{aligned} \tag{2.175}$$

As $a_{n\pm1} = a_n \pm 1$ we can separate the triplet sum into several parts $\propto 1/n+x$,

$$\sum_{n=1} \frac{3a_n^2 + 2a_n\frac{B_{\mathrm{so}}}{B} - 1}{\left(a_n + \frac{B_{\mathrm{so}}}{B}\right)a_{n-1}a_{n+1}} = \sum_{n=1}\left(\frac{1}{a_{n-1}} + \frac{1}{a_{n+1}} + \frac{1}{\left(a_n + \frac{B_{\mathrm{so}}}{B}\right)}\right) \tag{2.176}$$

$$= \frac{1}{a_0} - \frac{1}{a_1} + \sum_{n=1}\left(\frac{2}{a_n} + \frac{1}{\left(a_n + \frac{B_{\mathrm{so}}}{B}\right)}\right) \tag{2.177}$$

$$= -\frac{1}{a_0} - \frac{1}{a_1} - \frac{1}{\left(a_0 + \frac{B_{\mathrm{so}}}{B}\right)} + \sum_{n=0}\left(\frac{2}{a_n} + \frac{1}{\left(a_n + \frac{B_{\mathrm{so}}}{B}\right)}\right) \tag{2.178}$$

$$= -\frac{1}{a_0} - \frac{2a_0 + 1 + \frac{B_{\mathrm{so}}}{B}}{a_1\left(a_0 + \frac{B_{\mathrm{so}}}{B}\right)} + \sum_{n=0}\left(\frac{2}{a_n} + \frac{1}{\left(a_n + \frac{B_{\mathrm{so}}}{B}\right)}\right). \tag{2.179}$$

[14] This formula was actually first derived by Altshuler et al. (AALKh) [22] in 1981, one year after the HLN publication. As discussed previously, the authors used a spin splitting in the Hamiltonian to introduce a D'yakonov–Perel' spin–orbit relaxation, but treated the calculation in close analogy to the Elliott–Yafet relaxation used in the HLN appraoch. Apparently, this approach neglects the single spin winding contribution.

The last step enables to use the ψ-function Eq. (1.70), and the final result for the magneto-conductivity is

$$\Delta\sigma(B) = \frac{e^2}{\pi h}\left[\Psi\left(\frac{B_{\mathrm{so}}+B_{\mathrm{i}}}{B}\right)+\frac{1}{2}\Psi\left(\frac{2B_{\mathrm{so}}+B_{\mathrm{i}}}{B}\right)-\frac{1}{2}\Psi\left(\frac{B_{\mathrm{i}}}{B}\right)\right], \tag{2.180}$$

which is identical with Eq. (2.64). This result can also be found by taking the linear terms to zero directly in Eq. (2.161). Note that this equals Eq. (2.46), however, in the present case the result is derived by starting from a Hamiltonian describing a spin–orbit splitting and not by an artificial extension of the HLN equation. As long as the triple spin winding dominates the Fermi surface, the magneto-conductivity is only dependent on the spin relaxation times that are used for the D'yakonov–Perel' mechanism in HLN-theory [7, 22, 100]. If, on the other hand, only the linear Rashba (or linear Dresselhaus) term is kept in the Hamiltonian, another limit of the ILP result can be obtained that can be expressed analytically. This is the topic of the next section.

2.3.3 Rashba Spin–Orbit Coupling

When only the single spin winding contribution in the Bloch vector is considered, again the magneto-conductivity within ILP-theory can be expressed in a closed formula [113]. This corresponds to the linear Rashba Hamiltonian, Eq. (2.87) (or a Dresselhaus Hamiltonian, Eq. (2.78) where the triple winding contribution is negligible) and provides a useful fitting tool for experimental data in systems with strong Rashba effect [113].

In this case, the $\mathcal{L}$ operator takes the form

$$\frac{\mathcal{L}^{\mathrm{t}}}{\kappa} = \left\{a, a^{\dagger}\right\} + \frac{B_{\mathrm{i}}}{B} + i\sqrt{\frac{2B_{\mathrm{so}}}{B}}\left(J_{+}a^{\dagger} - J_{-}a\right) + \frac{B_{\mathrm{so}}}{B}\left(2 - J_{\mathrm{z}}^2\right), \tag{2.181}$$

which becomes again a 3×3 block matrix structure in the product space of Landau levels n, which are eigenfunctions of the operator $\left\{a, a^{\dagger}\right\}$, with the eigenfunctions of J_{z} with quantum numbers $S_{\mathrm{z}} = \{-1\,, 0\,, 1\}$ for $n > 0$:

$$\frac{\mathcal{L}^{(n)}}{\kappa} = \begin{pmatrix} (n-1)+\frac{1}{2}+\frac{B_{\mathrm{i}}+B_{\mathrm{so}}}{B} & i\sqrt{\frac{2nB_{\mathrm{so}}}{B}} & 0 \\ -i\sqrt{\frac{2nB_{\mathrm{so}}}{B}} & n+\frac{1}{2}+\frac{B_{\mathrm{i}}+2B_{\mathrm{so}}}{B} & i\sqrt{\frac{2(n+1)B_{\mathrm{so}}}{B}} \\ 0 & -i\sqrt{\frac{2(n+1)B_{\mathrm{so}}}{B}} & (n+1)+\frac{1}{2}+\frac{B_{\mathrm{i}}+B_{\mathrm{so}}}{B} \end{pmatrix}. \tag{2.182}$$

In this Rashba case, we find that the lowering of a Landau level is combined with a decrease of the spin projection quantum number, and the increase of a Landau level with the increase of the spin projection quantum number. Each Landau-level $\{n,\, S_{\mathrm{z}} = 0\}$ is intermixed with the Landau-level $\{n-1,\, S_{\mathrm{z}} = -1\}$ as well as $\{n+1,\, S_{\mathrm{z}} = 1\}$.[15] As this matrix still has the same

[15] This is just the reversed case as in the Dresselhaus case, Eq. (2.161), where an increase of a Landau level is combined with a decrease of spin projection quantum number.

structure as in the Dresselhaus case, the solution for the sum over inverse eigenvalues is quite similar:

$$\sum_{\text{triplet}} \frac{1}{E_m} = \frac{1}{a_0} + \frac{2a_0 + 1 + \frac{B_{\text{so}}}{B}}{a_1\left(a_0 + \frac{B_{\text{so}}}{B}\right) - 2\frac{B_{\text{so}}}{B}} \tag{2.183}$$

$$+ \sum_{n=1}^{n_{\max}} \left(\frac{3a_n^2 + 2a_n\frac{B_{\text{so}}}{B} - 1 - 2(2n+1)\frac{B_{\text{so}}}{B}}{\left(a_n + \frac{B_{\text{so}}}{B}\right) a_{n-1}a_{n+1} - 2\frac{B_{\text{so}}}{B}\left[(2n+1)a_n - 1\right]} \right), \tag{2.184}$$

where

$$\frac{B_{\text{so}}}{B} = \frac{1}{\kappa\tau_{\text{so}}} = \frac{2}{\kappa}\Omega_1^2\tau_1. \tag{2.185}$$

As in the previous section, the sum over Landau levels can be achieved by using the ψ-function if it can be expressed in terms of $1/n+x$. According to Ref. [113], the sum over inverse triplet eigenvalues (including the zero term) can be written in the form

$$\sum_{\text{triplet}} = \sum_{n=0} \left(\sum_{s=0,\pm1} \frac{u_s}{n + \frac{1}{2} + \frac{B_{\text{i}}}{B} - v_s} \right) + \frac{4B^2}{B^2 - 4\left(B_{\text{i}} + B_{\text{so}}\right)^2}, \tag{2.186}$$

where

$$u_s = \frac{3v_s^2 + 4v_s\left(B_{\text{so}}/B\right) + 5\left(B_{\text{so}}/B\right)^2 + 4\left(B_{\text{i}}/B\right)\left(B_{\text{so}}/B\right) - 1}{\prod\limits_{s' \neq s}\left(v_s - v_{s'}\right)}, \tag{2.187}$$

$$v_s = 2\varphi\cos\left[\theta - \frac{2\pi}{3}(1-s)\right], \tag{2.188}$$

$$\varphi = \sqrt{\frac{1 - 4\left(B_{\text{i}}/B\right)\left(B_{\text{so}}/B\right) - \left(B_{\text{so}}/B\right)^2}{3}}, \tag{2.189}$$

$$\theta = \frac{1}{3}\cos^{-1}\left[-\left(\frac{B_{\text{so}}/B}{\varphi}\right)^3 \left(1 + \frac{2B_{\text{i}}}{B_{\text{so}}}\right) \right] \tag{2.190}$$

Following the steps of the previous section, the magneto-conductivity can be expressed as

$$\Delta\sigma = \frac{e^2}{2\pi h}\left[\sum_{s=0,\pm1} u_s\psi\left(\frac{1}{2} + \frac{B_{\text{i}}}{B} - v_s\right) - \psi\left(\frac{1}{2} + \frac{B_{\text{i}}}{B}\right) - 2\ln\left(\frac{B_{\text{i}}}{B}\right) + \frac{4B^2}{4\left(B_{\text{so}} + B_{\text{i}}\right)^2 - B^2} + C \right]. \tag{2.191}$$

The constant C provides the vanishing of the magneto-conductivity in zero field:

$$C = -2\ln\left(1 + \frac{B_{\text{so}}}{B_{\text{i}}}\right) - \ln\left(1 + \frac{2B_{\text{so}}}{B_{\text{i}}}\right) + \frac{8}{\sqrt{7 + 16\left(B_{\text{i}}/B_{\text{so}}\right)}}\cos^{-1}\left(\frac{\left(2B_{\text{i}}/B_{\text{so}}\right) - 1}{\sqrt{\left[\left(2B_{\text{i}}/B_{\text{so}}\right) + 3\right]^2 - 1}}\right). \tag{2.192}$$

For $B \ll B_{\mathrm{so}}$ the HLN result is derived with the effective fields of the D'yakonov–Perel' approximation [113], see Fig. 2.13. In the high-field limit $B \gg B_{\mathrm{so}}$, the behavior differs considerably from the HLN result. We find

$$u_s \approx 1, \tag{2.193}$$

$$v_s \approx s\left(1 - \frac{2B_{\mathrm{i}}B_{\mathrm{so}}}{B^2}\right), \tag{2.194}$$

$$\varphi \approx \frac{1}{\sqrt{3}}\left(1 - \frac{2B_{\mathrm{i}}B_{\mathrm{so}}}{B^2}\right), \tag{2.195}$$

$$\theta \approx \frac{\pi}{6}, \tag{2.196}$$

and for large magnetic fields Eq. (2.191) reduces (up to a constant) to [113]

$$\Delta\sigma \approx \frac{e^2}{2\pi h}\left[\sum_{s=\pm 1}\psi\left(\frac{1}{2} + \frac{B_{\mathrm{i}}}{B - 2sB_{\mathrm{so}}}\right) - 2\ln\left(\frac{B_{\mathrm{i}}}{B}\right)\right], \tag{2.197}$$

and the spin–orbit coupling acts like a shift in $B - 2sB_{\mathrm{so}}$, restoring the positive magneto-conductivity. Note that the sum is only over $s = \pm 1$, as the $s = 0$ term cancels with the singlet contribution. The crossover appears for $B \approx B_{\mathrm{so}}$, where a pronounced WAL dip develops.

An interesting case appears when both, linear Dresselhaus and linear Rashba spin–orbit splitting are of similar strength [100]. Whereas both terms produce additive contributions for the spin relaxation time, they are not additive in the magneto-conductivity. Even more, if the first harmonics in Eq. (2.104) have the same strength Ω_1,

$$\boldsymbol{\Omega}(\mathbf{k}) = \Omega_1(\mathbf{k})\begin{pmatrix}\sin\phi - \cos\phi\\ \sin\phi - \cos\phi\end{pmatrix}, \tag{2.198}$$

there is no WAL signature in the magneto-conductivity, because the spin winding number is zero in this case.

2.3.4 Anisotropic Rashba Splitting

In this section, we go beyond the derivations found in the literature. We discussed in Sec. 2.2.2 an anisotropic Rashba Hamiltonian, which is described by the Bloch vector Eq. (2.98),

$$\boldsymbol{\Omega}_{\mathrm{R}}(\mathbf{k}) = \Omega_{\mathrm{R}}\left[\begin{pmatrix}\sin\phi\\ \cos\phi\end{pmatrix} + \begin{pmatrix}-\sin(3\phi)\\ \cos(3\phi)\end{pmatrix}\right]. \tag{2.199}$$

This Bloch vector is useful for the description of one of the involved band pairs in the six-band model of $LaAlO_3/SrTiO_3$ heterostructures, which we will discuss in Sec. 3.1.3.Following the calculation in Sec. 2.3.1, we find again a two spin formulation with the singlet part

$$\mathcal{L}^{\mathrm{s}} = Dq^2 + \frac{1}{\tau_{\mathrm{i}}}, \tag{2.200}$$

and a triplet part

$$\mathcal{L}^{\mathrm{t}} = \frac{1}{\tau_{\mathrm{i}}} + Dq^2 + +2\left(2 - J_z^2\right)(\tau_1 + \tau_3)\,\Omega_{\mathrm{R}}^2 + 2i\Omega_{\mathrm{R}}\sqrt{D\tau_1}\left(J_+q_+ - J_-q_-\right). \tag{2.201}$$

In the following, we adjust the definition of the effective spin–orbit scattering rate to the anisotropic Rashba Hamiltonian,

$$\frac{1}{\tau_{\mathrm{so}}} = 2\left(\tau_1 + \tau_3\right)\Omega_{\mathrm{R}}^2, \tag{2.202}$$

$$\frac{1}{\tau'_{\mathrm{so}}} = 2\tau_1\Omega_{\mathrm{R}}^2. \tag{2.203}$$

By using the quantized momentum operator in a magnetic field, Eqs. (2.146)–(2.148), this yields

$$\frac{\mathcal{L}^{\mathrm{s}}}{\kappa} = \left\{a, a^{\dagger}\right\} + \frac{B_{\mathrm{i}}}{B}, \tag{2.204}$$

$$\frac{\mathcal{L}^{\mathrm{t}}}{\kappa} = \left\{a, a^{\dagger}\right\} + \frac{B_{\mathrm{i}}}{B} + \left(2 - J_{\mathrm{z}}^2\right)\frac{B_{\mathrm{so}}}{B} + i\left(J_{+}a - J_{-}a^{\dagger}\right)\sqrt{\frac{2B'_{\mathrm{so}}}{B}}. \tag{2.205}$$

The eigenvalue of the singlet channel can be found directly, see Eq. (2.152). To find the eigenvalues of the triplet channel, we have to diagonalize the block-diagonal matrix similar to Eq. (2.161). For $n > 0$ this matrix for Landau level n and in the J_{z} basis $\{1, 0, -1\}$ is given by

$$\frac{\mathcal{L}^{(n)}}{\kappa} = \begin{pmatrix} (n-1) + \frac{1}{2} + \frac{B_{\mathrm{i}}+B_{\mathrm{so}}}{B} & i\sqrt{\frac{2nB'_{\mathrm{so}}}{B}} & 0 \\ -i\sqrt{\frac{2nB'_{\mathrm{so}}}{B}} & n + \frac{1}{2} + \frac{B_{\mathrm{i}}+2B_{\mathrm{so}}}{B} & i\sqrt{\frac{2(n+1)B'_{\mathrm{so}}}{B}} \\ 0 & -i\sqrt{\frac{2(n+1)B'_{\mathrm{so}}}{B}} & (n+1) + \frac{1}{2} + \frac{B_{\mathrm{i}}+B_{\mathrm{so}}}{B} \end{pmatrix}. \tag{2.206}$$

The basis of this matrix is the same as in the Dresselhaus case, but the structure of the entries is similar to the Rashba case. Its determinant is formally identical to the Dresselhaus case Eq. (2.163), as are its minors and the end result, apart from the different effective spin–orbit fields. The first and third harmonic are of same size in the anisotropic Rashba Hamiltonian, therefore the full summation over Landau levels has to be achieved to find the solution. The magneto-conductivity is given by

$$\Delta\sigma(B) = -\frac{e^2}{2\pi h}\left[\mathcal{S}(B) - \mathcal{S}(0) + \psi\left(\frac{1}{2} + \frac{B_{\mathrm{i}}}{B}\right) - \ln\left(\frac{B_{\mathrm{i}}}{B}\right)\right], \tag{2.207}$$

where

$$\mathcal{S}(B) = \frac{1}{a_0} + \frac{2a_0 + 1 + \frac{B_{\mathrm{so}}}{B}}{a_1\left(a_0 + \frac{B_{\mathrm{so}}}{B}\right) - 2\frac{B'_{\mathrm{so}}}{B}} + \sum_{n=1}^{\frac{B_{\mathrm{tr}}}{B}} \frac{3a_n^2 + 2a_n\frac{B_{\mathrm{so}}}{B} - 1 - 2(2n+1)\frac{B'_{\mathrm{so}}}{B}}{\left(a_n + \frac{B_{\mathrm{so}}}{B}\right)a_{n-1}a_{n+1} - 2\frac{B'_{\mathrm{so}}}{B}\left[(2n+1)a_n - 1\right]} \tag{2.208}$$

and a_n is given by Eq. (2.164),

$$a_n = n + \frac{1}{2} + \frac{B_{\mathrm{i}} + B_{\mathrm{so}}}{B}. \tag{2.209}$$

Note that the transport field enters again in the upper limit of the summation.

As τ_3 is restricted by the condition $\tau_1/9 < \tau_3 < \tau_1$ according to Eq. (2.174), the ratio of first and third effective spin–orbit field is limited by

$$0.5 < \frac{B'_{\mathrm{so}}}{B_{\mathrm{so}}} < 0.9. \tag{2.210}$$

Although of roughly the same order, the field B_{so} plays a slightly major role in the magneto-transport. The results for the anisotropic Rashba interaction therefore is in between the HLN result (where $B'_{so} \ll B_{so}$) and the ILP result for regular spin–orbit splitting (where $B'_{so} \sim B_{so}$) and its signature in magneto-transport is comparable to the red curves in Fig. 2.12.

2.4 Multiband Cooperon

2.4.1 Cooperon Equation for Multiband Models

The HLN-theory is not sensitive to complicated anisotropic Fermi surfaces or multiband effects, and only an effective diffusion constant as well as effective scattering rates have to be considered, leaving the general structure of the formula Eq. (2.31) unchanged [114, 115]. However, this is not true for the ILP-theory, where the specific band structure has a major influence on the magneto-transport, as we discussed in the previous section. Having a more complicated multiband model for oxide materials in mind (see Chap. 3), we like to approach a Cooperon evaluation where not only one, but two band pairs are involved. This step goes beyond the calculations in the literature and can be achieved in several ways:

- Two independent bands, where each band is individually spin–orbit split into sub-bands. In this case, the Dyson equation has to be solved for each of the band pairs following the ILP calculation. We show the results for this case in this section.
- Four bands with non-diagonal entries between arbitrary bands. The spin–orbit coupling allows mixing of all quantum numbers. Although a general solution is challenging to obtain, we examine a special case that can be solved in close analogy to the ILP calculation in Sec. 2.4.2.
- Beyond that, a combination of HLN and ILP approach is conceivable. For example, two uncoupled spin–orbit split band pairs can be mixed by local (spin–orbit) scattering events. ILP-theory describes the dispersive spin mixing within each band-pair, whereas the HLN-theory takes care of the local mixing between bands. This case is not covered within the framework of this thesis.

In the following, we focus on the implementation of dispersive spin mixing in a multiband Hamiltonian. Generally, to calculate the Cooperon in this case, we start with Eq. (2.106) and Eq. (2.107),

$$\delta\sigma(\omega \to 0) = -2e^2 N_F D\tau^2 \sum_{\alpha\beta} \int_{\mathbf{q}} C_{\alpha\beta\beta\alpha}(\mathbf{q}), \tag{2.211}$$

where the Cooperon is found by solving the Dyson equation,

$$\begin{aligned} C_{\alpha\gamma\beta\delta}(\mathbf{k},\mathbf{k}',\mathbf{q}) = {} & \frac{n_{imp}\left|V_{\mathbf{k},\mathbf{k}'}\right|^2}{\hbar^2}\delta_{\alpha\beta}\delta_{\gamma\delta} \\ & + \frac{n_{imp}}{\hbar^2}\int \frac{\mathrm{d}^2 g}{(2\pi)^2} \sum_{\nu,\mu} V_{\mathbf{k},\mathbf{g}} V_{-\mathbf{k},-\mathbf{g}} G^{ret}_{\alpha\nu}(\omega, \mathbf{g}+\mathbf{q}) G^{adv}_{\gamma\mu}(\omega, -\mathbf{g}) C_{\nu\mu\beta\delta}(\mathbf{g},\mathbf{k}',\mathbf{q}). \end{aligned} \tag{2.212}$$

In Eq. (2.212), the greek indices can take four different values, referring to spin and band index degree of freedom.

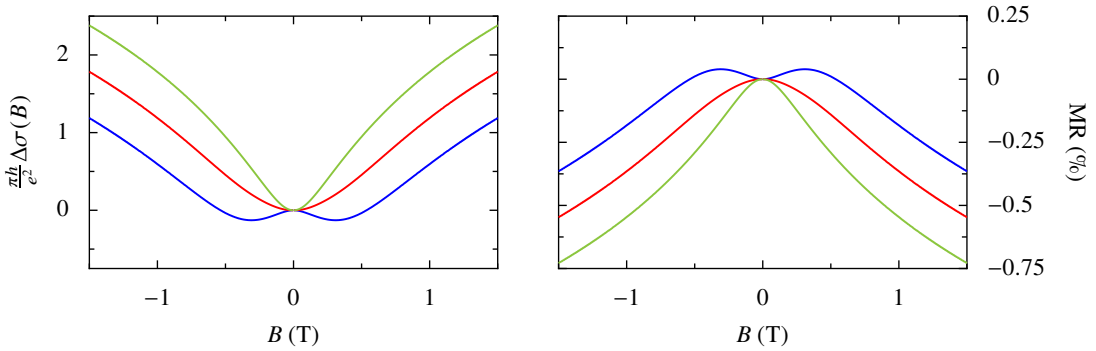

Figure 2.14: *ILP for two uncoupled bands: Single winding spin–orbit coupling.* In these plots, the effective fields are chosen to be $B_\mathrm{i} = 0.08\,\mathrm{T}$ and $B_\mathrm{o} \sim \infty$. The zero magnetic field resistivity for the magneto-resistivity plot is chosen to be $250\,\Omega$. Shown are magneto-transport results for two uncoupled bands with single spin winding spin–orbit coupling, $B'_\mathrm{so} = B_\mathrm{so} = 0.3\,\mathrm{T}$ (blue curve). If B_so of only one of the bands is reduced (to $B_\mathrm{so} = B'_\mathrm{so} = 0.03 < B_\mathrm{i}$), the signature of WAL is lost (red curve). If B_so is reduced for both band pairs, only the WL is left in the transport signature (green curve).

For the special case of two independent bands, the Green's functions involve the Hamiltonian

$$\mathcal{H} = \frac{\hbar^2\mathbf{k}^2}{2m} + \begin{pmatrix} \hbar\boldsymbol{\sigma}\cdot\boldsymbol{\Omega}^{(1)}(\mathbf{k}) & 0 \\ 0 & \hbar\boldsymbol{\sigma}\cdot\boldsymbol{\Omega}^{(2)}(\mathbf{k}) \end{pmatrix}, \tag{2.213}$$

where the (zero) off-diagonal entry is an entity of 2×2 spin space. The calculation of the Cooperon separates into two parts, where the Cooperon equation can be solved in each subspace individually. For both bands, the classification into singlet and triplet contributions is still valid. However, the spherical harmonics of the Cooperon might be different for each of the subspaces and require individual relaxation times for each band index. Each of the bands contributes additively to the conductivity, and the result is a mixture of two distinct (but eventually equal) contributions to the magneto-conductivity:[16]

$$\Delta\sigma(B) = \Delta\sigma^{(1)}\left(B, B_\mathrm{i}, \tau_n^{(1)}, \Omega_n^{(1)}\right) + \Delta\sigma^{(2)}\left(B, B_\mathrm{i}, \tau_n^{(2)}, \Omega_n^{(2)}\right), \tag{2.214}$$

where $n = \{1, 3\}$. For the case when the relaxation times and spin orbit fields are similar for the individual band pairs, the magneto-conductivity gains a simple factor of two in comparison with the single band result.

In the following, we compare different combinations of Rashba and Dresselhaus spin–orbit couplings for the individual band pairs, see Figs. 2.14–2.16. In general, if the effective spin–orbit field becomes smaller than the effective inelastic field, $B_\mathrm{so}, B'_\mathrm{so} < B_\mathrm{i}$, the signature of WAL is suppressed and only WL is recognizable in the transport data. For different combinations of single and triple winding spin–orbit coupling for the individual band pairs, generally the band with smaller spin–orbit coupling field dominates the magneto-transport curve. Note that

[16] Note that this additivity is different to the case when both, Rashba and Dresselhaus spin–orbit coupling take place within the same sub-band splitting: in that case the linear effects might even cancel each other exactly.

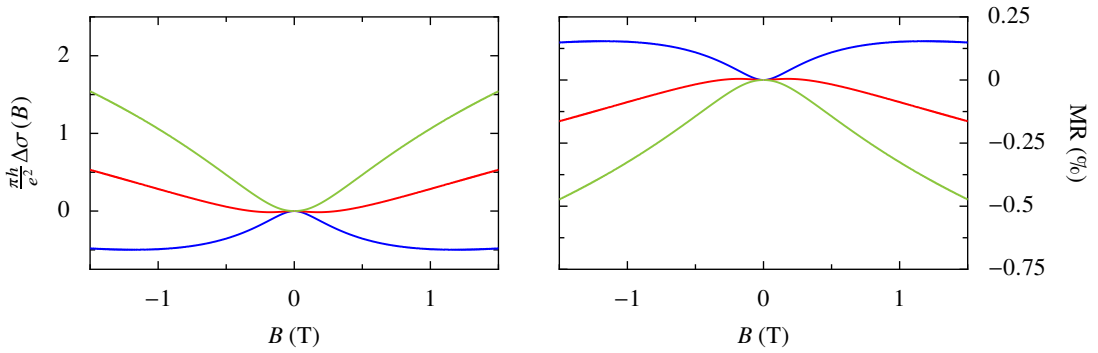

Figure 2.15: *ILP for two uncoupled bands: Triple winding spin–orbit coupling.* In these plots, the effective fields are chosen to be $B_\mathrm{i} = 0.08\,\mathrm{T}$ and $B_\mathrm{o} \sim \infty$. The zero magnetic field resistivity for the magneto-resistivity plot is chosen to be $250\,\Omega$. Shown are magneto-transport results for two uncoupled bands with triple spin winding spin–orbit coupling, $B'_\mathrm{so} = 0$, $B_\mathrm{so} = 0.3\,\mathrm{T}$ (blue curve). If B_so of only one of the bands is reduced (to $B_\mathrm{so} = 0.03 < B_\mathrm{i}$), the signature of WAL is lost (red curve). If B_so is reduced both band pairs, only the WL is left in the transport signature (green curve).

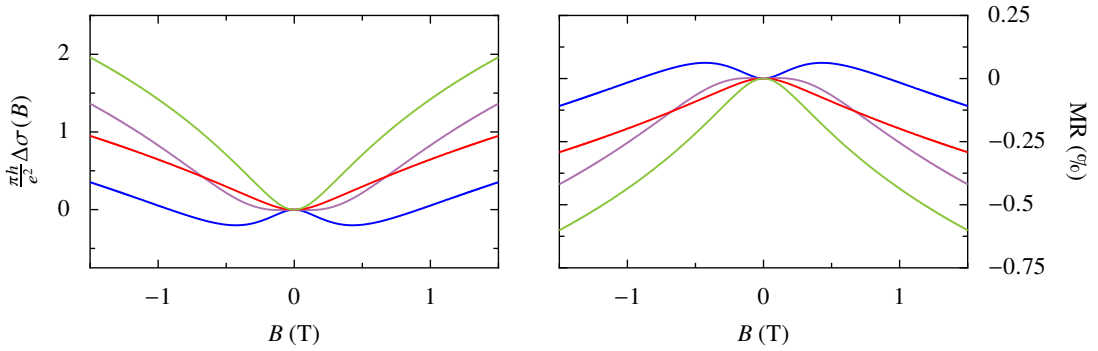

Figure 2.16: *ILP for two uncoupled bands: Single and triple winding spin–orbit coupling.* In these plots, the effective fields are chosen to be $B_\mathrm{i} = 0.08\,\mathrm{T}$ and $B_\mathrm{o} \sim \infty$. The zero magnetic field resistivity for the magneto-resistivity plot is chosen to be $250\,\Omega$. Shown are magneto-transport results for two uncoupled bands, one with single winding spin–orbit coupling, $B'_\mathrm{so} = B_\mathrm{so} = 0.3\,\mathrm{T}$, and the other with triple winding spin–orbit splitting $B'_\mathrm{so} = 0$, $B_\mathrm{so} = 0.3\,\mathrm{T}$ (blue curve). Curves are shown for a reduced linear term (to $B_\mathrm{so} = B'_\mathrm{so} = 0.03 < B_\mathrm{i}$, red curve) as well as a reduced cubic term ($B'_\mathrm{so} = 0.03 < B_\mathrm{i}$, violet curve). In both cases, the WAL signature becomes very weak. The WL signature is given when both terms are reduced (green curve).

the contributions of the two bands can even compensate each other for small fields, when WL and WAL of the same amplitude come together. In higher fields, however, the negative magneto-resistivity will dominate in any case. In this sense, the effect of WL has a stronger impact than the effect of WAL.

2.4.2 The Spin-3/2 Model

A special case of four level system is the equivalent to the spin-3/2 Hamiltonian:

$$\mathcal{H} = \frac{\hbar^2 \mathbf{k}^2}{2m} + \hbar \mathbf{S} \cdot \mathbf{\Omega}, \tag{2.215}$$

where the vectors $\mathbf{S}$ and $\mathbf{\Omega}$ act in the xy-plane. The general components of $\mathbf{S}$ are given by

$$S_\mathrm{x} = \begin{pmatrix} 0 & \sqrt{3} & 0 & 0 \\ \sqrt{3} & 0 & 2 & 0 \\ 0 & 2 & 0 & \sqrt{3} \\ 0 & 0 & \sqrt{3} & 0 \end{pmatrix}, \qquad S_\mathrm{y} = \frac{1}{i} \begin{pmatrix} 0 & \sqrt{3} & 0 & 0 \\ -\sqrt{3} & 0 & 2 & 0 \\ 0 & -2 & 0 & \sqrt{3} \\ 0 & 0 & -\sqrt{3} & 0 \end{pmatrix}, \qquad S_\mathrm{z} = \begin{pmatrix} 3 & 0 & 0 & 0 \\ 0 & 1 & 0 & 0 \\ 0 & 0 & -1 & 0 \\ 0 & 0 & 0 & -3 \end{pmatrix}, \tag{2.216}$$

and $\mathbf{S}$ defines an algebra for angular momentum 3/2. In the picture of two band pairs of basis $\{1\uparrow, 1\downarrow, 2\uparrow, 2\downarrow\}$, Hamiltonian Eq. (2.215) allows spin mixing only between the spin down level of band (1) with the spin up state of band (2), but not the mixing of the spin up state of (2) with the spin down state of (1).

- *Advantages of the model*: The spin-3/2 case allows to define ladder operators. The Cooperon equation can be classified by symmetric and anti-symmetric contributions of the two-spin problem for a spin-3/2 system. Beyond that, this Hamiltonian clearly conserves time reversal and rotational symmetry by construction. In this sense, the spin-3/2 scenario provides a generic model for a multiband WAL calculation.
- *Deficiencies of the model*: This clearly can only be a toy model for the description of electron spins. However, it can be considered as a system with spin-1/2 quantum number and a band index that acts as a pseudo-spin.

For the inhomogenous Cooperon equation, we find in analogy to the ILP calculation,

$$\begin{aligned} C_{\mathbf{k},\mathbf{k}'}(\mathbf{q}) = {} & \frac{n_\mathrm{imp} \left| V_{\mathbf{k},\mathbf{k}'} \right|^2}{\hbar^2} \\ & + \frac{2\pi N_\mathrm{F} n_\mathrm{imp} \tau_0}{\hbar} \int \frac{\mathrm{d}\phi}{2\pi} \left| V_{\mathbf{g},\mathbf{k}'} \right|^2 \Big\{ \quad 1 - \frac{\tau_0}{\tau_\mathrm{i}} - i\tau_1 \left(\mathbf{v}_\mathbf{g} \cdot \mathbf{q} \right) - i \left(\mathbf{S} + \mathbf{R} \right) \cdot \left(\tau_1 \mathbf{\Omega}_1 + \tau_3 \mathbf{\Omega}_3 \right) \\ & \qquad - \tau_0 \tau_1 \left[\left(\mathbf{v}_\mathbf{g} \cdot \mathbf{q} \right) + \left(\mathbf{S} + \mathbf{R} \right) \cdot \mathbf{\Omega}_1 \right]^2 \\ & \qquad - \tau_0 \tau_3 \left[\left(\mathbf{S} + \mathbf{R} \right) \cdot \mathbf{\Omega}_3 \right]^2 \quad \Big\} C^{(0)}_{\mathbf{g},\mathbf{k}'}. \end{aligned} \tag{2.217}$$

where we introduced $\mathbf{R}$ as the spin-3/2 operator in the second Green's function. In the following, we assume that only one type of spin–orbit coupling, either Rashba or Dresselhaus type, is

relevant. For this example, we take the (single and triple winding) Dresselhaus case. We find for the $\mathcal{L}$ operator,

$$\begin{aligned}\mathcal{L} = \frac{1}{\tau_\mathrm{i}} + \frac{v_\mathrm{F}^2\tau_1}{2}q^2 + \frac{\tau_1\Omega_1^2 + \tau_3\Omega_3^2}{2}\left[\left(S_\mathrm{x} + R_\mathrm{x}\right)^2 + \left(S_\mathrm{y} + R_\mathrm{y}\right)^2\right] \\ + \tau_1 v_\mathrm{F}\Omega_1\left[\left(S_\mathrm{y} + R_\mathrm{y}\right)q_\mathrm{y} - \left(S_\mathrm{x} + R_\mathrm{x}\right)q_\mathrm{x}\right].\end{aligned} \tag{2.218}$$

The addition of angular momentum is defined by

$$\mathbf{J} = \frac{\mathbf{S} + \mathbf{R}}{2}, \tag{2.219}$$

and it follows

$$\frac{\left(S_\mathrm{x} + R_\mathrm{x}\right)^2}{4} + \frac{\left(S_\mathrm{y} + R_\mathrm{y}\right)^2}{4} = J_\mathrm{x}^2 + J_\mathrm{y}^2, \tag{2.220}$$

with eigenvalues $j(j+1) - J_\mathrm{z}^2$, where $j = \{0,\ 1,\ 2,\ 3\}$ is the quantum number of total spin. By using the general ladder operators,

$$J_\pm = J_\mathrm{x} \pm iJ_\mathrm{y}, \tag{2.221}$$

$$q_\pm = q_\mathrm{x} \pm iq_\mathrm{y}, \tag{2.222}$$

the $\mathcal{L}$ operator reduces to

$$\mathcal{L}(j,m) = \frac{1}{\tau_\mathrm{i}} + Dq^2 + 2\left(\tau_1\Omega_1^2 + \tau_3\Omega_3^2\right)\left[j\left(j+1\right) - J_\mathrm{z}^2\right] - \Omega_1\sqrt{2\tau_1 D}\left(J_+q_+ + J_-q_-\right), \tag{2.223}$$

where we used the definition of the two-dimensional diffusion constant, Eq. (A.93). Using the relations for magnetic field quantization of momenta, Eqs. (2.146)–(2.148), and the relations involving the D'yakonov–Perel' relaxations, Eqs. (2.157)–(2.159), the $\mathcal{L}$ operator for the different spin sectors is

$$\frac{\mathcal{L}(j,m)}{\kappa} = \left\{a, a^\dagger\right\} + \frac{B_\mathrm{i}}{B} + \frac{B_\mathrm{so}}{B}\left[j(j+1) - J_\mathrm{z}^2\right] - \sqrt{\frac{B'_\mathrm{so}}{B}}\left(J_+a + J_-a^\dagger\right). \tag{2.224}$$

The magneto-conductivity is given by the sum over inverse eigenvalues of the $\mathcal{L}$ operator,

$$\Delta\sigma = \frac{e^2\kappa}{2\pi h}\sum_{n=0}^{n_\mathrm{max}}\left(-\frac{1}{E^{(0)}(n)} + \sum_{\{m\}}\frac{1}{E_m^{(1)}(n)} - \sum_{\{m\}}\frac{1}{E_m^{(2)}(n)} + \sum_{\{m\}}\frac{1}{E_m^{(3)}(n)}\right). \tag{2.225}$$

The set $\{m\}$ has to be chosen dependent on the $j = 0, 1, 2, 3$. It is essential that the argument regarding symmetric and anti-symmetric contributions, Eq. (2.139), still applies for the spin-3/2 case.

In analogy to the ILP spin-1/2 calculation, only the single winding contribution in the Bloch vector mixes spins of distinct Landau levels. The solution of this two-spin problem separates into different sectors that can be classified as singlet, triplet, quintet, and septet sector (see Fig. 2.17). For each sector, we use the corresponding ladder operators, which are constructed

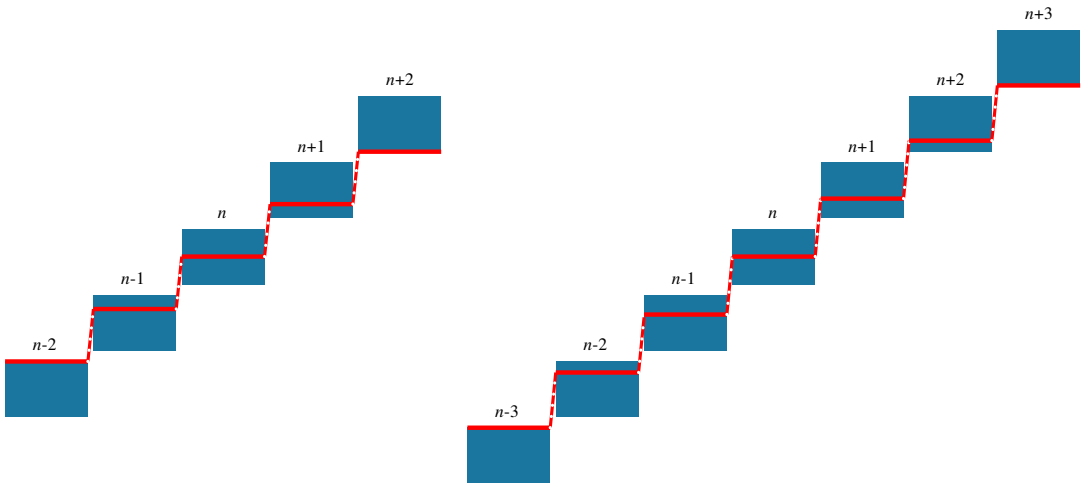

Figure 2.17: *Coupling of Landau levels.* Each effective Landau level is split according to the quantum numbers of quintet or septet (each blue rectangle represents the split group of Landau level with index n). The maximum number of coupled Landau levels (red) is five for the quintet and seven for the septet.

via the general relations (see, e.g., Ref. [116]),

$$\langle jm'|\, J^2 \,|jm\rangle = j(j+1)\delta_{mm'}, \tag{2.226}$$

$$\langle jm'|\, J_\mathrm{z} \,|jm\rangle = m\delta_{mm'}, \tag{2.227}$$

$$\langle jm'|\, J_+ \,|jm\rangle = \delta_{m'm+1}\sqrt{j(j+1)-mm'}, \tag{2.228}$$

$$\langle jm'|\, J_- \,|jm\rangle = \delta_{m'm-1}\sqrt{j(j+1)-mm'}. \tag{2.229}$$

In the following, we analyze the contributions from different spin sectors individually. To keep the notation in the calculation as compact as possible, we generalize the notation of Eq. (2.164),

$$a_{n,b} = n + \frac{1}{2} + \frac{B_\mathrm{i}}{B} + b\frac{B_\mathrm{so}}{B}, \tag{2.230}$$

where n is the label for the Landau level and b enumerates the additive contributions from the spin–orbit field.

First, we consider the case where ${}^{B'_\mathrm{so}}/_{B} = 0$, and no Landau levels are intermixed. The sum over inverse eigenvalues can then be calculated directly. For each of the spin sectors,

$$\sum_m \frac{\kappa}{E_m^{(j)}(n)} = \sum_{J_\mathrm{z}(j)} \frac{1}{n + \frac{1}{2} + \frac{B_\mathrm{i}}{B} + \frac{B_\mathrm{so}}{B}\left[j(j+1) - J_\mathrm{z}^2\right]}, \tag{2.231}$$

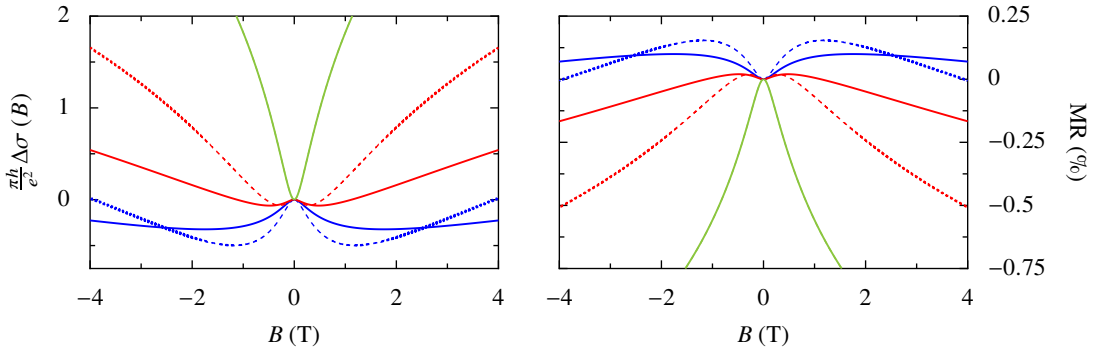

Figure 2.18: *Triple winding spin–orbit coupling in the spin-3/2 model.* In these plots, the effective fields are chosen to be $B_\mathrm{i} = 0.08\,\mathrm{T}$ and $B_\mathrm{o} \sim \infty$. The zero magnetic field resistivity for the magneto-resistivity plot is chosen to be $250\,\Omega$. Plots show the cases $B_\mathrm{so} = 0\,\mathrm{T}$ (solid green curve), $B_\mathrm{so} = 0.1\,\mathrm{T}$ (solid red curve), and $B_\mathrm{so} = 0.3\,\mathrm{T}$ (solid blue curve). For a comparison, the corresponding curves for two uncoupled bands with the same third harmonics are shown as dashed lines. The WAL signature is more pronounced in the uncoupled model.

and the magneto-conductivity is given by

$$\begin{aligned}\Delta\sigma = \frac{e^2}{2\pi h}\sum_{n=0}^{n_\mathrm{max}}\Bigg(& -\frac{1}{a_{n,0}} \\ & +\frac{1}{a_{n,2}}+\frac{2}{a_{n,1}} \\ & -\frac{1}{a_{n,6}}-\frac{2}{a_{n,5}}-\frac{2}{a_{n,2}} \\ & +\frac{1}{a_{n,12}}+\frac{2}{a_{n,11}}+\frac{2}{a_{n,8}}+\frac{2}{a_{n,3}}\Bigg).\end{aligned} \tag{2.232}$$

Without spin–orbit coupling, this reduces to the WL case for one spinless band, multiplied by four.

By using Eq. (1.70), the ψ-function, Eq. (1.67), and the notation combining ψ-function and logarithm, Eq. (1.75), the magneto-conductivity is given by

$$\begin{aligned}\Delta\sigma(B) = \frac{e^2}{\pi h}\Bigg[& \frac{1}{2}\Psi\left(\frac{B_\mathrm{i}+12B_\mathrm{so}}{B}\right)+\Psi\left(\frac{B_\mathrm{i}+11B_\mathrm{so}}{B}\right)+\Psi\left(\frac{B_\mathrm{i}+8B_\mathrm{so}}{B}\right) \\ & -\frac{1}{2}\Psi\left(\frac{B_\mathrm{i}+6B_\mathrm{so}}{B}\right)-\Psi\left(\frac{B_\mathrm{i}+5B_\mathrm{so}}{B}\right)+\Psi\left(\frac{B_\mathrm{i}+3B_\mathrm{so}}{B}\right) \\ & -\frac{1}{2}\Psi\left(\frac{B_\mathrm{i}+2B_\mathrm{so}}{B}\right)+\Psi\left(\frac{B_\mathrm{i}+B_\mathrm{so}}{B}\right)-\frac{1}{2}\Psi\left(\frac{B_\mathrm{i}}{B}\right)\Bigg].\end{aligned} \tag{2.233}$$

A plot for the magneto-transport curves for the triple multiband winding is shown in Fig. 2.18.

By deriving the low field limit of the magneto-conductance, we find

$$\Delta\sigma(s=\frac{3}{2};B\to 0;B_{\mathrm{so}}\gg B_{\mathrm{i}})\approx\frac{e^2}{\pi h}\frac{B^2}{48}\left(\frac{0.48}{B_{\mathrm{so}}^2}-\frac{1}{B_{\mathrm{i}}^2}\right). \tag{2.234}$$

Compared to the spin-1/2 result,

$$\Delta\sigma(s=\frac{1}{2};B\to 0;B_{\mathrm{so}}\gg B_{\mathrm{i}})\approx\frac{e^2}{\pi h}\frac{B^2}{48}\left(\frac{2.25}{B_{\mathrm{so}}^2}-\frac{1}{B_{\mathrm{i}}^2}\right), \tag{2.235}$$

we find the impact of the spin–orbit coupling in the spin-3/2 model is much smaller. The formula for higher half-integer spin models with triple winding spin–orbit coupling can be derived analogously.

A single winding contribution to the spin–orbit coupling changes the $\mathcal{L}$ matrix from a diagonal into a tridiagonal matrix. The sum over inverse eigenvalues is computed by considering the determinant of the matrices and their diagonal minors via Eq. (2.162) (details of this calculation are listed in App. B). Whereas the triple winding Bloch vector for spin-3/2 shows no qualitative difference compared to the spin-1/2 case, the single winding contribution results in an additional "shoulder"-like structure in the magneto-conductivity (see Fig. 2.19).

In the original ILP-theory, the two spins forming the Cooper channel can build a singlet and a triplet state. In the triplet state, the magnetic field splits the threefold degenerate eigenvalues into Landau levels of different total spin quantum number. The single winding term in the Hamiltonian (but not the triple winding term!) mixes these split Landau levels for different spin quantum numbers, which finally creates a magneto-resistivity with stronger amplitude than HLN-theory. In the spin-3/2 case, besides the singlet and triplet, also quintet and septet contributions have to be considered. A single spin-winding term in the Bloch vector now mixes the states within triplet, quintet, and septet and results in a much stronger coupling of the effective Landau levels: the coupled Landau level ladder becomes considerably larger in this scenario. In this sense, it is the physics of coupled Landau levels in the higher spin channels of the Cooperon that determines the magneto-resistivity of two-dimensional multiband systems.

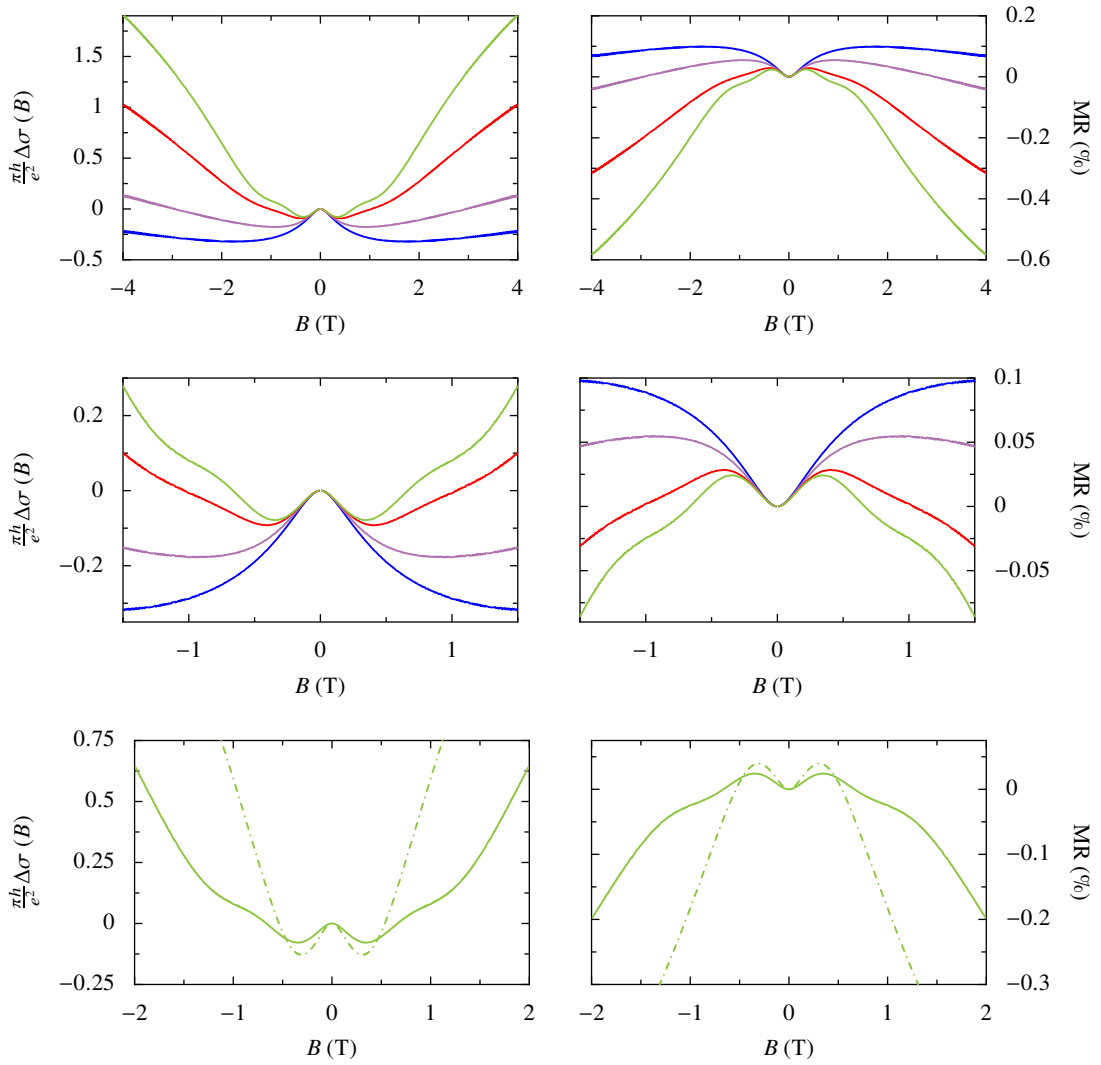

Figure 2.19: *Dresselhaus spin–orbit splitting in the spin-3/2 model.* In these plots, the effective fields are chosen to be $B_\mathrm{i} = 0.08\,\mathrm{T}$, $B_\mathrm{so} = 0.3\,\mathrm{T}$ and $B_\mathrm{o} \sim \infty$. The zero magnetic field resistivity for the magneto-resistivity plot is $250\,\Omega$. $B'_\mathrm{so}/B_{\mathrm{so}=0}$ corresponds to the solely triple winding spin–orbit coupling (blue curve). $B'_\mathrm{so}/B_{\mathrm{so}=1}$ corresponds to the solely single winding spin–orbit coupling (green curve). In between, the cases of $B'_\mathrm{so}/B_\mathrm{so} = 0.5$ (violet curve) and $B'_\mathrm{so}/B_\mathrm{so} = 0.9$ (red curve) are shown. Plots in the middle are a closeup of the upper plots in the smaller field region. Whereas the over-all shape is similar to the spin-1/2 case, the single winding spin–orbit coupling introduces a richer structure to the magneto-transport. In the lower plots, we compare the single winding spin-3/2 case (solid line) with the case of two uncoupled spin-1/2 bands (dash-dotted lines). For very small spin–orbit coupling, the results are similar, but for larger magnetic fields, the two cases differ considerably.

Summary of Chapter 2

In this chapter, I examined the impact of spin–orbit coupling on the theory of weak localization. Spin–orbit coupling results in weak anti-localization, a quantum correction that decreases the resistance, opposite to weak localization. Transport in magnetic fields shows a positive magneto-resistivity for small magnetic fields, and a negative magneto-resistivity when the magnetic field outreaches the effect of the spin–orbit coupling. Beyond these very general results, the microscopic picture of the spin–orbit coupling influences the explicit shape of the magneto-resistivity in several ways.

First, I reviewed the Hikami–Larkin–Nagaoka-theory (HLN). This theory is based on spin–orbit scatterers and the Elliott–Yafet spin relaxation. From a microscopic point of view, this theory cannot explain a positive magneto-resistivity in quasi-two-dimensional systems, because the relevant spin–orbit scattering rates for Elliott–Yafet processes vanish in the two-dimensional plane. Iordankii–Lyanda-Geller–Pikus-theory (ILP) describes spin–orbit coupling in systems with broken inversion symmetry, where the bands are spin-split and D'yakonov–Perel' spin relaxation becomes important. The spin winding at the Fermi surface of the spin-split bands has a significant influence on the magneto-resistivity. A triple spin winding in ILP-theory produces a very similar result for the magneto-resistivity as does HLN-theory by considering spin–orbit scatterers. However, single spin winding, which is typical for the Rashba and Dresselhaus effect in two-dimensional systems, results in a much more pronounced amplitude of magneto-resistivity that cannot be achieved with HLN-theory. I emphasize that ILP-theory has to be chosen for the correct description of WAL in low-dimensional oxide materials. The magneto-resistivity result does not depend on specific broken symmetries like in the Rashba or Dresselhaus effect, but rather on the dominant spin winding number at the Fermi surface of the spin-split bands.

In the next chapter, I will discuss magneto-transport data obtained from oxide materials. In preparation for this discussion, I extended ILP-theory for spin–orbit coupling that is relevant for the $LaAlO_3/SrTiO_3$ heterostructure. I introduced an isotropic Rashba Hamiltonian with triple spin winding as well as an anisotropic Rashba Hamiltonian with single and triple spin winding components. I showed that ILP-theory applies also to these models and gave constraints for the expected spin–orbit scattering rates. Beyond these effective band models, I extended the ILP-theory to a spin-$^3/_2$ system. This four-level Hamiltonian is a generic model for a multiband ILP theory, which is highly relevant for the description of oxide materials. Whereas the triple spin winding for the spin-$^3/_2$ case shows no particular difference compared to the spin-$^1/_2$ case, the single spin winding revealed an additional structure in the spin-$^3/_2$ case in form of a "shoulder" in the magneto-resistivity, produced by the coupling between Landau levels in the quintet and septet channel of the Cooperon.

3 Anti-Localization in Oxide Heterostructures

Contents

In the previous chapters, we introduced theories describing WAL and the sMIT in two-dimensional electronic systems. Now this formalism will be employed to investigate experimental data observed at interfaces of oxide materials.

Nowadays, the physics of silicon-based semiconductors is the driving force behind electronic devices all over the world and in everyday life. In semiconductors, electronic behavior is mainly determined by s- and p-symmetric orbitals, and a free electron gas description with effective masses offers a satisfying description. However, it becomes challenging for the semiconductor industry to push the limits of technical possibilities regarding speed and miniaturization of the devices.

In the search for new applicable materials, oxides emerged as promising candidates, providing new kinds of functionality for electronics and spintronics (see, e.g., Refs. [117–120]). Prominent examples are high-T_c superconducting cuprates, colossal magneto-resistance manganites [121, 122], iridates with conjectured spin-liquid behavior [123], and the $LaAlO_3/SrTiO_3$ heterostructure [124], which will be in the focus of this chapter.

One key feature of oxide materials is certainly the role of oxygen. Its electronegativity produces much stronger local fields in the unit cell then usually found in semiconductors. In addition, the electronic counterpart is often played by a transition metal: the metal's electrons of s-orbital character are transferred to the oxygen, and the electrons residing in correlated d-orbitals determine the Fermi surface properties. These correlations seem to introduce rich physics like magnetism, high-temperature superconductivity, metal–insulator transitions, and multiferroicity. Due to the strong local interplay of charge, orbital, spin, and lattice degrees

of freedom, physics generally appears to be much richer as in conventional semiconductors. These different electronic phases are often very sensitive to external parameters as well as growth conditions, opening a door for tuning, controlling and switching between specific ground state properties. The demonstration of ordinary [125] and fractional quantum Hall effect in oxides [126], beforehand only detectable in very clean silicon and graphene based materials, had been acknowledged a hallmark regarding the high control in growth techniques now available for oxide materials. However, high-purity semiconductor interfaces are still superior regarding a high electron mobility, whereas electron densities are often higher at metallic oxide interfaces by an order of magnitude or more [127].

Interfaces and surfaces (which are interfaces with the vacuum) bring another dimension to the functionality of such materials, as is well known for semiconductor devices [128]. Interfaces of oxide materials aim to combine properties of the parent compounds. However, another important aspect is the breaking of inversion symmetry at the interface. The symmetry breaking can lead to drastic changes of the sensitive ground state in oxides, which can induce fundamentally different behavior at the interface that cannot be found in the bulk compounds. One example is the building of a two-dimensional electron gas between two bulk insulators, which are not only stronger confined than the two-dimensional electron gas of semiconductor quantum wells, but also feature several separated quantum wells parallel to the interface [127, 129–132].

Thanks to experimental collaborators, we have the opportunity to analyze experimental data obtained from three very different oxide interfaces:

- *$LaAlO_3/SrTiO_3$ heterostructures.* The interface between the non-magnetic band insulators $LaAlO_3$ and $SrTiO_3$ shows a metallic interface with superconducting and magnetic ground-state properties and has a high potential for applicable devices [117, 130, 133, 134]. Physics in these systems seems to be controlled by the correlated d-orbitals of the transition metal titanium. Data is provided by Zabaleta and has been measured in the group of Mannhart at the Max Planck Institute for Solid State Research Stuttgart [9, 135]. Magneto-transport is examined under hydrostatic pressure.

- *Thin metallic monolayers of $BaPbO_3$ grown on $SrTiO_3$.* Data is provided by Meir and has been measured in the group of Hammerl at the Chair of Experimental Physics VI at the University of Augsburg [136, 137]. Presumably, the electronic structure is determined by s- and p-symmetric orbitals, incorporating a strong spin–orbit coupling by the heavy metal lead.

- *Superconducting bilayers of $BaPbO_3/BaBiO_3$ grown on $SrTiO_3$.* These only recently investigated heterostructures are also in the focus due to topological and superconducting properties. Again, the electronic structure is presumably determined by s- and p-orbitals, as well as the strong spin–orbit coupling of the heavy metals lead and bismuth. Data is provided by Meir [136, 137].

In the first section of this chapter, we review theoretical and experimental investigations on the $LaAlO_3/SrTiO_3$ heterostructures from recent years. Besides its many other intriguing properties, magneto-transport measurements on $SrTiO_3$ surfaces and $LaAlO_3/SrTiO_3$ heterostructures revealed a pronounced signature of WAL. Its origin, however, as well as the specific microscopic picture, are still under debate. One issue is that the WAL structure is often hidden by multiband Hall effects, and there has not been a convincing treatment for the multiband data so far. We

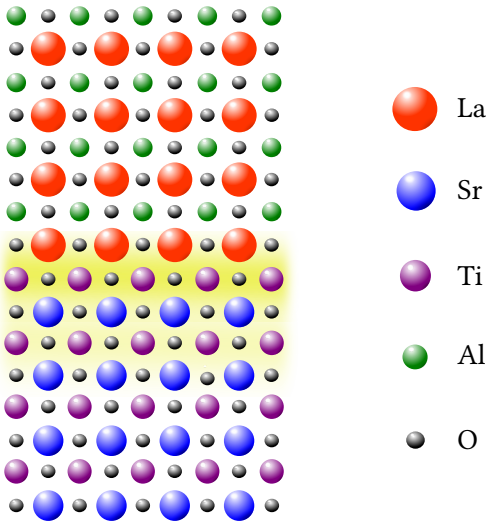

Figure 3.1: *Heterostructure of $LaAlO_3$ on $SrTiO_3$.* An electronic interface between the bulk insulators $LaAlO_3$ and $SrTiO_3$ is created if the $SrTiO_3$ substrate is terminated with a TiO_2 plane and the $LaAlO_3$ film has a thickness of at least four unit cells. The electron liquid at the interface (yellow) shows high mobility and charge carrier density.

analyze experimental data applying the theories discussed in Chap. 2 to the $LaAlO_3/SrTiO_3$ system by disentangling the multiband and WAL contributions in a self-consistent fitting procedure. Subsequently, we analyze recent data gained in thin films of $BaPbO_3$ and $BaPbO_3/BaBiO_3$. We close this chapter with the recommendation to search for the sMIT in oxide interfaces, a phase transition that has not been observed so far.

3.1 $LaAlO_3/SrTiO_3$ Heterostructures

3.1.1 Two-Dimensional Electronic Interface

One important class of oxides is the ABO_3 perovskite structure. Along the [001]-direction, the perovskite structure is formed by alternating layers of AO and BO_2 (see Fig. 3.1). A and B can be occupied by a great diversity of metallic cations and the structure compatibility allows to grow heterostructures by stacking layers of different oxides [126]. The perhaps most prominent perovskite in this regard is $SrTiO_3$, nowadays a standard substrate material that can be produced in form of high quality single crystals.

In the ideal bulk ABO_3 perovskite structure, the B-ion is surrounded by six oxygen ions in a cubic symmetry (see Fig. 3.2). This octahedral coordination of the metal ion, in this case the titanium atom, results in a crystal field that splits the degenerate d-orbitals into three-fold degenerate t_{2g} orbitals $\{yz, zx, xy\}$ and two-fold degenerate e_g orbitals $\{x^2 - y^2, 3z^2 - r^2\}$ (see, e.g., Ref. [138]).

The crystal field depends strongly on the local environment, and an interface with vacuum or another oxide can shift the energy levels and deforms the orbitals considerably. For the surface of the bulk insulator $SrTiO_3$, it appears that the titanium t_{2g} bands are pushed below the Fermi energy and metallic behavior and even superconductivity occurs [108, 139–142]. Composing different heterostructures on a $SrTiO_3$ substrate defines a key mechanism to tune, control and change the properties of the t_{2g} orbitals.[1] It has turned out that not only the chosen perovskite material changes the interface properties, but also environmental conditions during

[1] This seems not to be the case in the $BaPbO_3$ and $BaBiO_3$ based samples that are are grown on a $SrTiO_3$ substrate and discussed in Sec. 3.3—the electrons examined there presumably originate from the lead and bismuth atoms, and physics is controlled by s- and p-orbitals.

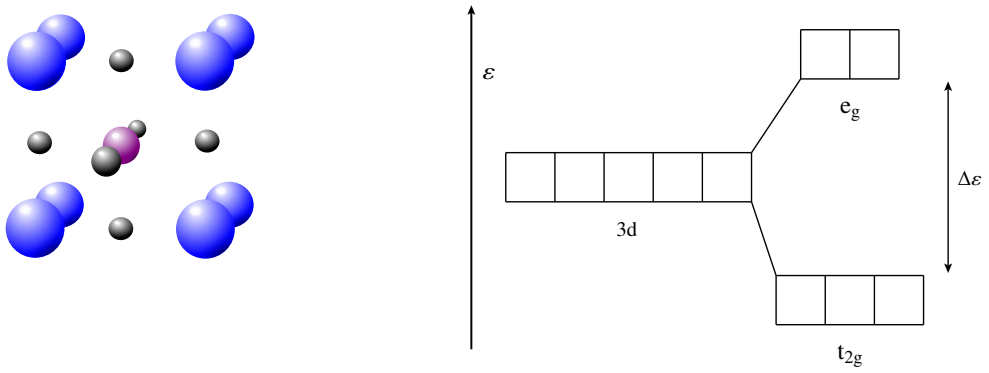

Figure 3.2: *Octahedral coordination of the transition metal and level splitting.* (a) The transition metal ion (magenta) is surrounded by oxygen in a cubic symmetry (gray). (b) This causes the degenerate d-orbitals to split into doubly degenerate e_g orbitals and threefold degenerate t_{2g} bands.

crystal growth, like oxygen background pressure or the number of layers grown upon the interface.

In 2004, Ohmoto and Hwang discovered a conducting interface in $LaAlO_3/SrTiO_3$ heterostructures [143]. Both bulk materials are band insulators with a large energy gap of 5.6 eV in $LaAlO_3$ and 3.2 eV in $SrTiO_3$, and the lattices are matching well with lattice constants of 3.789 Å and 3.905 Å, respectively [143]. To provide the conducting interface, $SrTiO_3$ has to be terminated with a TiO_2 layer, which can be achieved by etch treatment of the $SrTiO_3$ substrate [144, 145]. The charge carriers in the electronic interface showed a high mobility of $\mu \approx 10^4\ \mathrm{cm^2/Vs}$ and a high electron density $n \approx 10^{17}\ \mathrm{1/cm^2}$ [143]. Quantum oscillations did not change under rotation of the magnetic field, and it has been concluded that the electronic layer reacts like a three-dimensional system regarding electronic transport [143, 146]. Furthermore, it is debated that this specific electron liquid extends several hundreds of micrometers through the substrate and forms due to oxygen vacancies, because it vanishes for higher oxygen background pressure during the crystal growth [146]. Also, the properties of this electron liquid are in agreement with earlier experiments on doped $SrTiO_3$ [147]. Structures of this kind are often referred to as $LaAlO_3/SrTiO_{3-\delta}$, to underline the importance of oxygen vacancies.

A different kind of electron liquid has been generated by using a higher partial oxygen pressure during the cooling process, reducing oxygen vacancies: Thiel et al. [148] have found that the interface became conducting with a minimum of 4 $LaAlO_3$ layers grown on the $SrTiO_3$ substrate, whereas below the critical thickness, all samples have shown insulating behavior [148, 149]. Removal of the top layer of a conducting sample produces an insulating sample, indicating a different mechanism for the conductive layer than bulk oxygen vacancies. This electron liquid features a much lower density of $n \approx 10^{13}\ \mathrm{1/cm^2}$ and a mobility of $\mu \approx 10^3\ \mathrm{cm^2/Vs}$ [148]. The electron liquid can be widely tuned via back- or top gating, depending on whether the $SrTiO_3$ substrate or the top $LaAlO_3$ layer is taken as dielectric [150]. A striking argument for two-dimensionality is the signature of quantum oscillations in these samples, which strongly depend on the magnetic field orientation [151]. This electron liquid has been found to become a superconductor for temperatures around 200 mK and the superconducting

layer has been approximated to a thickness below 10 nm [152]. Furthermore, experiments with conducting-tip atomic force microscopy [153, 154] and photo-electron spectroscopy [155] have revealed that the electron liquid in these samples is confined within at most 10 nm at the interface and behaves like a two-dimensional system.

Several exciting characteristics have been found in these structures: besides the superconductivity in the interface system, some samples showed magnetic order at low temperatures [156], and even the coexistence of both, superconductivity and magnetism, has been observed with in-plane magnetic moment at the interface [157–159]. Further theoretical [160] and experimental [161] investigations relate this magnetism to titanium d_{xy} orbitals or oxygen vacancies. Even at room temperature, Ref. [162] has found in-plane ferromagnetic domains when the charge carriers are depleted. Beyond that, also the vicinity to a ferroelectric quantum critical point in $SrTiO_3$ is discussed to strongly influence the physics at the interface [163]. Furthermore, a strong spin–orbit coupling has been detected, which is tunable by gate voltage [95, 164] or current driven [165], and transport seems to be strongly influenced by dislocations [166].

Although the $LaAlO_3/SrTiO_3$ heterostructure has been investigated intensively, the exact mechanism for the emergence of this two dimensional electron liquid is still under debate. Mechanisms that received broad acceptance are the polar catastrophe scenario [167], or charge carriers induced by intermixing, or defects (see also the recent reviews, Refs. [168–170]):

- *Defect induced charge carriers.* This scenario pictures the emergence of conducting electrons at the interface via oxygen vacancies. An oxygen vacancy provides two electrons that populate the t_{2g} bands.
- *Charge carriers provided by chemical intermixing.* Directly at the interface, lanthanum ions might substitute strontium ions. Because lanthanum offers an additional electron in comparison with strontium, this mechanisms acts again as electron doping.
- *Intrinsic mechanism: Avoiding a polar catastrophe.* This scenario is supported by the critical layer thickness of the polar $LaAlO_3$. The planes of $(LaO)^+$ and $(AlO_2)^-$ create atomic layers with alternating charge. On top of the unpolar TiO_2 termination, this results in an electric potential that increases with layer thickness of $LaAlO_3$. At a critical thickness, electrons are transferred from the top of the heterostructure to the interface, avoiding the "polar catastrophe". This mechanism is also discussed in similar polar heterostructures like $LaVO_3/SrTiO_3$ [171].

Although the polar catastrophe scenario is supported by *ab initio* calculations [135, 172–175], several experimental findings seem to disagree with this picture, e.g. the absence of a measurable polar potential [176, 177] or the formation of an electron liquid also for amorphous or un-oriented $LaAlO_3$ on top of $SrTiO_3$ [178, 179]. More recently, combinations of the mechanisms described above are discussed in the literature, like an emergence of oxygen vacancies at the top layer of $LaAlO_3$, induced by a rather small polar discontinuity effect [169].

3.1.2 Effective Six-Band Model

Several experimental investigations at the interface of $LaAlO_3/SrTiO_3$ heterostructures have contributed to a picture of a multiband system with charge carriers of the several titanium t_{2g} bands [156, 180–186]. To investigate the strong spin–orbit coupling in the heterostructure, an effective six-band model for the t_{2g} bands at the $SrTiO_3$ interface (with special focus on the $LaAlO_3/SrTiO_3$ heterostructure) has been established based on *ab initio* calculations [187–192].

In the following, we discuss a Hamiltonian in second quantized form,

$$\mathcal{H} = \sum_{\mathbf{k}} \mathrm{C}_{\mathbf{k}}^{\dagger} \mathrm{H}_{\mathbf{k}} \mathrm{C}_{\mathbf{k}}, \tag{3.1}$$

where $\mathrm{C}^{\dagger}$ and C are creation and annihilation vectors in the product space of the $\mathrm{t_{2g}}$ orbitals $\{\mathrm{yz}, \mathrm{xz}, \mathrm{xy}\}$, and spin. The dispersion along the $\mathrm{t_{2g}}$ orbitals is highly anisotropic and requires the implementation of heavy and light effective charge carrier masses m_{l} and m_{h}. Furthermore, the surface of the perovskite structure provides a confinement potential and affects the $\mathrm{t_{2g}}$ bands according to their spatial symmetry. As the $\mathrm{d_{xz}}$ and $\mathrm{d_{yz}}$ orbitals have a larger overlap in z-direction as the $\mathrm{d_{xy}}$ orbital, these bands are shifted apart by an energy gap Δ_{z}. The resulting kinetic part of the Hamiltonian matrix is then specified by

$$\mathrm{H}_{\mathbf{k}}^{0} = \begin{pmatrix} \frac{\hbar^2 k_{\mathrm{x}}^2}{2m_{\mathrm{h}}} + \frac{\hbar^2 k_{\mathrm{y}}^2}{2m_{\mathrm{l}}} & 0 & 0 \\ 0 & \frac{\hbar^2 k_{\mathrm{x}}^2}{2m_{\mathrm{l}}} + \frac{\hbar^2 k_{\mathrm{y}}^2}{2m_{\mathrm{h}}} & 0 \\ 0 & 0 & \frac{\hbar^2 k_{\mathrm{x}}^2}{2m_{\mathrm{l}}} + \frac{\hbar^2 k_{\mathrm{y}}^2}{2m_{\mathrm{l}}} - \Delta_{\mathrm{z}} \end{pmatrix} \otimes \sigma_0, \tag{3.2}$$

where σ_0 is a unity matrix in spin space. To take the electric field of the titanium cores into account, an atomic (momentum independent) spin–orbit coupling is introduced via

$$\mathrm{H}_{\mathbf{k}}^{\mathrm{aso}} = \Delta_{\mathrm{aso}} \begin{pmatrix} 0 & i\sigma_{\mathrm{z}} & -i\sigma_{\mathrm{y}} \\ -i\sigma_{\mathrm{z}} & 0 & i\sigma_{\mathrm{x}} \\ i\sigma_{\mathrm{y}} & -i\sigma_{\mathrm{x}} & 0 \end{pmatrix}, \tag{3.3}$$

with spin–orbit strength Δ_{aso}. The third ingredient is an orbital mixing due to the interface potentials, described by[2]

$$\mathrm{H}_{\mathbf{k}}^{\mathrm{i}} = \Delta_{\mathrm{m}} \begin{pmatrix} 0 & 0 & ik_{\mathrm{x}} \\ 0 & 0 & ik_{\mathrm{y}} \\ -ik_{\mathrm{x}} & -ik_{\mathrm{y}} & 0 \end{pmatrix} \otimes \sigma_0, \tag{3.4}$$

where Δ_{m} is the energy of the orbital mixing.

The full Hamiltonian matrix in momentum and spin dependent orbital space is consequently given by

$$\mathcal{H} = \sum_{\mathbf{k}} \begin{pmatrix} c_{\mathrm{yz},\mathbf{k},\uparrow}^{\dagger} \\ c_{\mathrm{yz},\mathbf{k},\downarrow}^{\dagger} \\ c_{\mathrm{xz},\mathbf{k},\uparrow}^{\dagger} \\ c_{\mathrm{xz},\mathbf{k},\downarrow}^{\dagger} \\ c_{\mathrm{xy},\mathbf{k},\uparrow}^{\dagger} \\ c_{\mathrm{xy},\mathbf{k},\downarrow}^{\dagger} \end{pmatrix}^{\mathrm{T}} \begin{pmatrix} \xi_{\mathbf{k}}^{\mathrm{yz}} & 0 & i\Delta_{\mathrm{aso}} & 0 & i\Delta_{\mathrm{m}} k_{\mathrm{x}} & -\Delta_{\mathrm{aso}} \\ 0 & \xi_{\mathbf{k}}^{yz} & 0 & -i\Delta_{\mathrm{aso}} & \Delta_{\mathrm{aso}} & i\Delta_{\mathrm{m}} k_{\mathrm{x}} \\ -i\Delta_{\mathrm{aso}} & 0 & \xi_{\mathbf{k}}^{\mathrm{xz}} & 0 & i\Delta_{\mathrm{m}} k_{\mathrm{y}} & i\Delta_{\mathrm{aso}} \\ 0 & i\Delta_{\mathrm{aso}} & 0 & \xi_{\mathbf{k}}^{\mathrm{xz}} & i\Delta_{\mathrm{aso}} & i\Delta_{\mathrm{m}} k_{\mathrm{y}} \\ -i\Delta_{\mathrm{m}} k_{\mathrm{x}} & \Delta_{\mathrm{aso}} & -\Delta_{\mathrm{m}} i k_{\mathrm{y}} & -i\Delta_{\mathrm{aso}} & \xi_{\mathbf{k}}^{\mathrm{xy}} - \Delta_{\mathrm{z}} & 0 \\ -\Delta_{\mathrm{aso}} & -i\Delta_{\mathrm{m}} k_{\mathrm{x}} & -i\Delta_{\mathrm{aso}} & -i\Delta_{\mathrm{m}} k_{\mathrm{y}} & 0 & \xi_{\mathbf{k}}^{\mathrm{xy}} - \Delta_{\mathrm{z}} \end{pmatrix} \begin{pmatrix} c_{\mathrm{yz},\mathbf{k},\uparrow} \\ c_{\mathrm{yz},\mathbf{k},\downarrow} \\ c_{\mathrm{xz},\mathbf{k},\uparrow} \\ c_{\mathrm{xz},\mathbf{k},\downarrow} \\ c_{\mathrm{xy},\mathbf{k},\uparrow} \\ c_{\mathrm{xy},\mathbf{k},\downarrow} \end{pmatrix}. \tag{3.5}$$

[2] In Joshua et al. [193], a relative minus sign is between the k_{x} and the k_{y} entry of the orbital intermixing Hamiltonian. Note that this produces a different sign in the winding number of the spin quantization axis at the Fermi surface.

We consider values provided by DFT calculations [190],

$$m_\mathrm{h} = 6.8 m_\mathrm{e}, \tag{3.6}$$
$$m_\mathrm{l} = 0.41 m_\mathrm{e}, \tag{3.7}$$
$$\Delta_\mathrm{z} = 50\,\mathrm{meV}, \tag{3.8}$$
$$\Delta_\mathrm{aso} = 9.65\,\mathrm{meV}, \tag{3.9}$$
$$\Delta_\mathrm{m} = 20\,\mathrm{meV}. \tag{3.10}$$

The bands of Hamiltonian Eq. (3.5) for these parameters are shown in Fig. 3.3. Whereas the orbital mixing term, Eq. (3.4), vanishes at the Γ point and mixes the bands considerably only near the band crossings, the spin–orbit coupling, Eq. (3.3), mixes the bands momentum independent. Both effects combined result in an effective momentum dependent spin–orbit coupling of the three t_{2g} bands, Eq. (3.2). The momentum dependent band splitting is shown in Fig. 3.4. The six-band model is consistent with band structure measurements using X-ray absorption spectroscopy and ARPES on $LaAlO_3/SrTiO_3$ interfaces as well as $SrTiO_3$ surfaces [139, 140, 182, 194].

An electric gate field controls the charge carrier density at the interface and the gap of the effective spin–orbit splitting changes filling dependent. Therefore, this Rashba-like effect does not necessarily show a linear dependence in momentum due to its multiband origin.

The spin–orbit splitting of the bands is strongly anisotropic. For the k_x-direction $\left(k_y = 0\right)$, the splitting of the lower and upper band pair is nearly linear at the Γ-point, whereas the middle band pair splitting is cubic for small momenta. The splitting of the upper band pair in very small this direction. For the $\left(k_x = k_y\right)$-direction, the situation is different. Again, the lower and upper band pair splitting is nearly linear in momentum, but the splitting for the middle band pair is negligible near the Γ point. Near the avoided crossing, the splitting in the lower band pair decreases fast with momentum, whereas the splitting in the middle band pair increases strongly.

In the following, we discuss some unsolved issues regarding the simplified six-band model. The *ab initio* calculations show that there are actually many more bands involved, originating from deeper titanium layers in the substrate, and which might not be adequately captured in the six-band model. The xy-band from the interface titanate layer seems to have too low energy to be identified with the one measured in magneto-transport experiments [195]. Instead, the lower edge of the xy-bands of the first and second titanate layer are quite close to the Fermi surface. Unlike the interface xy-band, the charge carriers in those bands are not that strongly confined in two dimensions and these bands also have a much smaller spin–orbit splitting due to the weaker orbital mixing [195]. Recent DFT-based simulations have come to the conclusion that until the fourth titanium layer, xy bands can contribute to the charge carriers at the interface [135]. The xz/yz carriers, a priori less confined, even contribute beyond the sixth layer and therefore feature a more three-dimensional-like behavior [186]. This theoretical picture is in agreement with experiments, where for $n = 0.9 \times 10^{14}\ {}^1/_{\mathrm{cm}^2}$ the electron concentration at the interface sharply drops at a depth of 2 nm and then builds a tail until a depth of 11 nm. The sharp concentration drop can be related to the xy carriers, the tail to the xz/yz carriers [185].

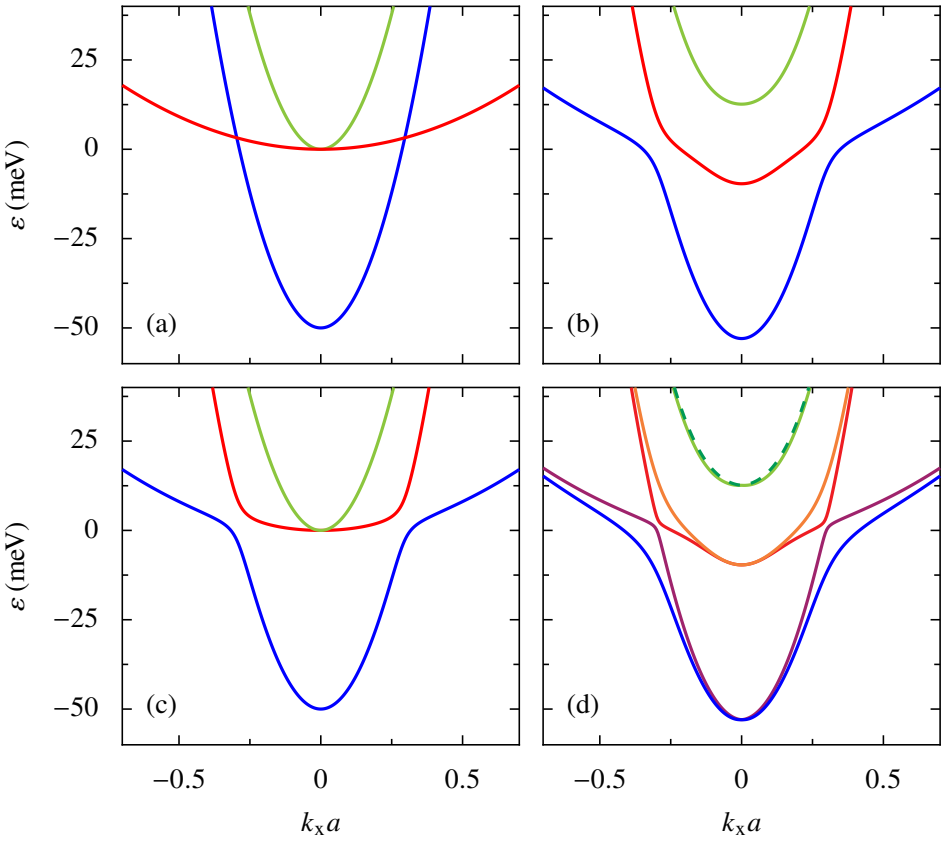

Figure 3.3: *Effective six-band model of the electron liquid at the $LaAlO_3/SrTiO_3$ interface.* Parameters are taken from DFT calculations [190]: $m_h = 6.8m_e$, $m_l = 0.41m_e$, $\Delta_{aso} = 9.65\,\text{meV}$, $\Delta_{con} = 20\,\text{meV}$. (a) Spin-degenerate three-band model for the t_{2g} bands with shifted d_{xy} band (blue). The d_{xz} (green) and d_{yz} bands (red) are strongly anisotropic. (b) The t_{2g} bands with atomic spin–orbit coupling included. The three bands are still double degenerate. (c) t_{2g} bands with interface induced inter-orbital mixing. These bands are also still double degenerate. (d) Six band model of the $LaAlO_3/SrTiO_3$ t_{2g} bands with interface induced inter-orbital mixing and atomic spin orbit coupling. The bottom band pair (blue and violet) has a strong d_{xy} character near the Γ-point. The middle (red and orange) band pair and the upper band pair (solid light green and dashed dark green) have a mixed d_{xz}/d_{yz} character.

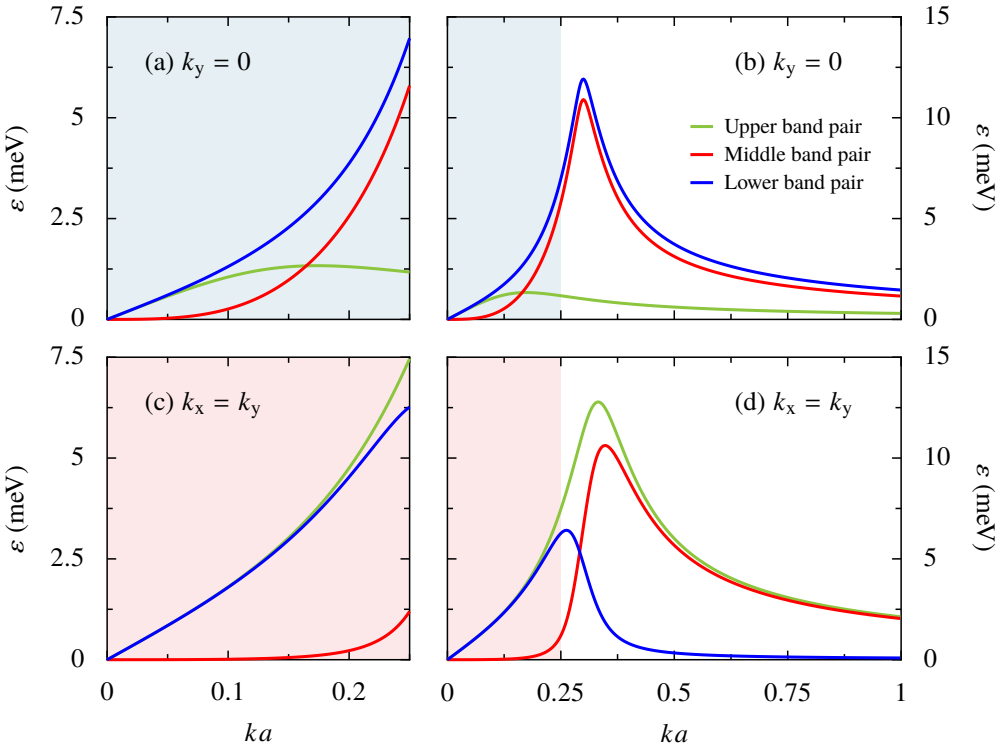

Figure 3.4: *Effective spin–orbit splitting in the six-band model.* The effective splitting is strongly anisotropic in momentum space. (a) Along the k_x-direction $(k_y = 0)$, the splitting in the lower and upper band pairs is linear in momentum, but cubic in the middle band pair. (b) Away from the avoided crossings at $ka \approx 0.3$, the splittings reach a maximum, before decreasing for high momenta. (c) In the $(k_x = k_y)$-direction, the splittings in the lower and upper band pair are still linear in momentum, but with a slightly higher slope. The splitting in the middle band pair does nearly vanish for small momenta. (d) For higher momenta in the $(k_x = k_y)$-direction, the role of upper and lower band pair is exchanged in comparison with the k_x-direction. Beyond the avoided crossing, the almost degeneracy passes onto the lower band pair.

3.1.3 Spin Structure and Effective Spin–Orbit Hamiltonians

The expectation value of the spin operator $\boldsymbol{\sigma}$ is a meaningful quantity only for a single, spin-split band pair. However, the effective six-band model includes three band pairs of different orbitals, and we can define a spin operator for this Hamiltonian by considering a $\{\mathrm{yz}, \mathrm{xz}, \mathrm{xy}\}$ basis,

$$\tilde{\boldsymbol{\sigma}} = \begin{pmatrix} \boldsymbol{\sigma}_{\mathrm{yz}} & 0 & 0 \\ 0 & \boldsymbol{\sigma}_{\mathrm{xz}} & 0 \\ 0 & 0 & \boldsymbol{\sigma}_{\mathrm{xy}} \end{pmatrix}, \tag{3.11}$$

where the diagonal entries represent the spin operators for each band of $\{\mathrm{yz}, \mathrm{xz}, \mathrm{xy}\}$-orbital character. Due to the non-diagonal terms in the Hamiltonian Eq. (3.5), the orbitals are becoming intermixed. The expectation value of the full spin Eq. (3.11) is then given by (complex) linear combinations of spin states from the different bands. As a result, the individual spin eigenstates for each band pair are no longer normalized.

To consider the spin winding number around the Fermi surface, we introduce a winding number w_i as defined in Eq. (2.83) for each band, as well as a winding number $W = \sum_i w_i$ for the complete system. We investigate the spin structure in the six-band model and picture the normalized spin states in Fig. 3.5. If we consider the spin expectation value allocated to the three band pairs, we find the following characteristics:

- For the lower band pair, the spin structure is similar to that of the Rashba Hamiltonian, see Fig. 2.7. Although the splitting becomes anisotropic near the avoided crossing, the spin at the Fermi surface follows the Rashba-like spin topology and has winding number $w_{1,\,2} = +1$ for each Fermi surface of the spin-split pair of bands.

- The spin structure of the higher band pair is similar to the cubic Dresselhaus spin–orbit coupling, see Fig. 2.6, though rotated by 30° and winding in opposite direction, which results in a spin winding number $w_{5,\,6} = -3$ for each Fermi surface. However, contrary to the cubic Dresselhaus effect, the band splitting is anisotropic and linear in momentum, at least near the Γ-point.

- The middle band pair shows different spin windings at the two Fermi surfaces: the lower band shows a Rashba-like spin structure with winding number $w_3 = +1$, but the higher one shows a Dresselhaus-like spin structure with winding number $w_4 = -3$. Still, the spin-structure along the $(k_{\mathrm{x}} = 0)$-direction as well as the $\left(k_{\mathrm{y}} = 0\right)$-direction is similar to the anisotropic Rashba Hamiltonian, see Fig. 2.9.

If only the lower band pair is partially filled, the winding number of the complete system is given by $W = +2$. As soon as the middle band pair becomes filled, we find a winding number of $W = 0$. Filling of the upper band pair changes the winding number to $W = -6$. The different topologies of the middle band pair make it evident that the separation into distinct band pairs, as often discussed in the literature, is only an artificial arrangement.

From theoretical and experimental investigations, we expect only the lower and middle band pair to be of relevance (see Sec. 3.1.2). To construct an effective spin–orbit Hamiltonian for the band pairs, both, spin structure and band splitting have to be considered. The lowest band pair can be well described by the Rashba Hamiltonian, as often discussed in the literature [108, 124]. We assume that the Hamiltonian near the Γ point can be written in the form [191]:

$$\mathcal{H}_{\mathbf{k}}^{\mathrm{bot}} = -\alpha^{\mathrm{bot}} \left(\boldsymbol{\sigma} \times \mathbf{k}\right) \cdot \hat{z}. \tag{3.12}$$

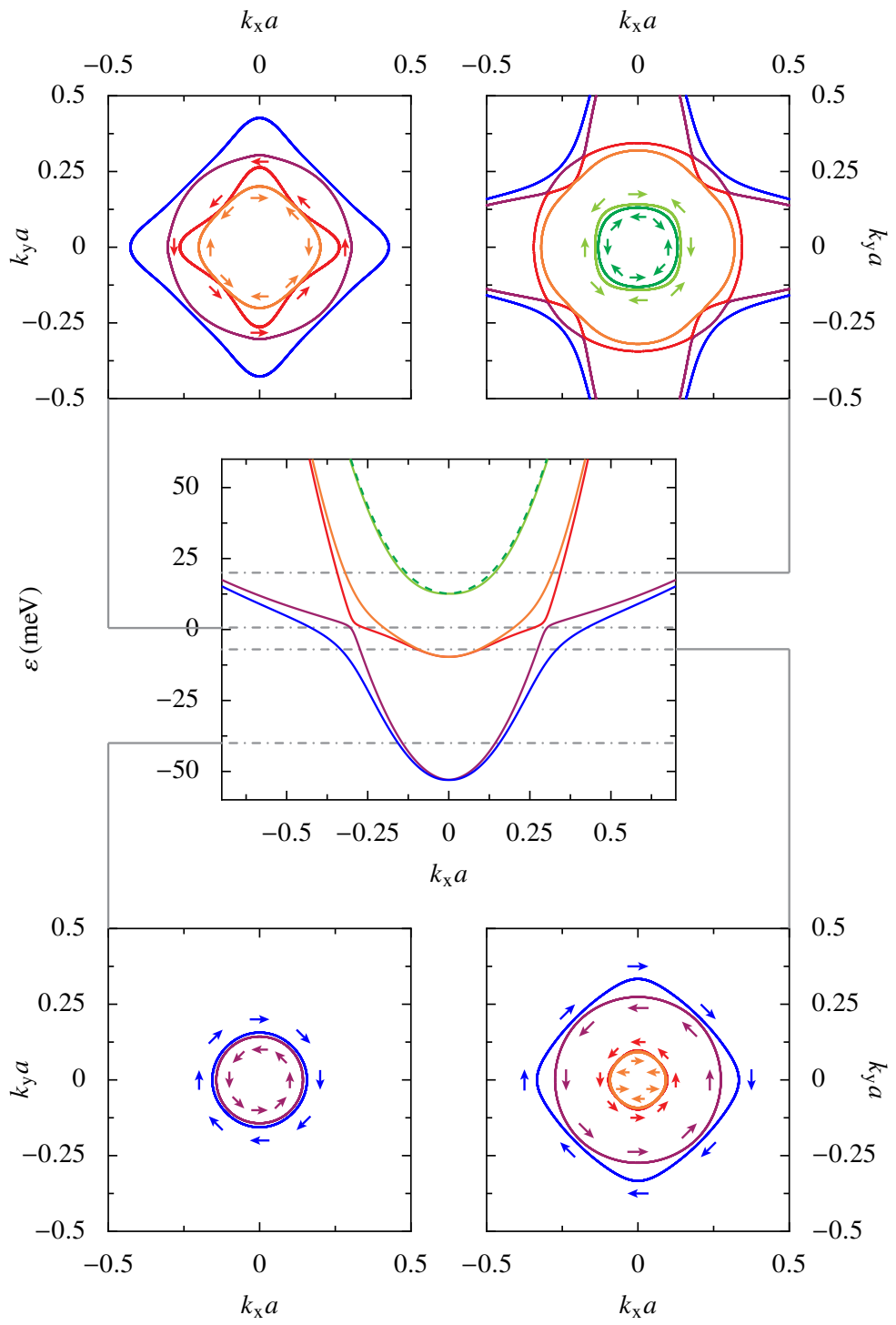

Figure 3.5: *Spin structure of the six-band model for $LaAlO_3/SrTiO_3$.* For different fillings, the Fermi surfaces and the corresponding direction of the local spin quantization axis in momentum space are shown. The winding numbers w_i of the spin quantization axis is from lowest to highest band: +1, +1, +1, −3, −3, −3. Remarkably, the middle band pair features two very different topologies.

Apart from the global minus sign, the properties of this Hamiltonian are described in Sec. 2.2.1.

However, the picture is not that clear for the middle band pair. The two Fermi surfaces exhibit a different topology of spin winding, which cannot be captured by an effective two-band model. Despite the unfitting winding numbers and the strongly anisotropic splitting in the middle band pair, it has been assumed in the literature that the middle band pair can be approximated as an effective cubic Rashba-type [108, 196]. Only recently, a suggestion for the middle band has been given by an anisotropic Rashba description in Ref. [109], where the anisotropic band splitting is taken into account. Likewise, we suggest the following effective spin–orbit Hamiltonian for the middle band pair near the Γ point:

$$\mathcal{H}_{\mathbf{k}}^{\mathrm{mid}} = \alpha^{\mathrm{mid}} \left(k_{\mathrm{x}}^2 - k_{\mathrm{y}}^2 \right) (\boldsymbol{\sigma} \times \mathbf{k}) \cdot \hat{z}. \tag{3.13}$$

This Hamiltonian Eq. (3.13) has been discussed in Sec. 2.2.2. The eigenvalues contain a degeneracy for $k_{\mathrm{x}} = k_{\mathrm{y}}$, whereas the six-band model encounters only approximate degeneracy, and the spin winding number is no meaningful quantity in this case. However, except for these points of degeneracy, the model captures the correct spin structure at least roughly and the dispersion of the middle band pair of the full six-band model is reproduced quite well.

We will compare the above models to an effective WAL investigation of magneto-transport data in the following sections. However, a crucial difference of the spin structure of the six-band model and the effective band pair Hamiltonians is that the spin vectors of the individual bands are not normalized within the six-band model. In fact, only the lowest band pair shows nearly normalized spin states. In the middle and higher band pairs, the linear combinations of anti-parallel spins lead to a very small weight of the spin vector, partly only 0.5% of the weight found in the lowest band pair (see also Ref. [197]). Also, the spin weight is generally different in the two bands within one pair due to the mixture of spins from all original orbitals. This also explains how the spins can appear parallel in Fig. 3.3 within one band pair. It is very doubtful whether these band-pair models are a good description of the six-band models, because apparently a single band pair of that model, taken for itself, does not provide the necessary basis for the spin quantity in the six-band model. The full multiband nature can only be captured by computation of the Cooperon for the full six-band Hamiltonian. Unfortunately, so far there seems no strategy to be known for solving this issue, except possibly a numerical investigation (see also the discussion in Chap. 4).

3.2 Data Analysis I: $LaAlO_3/SrTiO_3$ Under Pressure

Due to the strong interplay of lattice, orbital, charge and spin degrees of freedom, physical properties of oxide materials depend strongly on the microscopic lattice structure. Pressure is therefore a powerful tool for investigations in these materials and for tuning the ground state. For example, it has been reported that epitaxial strain can turn paraelectric $SrTiO_3$ films into ferroelectrics around room temperature [198]. Also, the critical thickness of $LaAlO_3$ layers to create the two-dimensional electron liquid is altered under pressure [199–201].

Recently, the effect of hydrostatic pressure on the electronic interface of $LaAlO_3/SrTiO_3$ has been examined [135]. Whereas uniaxial or biaxial pressure, as used for example in Ref. [199], primarily alters the shape of the unit cell, hydrostatic pressure changes the cell's volume. At room temperatures, a large drop of the resistivity has been found, whereas the resistivity at low temperatures shows a slight increase. These results are similar to the reports of Fuchs et al. [202]. A simplified analysis using a single charge carrier type hints at a considerable

increase of the electron density by around 100% for 1.6 GPa, whereas the mobility of the charge carriers drops significantly to less than 50% compared to ambient pressure [135]. This increase of charge carriers at the interface has been found to be reversible up to ~ 2 GPa. Supporting *ab initio* calculations indicate that the discontinuity of the $LaAlO_3$ layer, accountable for a reduction of charge carrier density for ambient pressure, is reduced under pressure [135]. Furthermore, pressure decreases the dielectric parameters of both $LaAlO_3$ and $SrTiO_3$ and therefore defects and impurities are less screened, which hints to an enhancement of scattering processes and an effective decrease of the mobility.

After a review of the current state of research on magneto-transport in the $LaAlO_3/SrTiO_3$ interface, we analyze experimental data gained under hydrostatic pressure. This analysis involves multiband effects and WAL and goes beyond the simplified one-band picture used in Ref. [135].

3.2.1 Magneto-Transport up to Date

Transport in magnetic fields is a useful tool to investigate transport properties like two- or three-dimensionality [203], multiband behavior, or quantum corrections to the conductivity. Admittedly, magneto-transport in $LaAlO_3/SrTiO_3$ interfaces has been puzzling and the contradicting findings are heavily discussed in the literature [170]. In the following, we review some of the findings that are relevant for our data analysis.

Magnetic field out-of-plane

Hall measurements, as well as Shubnikov-de-Haas oscillations, have proven the presence of several kinds of charge carriers in the heterostructure [146, 151, 180, 181, 204–209]. A Lifshitz transition (see Ref. [210]) has been described in Ref. [193], where the electron system changes from one-band behavior to an effective two-band system when the electron sheet density exceeds the critical value of $n_c \approx 1.68 \times 10^{13} 1/\mathrm{cm}^2$. The multiband effect can be tuned via gate voltage [164].

As a second ingredient, spin–orbit coupling plays a dominant role at the interface. Beginning in 2010, WAL was identified in $LaAlO_3/SrTiO_3$ heterostructures by tuning through a large range of effective spin–orbit splittings with a gate voltage [95, 96, 158, 164, 211, 212]. For low electron density, negative magneto-resistance is found at the interface, indicating WL. By increasing the charge carrier density, the magneto-resistance curves become flatter and a WAL dip occurs. The maximum of this dip becomes more and more pronounced when the electron density is further increased. This has been interpreted as an effective spin–orbit field that grows strongly with gate voltage (and electron density), which is in agreement with multiband models. Interestingly, superconductivity seems to set in when the spin–orbit splitting reaches a maximum, which is at the Lifshitz point [193]. A precise understanding of WAL in these systems can therefore also hint to the mechanisms responsible for superconductivity. However, the WAL structure is often overlaid with the dominant multiband effects, prohibiting a simple analysis.

Regarding the multiband structure and the WAL, mainly two scenarios[3] are discussed in the literature [108] as a possible interpretation of the experimental data in $LaAlO_3/SrTiO_3$ heterostructures:

[3] As well as a quasi-one-dimensional scenario not discussed here [108].

- For low electron filling, only the lowest d_{xy} band is occupied. As this band can be described by an effective Rashba Hamiltonian, ILP-theory with single spin winding should provide good agreement with the data.
- If a higher filling is realized, transport is dominated by the d_{xz}/d_{yz} bands, and is described by a cubic spin–orbit splitting near the Γ point. The cubic Rashba effect has been discussed for interfaces of transition metal oxides as well as semiconductors [108, 108, 196, 213–215] and correspond to a triple spin winding at the Fermi surface.

So far, there has been no clear confirmation whether one of these two scenarios is actually realized. Furthermore, we stress that neither the cubic splitting nor the triple winding Hamiltonian provides a good approximation of the middle band pair of the six-band model and we strongly disagree with that proposal (see Sec. 3.1.3). However, a clear identification of the orbital nature of the charge carriers involved in transport would shed some light into the still debated origin of superconductivity in these systems [108].

Magnetic field in-plane

Transport measurements for a magnetic field parallel to the interface can be used to determine further insights into the material's properties. For example, Maekawa–Fukuyama theory predicts a positive magneto-resistance that saturates for higher fields [69] (see Sec. 2.1.2). On the other hand, electron–electron interactions also can produce a positive magneto-resistance in parallel as well as perpendicular field, in contrast to Maekawa–Fukuyama theory [216, 217] (see Sec. D.2). However, parallel magneto-resistance measurements at the $LaAlO_3/SrTiO_3$ heterostructure give a so far unresolved picture, and more questions have been raised instead of clear answers.

In many reports, the parallel magneto-resistance is negative and highly anisotropic. If the magnetic field has an out-of-plane component, magneto-resistance becomes positive immediately [203, 218–220]. In some reports, the magneto-resistance appears to be positive for small fields and becomes finally negative for higher fields [95, 211, 221]. This in-plane magneto-resistance effect has not been observed in non-polar $SrTiO_3$-based heterostructures and could be an effect of the special band structure of the heterostructure of the polar catastrophe scenario [222]. Indeed, the Lifshitz point seems to separate between different qualities of anisotropic behavior [223]. Explanations for this behavior in the literature vary from a coupling to local magnetic moments [224, 225] to Boltzmann theory with extended scatterers in the three-band model [218].

3.2.2 Multiband Weak Anti-Localization Analysis

After this review of magneto-transport reports in the recent literature, we apply the theories described in Chap. 2 in combination with a multiband treatment to analyze experimental data measured in the $LaAlO_3/SrTiO_3$ heterostructure under pressure. The samples have been grown and measured by Zabaleta in the group of Mannhart at the Max Planck Institute for Solid State Research in Stuttgart [9, 135]. The results of the analysis are published in Ref. [9]. Here, we seize the opportunity to discuss the analysis in detail.

The magneto-resistance has been measured for different pressures and temperatures in two different samples (Sample A, see Fig. 3.6, and Sample B). For ambient pressure, the Hall measurement (transversal magneto-resistance, R_{xy}) shows a strong multiband signal with

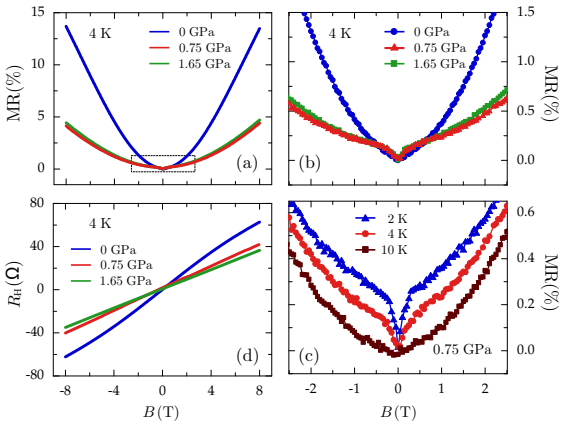

Figure 3.6: *Magneto-transport data obtained in Sample A.* Magneto-resistance (MR) shows a quadratic behavior in magnetic fields. The transversal resistance ($R_{\rm H}$ in the plot) is nearly linear with a small cubic contribution. Figure provided by Zabaleta; taken from Ref. [9].

linear as well as cubic contributions in the magnetic field dependence. Longitudinal magneto-resistance shows a quadratic upturn. Surprisingly, it is only under pressure that the multiband character becomes sufficiently suppressed to reveal the WAL contribution. Therefore pressure seems to be a useful tool to single out the multiband and WAL effects in these heterostructures.

In earlier reports on $SrTiO_3$ surfaces, where a similar response in magneto-transport has been found, the multiband Hall effect has been identified via the quadratic behavior in higher magnetic fields and has been treated as a background to extract a WAL contribution [196]. However, this is a biased evaluation, because it might be suitable for the assumption of triple winding spin–orbit coupling, but not for single winding, where the WAL magneto-response for larger magnetic fields is quite considerable, see Fig. 2.13. Instead, we develop a self-consistent separation of the multiband Hall contributions and the WAL correction in this section for the full measured magnetic field range.

Before discussing the results, we reflect the preconditions for the fitting procedure:

- We find directly in the data that the sheet Resistance $R_{\rm sh}$ grows quadratically with magnetic field. For small fields, a dip is visible, indicating a WAL contribution, see Fig. 3.6. The Hall resistance $R_{\rm xy}$ is approximately linear, but has a noticeable cubic contribution.

- Due to the quadratic upturn in the magneto-resistance and the cubic contribution in the Hall measurement, we use a multiband description for the Hall effect. We assume two efffective bands involved in transport. This also is the maximum number of bands that can be resolved using the information of constant, linear, quadratic, and cubic contribution in the magnetic field dependence, because two charge carrier densities, n_1 and n_2, as well as two mobilities, μ_1 and μ_2, are required as fitting parameters. The multiband Hall effect is expressed in the form

$$R_{\rm sh} = a_0 + a_2 B^2, \tag{3.14}$$

$$R_{\rm xy} = a_1 B + a_3 B^3. \tag{3.15}$$

- Regarding WAL, we find no indication for a four-band spin–orbit coupling with single winding spins (compare with Fig 2.19).

- Therefore, we assume that only one of the charge carrier types contribute to WAL. This introduces three additional fitting parameters, the inelastic scattering field $B_{\rm i}$, the single

winding field B'_{so} and the full field B_{so}, see Eq. (2.170). We leave it to the fitting to adjust single and triple winding spin–orbit coupling.

- We expect a single spin winding result in case the d_{xy} band dominates the WAL, see Eq. (3.12), and a mixture of single and triple spin winding if the d_{xz}/d_{yz} dominates the WAL, see Eq. (3.13).
- Unfortunately, as discussed before, the magneto-resistance in parallel field configuration is rather complicated and cannot contribute to a clearer picture in this heterostructure (see additional information in Ref. [9]).
- We neglect superconducting fluctuations in the analysis (see App. D.1), because the superconducting transition temperature, $T_c \approx 200\,\mathrm{mK}$ is an order of magnitude below the lowest temperature in the measurement.

The details of the fitting procedure are described in Sec. C.2. We find remarkable agreement with theory throughout the whole data range. Examples of fitting curves are shown in Fig. 3.7. First, we like to address the results for the WAL. In all fits, we find that $B'_{so} = 0$, and only B_{so} is finite. This relates directly to a spin–orbit coupling with triple spin winding at the Fermi surface. In fact, testing the simpler (HLN-like) formula Eq. (2.180), which results from triple winding spin–orbit coupling in the first place, we find fits can be achieved likewise, but no fits can be found using the single spin winding formula Eq. (2.191), as shown in Fig. 3.8. The fitted value for the spin–orbit field is $B_{so} \approx 0.2\,\mathrm{T}$ in both samples, even for different temperatures and pressures, see Fig. 3.9. The effective inelastic field is $B_i \approx 0.005\,\mathrm{T}$ for 2 K and $B_i \approx 0.015\,\mathrm{T}$ for 4 K, in agreement with the generally expected temperature dependence. Like it is the case for B_{so}, the values for B_i are very similar in both samples.

Next, we discuss the singled out multiband results. The Hall measurement shows directly that $a_1 > 0$ and $a_3 > 0$ for almost all curves. This already indicates the presence of two distinguished charge carrier types, where one is electron-like and the other is hole-like (see the discussion in Sec. C.1.3 as well as Sec. C.2.1). The self-consistent evaluation actually confirms one electron- and one hole-type charge carrier for all measured curves. The specific multiband parameters are shown in Fig. 3.10. We find that the density of the electron-like charge carriers increases by 170% at 1.13 GPa with respect to ambient pressure, whereas the mobility drops to 50% of its ambient pressure value, similar to the results of the simplified single-carrier analysis in Ref. [135]. The effect is opposite for the hole-like carriers, which have not been extracted before, and where the density drops strongly for even slight pressure.

Generally, in a multiband system, it matters which of the charge carriers introduces the WAL into magneto-transport. However, we show in Sec. C.2.2 that this effect is negligible in our case. Neither the multiband parameters nor the WAL parameters change qualitatively and the finding of holes is independent of the assignment of the WAL. Therefore, it remains open whether the electron- or hole-like charge carriers are affected by the strong spin–orbit coupling. However, is it reasonable that the high mobility electron-like charge carriers are linked to the WAL.

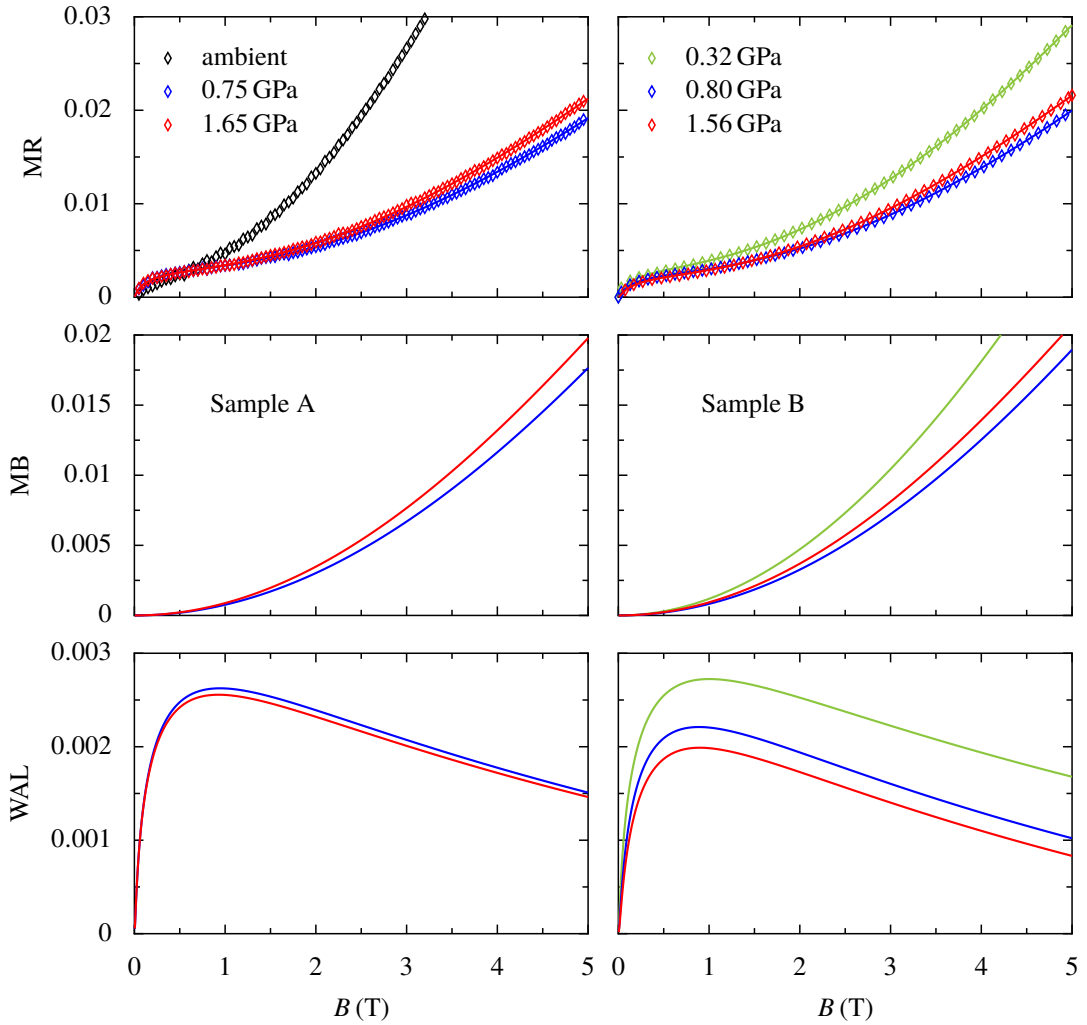

Figure 3.7: *Self-consistent fits for magneto-resistance (MR) in $LaAlO_3/SrTiO_3$ under pressure.* Some examples of the 2 K data are shown. We separate the multiband contribution (MB) from the WAL contribution in a self-consistent fitting procedure. Whereas pressure suppresses the multiband character (compare the black and blue curves for sample A), even higher pressures (red curve) lead to a small increase of the MR. The data in the samples A and B are very comparable. This figure is also partly shown in [9]; Data courtesy of Zabaleta.

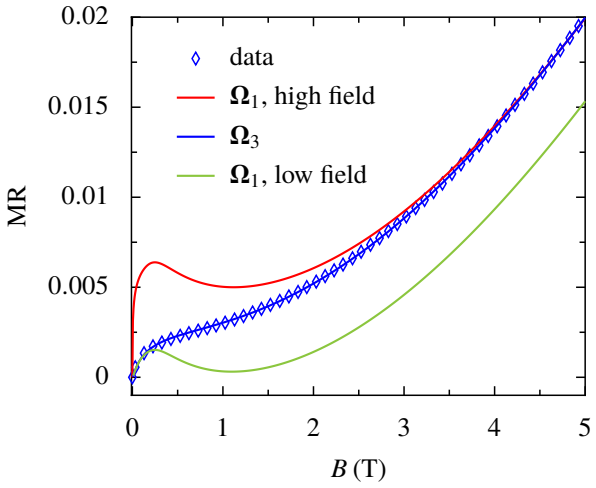

Figure 3.8: *Comparison of single and triple spin winding fits to experimental data.* We show as an example the results for sample B at 2 K and 0.80 GPa. Triple winding spin–orbit coupling Ω_3, using Eq. (2.180), is in good agreement with the experimental data for $B_\mathrm{i} = 6\,\mathrm{mT}$ and $B_\mathrm{so} = 0.2\,\mathrm{T}$ (blue). By using single winding Ω_1 and Eq. (2.191) with the same parameters for B_i and B_so, agreement is only found for low magnetic fields (green). On the other hand, the high field curve can be fitted using single winding, but the fit overshoots in the low field regime (red). For the single winding spin–orbit coupling, no choice of parameters allows to fit the data for all measured fields. This plot is also shown in Ref. [9]. Data courtesy of Zabaleta.

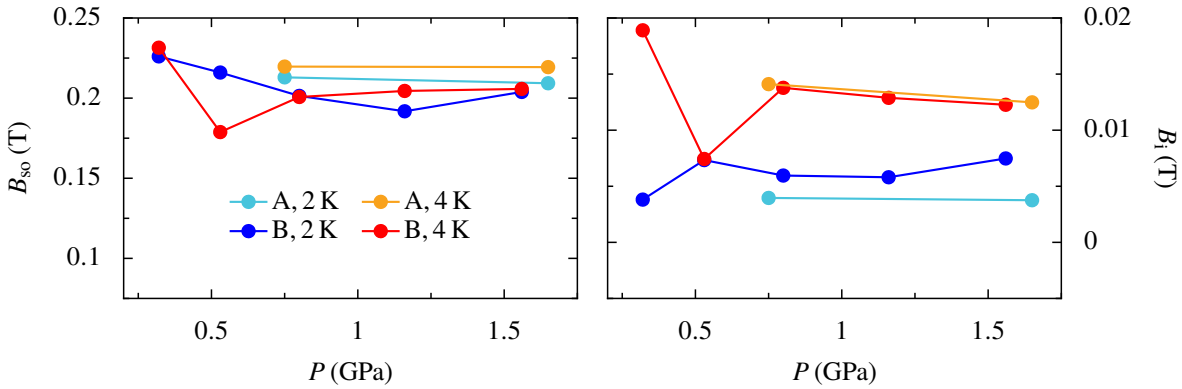

Figure 3.9: *Fitting results for WAL parameters.* In all fitted curves, the single winding field B'_so is zero. The parameter B_so, describing solely triple winding in this case, is finite and quite consistent for different samples, pressures and temperatures. The inelastic scattering field shows the expected temperature behavior (apart from one value of the 4 K measurement) and is also very similar in the two different samples. This plot is also shown in Ref. [9].

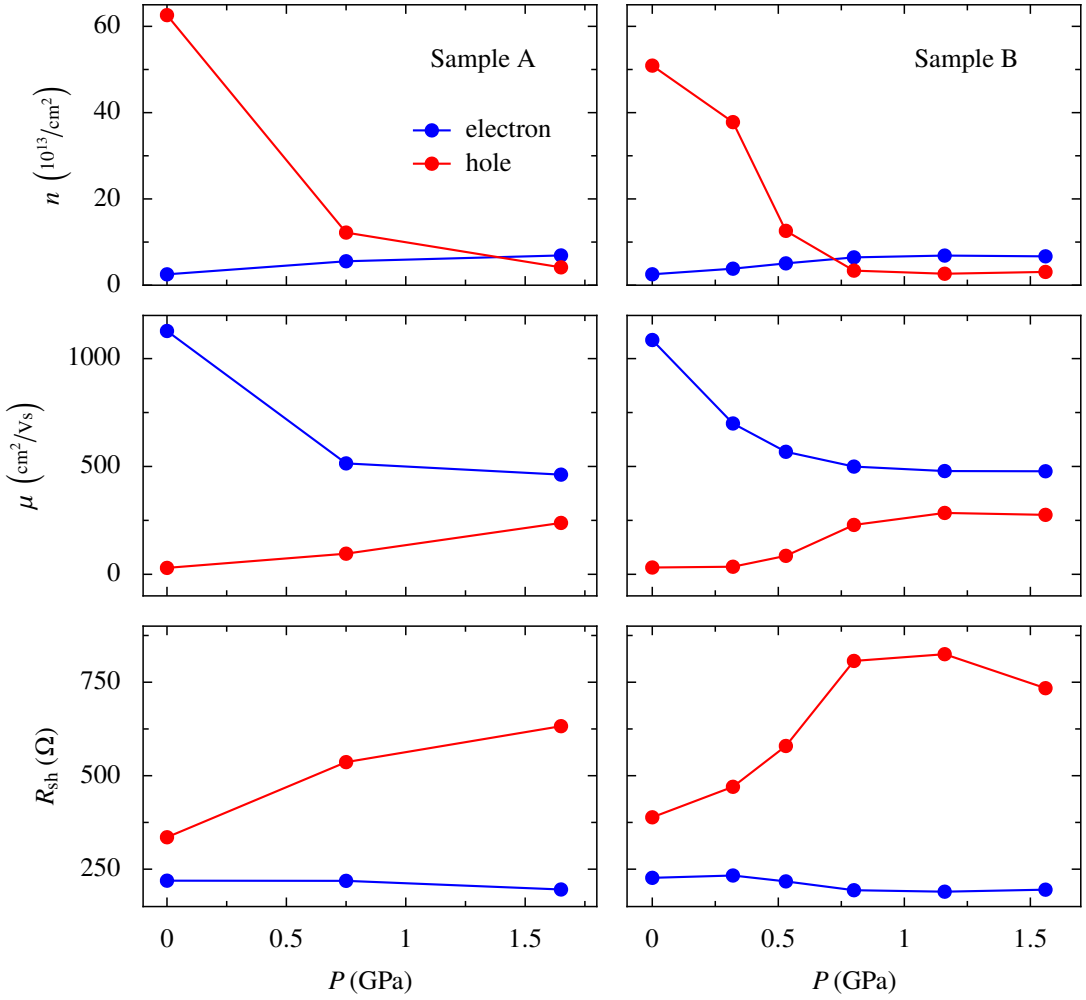

Figure 3.10: *Fitting results for the charge carrier densities n and mobilities μ.* The fitting procedure reveals one electron-like as well as one hole-like charge carrier type. The specific values for n and μ are comparable in both samples. Whereas the density of the electron-like carrier increases and the mobility decreases under pressure, the behavior is opposite for the hole-like charge carrier. The individual sheet resistance R_{sh} for each charge carrier on its own has a larger value for the hole-like charge carrier. This plot is also shown in Ref. [9].

In the following, we discuss how further attempts to explain the data without a of hole-like charge carrier can be ruled out. This discussion covers the anomalous Hall effect (AHE), electron–electron interaction and a negative curvature of the bands in the six-band model.

- *Anomalous Hall effect.* AHE (see Sec. D.3 for a general discussion) has been reported in several samples of $LaAlO_3/SrTiO_3$ [164, 223, 225]. It has an impact on the transverse conductivity, where it results in two linear regimes in the Hall signal for different magnetic field ranges. The slope of the second regime, when a hypothetical averaged magnetization saturates, must be smaller than in the low field regime. Such a signature can be clearly excluded in the data of samples shown here. However, in Ref. [225], an AHE has been found that increases not linearly in small fields, but with a larger power than one. In this special case, the slope of the low and high field regime are nearly the same, but the signature of the AHE shows up in an intermediate regime, where the curvature of the Hall signature changes. Therefore, this kind of AHE can create an effective positive cubic Hall contribution. However, we do not detect a change of curvature in the examined samples.

- *Electron–electron interaction.* In the following, we address the question of electron–electron interaction as a possible origin of the unusual magneto-transport (see Section D.2). Similar to the data presented here, Fuchs et al. found parabolic magneto-resistance for low temperatures and ambient pressure, and a much weaker signal under pressure, reminiscent of WAL. Therefore, these data are comparable with the data by the Stuttgart group.[4] The coexistence of the positive magneto-resistance as well as increasing resistance with lower temperature has been interpreted in terms of quantum corrections originating from interaction [202]. However, replacment of WAL with the interaction contribution in the fitting routine does not result in meaningful fits for the data. Instead, the puzzle of increasing resistance and the presence of WAL can be resolved within the multiband picture. One of the bands shows metallic behavior, while the other displays insulating behavior and might be localized at lower temperatures, which would be consistent with measurements by other groups [95, 158]. The combined measurement of both parallel channels then still provides an increasing resistance for lower temperatures.

- *Negative curvature.* Although the curvature of the bands in the six-band model becomes negative near the avoided crossings, see Fig. 3.3, this is no indication for the appearance of holes in the Hall effect. For the latter, the cyclotron mass, not the band mass is to be considered. The description of electrons and holes is completely equivalent, however, it is easier to consider the closed orbits, where the standard multiband equations, Eq. (C.13) and Eq. (C.14), result [227]. For the expected filling in the six-band model, all occupied states are electron-like and have to be described by closed orbits.

Finally, we discuss a possible error in the cubic Hall term, a_3. Although the relative error within the fitting procedure is less than a percent in all cases, a systematic error in the small cubic contribution is imaginable. In the following, we examine if such a systematic error in the cubic term can be responsible for the observation of hole-like charge carriers. For this purpose, we keep the values of a_1 and a_2 constant and change only a_3. The critical value, when the interpretation of electron–hole transport switches to electron–electron transport, is shown

[4] And also with the report by Lin et al. [226]. The latter, however, used HLN-theory to explain the data.

A	P (GPa)	T(K)	Δa_3 (%)	B	P (GPa)	T(K)	Δa_3 (%)	P (GPa)	T(K)	Δa_3 (%)
	0	2	12		0	2	14	0.81	2	362
		4	4			4	13		4	386
	0.75	2	180		0.32	2	26	1.16	2	286
		4	181			4	21		4	276
	1.65	2	511		0.53	2	135	1.56	2	351
		4	528			4	159		4	276

Table 3.1: *Hypothetical critical error in the cubic Hall parameter a_3 assuming electron–electron transport.* By keeping a_0, a_1, and a_2 in Eq. (C.13) and Eq. (C.14) konstant, we examine a hypothetical experimental error in a_3 assuming electron–electron transport instead of the actual extracted electron–hole transport. We find that for ambient pressure, the measurement is in the vicinity of electron–electron transport, but under high pressure transport is deep in the electron–hole regime.

in Table 3.1. For ambient pressure, the critical value for electron–electron transport is not inconsiderably far from the measurement, 12–14% at 2 K and 4–13% at 4 K. However, under pressure the sample clearly enters a different regime and electron–electron transport is far from interpreting the measurement consistently (see Fig. 3.11). For this reason, we argue that electron–hole transport is the reasonable explanation for the complete data set.

We conclude that the finding of holes is a stable result of the fitting procedure and cannot be easily linked to the standard six-band model. First of all, a surface hole band, predicted by *ab initio* calculations [228], has been observed in experiments only when a capping layer of $SrTiO_3$ is grown on the heterostructure [228, 229], which is not the case for the samples discussed here. Furthermore, the isotropic triple winding spin splitting only provides a description for the highest band pair, which has so far not been considered from the experimental side.

However, we like to mention an analysis by Lechermann et al., where a DFT+DMFT calculation including oxygen vacancies had been performed. These vacancies produce an e_g type band [230] that might appear hole-like for typical fillings at the interface [231]. Clearly, further investigations are necessary to resolve the nature of these hole carriers.

To close this section, we summarize the results from the fitting procedure:

- We find no indications for electron–electron interaction or an AHE in this data set.
- The data can be fitted remarkably well by a self-consistent treatment of WAL and the multiband Hall effect.
- The WAL is best described by a triple winding spin–orbit coupling. Although there have been reports about this result in the literature (see most recently, Ref. [232]), we disagree that it can be easily linked to the established six-band model of $LaAlO_3/SrTiO_3$.
- For ambient pressure, we find a low-density, high-mobility electron-like charge carrier and a low-mobility, high-density hole-like charge carrier.
- Under pressure, the WAL parameters do not change considerably, whereas the multiband parameters approach each other.
- Strong spin–orbit coupling and high electron densities, as well as the absence of electron–electron interactions, suggest a detectable sMIT in these materials.

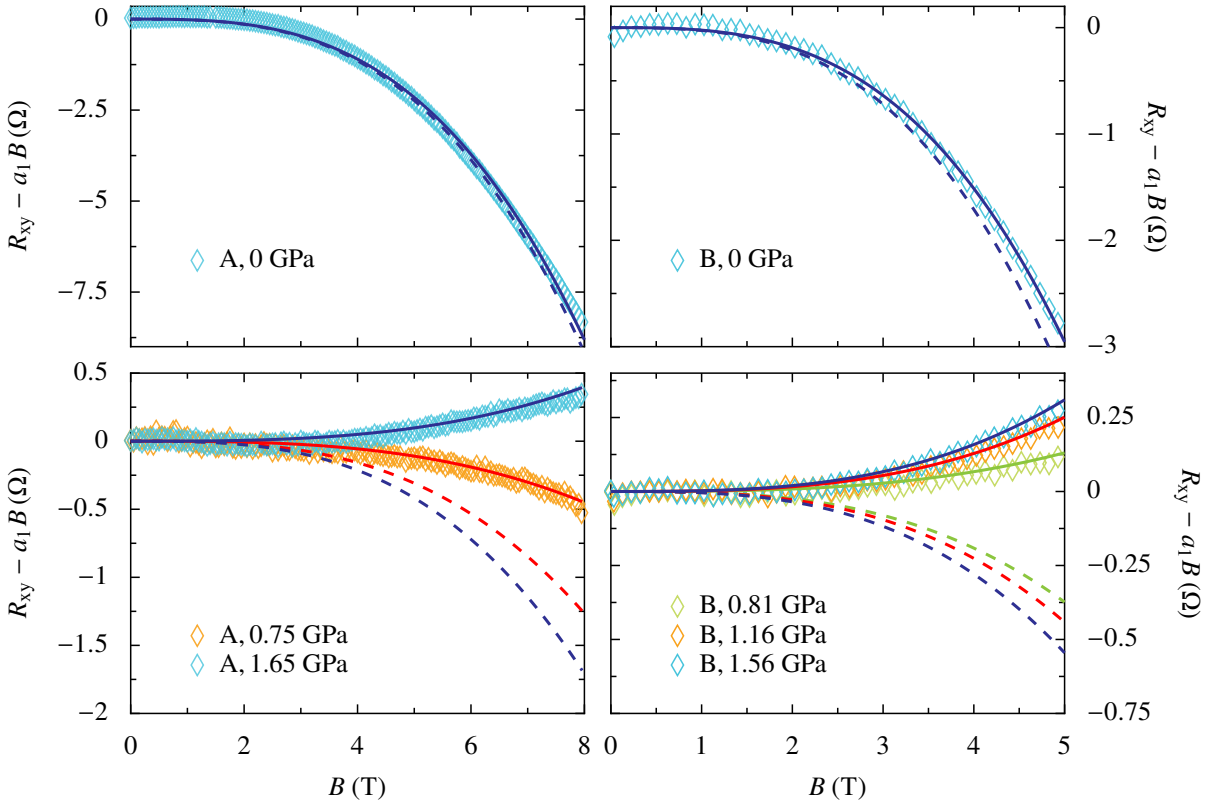

Figure 3.11: *Cubic contribution to the Hall signal.* Fits for the cubic contribution of the Hall signal are plotted as solid lines. We find the critical cubic contribution a_3 (dashed lines) by changing a_3 until the interpretation of electron–hole transport switches to electron–electron transport. Whereas for ambient pressure, the electron–electron regime could be brought in agreement with the measurement, the curves gained under pressure are far in the electron–hole regime. This figure is also shown in [9]. Data courtesy of Zabaleta.

3.3 Data Analysis II: Thin Films Based on Barium Oxides

Recently, a new type of two-dimensional oxide material has been investigated in the group of Hammerl at the Chair of Experimental Physics VI at University of Augsburg [136]. The samples, which provide the data shown in this thesis, have been grown and characterized by Meir [137]. These samples are created from thin layers of $BaPbO_3$ as well as bilayers of $BaBiO_3$ and $BaPbO_3$ on a $SrTiO_3$ substrate.

Charge density wave ordered bulk $BaBiO_3$ is not only a superconductor, but provides a topological insulating phase under electron doping, as found in *ab initio* calculations [233]. Also, bulk $BaPbO_3$ can be tuned to a topological metal under electron doping [234], and becomes superconducting under lead-doping with transition temperature above 20 K [235, 236]. Heterostructures of these materials have the great potential to bring together strong spin–orbit coupling, topology, and superconductivity along with the reduced symmetry of the interface.

In the following, we study the signature of strong spin–orbit coupling, incorporated by the heavy elements lead and bismuth, by analysis of magneto-transport in these samples. Details

on the growth of the samples are provided in the doctoral thesis of Meir [137]. Note that these first samples have not been structured for electric measurements, and the significance of the results from the fitting procedure is limited. However, structured samples have been grown quite recently by Bartel in the group of Hammerl [237], and will soon be in the focus of investigations regarding anti-localization [238].

3.3.1 Monolayer of $BaPbO_3$

First, we investigate magneto-transport data on the metallic $BaPbO_3$ monolayers on $SrTiO_3$. Magneto-transport data, see Fig. 3.12 (a), shows a clear signature of WAL: the magneto-resistance is positive for small magnetic fields and a maximum occurs at intermediate fields. The Hall resistance (not shown here) is linear [137], indicating a single charge carrier system with a high electron density. Due to the unstructured measurement, the sheet resistance, R_{sh}, is only known up to a geometrical factor f, which might depend on external parameters,

$$R_{\mathrm{sh}} = fR, \tag{3.16}$$

thus this factor has to be included as parameter in Eq. (C.14),

$$\frac{R(B) - R(0)}{R(0)} = \frac{1}{1 + fR(0)\Delta\sigma(B)} - 1, \tag{3.17}$$

where the magnetic field dependent quantum correction to the conductivity, $\Delta\sigma$, is given by the expression from ILP-theory. Fits are shown in Fig. 3.12 (a) and describe the experimental data very well. Exactly as in the $LaAlO_3/SrTiO_3$ case, the spin–orbit coupling is determined by triple spin winding at the Fermi surface, whereas the single winding contribution is zero. The geometrical factor is f =2.4±0.15 throughout the complete measured temperature range, see Fig. 3.12 (b). The spin–orbit field is given by $B_{\mathrm{so}} \approx 0.16\,\mathrm{T}$ throughout the temperature range, see Fig. 3.12 (b). Note that even for 20 K, the WAL signature is still clearly visible in the data.

To estimate the temperature dependence of the inelastic scattering rate, we assume $1/\tau_i \propto T^p$. In a log–log plot of the temperature dependent inelastic scattering field, see Fig. 3.12 (d), we identify two different temperature regimes. In each regime, we estimate the exponent p via

$$p = \frac{\ln\left(\frac{B_i(T_2)}{B_i(T_1)}\right)}{\ln\left(\frac{T_2}{T_1}\right)}, \tag{3.18}$$

and find $p \sim 1$ in the regime between 2 K and 6 K and $p \sim 1.75$ between 7 K and 20 K, in agreement with other two-dimensional systems (see Sec. 1.4.1). As will be discussed in Sec. 3.4, these samples of thin $BaPbO_3$ monolayers are of great interest for the sMIT, and further experiments in the near future are expected to be promising [10].

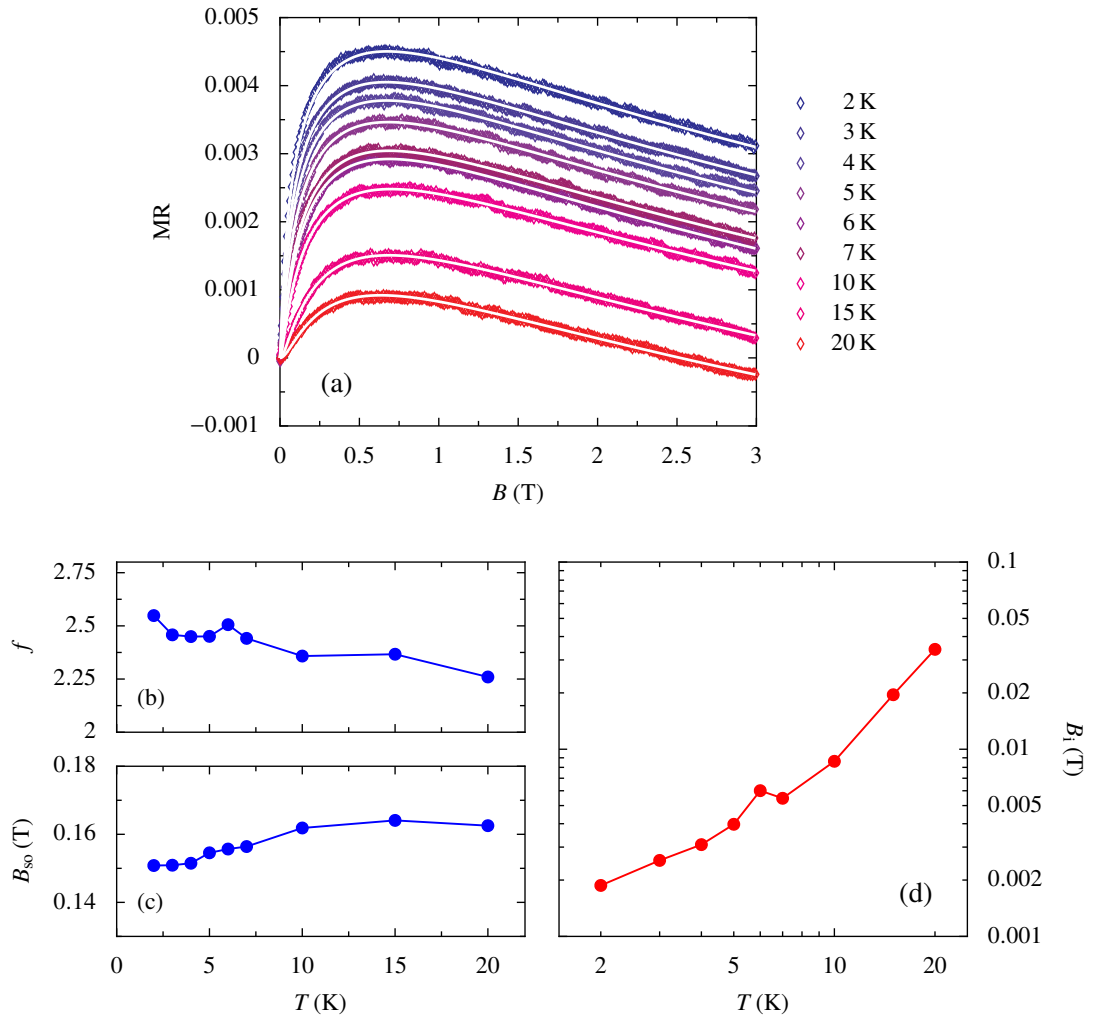

Figure 3.12: *Magneto-resistance in thin films of $BaPbO_3$.* (a) Fits using ILP-theory (white curves) are in good agreement with the experimental data. The spin–orbit coupling is characterized by triple spin winding, whereas the contribution from single spin winding vanish, similar to the $LaAlO_3/SrTiO_3$ data. (b) The fitted geometrical factor is $f = 2.4 \pm 0.15$ and very stable throughout all temperatures. (c) The parameter for the spin–orbit coupling, B_{so}, is also very stable for all temperatures. (d) By showing the inelastic scattering field, $B_i \propto T^p$, in a log–log plot, we determine the exponent $p \sim 1$ for temperatures between 2 K and 6 K and $p \sim 1.75$ above. Data courtesy of Meir [137].

3.3.2 Bilayers of $BaBiO_3/BaPbO_3$: First Glance

Bilayers of $BaBiO_3/BaPbO_3$ on $SrTiO_3$ (the stacking order is $SrTiO_3/BaBiO_3/BaPbO_3$) are much more intriguing than the monolayer. Quite remarkably, this kind of bilayer shows stress-induced two-dimensional superconductivity around $T_c \sim 3$–$4\,\mathrm{K}$ [136]. Near the transition temperature, magneto-transport is expected to be controlled by superconducting fluctuations, besides the WAL, induced by the strong spin–orbit coupling of bismuth.

The magneto-resistance (see Fig. 3.13) for small fields is positive, and shows a faint maximum at intermediate magnetic fields, which is a hint for WAL. However, the amplitude of the positive magneto-resistance grows strongly with decreasing temperature, which cannot be explained by WAL alone, but reminds of Maki-Thomson superconducting fluctuations (the relevant superconducting fluctuations are discussed in more detail in Sec. D.1). Hall measurements indicate a single charge carrier picture with high electron density [137]. Like the monolayer samples discussed in the last section, the bilayers are unstructured, and the geometric factor f has to be adapted in the fitting.

First, we neglect the superconducting fluctuations and fit the magneto-resistance with ILP-theory for adjusted geometric value f^{MR}. Although the fitting curve agrees well with the data, see Fig. 3.13 (a), the values for f^{MR} deviate considerably. The factor is $f^{\mathrm{MR}} = 2.4$ for 8 K, but is enhanced continuously up to $f^{\mathrm{MR}} = 6.7$ at 5 K. A similar sample (not shown here) confirms this effect. As the zero-magnetic-field value of the resistance does not change more than $\sim 2\%$ throughout the same temperature range, this scenario seems to be very unlikely despite the convincing fits. Still, the higher temperature fits might be valid, because superconducting fluctuations are small in this case. Furthermore, the value for the geometric factor is similar than in the metallic monolayer sample, which is produced under similar conditions (see Sec. 3.3.1).

The vicinity of the superconducting transition causes further quantum corrections appearing in magneto-transport (see Sec. D.1). We analyze the temperature dependence of the resistance in order to examine the parameters for the superconducting fluctuations. Both, WL, Eq. (2.42), as well as WAL, Eq. (2.44), cause a logarithmic temperature dependence in the conductivity. However, the prefactors in the WL and WAL formulas include a different sign. On the other hand, Coulomb interaction in the diffusion channel (ID) also enters in the temperature dependence via a logarithmic term [239], and the consideration of all three effects results in an effective fitting formula

$$\delta\sigma^{\mathrm{WL/WAL+ID}} = \frac{e^2}{\pi h} a' \ln\left(\frac{T}{T_o}\right), \tag{3.19}$$

where T_o is an effective temperature scale determined by elastic scattering and

$$a' = (ap + C) \tag{3.20}$$

where in case of WL, $a = 1$, in case of WAL $a = -1/2$, and the exponent of the temperature dependence is of order $p \approx 1$–2. The Coulomb contribution in the diffusion channel is considered to be of order unity.

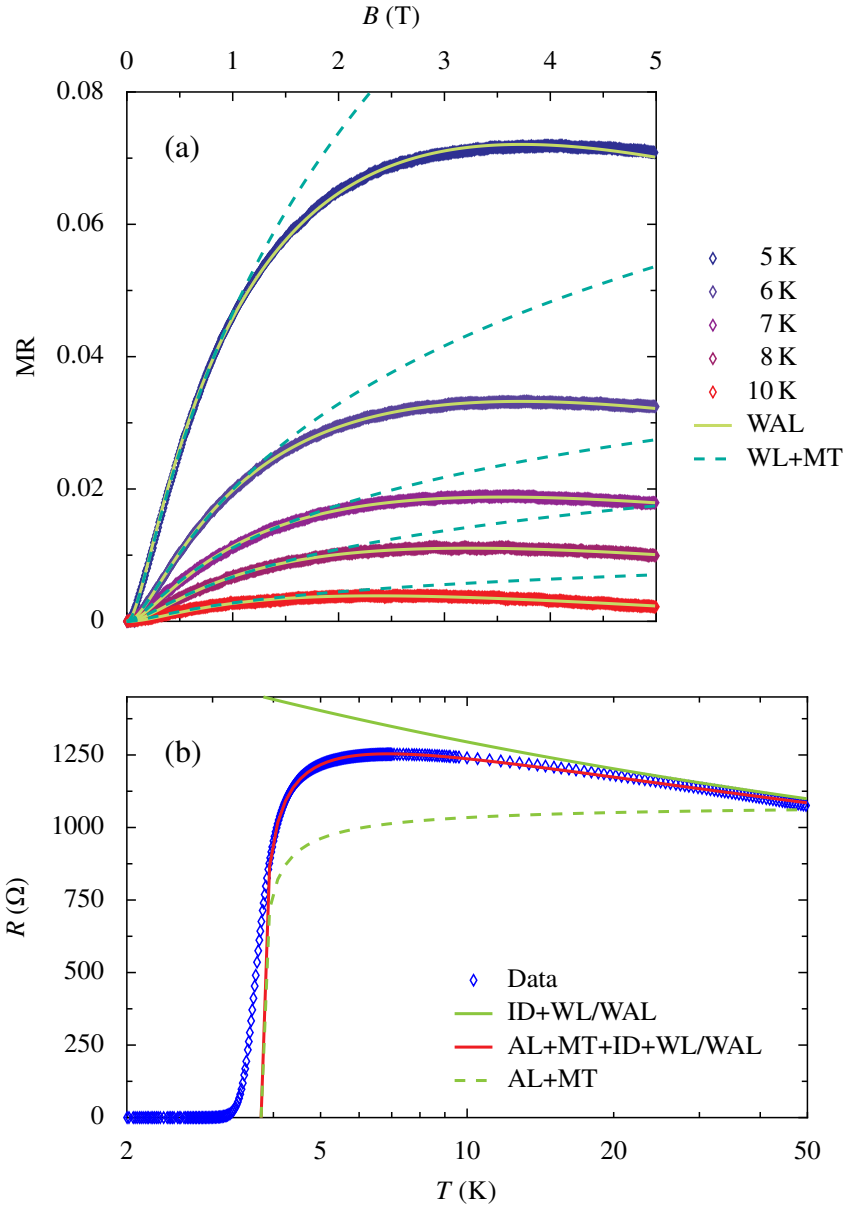

Figure 3.13: *Magneto-resistance and temperature dependent resistance in thin bilayers of $BaBiO_3/BaPbO_3$.* (a) Magneto-transport can be well fitted with WAL (solid curves). However, the geometrical factor f^{MR} in this case deviates from $f^{\mathrm{MR}} = 2.4$ at high temperatures to $f^{\mathrm{MR}} = 6.7$ for the 5 K measurement. Considering the superconducting transition temperature $T_c = 3.77$ K from the $R(T)$ curve, fits using weak localization (WL) and Maki–Thompson fluctuations (MT) lead to good agreement in low fields below 1 T, but deviate considerably for higher magnetic fields. (b) The temperature dependence of the resistance can be well described by a combination of superconducting fluctuations (AL and MT) and the logarithmic term containing WL or WAL as well as interaction in the diffusion channel (ID). However, the geometric factor in this plot is $f^{\mathrm{T}} = 0.32$ and is not in agreement with the value from the MR fit. For $T < T_c$, a BKT transition takes place [136]. Data courtesy of Meir [137].

The temperature dependent contribution of superconducting fluctuations is described by Aslamazov–Larkin (AL) and Maki–Thomson (MT) fluctuations[5] (see Sec. D.1)

$$\delta\sigma^{\mathrm{AL+MT}} = \frac{e^2}{\pi h}\left[\frac{\pi^2}{8\ln\left(\frac{T}{T_\mathrm{c}}\right)} + \frac{\pi^2}{4\left(\ln\left(\frac{T}{T_\mathrm{c}}\right) - \delta_\mathrm{MT}\right)}\ln\left(\frac{\ln\left(\frac{T}{T_\mathrm{c}}\right)}{\delta_\mathrm{MT}}\right)\right], \tag{3.21}$$

where

$$\delta_\mathrm{MT} = \frac{e^2}{h}\frac{\pi f R_0}{8}\ln\left(\frac{h}{e^2}\frac{1}{2fR_0}\right). \tag{3.22}$$

We follow the description in Ref. [239] and use the reference resistance value $R_0 = R(50\,\mathrm{K})$ as reference, where it is assumed that all quantum contributions are zero. The fitting formula for the temperature dependent resistance is given by

$$R(T, \left\{T_\mathrm{c}, f^\mathrm{T}, a', T_0\right\}) = \frac{1}{\frac{1}{R_0} + f^\mathrm{T}\left[\delta\sigma^{\mathrm{AL+MT}}\left(\left\{T_\mathrm{c}, f^\mathrm{T}\right\}\right) + \delta\sigma^{\mathrm{WL+ID}}\left(\{a', T_0\}\right)\right]}, \tag{3.23}$$

The fitting values are given by

$$T_\mathrm{c} = 3.77\,\mathrm{K}, \tag{3.24}$$

$$f^\mathrm{T} = 0.32, \tag{3.25}$$

$$a' = 21.67, \tag{3.26}$$

$$T_0 = 63\,\mathrm{K}. \tag{3.27}$$

The best fit is shown in Fig. 3.13. The values for a', f^T and T_c are very stable: they do not differ considerably when the reference value R_0 is changed. However, the variable f^T deviates considerably from the value f^MR.

In the following, we discuss the results of the $R(T)$ and MR(B) fits:

- A WAL fit with triple winding spin–orbit coupling is in good agreement with the magneto-resistance data, when the geometric factor is allowed to change between $f^\mathrm{MR}(10\,\mathrm{K}) = 2.4$ and $f^\mathrm{MR}(5\,\mathrm{K}) = 6.7$. The 10 K value is similar to the value in the monolayer samples that are produced under comparable conditions (see Sec. 3.3.1).

- The value for T_c in the $R\,(T)$ fit is slightly larger than the temperature of the Berezinskiĭ–Kosterlitz–Thouless transition T_BKT reported in Ref. [136], as is expected:

$$T_\mathrm{c} \approx 3.77\,\mathrm{K} > 3.23\,\mathrm{K} \approx T_\mathrm{BKT}. \tag{3.28}$$

- Apparently, the fitted geometric factor from the magneto-transport measurement and from the $R(T)$ curve, $f^\mathrm{T} = 0.32$, do not agree. This issue should be solved by measurements in a structured sample, where the geometric factor is fixed.

- The value for a' in the $R(T)$ fit seems to be rather large, but the prefactor for the WL term is given by $fa' = 6.93$, which is reasonable. If we assume that $f = 2.4$, we find $a' = 2.89$, a value that would be composed from WL ($a = 1$), the temperature coefficient $p \approx 1 - 2$ and the ID contribution $C \approx 1$. However, by keeping the value $f = 2.4$ fixed during the fitting process, no useful fits can be produced for the $R(T)$ curve.

[5] Note that Eq. 3.21 is in agreement with [88, 240, 241], but not with [242], where δ_MT is replaced by $\delta_\mathrm{MT}T/T_\mathrm{c}$. However, the fitting results do not deviate considerably between these two versions, because this contribution will only become noticable at $T \sim T_\mathrm{c}$.

- When the $T_c = 3.77\,\mathrm{K}$ is used in a MT correction for magneto-transport (AL fluctuations are neglected for 5 K and above), the resulting amplitude is much larger than the measured signal. We stress that WAL as well as interaction would increase the positive magneto-resistance even further. WL results in a negative magneto-resistance and is the only combination with MT fluctuations to explain the data. However, this combination can only fit the data for weak magnetic fields below 1–2 T, and the negative slope of the curve for higher fields cannot be captured.

Apparently, the fits of $R(T)$ and $R(B)$ are not in agreement with each other for the bilayers. From the above evaluation we conclude that WAL gives the best explanation for the magneto-transport data, when the geometric factor is allowed to change with temperature. Maki–Thomson fluctuations are expected in magneto-transport, but their amplitudes seem to be smaller than expected for this temperature range.

For future projects, structured samples grown by Bartel will be examined to narrow down interfering effects [238]. Possibly, also electron–electron interaction has to be considered. On the other hand, also the combined theory of spin–orbit coupling and superconductivity for these materials should be revisited.

3.4 Symplectic Transition in Oxide Heterostructures

The theory of scaling, as shown in Sec. 1.3.2 and Sec. 1.3.3, is a one-particle theory. In the 1980s, Finkel'stein [243, 244] and Castellani et al. [245] included electron–electron interaction into the renormalization equation of the non-linear σ-model. Contrary to the expectation that interaction will have no qualitative influence on the scaling arguments, it has been found that interaction in a weakly disordered system can overcome localization, indicating a metallic state at low temperatures. However, this perturbative approach breaks down for too low temperatures and the interaction strength in the spin-triplet channel diverges. This has been interpreted as a magnetic instability [246], and the metallic state at low temperatures has not been taken seriously at that time.

Therefore it came as a surprise when a MIT in two dimensions actually has been observed in experiment. In 1994, Kravchenko et al. discovered a MIT for the electron liquid in Si-MOSFETs [247–249] (for a review see [4]). By applying an external electric gate field, the electron density in the two-dimensional plane is tuned, what in turn changes the screening of the charge carriers, and with it, the interaction strength. The latter can be estimated via the Wigner–Seitz radius $\langle r \rangle$ in two dimensions, which is found by considering the mean area per particle, $n \langle r \rangle^2 \pi = 1$, where n is the sheet density. The dimensionless Wigner–Seitz radius r_s is defined by [4]

$$r_s = \frac{1}{a_B^* \sqrt{\pi n}}, \tag{3.29}$$

where a_B^* the Bohr radius of the semiconductor, which is given by

$$a_B^* = \varepsilon_r \left(\frac{m_e}{m} \right) a_B, \tag{3.30}$$

where ε_r is the relative permittivity, m_e is the free electron mass, m is the effective mass and a_B is the Bohr radius. The Wigner-Seitz radius r_s can be expressed as [4]

$$r_s \propto \frac{\varepsilon_C}{\varepsilon_{kin}}, \tag{3.31}$$

because in two dimensions, $\varepsilon_{\text{kin}} \propto n$ and $\varepsilon_{\text{C}} \propto {}^{e^2}/_{\langle r \rangle} \propto \sqrt{n}$.

The ultra clean Si-MOSFETs allow measurements for charge carrier densities as low as $n = 10^{11}\ {}^{1}/_{\text{cm}^2}$, where screening of Coulomb interaction is weak. Estimations for these systems yield $\varepsilon_{\text{C}} \approx 10\,\text{meV}$, whereas the Fermi energy $\varepsilon_{\text{F}} \approx 0.6\,\text{meV}$. As a result, these samples actually comprise a strongly correlated electron liquid with a Wigner–Seitz radius $r_{\text{s}} \approx 10$ rather than an electron gas [4].

Kravchenko et al. have found scaling behavior on both sides of a MIT. This scaling behavior does not obey a scaling law as described by Eq. (1.38) and shown in Fig. 1.8, but rather shows a temperature dependent separatrix. To explain the experimental data, Punnoose and Finkel'stein considered a two-parameter scaling theory in the early 2000s, where one scaling parameter corresponds to disorder, the other to electron–electron interaction [250, 251]. It has turned out that valley degeneracy, a common phenomenon in semiconductors, is crucial for the finding of a reasonable solution. The above mentioned magnetic instability becomes suppressed very fast by the number of valley degeneracy. The double degenerate valleys in silicon seem to be sufficient to explain the experimental data in terms of the two-parameter scaling theory without any fitting parameters [252, 253]. The experimental data is also in agreement with many other interacting two-dimensional systems like SiGe, AlAs, and GaAs/AlGaAs heterostructures [4].

A magnetic field leads to a considerable change of the transition properties. The magnetoresistance enhances sharply with the magnetic field and saturates when the spins in the system are fully polarized [254–256]. In this regime, the MIT is suppressed and the sample is insulating [254, 257, 258]. Also, in the vicinity of the MIT, an increase of the spin susceptibility is found [259–261]. This increase seems to be only dependent on the interaction strength r_{s}, and not on the effective mass, or the disorder [262]. This has also been interpreted as evidence that this MIT is purely interaction driven.

So far, the MIT observed in two-dimensional semiconducting devices has been interpreted successfully in terms of the interaction driven metallic state. What about identifying the spin–orbit driven sMIT? In oxide materials, spin–orbit is relatively strong and the electron densities are rather high: in $LaAlO_3/SrTiO_3$ heterostructures, electron density range between $n \sim 10^{13}\ {}^{1}/_{\text{cm}^2}$ and $n \sim 10^{14}\ {}^{1}/_{\text{cm}^2}$. To estimate the Wigner-Seitz radius in analogy to semiconductors, we use the relative permittivity, which is $\epsilon_{\text{r}} \sim 5$–$15$ for low temperatures, and for the effective mass we have ${}^{m^*}/_{m_e} \sim 0.41$ for the light xy-type charge carriers. For the low electron densities, $r_{\text{s}} \approx 2$ is still comparable to that in Si-MOSFETs. However, we find $r_{\text{s}} < 1$ already for slightly higher fillings even still below the Lifshitz transition. In this case, the sMIT might be observable.

In fact, a MIT has been observed in $LaAlO_3/SrTiO_3$ heterostructures by tuning of electron density [148, 212, 263]. Beyond a critical density n_{c}, ohmic electric transport has been confirmed. Below n_{c}, conductivity sets in only above a threshold voltage in the electric field, which grows approximately linear with the distance from n_{c} [212]. However, a sMIT has not been confirmed to far in this heterostructure.

We recommend the following procedure, following the investigations in semiconductors: critical behavior in potential devices can be confirmed with the scaling law Eq. (1.38), see Fig. 1.8. Instead of disorder strength $(W_{\text{c}} - W)$, the reduced density $(n - n_{\text{c}})$ can be used as a control parameter by changing the gate voltage. For low temperatures (considerably below 1 K), resistance curves should fall into two classes above and below a critical electron density. If the separatrix of critical density is temperature independent, the data is described by a one-parameter scaling theory, in contrast to the interaction driven MIT in Si-MOSFETs, where the separatrix is strongly temperature dependent. Furthermore, we expect that the spin susceptibility and a parallel magnetic field will not play the roles that they do in the

interaction driven phase transition. We recommend to search for the sMIT in two-dimensional oxide materials at even lower temperatures then before, using pressure, and/or gate voltage as control parameter. Corresponding samples as well as experiments are expected soon, provided by the group of Hammerl [10].

Summary of Chapter 3

I have applied the theoretical results on WAL, described in detail in Chap. 2, to the analysis of magneto-transport data obtained in three different two-dimensional electron systems in oxide materials:

- heterostructure of $LaAlO_3/SrTiO_3$,
- monolayer of $BaPbO_3$ (on $SrTiO_3$),
- bilayer of $BaPbO_3/BaBiO_3$ (on $SrTiO_3$).

The $LaAlO_3/SrTiO_3$ heterostructure, widely discussed in the literature, often shows multiband behavior along with WAL signatures in magneto-transport. Hydrostatic pressure, used by our collaborators [9], leads to a significant exposure of the WAL contribution. In my self-consistent data analysis, I find WAL that is assigned to a triple spin winding at the Fermi surface, consistent with reports in the literature based on cruder fitting routines. Furthermore, the multiband evaluation reveals an unexpected hole-like charge carrier type. Both findings are very robust, but cannot be resolved within the standard six-band model for the $LaAlO_3/SrTiO_3$ interface. Future investigations are necessary to solve this issue.

The analysis of the $BaPbO_3$ monolayer sample reveals single-band behavior and a clear signature of WAL in magneto-transport. Like in $LaAlO_3/SrTiO_3$, the corresponding spin–orbit coupling has triple spin winding at the Fermi surface. I propose a detectable sMIT—never been observed so far—for this material on account of the higher charge carrier density compared to semiconductor quantum wells. This results in a better screening of electron–electron interaction effects and rules out the interaction driven MIT.

Evaluation of the data on $BaPbO_3/BaBiO_3$ bilayers have not yet lead to solid conclusions. The vicinity of the superconducting transition introduces fluctuations, which cannot be simply included into the WAL fitting. Further experimental and theoretical investigations will help to understand this exciting new material.

4 Conclusion and Outlook

In the conclusion of my thesis, I like to address the questions that motivated this project in the first place. I give decisive answers to several of these questions, but I have also found many further interesting questions, raising in progress of this thesis. I emphasize that the theoretical work regarding the analysis of magneto-transport data goes hand in hand with the experimental investigations of our collaborators. This has given me the opportunity to discuss recent data and contemplate upcoming steps for further experiments jointly.

The central topic of this thesis is the disordered two-dimensional electron system in oxide materials with strong spin–orbit coupling. I have discussed the two limiting cases of weak disorder, related to weak anti-localization (WAL) as well as strong disorder, providing a symplectic metal–insulator transition (sMIT). The following questions have been pursued in this thesis:

- *What are the characteristics of WAL in two dimensions?* The well known weak localization, formulated in diagrammatic perturbation theory for disorder, results in a reduction of conductivity, induced by self-interference of scattered charge carriers. Under consideration of spin–orbit coupling, the same self-interference leads to the contrary effect of WAL. Hikami–Larkin–Nagaoka-theory involves Elliott–Yafet spin relaxation, where spin-flips take place at scattering events, and which is permitted even when the spatial inversion symmetry is not explicitly broken. This theory has already been discussed in more recent textbooks. However, the WAL theory for the D'yakonov–Perel' relaxation, where the spin–orbit coupling is incorporated in the kinetic term of the Hamiltonian, is less known. This theory has been established by Iordanskii, Lyanda-Geller and Pikus for electron systems where the spatial inversion symmetry is broken. Remarkably, even if the microscopic pictures of these theories are very different, the qualitative results are comparable: the resistance is decreased by the spin–orbit coupling, and magneto-transport in perpendicular field is positive for small fields as well as negative when the external field becomes considerably stronger than the spin–orbit coupling effect. However, the dispersive spin–orbit coupling leads to distinct quantitative results when the spin winding number around the Fermi surface is one or three. For a threefold winding, the result is similar to the spin scattering scenario. For single spin winding, the amplitude of the magneto-resistance is much more pronounced. I emphasize that the dispersive spin–orbit coupling provides the correct description for the observed WAL in oxide heterostructures, because the spin–orbit scattering scenario produces no WAL signature for magneto-transport in two-dimensional systems.

- *What are the characteristics of the sMIT in two dimensions?* The sMIT is described by a one-parameter scaling theory (which is given by the disorder strength) and is characterized by a critical exponent of $\nu \approx 2.75$. Unlike the three-dimensional case, the conductivity does not vanish at the transition, but is given by a finite critical value. It should be possible to confirm the sMIT in a measurement of the temperature dependent conductivity for different values of some control parameter, assuming that the material really obeys the

one-parameter scaling theory. Control parameters, amongst others, can be charge carrier density (controlled by an external gate field) or hydrostatic pressure.

- *Can we understand the unusual magneto-transport in $LaAlO_3/SrTiO_3$ heterostructures?* Partly. Magneto-transport for magnetic fields parallel to the interface is still poorly understood. However, I have shown that magneto-transport data for the perpendicular magnetic field configuration can be fitted very well by considering a multiband Hall effect along with WAL in a self-consistent analysis to separate the two very diverse effects. This self-consistent procedure goes beyond the analysis in the recent literature and is unbiased regarding different microscopic mechanisms for the spin–orbit coupling. The detailed analysis of the two effects actually leads to more specific questions, which I address in the following.

- *What microscopic mechanism controls WAL in two-dimensional oxides?* The multiband WAL theory that I developed results in a magneto-transport signature that is distinguishable from the single band theory only for dominant single winding spin–orbit coupling. However, this particular signature is not detected in the data set discussed in this thesis. Therefore, I have used a dispersive spin–orbit coupling for only one effective band pair in the fitting procedure. These fits are in remarkable agreement with the data from the $LaAlO_3/SrTiO_3$ heterostructure, as well as the $BaPbO_3$ monolayer, and show very clearly that the WAL is exclusively generated by a triple winding spin–orbit coupling. This result is in agreement with earlier reports on the $LaAlO_3/SrTiO_3$ heterostructure based on cruder fitting routines, and is now confirmed in my self-consistent analysis. However, the triple spin winding interpretation disagrees with common effective band models for $LaAlO_3/SrTiO_3$, where single spin winding is dominant for realistic fillings—this issue has to be investigated in the future. The same triple spin winding result for the $BaPbO_3$ monolayer is a new finding and identifies the strong spin–orbit coupling in this material.

- *How to construct a more realistic WAL model for complicated multiband systems like in the $LaAlO_3/SrTiO_3$ heterostructure?* I extended WAL for dispersive spin–orbit coupling by derivation of the magneto-resistance for a spin-$^3/_2$ Hamiltonian. This model describes a spin-split four-level system that can be related to conventional spin and additional pseudo-spin index, introduced by a second band pair. I found that the response in case of a triple spin winding at the Fermi surface is very similar to the corresponding single band pair results and does not permit a distinctive decision regarding the number of involved bands. The single spin winding case, on the other hand, introduces an additional structure in the magneto-response. It is an open question how to further generalize the spin-$^3/_2$ Hamiltonian to more advanced four-level Hamiltonians and still allow for an analytical solution of the Cooperon equation. A numerical approach that calculates the WAL for the six-band model of $LaAlO_3/SrTiO_3$ directly still has to be tested.

- *What is the orbital character of charge carriers involved in magneto-transport at the $LaAlO_3/SrTiO_3$ heterostructure?* Strikingly, this is not known for the data set presented in this thesis. I expected to find two different kinds of electron-like charge carriers, which can be assigned to the d_{xy} and d_{xz}/d_{yz} charge carriers of the established six-band model of $LaAlO_3/SrTiO_3$. My finding, however, is fundamentally different: within the standard multiband Hall effect scheme, an irrevocable result for the $LaAlO_3/SrTiO_3$ samples is the existence of one high-mobility, low-density electron-like charge carrier, as well as

one low-mobility, but high-density hole-like charge carrier. I stress that this result is independent of different pressures and temperatures used in the experiment. The origin of these hole-like carriers is not yet settled, nor is the orbital character of the electron-like charge carrier.

- *Why has the sMIT not been observed in experiments yet?* During the 1990s, a metal–insulator transition was actually identified in two-dimensional semiconductor devices. This MIT shows behavior controlled by a two-parameter scaling theory, instead of the one-parameter scaling theory of the sMIT. This transition is found for very low charge carrier density and has been tracked down to be disorder as well as interaction driven, because electron–electron interaction is only poorly screened for this case. So far, all devices showing a MIT have been allocated to the two-parameter transition. Apparently, spin–orbit coupling has been too weak and electron–electron interaction too strong to observe the sMIT in semiconductor devices.
- *Can we expect the sMIT to be observed in two-dimensional electron systems of oxide materials?* Yes. Electron densities are much higher in oxide materials as they are in semiconductor quantum wells, and the screening of electron–electron interaction is much stronger. Paired with the very strong spin–orbit coupling of the involved materials, the sMIT cannot be ruled out by a simple interaction strength argument. Instead, I propose the sMIT to be realized in two-dimensional oxide materials.

Beyond this thesis, there are several directions where to take this project in the near future:

- *Experimental realization of the sMIT.* Several samples of low dimensional oxide materials are grown now in our group in Augsburg to search for the signature of the sMIT [10]. On the other hand, also recent developments regarding artificial lattices with cold atoms give cause to hope for a discovery of the sMIT.
- *Understanding the WAL in complicated multiband models.* Golub and Glazov expanded the theory of WAL to the ballistic regime, where a modified Cooperon allows for corrections due to closed paths with only very few (like three) scattering events [264–266]. This theory has successfully been used to fit experimental data in high mobility samples [266–270]. Based on this approach, a numerical simulation for WAL has been suggested recently [271]: By modeling a random walk in two dimensions, a high amount of self-intersecting paths is created. Along each of these paths, the particle propagates between collisions with the corresponding Hamiltonian, time step after time step. By following these paths and their time-reversed counterparts, the WAL contribution to the conductivity can be simulated for an arbitrary Hamiltonian. So far, it is an open question whether this numerical investigation is applicable for the six-band model of the $LaAlO_3/SrTiO_3$ heterostructure, but this would provide a clear answer whether this effective model is sufficient for a correct description of magneto-transport. In this respect, it will also be very interesting in general to test the universality classes for multiband systems.
- *Explanation for the observed hole band in $LaAlO_3/SrTiO_3$.* The origin of the hole band, which I have identified in the analysis of magneto-transport in $LaAlO_3/SrTiO_3$, still lacks an explanation. I like to address two scenarios that are currently actively pursued in

our group to provide an answer to that issue. The first scenario involves an evaluation of the conductivity in the $LaAlO_3/SrTiO_3$ six-band model in magnetic field by exact diagonalization, investigated by Lettl [272]. First results hint to interesting hole features even far below half filling. Another scenario involves oxygen vacancies that enable hole-like e_g states near the Fermi surface, as described first by Lechermann et al. in 2014 [231]. Recent investigations indicate that this scenario also can explain the observed hole band.

- *Strong spin–orbit coupling in strongly correlated systems.* Recently, those systems have attracted considerable interest where spin–orbit coupling and electronic correlations are of likewise importance. These systems cannot be classified by the conventional symmetry considerations based on the single-particle description. This topic relates to the physics of correlated topological systems, as well as many-body localization [273–275], where the inclusion of spin–orbit coupling will be definitely fascinating.

I emphasize that research on low-dimensional oxide materials with strong spin–orbit coupling will certainly provide exciting physics also in the near future.

A Disordered Electronic System

Contents

In this appendix, we examine the impact of disorder in one-particle Green's functions as well as in particle–hole propagators. We derive expressions for the Drude as well as the Boltzmann conductivity, and, in the last section, we discuss the diffusion pole in the electron density response. Many parts of this calculation transfer to the Cooperon calculation in Chap. 1 and Chap. 2. The principles discussed in this chapter can be found in more detail in standard textbooks on quantum transport like Castro & Raimondi [33], Mahan [276], Nolting [277], Rammer [70], and Coleman [23].

A.1 Impurity-Dressed Green's Function

In this section, we follow mainly the derivation shown in Ref. [70]. We define the impurity potential, as well as the local electron density, in second quantization,

$$V(\mathbf{r}) = \sum_j V_{\text{imp}}(\mathbf{r} - \mathbf{r}_j), \tag{A.1}$$

$$n(\mathbf{r}) = \psi^\dagger(\mathbf{r})\psi(\mathbf{r}), \tag{A.2}$$

where the impurities are located at positions $\mathbf{r}_j$. In momentum space, this translates into

$$\begin{aligned} V(\mathbf{q}) &= \sum_j \int \mathrm{d}^d r e^{-i\mathbf{q}\cdot\mathbf{r}} V_{\text{imp}}(\mathbf{r} - \mathbf{r}_j) \\ &= \sum_j e^{-i\mathbf{q}\cdot\mathbf{r}_j} \int \mathrm{d}^d (r - r_j) e^{-i\mathbf{q}\cdot(\mathbf{r}-\mathbf{r}_j)} V_{\text{imp}}(\mathbf{r} - \mathbf{r}_j) \\ &\equiv V_{\mathbf{q}} \sum_j e^{-i\mathbf{q}\cdot\mathbf{r}_j} \end{aligned} \tag{A.3}$$

and

$$\begin{aligned} n(\mathbf{q}) &= \frac{1}{L^{2d}} \int \mathrm{d}^d r e^{-i\mathbf{q}\cdot\mathbf{r}} \sum_{\mathbf{k}\mathbf{k}'} e^{-i(\mathbf{k}'-\mathbf{k})\cdot\mathbf{r}} c^\dagger_{\mathbf{k}'} c_{\mathbf{k}} \\ &= \frac{1}{L^d} \sum_{\mathbf{k}} c^\dagger_{\mathbf{k}-\mathbf{q}} c_{\mathbf{k}}, \\ &= \frac{1}{L^d} \sum_{\mathbf{k}} c^\dagger_{\mathbf{k}_-} c_{\mathbf{k}_+}, \end{aligned} \tag{A.4}$$

where L^d is the volume of the system and we introduced

$$\mathbf{k}_\pm = \mathbf{k} \pm \frac{\mathbf{q}}{2}. \tag{A.5}$$

The impurity interaction V_D in the Dirac picture can therefore be defined as

$$V_\mathrm{D}(\tau) = \frac{1}{L^d} \sum_j \sum_{\mathbf{k}\mathbf{q}} e^{-i\mathbf{q}\cdot\mathbf{r}_j} V_\mathbf{q} c^\dagger_{\mathbf{k}_-}(\tau) c_{\mathbf{k}_+}(\tau), \tag{A.6}$$

where τ denotes imaginary time. Equation (A.6) allows for a shift of momentum, but conserves energy, describing elastic impurity scattering.

In the following, we calculate the contributions of elastic scattering to the Matsubara Green's function in a perturbational approach (see standard textbooks like Refs. [276–278]). The Matsubara Green's function is defined for imaginary time $\tau = it$, where τ is defined in the interval $0 < \tau < \hbar\beta$, and $\beta = 1/k_\mathrm{B}T$. The Green's function can be evaluated for a perturbation $V_\mathrm{D}(\tau)$ in diagrammatic perturbation theory by considering all the different, but connected diagrams,

$$\mathcal{G}(\mathbf{k},\tau) = -\sum_{n=0}^{\infty} \left(-\frac{1}{\hbar}\right)^n \int_0^{\hbar\beta} \mathrm{d}\tau_1 \cdots \int_0^{\hbar\beta} \mathrm{d}\tau_n \left\langle T_\tau c_\mathbf{k}(\tau) V_\mathrm{D}(\tau_1) \cdots V_\mathrm{D}(\tau_n) c^\dagger_\mathbf{k}(0) \right\rangle, \tag{A.7}$$

where T_τ is imaginary time ordering and the expansion of the Matsubara Green's function can therefore be written as

$$\mathcal{G}(\mathbf{k},\tau) = -\left\langle T_\tau c_\mathbf{k}(\tau) c^\dagger_\mathbf{k}(0) \right\rangle + \frac{1}{\hbar} \int_0^{\hbar\beta} \mathrm{d}\tau_1 \left\langle T_\tau c_\mathbf{k}(\tau) V_\mathrm{D}(\tau_1) c^\dagger_\mathbf{k}(0) \right\rangle + \cdots \tag{A.8}$$

$$= \mathcal{G}_0(\mathbf{k},\tau) + \mathcal{G}_1(\mathbf{k},\tau) + \cdots \tag{A.9}$$

where $\mathcal{G}_0$ is the bare Green's function.

However, in a disordered system, translational symmetry is generally broken and momentum is not conserved. By allowing a scattering $\mathbf{k}'' \to \mathbf{k}$, we find the following contribution $\mathcal{G}_1$ in first order perturbation theory in the scattering potential:

$$\mathcal{G}_1(\mathbf{k},\mathbf{k}'',\tau) = \frac{1}{\hbar L^d} \sum_{\mathbf{k}'\mathbf{q}'} \sum_j e^{-i\mathbf{q}'\cdot\mathbf{r}_j} V_{\mathbf{q}'} \int_0^{\hbar\beta} \mathrm{d}\tau_1 \left\langle T_\tau c_\mathbf{k}(\tau) c^\dagger_{\mathbf{k}'_-}(\tau_1) c_{\mathbf{k}'_+}(\tau_1) c^\dagger_{\mathbf{k}''}(0) \right\rangle, \tag{A.10}$$

where

$$\mathbf{k}'_{\pm} = \mathbf{k}' \pm \frac{\mathbf{q}'}{2}. \tag{A.11}$$

The only connected term gives

$$\begin{aligned}\mathcal{G}_1(\mathbf{k},\mathbf{k}'',\tau) &= \frac{1}{\hbar L^d}\sum_{\mathbf{k}'\mathbf{q}'}\sum_j e^{-i\mathbf{q}'\cdot\mathbf{r}_j}V_{\mathbf{q}'}\int_0^{\hbar\beta}\mathrm{d}\tau_1\ \left\langle T_\tau c_{\mathbf{k}}(\tau)c^\dagger_{\mathbf{k}'_-}(\tau_1)\right\rangle\left\langle T_\tau c_{\mathbf{k}'_+}(\tau_1)c^\dagger_{\mathbf{k}''}(0)\right\rangle \\ &= \frac{1}{\hbar L^d}\sum_{\mathbf{q}'}\sum_j e^{-i\mathbf{q}'\cdot\mathbf{r}_j}V_{\mathbf{q}'}\int_0^{\hbar\beta}\mathrm{d}\tau_1\ \mathcal{G}_0(\mathbf{k},\tau-\tau_1)\mathcal{G}_0(\mathbf{k}+\mathbf{q}',\tau_1)\delta_{\mathbf{k}+\mathbf{q}',\mathbf{k}''}.\end{aligned} \tag{A.12}$$

However, the impurity potential results in a breaking of translational symmetry. It is restored by considering an impurity average, which is achieved by taking the average over an ensemble of subsystems with different impurity distributions, but equal impurity density [70]. The impurity average of the scattering potential in Eq. (A.12) is given by

$$\left\langle\sum_j e^{-i\mathbf{q}\cdot\mathbf{r}_j}\right\rangle_{\mathrm{imp}} = N_{\mathrm{imp}}\delta_{\mathbf{q},0}, \tag{A.13}$$

where N_{imp} is the number of impurities. By defining the impurity density, $N_{\mathrm{imp}}/L^d = n_{\mathrm{imp}}$, we find for the impurity averaged Green's function

$$\mathcal{G}_1(\mathbf{k},\tau) = \frac{n_{\mathrm{imp}}V_{\mathbf{q}=0}}{\hbar}\int_0^{\hbar\beta}\mathrm{d}\tau_1\ \mathcal{G}_0(\mathbf{k},\tau-\tau_1)\mathcal{G}_0(\mathbf{k},\tau_1), \tag{A.14}$$

where the momentum is conserved formally by averaging. We change into frequency space by Fourier transformation of Eq. (A.14) as well as replacing the Green's functions by their Fourier expansion,

$$\mathcal{G}(\tau) = \frac{1}{\hbar\beta}\sum_n e^{-i\omega_n\tau}\mathcal{G}(i\omega_n), \tag{A.15}$$

where the fermionic Matsubara frequencies are discrete, $\omega_n = (2n+1)\pi/\hbar\beta$, we find

$$\begin{aligned}\mathcal{G}_1(\mathbf{k},i\omega_n) &= \frac{n_{\mathrm{imp}}V_{\mathbf{q}=0}}{\hbar}\frac{1}{(\hbar\beta)^2}\sum_{l,m}\int_0^{\hbar\beta}\mathrm{d}\tau\int_0^{\hbar\beta}\mathrm{d}\tau_1 e^{i(\omega_n-\omega_l)\tau}e^{i(\omega_l-\omega_m)\tau_1}\mathcal{G}_0(\mathbf{k},i\omega_l)\mathcal{G}_0(\mathbf{k},i\omega_m) \\ &= \frac{n_{\mathrm{imp}}V_{\mathbf{q}=0}}{\hbar}\left[\mathcal{G}_0(\mathbf{k},i\omega_n)\right]^2 \\ &\equiv \frac{1}{\hbar}\mathcal{G}_0(\mathbf{k},i\omega_n)\Sigma_1(\mathbf{k},i\omega_n)\mathcal{G}_0(\mathbf{k},i\omega_n),\end{aligned} \tag{A.16}$$

where we defined the energy contribution for single scattering,

$$\Sigma_1 = n_{\mathrm{imp}}V_{\mathbf{q}=0}. \tag{A.17}$$

This process can be depicted in momentum space using Feynman diagrams, see Fig. A.1 (a). This

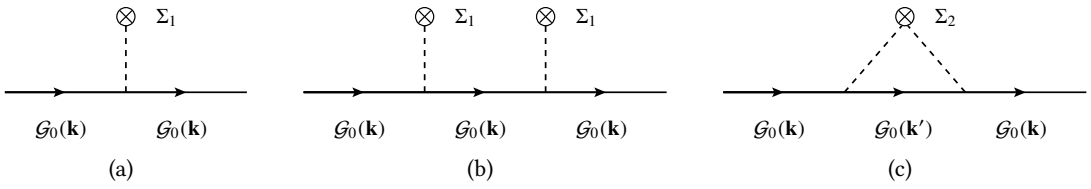

Figure A.1: *Lowest order energy contributions of elastic scattering to the one-particle Green's function.* (a) A single scattering contribution, recognizable by the single dashed line, does not change the momentum during the propagation. The energy contribution from this event results in a constant shift. Second order scattering can be decomposed into two single scattering events (b) or a double-scattering process at the same impurity (c). Process (b) also results in a constant shift of energy. Process (c) results in a non-trivial contribution to the energy, because momentum is not conserved between the first and second scattering process.

contribution is of order n_{imp} and appears as constant shift to the Hamiltonian, because it carries no frequency dependence. It can be absorbed into the chemical potential or renormalized to zero.

For the second order contribution, $\mathcal{G}_2$, we consider the impurity average over

$$\begin{aligned}\left\langle \sum_{jl} e^{-i\mathbf{q}_1\cdot\mathbf{r}_j} e^{-i\mathbf{q}_2\cdot\mathbf{r}_l} \right\rangle_{\text{imp}} &= \left\langle \sum_{j=l} e^{-i(\mathbf{q}_1+\mathbf{q}_2)\cdot\mathbf{r}_j} + \sum_{j\neq l} e^{-i\mathbf{q}_1\cdot\mathbf{r}_j} e^{-i\mathbf{q}_2\cdot\mathbf{r}_l} \right\rangle_{\text{imp}} \\ &= N_{\text{imp}}(N_{\text{imp}}-1)\delta_{\mathbf{q}_1,0}\delta_{\mathbf{q}_2,0} + N_{\text{imp}}\delta_{\mathbf{q}_1+\mathbf{q}_2,0},\end{aligned} \tag{A.18}$$

where the first term corresponds to scattering from two distinct impurities and can again be shifted into the chemical potential, see Fig. A.1 (b). The second term corresponds to double scattering at the same impurity and is of order n_{imp}. We can depict this event by considering a transfer of momentum to the impurity at one scattering event and transferring the same amount of momentum back at the second scattering event, see Fig. A.1 (c). This multiple scattering process at the same impurity yields a non-trivial contribution. Similarly as in lowest order, we find for the only connected diagrams

$$\begin{aligned}\mathcal{G}_2(\mathbf{k},\tau) = &-\frac{n_{\text{imp}}}{\hbar^2 L^d} \sum_{\mathbf{k}',\mathbf{k}''} \sum_{\mathbf{q}',\mathbf{q}''} V_{\mathbf{q}'} V_{\mathbf{q}''} \delta_{\mathbf{q}',-\mathbf{q}''} \times \\ &\int_0^{\hbar\beta} \mathrm{d}\tau_1 \int_0^{\hbar\beta} \mathrm{d}\tau_2 \left\langle T_\tau c_{\mathbf{k}}(\tau) c^\dagger_{\mathbf{k}'_-}(\tau_1) \right\rangle \left\langle T_\tau c_{\mathbf{k}'_+}(\tau_1) c^\dagger_{\mathbf{k}''_-}(\tau_2) \right\rangle \left\langle T_\tau c_{\mathbf{k}''_+}(\tau_2) c^\dagger_{\mathbf{k}}(0) \right\rangle \\ = &\frac{n_{\text{imp}}}{\hbar^2 L^d} \sum_{\mathbf{q}} V_{\mathbf{q}} V_{-\mathbf{q}} \int_0^{\hbar\beta} \mathrm{d}\tau_1 \int_0^{\hbar\beta} \mathrm{d}\tau_2 \; \mathcal{G}_0(\mathbf{k},\tau-\tau_1)\mathcal{G}_0(\mathbf{k}+\mathbf{q},\tau_1-\tau_2)\mathcal{G}_0(\mathbf{k},\tau_2),\end{aligned} \tag{A.19}$$

where

$$\mathbf{k}''_\pm = \mathbf{k}'' \pm \frac{\mathbf{q}''}{2}. \tag{A.20}$$

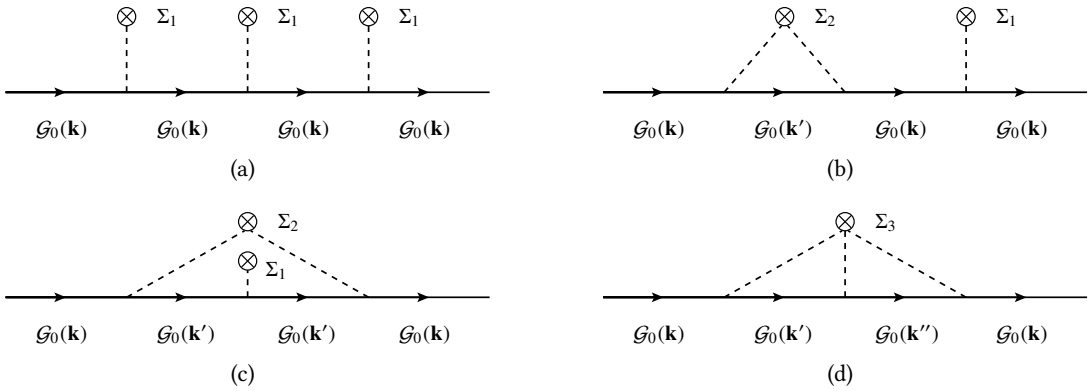

Figure A.2: *Energy contributions origin in three scattering events.* Triple scattering events can be separated into three different contributions. Three independent scatterings, depicted in (a), are of order n_{imp}^3 and result in a redefinition of the energy scale. Combinations of one single scattering event and a double-scattering event are depicted in (b) and (c). These are of order n_{imp}^2 and can be neglected. Only the contribution of scattering three times off the same impurity yileds a nontrivial energy contribution of order n_{imp}.

Note that each Green's function absorbs a minus sign. Inserting the Fourier transforms, we find

$$\mathcal{G}_2(\mathbf{k}, i\omega_n) = \frac{n_{\text{imp}}}{\hbar^2 L^d} \sum_{\mathbf{q}} \mathcal{G}_0(\mathbf{k}, i\omega_n) V_{-\mathbf{q}} \mathcal{G}_0(\mathbf{k}+\mathbf{q}, i\omega_n) V_{\mathbf{q}} \mathcal{G}_0(\mathbf{k}, i\omega_n). \tag{A.21}$$

If we allow a continuous $\mathbf{q}$ variable, the relevant energy contribution according to Eq. (A.16) can be expressed as

$$\Sigma_2(\mathbf{k}, i\omega_n) = \frac{n_{\text{imp}}}{\hbar} \int \frac{\mathrm{d}^d q}{(2\pi)^d} V_{\mathbf{k}-\mathbf{q}} V_{\mathbf{q}-\mathbf{k}} \mathcal{G}_0(\mathbf{q}, i\omega_n). \tag{A.22}$$

Note that each interaction term comes with a factor L^{-d}, where one of those factors is absorbed into the impurity density n_{imp} and the remaining factors are absorbed into the momentum integrals.

Considering higher order terms, we separate the triple scattering event into different contributions, see Fig. A.2. There is one contribution of order n_{imp}, where triple scattering takes place at the same impurity. The double scattering processes contain one dangling impurity line; these contributions are therefore of order n_{imp}^2, whereas three single scattering events are of order n_{imp}^3. For the triple scattering energy contribution, we find

$$\Sigma_3(\mathbf{k}, i\omega_n) = \frac{n_{\text{imp}}}{\hbar^2} \int \frac{\mathrm{d}^d q_1}{(2\pi)^d} \int \frac{\mathrm{d}^d q_2}{(2\pi)^d} V_{\mathbf{k}-\mathbf{q}_1} \mathcal{G}_0(\mathbf{q}_1, i\omega_n) V_{\mathbf{q}_1-\mathbf{q}_2} \mathcal{G}_0(\mathbf{q}_2, i\omega_n) V_{\mathbf{q}_2-\mathbf{k}}. \tag{A.23}$$

In fourth order in the scattering, we find three interesting diagrams, see Fig. A.3. All these diagrams obey different momentum conservation conditions.

Proceeding and considering higher and higher order in perturbation theory creates more and more diagrams, which all contribute to the impurity dressed Green's function. As we have

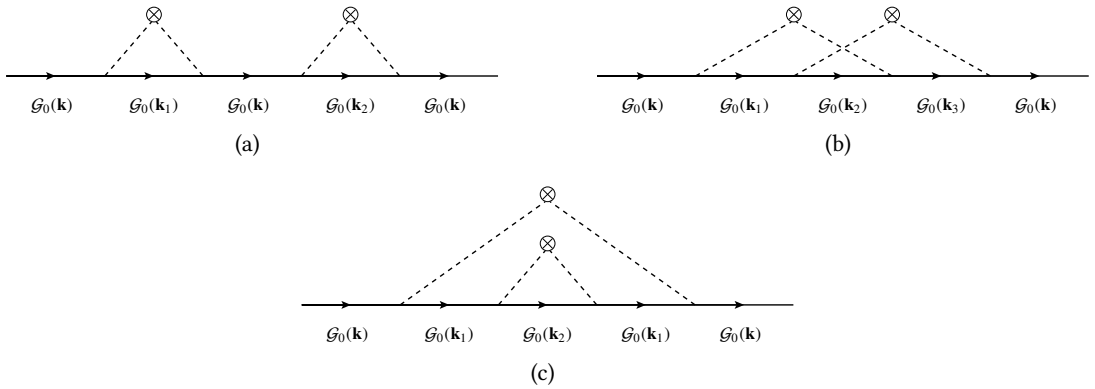

Figure A.3: *Combinations of two double scattering diagrams.* Double scattering events appear in different combinations in the fourth order perturbation theory. Two individual double scatterings (a), two intertwined double scattering processes (b), and one double scattering encapsuled by the other (c). All provide different energy contributions and obey different momentum conservation conditions.

shown, these diagrams can be represented by combinations of free propagators and distinguished, complicated scattering events. All these diagrams can be captured self-consistently by a Dyson equation [277, 278]

$$\mathcal{G} = \mathcal{G}_0 + \frac{1}{\hbar}\mathcal{G}_0\Sigma\mathcal{G} \tag{A.24}$$

which defines the self-energy Σ and is formally solved by

$$\begin{aligned}\mathcal{G}(\mathbf{k}, i\omega_n) &= \frac{\mathcal{G}_0(\mathbf{k}, i\omega_n)}{1 - \frac{1}{\hbar}\mathcal{G}_0(\mathbf{k}, i\omega_n)\Sigma(\mathbf{k}, i\omega_n)} \\ &= \frac{\hbar}{i\hbar\omega_n - \xi_\mathbf{k} - \Sigma(\mathbf{k}, i\omega_n)},\end{aligned} \tag{A.25}$$

where for the last step we used the representation of the bare Matsubara Green's function,

$$\mathcal{G}_0(\mathbf{k}, i\omega_n) = \frac{\hbar}{i\hbar\omega_n - \xi_\mathbf{k}}. \tag{A.26}$$

The full self energy, however, is a complicated object. Using the Born approximation, we neglect all multi scattering processes involving triple scattering or higher (see, e.g., Chap. 3 in Ref. [70]), and we are left with all possible combinations of double scattering events. Furthermore, we neglect all diagrams containing crossed impurity lines, because they produce terms of higher order (see also Ref. [70], pp. 153).

The diagrams that are left for the evaluation (which are still infinitely many) are the so called rainbow diagrams, which can be described by the Σ_2 energy contribution, see Fig. A.3 (c) and Fig. A.4. If we expect the interaction strength to be independent on the momentum transfer,

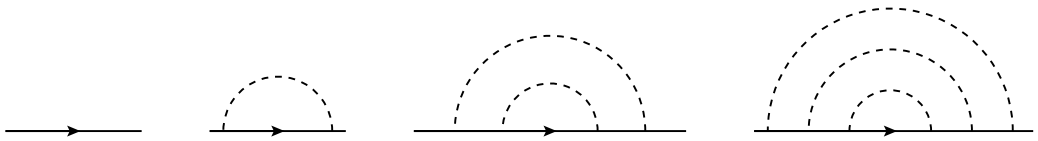

Figure A.4: *Rainbow diagrams.* The so-called rainbow diagrams represent the Gaussian approximation and contain all double-scattering processes without intersecting or dangling impurity scattering lines. Still infinitely many, these diagrams can be included up to all orders self-consistently.

the second order energy contribution, Eq. (A.22), simplifies to

$$\begin{aligned}\Sigma_2(i\omega_n) &= \frac{V^2 n_{\text{imp}}}{\hbar}\int \frac{\mathrm{d}k^d}{(2\pi)^d}\frac{\hbar}{i\hbar\omega_n - \xi_{\mathbf{k}}} \\ &= V^2 n_{\text{imp}} N_{\text{F}} \int_{-\mu}^{\infty} \mathrm{d}\xi \frac{1}{i\hbar\omega_n - \xi},\end{aligned} \tag{A.27}$$

where we transformed the momentum integral into an energy integral by using

$$\xi(\mathbf{k}) \;=\; \frac{\hbar^2\mathbf{k}^2}{2m} \;-\; \mu, \tag{A.28}$$

where μ is the chemical potential and take the density of states at the Fermi energy N_{F} (per spin) as a factor into account. In the following we are interested in the imaginary part of the self energy and absorb the real part into the chemical potential. As the Fermi energy ε_{F} is the largest energy scale, we set $\mu \approx \varepsilon_{\text{F}} \approx \infty$ and find

$$\begin{aligned}\Im\left\{\Sigma_2(i\omega_n)\right\} &= -V^2 n_{\text{imp}} N_{\text{F}} \int_{-\infty}^{\infty} \mathrm{d}\xi \frac{\hbar\omega_n}{\xi^2 + (\hbar\omega_n)^2} \\ &= -V^2 n_{\text{imp}} N_{\text{F}} \int_{-\infty}^{\infty} \frac{\mathrm{d}\xi}{\hbar\omega_n} \frac{1}{1 + \frac{\xi^2}{(\hbar\omega_n)^2}} = \\ &= -\pi V^2 n_{\text{imp}} N_{\text{F}} \mathrm{sgn}(\omega_n),\end{aligned} \tag{A.29}$$

which only depends on the sign of ω_n. To calculate the next rainbow diagram, the self energy has to be included into the Green's function of Eq. (A.27). Because the result does only depend on the sign of ω_n, the result is already self-consistent. Therefore, in Born approximation, the self-energy up to all orders is given by

$$\Im\left\{\Sigma(i\omega_n)\right\} = -\pi V^2 n_{\text{imp}} N_{\text{F}} \mathrm{sgn}(\omega_n) \equiv -\frac{\hbar}{2\tau_0}\mathrm{sgn}(\omega_n), \tag{A.30}$$

where we defined the elastic scattering rate

$$\frac{\hbar}{\tau_0} = 2\pi n_{\text{imp}} N_{\text{F}} V^2. \tag{A.31}$$

A factor of 2 is taken into account for the spin degeneracy. The disorder-dressed Matsubara Green's function results in [276–278]

$$\mathcal{G}(\mathbf{k}, i\omega_n) = \frac{\hbar}{i\hbar\omega_n - \xi_{\mathbf{k}} + \frac{i\hbar}{2\tau_0}\mathrm{sgn}(\omega_n)}, \tag{A.32}$$

and the real time Green's functions are obtained by taking $i\omega_n \to \omega \pm i0^+$ and $\mathrm{sgn}(\omega_n) \to \mathrm{sgn}(\pm 0^+)$, thus the retarded and advanced disorder-dressed Green's functions are given by [276–278]

$$G^{\mathrm{ret/adv}}(\mathbf{k}, \omega) = \frac{\hbar}{\hbar\omega - \xi_{\mathbf{k}} \pm \frac{i\hbar}{2\tau_0}}. \tag{A.33}$$

A.2 Drude Conductivity

We begin with Kubo's linear response formula [279] in thermal representation using Matsubara Green's functions [280]. For an external perturbation that is specified by momentum $\mathbf{q}$ and (bosonic) Matsubara frequency $i\omega_n$,

$$\sigma_{\alpha\beta}(\mathbf{q}, i\omega_n) = \frac{1}{\omega_n}\left[\Pi_{\alpha\beta}(\mathbf{q}, i\omega_n) + \frac{e^2 n}{m}\delta_{\alpha\beta}\right], \tag{A.34}$$

$$\Pi_{\alpha\beta}(\mathbf{q}, i\omega_n) = -\frac{1}{\hbar L^d}\int_0^{\hbar\beta} \mathrm{d}\tau e^{i\omega_n\tau}\left\langle T_\tau j_\alpha(\mathbf{q}, \tau) j_\beta(-\mathbf{q}, 0)\right\rangle, \tag{A.35}$$

where the conductivity tensor $\sigma_{\alpha\beta}$ is given by a diamagnetic part, proportional to the charge carrier density n, as well as the current–current correlation function $\Pi_{\alpha\beta}$, where $\mathbf{j}$ is the current density operator. The bracket denotes impurity averaging. The representation using retarded Green's functions is derived by analytic continuation

$$\tau \to it \tag{A.36}$$

$$i\omega_n \to \omega, \tag{A.37}$$

which yields

$$\sigma_{\alpha\beta}(\mathbf{q}, \omega) = \frac{i}{\omega}\left[\Pi_{\alpha\beta}(\mathbf{q}, \omega) + \frac{e^2 n}{m}\delta_{\alpha\beta}\right], \tag{A.38}$$

$$\Pi_{\alpha\beta}(\mathbf{q}, \omega) = -\frac{i}{\hbar L^d}\int_{-\infty}^{\infty} \mathrm{d}t e^{i\omega(t-t')}\Theta(t-t')\left\langle\left[j_\alpha(\mathbf{q}, t), j_\beta^\dagger(\mathbf{q}, t')\right]\right\rangle, \tag{A.39}$$

where Θ is the Heaviside function. In perturbation theory for impurity scattering, different particle–hole propagators between current vertices have to be considered, see Fig. A.5. In lowest order, the bare particle–hole propagator with disorder-dressed Green's functions yields the Drude conductivity, which we will derive in this section. Taking the so-called ladder diagrams of impurity scattering between the particle and hole propagators into consideration, the Boltzmann conductivity is derived, which we will discuss in the next section. The maximally crossed diagrams are in the focus of Chap. 2 and provide the WL and WAL contributions, which is the first order quantum correction to the conductivity.

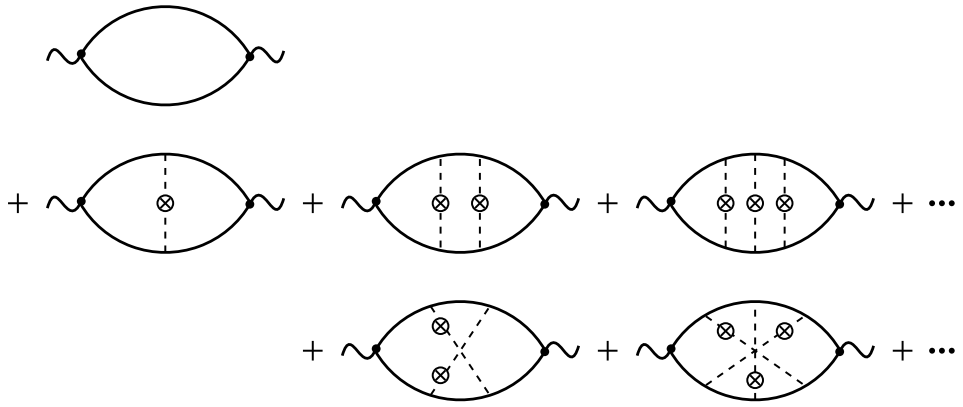

Figure A.5: *Disorder-averaged current–current correlation function.* Perturbation theory for impurity scattering yields qualitatively different particle–hole diagrams between the current vertices. A current vertex (black circle in the picture) contributes a factor $e\hbar\mathbf{k}/m$. Evaluation of the bare particle–hole propagator (with disorder-dressed Green's functions) leads to the Drude conductivity of isotropic scattering. The ladder diagrams treat non-isotropic scattering and result in the Boltzmann conductivity. The maximally crossed diagrams result in a quantum correction called weak (anti-)localization and are in the focus of Chap. 2.

The current operator in second quantized form is given by

$$\mathbf{j}(\mathbf{r}) = -\frac{i\hbar e}{2m}\left\{\psi^\dagger(\mathbf{r})\left[\nabla\psi(\mathbf{r})\right] - \left[\nabla\psi^\dagger(\mathbf{r})\right]\psi(\mathbf{r})\right\}, \tag{A.40}$$

which is in Fourier space

$$\begin{aligned}\mathbf{j}(\mathbf{q}) &= -\frac{i\hbar e}{2m}\int \mathrm{d}^d r e^{-i\mathbf{q}\cdot\mathbf{r}}\left\{\psi^\dagger(\mathbf{r})\left[\nabla\psi(\mathbf{r})\right] - \left[\nabla\psi^\dagger(\mathbf{r})\right]\psi(\mathbf{r})\right\} \\ &= -\frac{i\hbar e L^d}{2m}\int \mathrm{d}^d r e^{-i\mathbf{q}\cdot\mathbf{r}}\sum_{\mathbf{k},\mathbf{k}'} e^{-i(\mathbf{k}-\mathbf{k}')\cdot\mathbf{r}}\left[i\mathbf{k}' + i\mathbf{k}\right] c_{\mathbf{k}}^\dagger c_{\mathbf{k}'} \\ &= \frac{e}{m}\sum_{\mathbf{k}} \hbar\mathbf{k} c_{\mathbf{k}_-}^\dagger c_{\mathbf{k}_+}.\end{aligned} \tag{A.41}$$

Therefore, each current vertex contributes a factor $e\hbar\mathbf{k}/m$ to the correlation function,

$$\Pi(\mathbf{q}, i\omega_n) = -\frac{e^2}{\hbar L^d m^2}\int_0^{\hbar\beta} \mathrm{d}\tau e^{i\omega_n\tau}\sum_{\sigma\sigma'}\sum_{\mathbf{k}\mathbf{k}'}\hbar^2(\mathbf{k}\cdot\mathbf{k}')\left\langle T_\tau c_{\mathbf{k}_+\sigma}(\tau)c_{\mathbf{k}_-\sigma}^\dagger(\tau)c_{\mathbf{k}'_-\sigma'}(0)c_{\mathbf{k}'_+\sigma'}^\dagger(0)\right\rangle. \tag{A.42}$$

Using Wick's generalized theorem [277], we separate the correlation function into products of one-particle Matsubara Green's functions,

$$\begin{aligned}\left\langle T_\tau c_{\mathbf{k}_+\sigma}(\tau)c_{\mathbf{k}_-\sigma}^\dagger(\tau)c_{\mathbf{k}'_-\sigma'}(0)c_{\mathbf{k}'_+\sigma'}^\dagger(0)\right\rangle &= \left\langle T_\tau c_{\mathbf{k}_+\sigma}(\tau)c_{\mathbf{k}_-\sigma}^\dagger(\tau)\right\rangle\left\langle T_\tau c_{\mathbf{k}'_-\sigma'}(0)c_{\mathbf{k}'_+\sigma'}^\dagger(0)\right\rangle \\ &\quad - \left\langle T_\tau c_{\mathbf{k}_+\sigma}(\tau)c_{\mathbf{k}'_+\sigma'}^\dagger(0)\right\rangle\left\langle T_\tau c_{\mathbf{k}'_-\sigma'}(0)c_{\mathbf{k}_-\sigma}^\dagger(\tau)\right\rangle.\end{aligned} \tag{A.43}$$

The first term in Eq. (A.43) corresponds to Green's functions with no dependence in τ, and this term does not contribute to the integration in Eq. (A.42). We evaluate the second term by perturbative expansion of the Matsubara Green's function. As a first step, we approximate

$$\left\langle T_\tau c_{\mathbf{k}_+\sigma}(\tau) c^\dagger_{\mathbf{k}_-\sigma}(\tau) c_{\mathbf{k}'_-\sigma'}(0) c^\dagger_{\mathbf{k}'_+\sigma'}(0) \right\rangle \approx -\mathcal{G}^0_\sigma(\mathbf{k}_+,\tau)\mathcal{G}^0_\sigma(\mathbf{k}_-,-\tau)\delta_{\sigma,\sigma'}\delta_{\mathbf{k},\mathbf{k}'}\delta_{\mathbf{q},\mathbf{q}'}. \tag{A.44}$$

However, the term Eq. (A.44), which contains the bare particle–hole propagator with only bare Green's functions, gives no contribution to the conductivity [276]. The next order is given by

$$\left\langle T_\tau c_{\mathbf{k}_+\sigma}(\tau) c^\dagger_{\mathbf{k}_-\sigma}(\tau) c_{\mathbf{k}'_-\sigma'}(0) c^\dagger_{\mathbf{k}'_+\sigma'}(0) \right\rangle \approx -\mathcal{G}_\sigma(\mathbf{k}_+,\tau)\mathcal{G}_\sigma(\mathbf{k}_-,-\tau)\delta_{\sigma,\sigma'}\delta_{\mathbf{k},\mathbf{k}'}\delta_{\mathbf{q},\mathbf{q}'}, \tag{A.45}$$

which describes the bare particle–hole propagator for impurity-dressed Green's functions. This contribution will result in the Drude conductivity. After summation over the spin index, we find

$$\Pi_{\alpha\beta}(\mathbf{q}, i\omega_n)^{(0)} = \frac{2e^2}{\hbar L^d m^2} \int_0^{\hbar\beta} \mathrm{d}\tau e^{i\omega_n\tau} \sum_{\mathbf{k}} \hbar^2 k_\alpha k_\beta \mathcal{G}(\mathbf{k}_+,\tau)\mathcal{G}(\mathbf{k}_-,-\tau). \tag{A.46}$$

In the following, we replace the Green's functions $\mathcal{G}(\pm\tau)$ by their Fourier transforms, described by Eq. (A.15) with (fermionic) frequencies ω'_n, ω''_n, and change the discrete momentum sum into an integral (see also Eq. (1.40))

$$\frac{1}{L^d}\sum_{\mathbf{k}} \to \int \frac{\mathrm{d}k^d}{(2\pi)^d} \equiv \int_{\mathbf{k}} \tag{A.47}$$

thus

$$\begin{aligned}
\Pi_{\alpha\beta}(\mathbf{q}, i\omega_n)^{(0)} &= \frac{2e^2}{\hbar L^d m^2} \sum_{\mathbf{k}} \frac{\hbar^2 k_\alpha k_\beta}{\hbar^2\beta^2} \sum_{i\omega'_n, i\omega''_n} \int_0^{\hbar\beta} \mathrm{d}\tau e^{i(\omega_n-\omega'_n+\omega''_n)\tau} \mathcal{G}(\mathbf{k}_+, i\omega'_n)\mathcal{G}(\mathbf{k}_-, i\omega''_n) \\
&= \frac{2e^2}{\hbar L^d m^2} \sum_{\mathbf{k}} \frac{\hbar^2 k_\alpha k_\beta}{\hbar\beta} \sum_{i\omega'_n} \mathcal{G}(\mathbf{k}_+, i\omega'_{n,+})\mathcal{G}(\mathbf{k}_-, i\omega'_{n,-}) \\
&= \frac{2e^2}{\hbar m^2} \frac{1}{\beta\hbar} \sum_{i\omega'_n} \int_{\mathbf{k}} \hbar^2 k_\alpha k_\beta \mathcal{G}(\mathbf{k}_+, i\omega'_{n,+})\mathcal{G}(\mathbf{k}_-, i\omega'_{n,-})
\end{aligned} \tag{A.48}$$

where we defined $\omega'_{n,\pm} = \omega'_n \pm \omega_n/2$.

For the evaluation of the particle–hole propagator with impurity-dressed Green's functions, we use the complex function

$$f(z) = \frac{1}{e^{\beta\hbar z}+1}. \tag{A.49}$$

This function has poles on the imaginary axis at $z = i\omega_n = {}^{i\pi(2n+1)}/_{\hbar\beta}$, and the residuum for each pole is given by $-{}^1/_{\hbar\beta}$. This allows us to use analytic continuation $i\omega_n \to z$ and [33, 278]

$$\frac{1}{\beta\hbar}\sum_{i\omega_n} \frac{e^{-\beta\hbar\omega_n\eta}}{i\omega_n - \varepsilon_{\mathbf{k}}} = -\frac{1}{2\pi i}\oint_C \mathrm{d}z \frac{e^{i\beta\hbar z\eta}}{e^{\beta\hbar z}+1}\frac{1}{z-\varepsilon_{\mathbf{k}}}, \tag{A.50}$$

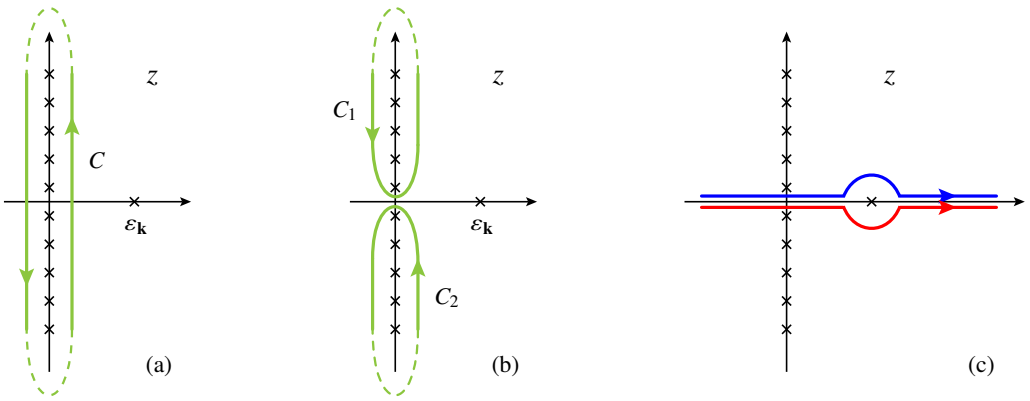

Figure A.6: *Green's functions and contour integrals.* (a) Sum over all poles in the Matsubara Green's function, represented by a contour integral, see Eq. (A.50). (b) Splitting of the contour, see Eq. (A.51). (c) Deforming of the contour parallel to the real axis results in integrals over retarded and advanced Green's functions.

where we use the factors involving $\eta = 0^+$ for $n > 0$ and $\eta = 0^-$ for $n < 0$ as a cutoff and the contour C encloses only the poles on the imaginary axis (see Fig. A.6). Now we split the contour into two parts, where the poles for positive imaginary part and the poles for negative imaginary part are integrated separately,

$$\frac{1}{\beta\hbar}\sum_{i\omega_n}\frac{e^{-\beta\hbar\omega_n\eta}}{i\omega_n-\varepsilon_{\mathbf{k}}} = -\frac{1}{2\pi i}\left[\oint_{C_1} \mathrm{d}z \frac{e^{i\beta\hbar z 0^+}}{e^{\beta\hbar z}+1}\frac{1}{z-\varepsilon_{\mathbf{k}}} + \oint_{C_2} \mathrm{d}z \frac{e^{i\beta\hbar z 0^-}}{e^{\beta\hbar z}+1}\frac{1}{z-\varepsilon_{\mathbf{k}}}\right]. \tag{A.51}$$

We deform the contour to follow the real axis and change the direction of C_2. The integral is well defined for large, positive values of $\Re\{z\} = \omega$, but for the negative values the additional factor $\exp(\beta\hbar\omega 0^+)$ is needed for both integrals to ensure convergence. We find [33, 278]

$$\begin{aligned}\frac{1}{\beta\hbar}\sum_{i\omega_n}\frac{e^{-\beta\hbar\omega_n\eta}}{i\omega_n-\varepsilon_{\mathbf{k}}} &= -\frac{1}{2\pi i}\int_{-\infty}^{\infty}\mathrm{d}\omega\frac{e^{\beta\hbar\omega 0^+}}{e^{\beta\hbar\omega}+1}\left[\frac{1}{\omega-\epsilon_{\mathbf{k}}+i0^+}-\frac{1}{\omega-\epsilon_{\mathbf{k}}+i0^-}\right] \\ &= -\frac{1}{2\pi i}\int_{-\infty}^{\infty}\mathrm{d}\omega f(\hbar\omega)e^{\beta\hbar\omega 0^+}\left[G^{\mathrm{ret}}(\mathbf{k},\omega)-G^{\mathrm{adv}}(\mathbf{k},\omega)\right],\end{aligned} \tag{A.52}$$

where $f(\hbar\omega)$ is the Fermi function.

For the two-particle correlation function, we find products of Matsubara Green's functions in Eq. (A.52). We need to separate the cases whether $\omega'_+\omega'_- \gtrless 0$, that is, if both poles lie in the same or in different half planes. For $\omega'_{n,+}\omega'_{n,-} > 0$, we find analog to Eq. (A.52),

$$\Pi_{\alpha\beta}(\mathbf{q},\omega)^{(0),>} = \frac{ie^2}{\pi\hbar m^2}\int_{\mathbf{k}}\hbar^2 k_\alpha k_\beta\int_{-\infty}^{\infty}\mathrm{d}\omega'\left\{f(\omega'_+)\left[G^{\mathrm{ret}}(\mathbf{k}_+,\omega'_+)\right]^2 - f(\omega'_-)\left[G^{\mathrm{adv}}(\mathbf{k}_-,\omega'_-)\right]^2\right\}. \tag{A.53}$$

The last expression can easily be calculated if zero temperature is considered, where

$$f(\varepsilon, T\to 0) = \Theta(-\varepsilon), \tag{A.54}$$

where Θ fixes the upper integration limits for each of the additive terms in Eq. (A.53). Furthermore, it directly follows from Eq. (A.33) that

$$\left[G^{\mathrm{ret(adv)}}(\omega)\right]^2 = -\frac{\partial}{\partial\omega}G^{\mathrm{ret(adv)}}(\omega), \tag{A.55}$$

and the result for the correlation function gets independent of ω,

$$\Pi_{\alpha\beta}(\mathbf{q})^{(0),>} = -\frac{ie^2}{\pi\hbar m^2}\int_{\mathbf{k}} \hbar^2 k_\alpha k_\beta \left[G^{\mathrm{ret}}(\mathbf{k}_+,0) - G^{\mathrm{adv}}(\mathbf{k}_-,0)\right]. \tag{A.56}$$

In the limit $\mathbf{q}\to 0$, we find

$$G^{\mathrm{ret}}(\mathbf{k},0) - G^{\mathrm{adv}}(\mathbf{k},0) = 2i\Im\left\{G^{\mathrm{ret}}(\mathbf{k},0)\right\} = -2i\pi\delta(\hbar\omega-\varepsilon_{\mathrm{F}}), \tag{A.57}$$

and by using

$$\delta(\hbar\omega-\varepsilon_{\mathrm{F}}) = N_{\mathrm{F}}\delta(k-k_{\mathrm{F}}), \tag{A.58}$$

where N_{F}, again, is the density of states per spin, and further replacing the angle average

$$\int \frac{\mathrm{d}S_d(\mathbf{k})}{S_d(\mathbf{k})} = \frac{1}{d} \tag{A.59}$$

where S_d is the unit sphere in d dimensions and $\varepsilon_{\mathrm{F}} = {}^{\hbar^2k_{\mathrm{F}}^2}/_{2m}$ as well as

$$n = \frac{4N_{\mathrm{F}}\varepsilon_{\mathrm{F}}}{d}, \tag{A.60}$$

then we find

$$\Pi(0,\omega)^{(0),>} = -\frac{e^2 n}{m}. \tag{A.61}$$

This contribution exactly cancels the diamagnetic part of the conductivity in Eq. (A.38).

However, in the case $\omega'_{n,+}\omega'_{n,-} < 0$ we find poles on both sides of the complex plane and have to combine retarded and advanced Green's functions, employing Eq. (A.52):

$$\begin{aligned}\Pi_{\alpha\beta}(\mathbf{q},\omega)^{(0),<} &= \frac{ie^2}{\pi\hbar m^2}\int_{-\infty}^{\infty}\mathrm{d}\omega'\int_{\mathbf{k}}\hbar^2k_\alpha k_\beta\left[f(\omega'_+)-f(\omega'_-)\right]G^{\mathrm{ret}}(\mathbf{k}_+,\omega'_+)G^{\mathrm{adv}}(\mathbf{k}_-,\omega'_-)\\ &= \frac{ie^2}{\pi\hbar m^2}\int_{-\infty}^{\infty}\mathrm{d}\omega'\int_{\mathbf{k}}\hbar^2k_\alpha k_\beta\left[f(\omega'+\omega)-f(\omega')\right]G^{\mathrm{ret}}(\mathbf{k}_+,\omega'+\omega)G^{\mathrm{adv}}(\mathbf{k}_-,\omega')\end{aligned} \tag{A.62}$$

Regarding Eq. (A.38), and shifting $\omega'+\omega\to\omega'$, we find for the conductivity

$$\sigma_{\alpha\beta}(\mathbf{q},\omega) = \frac{e^2}{\pi m^2}\int_{-\infty}^{\infty}\mathrm{d}\omega'\frac{f(\hbar\omega'-\hbar\omega)-f(\hbar\omega')}{\hbar\omega}\int_{\mathbf{k}}\hbar^2k_\alpha k_\beta G^{\mathrm{ret}}(\mathbf{k}_+,\omega')G^{\mathrm{adv}}(\mathbf{k}_-,\omega'-\omega). \tag{A.63}$$

We take the limit of $\mathbf{q} \to 0$ and split the momentum integral into an angular and an absolute value part. Since the product of Green's functions is strongly peaked at the Fermi energy, we use

$$\begin{aligned} &\int \frac{\mathrm{d}k^d}{(2\pi)^d} \hbar^2 k_\alpha k_\beta G^{\mathrm{ret}}(\mathbf{k}, \omega') G^{\mathrm{adv}}(\mathbf{k}, \omega' - \omega) \\ &\approx \int \frac{\mathrm{d}S_d(\mathbf{k})}{S_d} \hbar^2 \mathbf{k}_\mathrm{F}^2 \int \mathrm{d}k G^{\mathrm{ret}}(\mathbf{k}, \omega') G^{\mathrm{adv}}(\mathbf{k}, \omega' - \omega), \end{aligned} \tag{A.64}$$

We transform the latter momentum integral into an energy integral, see Eq. (A.27) as well as Eq. (A.28),

$$\int \mathrm{d}k G^{\mathrm{ret}}(\mathbf{k}, \omega') G^{\mathrm{adv}}(\mathbf{k}, \omega' - \omega) = N_\mathrm{F} \int_{-\infty}^{\infty} \mathrm{d}\xi_\mathbf{k} G^{\mathrm{ret}}(\mathbf{k}, \omega') G^{\mathrm{adv}}(\mathbf{k}, \omega' - \omega) \tag{A.65}$$

$$= N_\mathrm{F} \int_{-\infty}^{\infty} \mathrm{d}\xi_\mathbf{k} \frac{\hbar}{\xi_\mathbf{k} - \hbar\omega' - \frac{i\hbar}{2\tau_0}} \frac{\hbar}{\xi_\mathbf{k} - \hbar(\omega' - \omega) + \frac{i\hbar}{2\tau_0}} \tag{A.66}$$

$$= \frac{2\pi N_\mathrm{F}}{1 - i\omega\tau_0} \tau_0 \hbar, \tag{A.67}$$

which is independent of ω'. The last step follows directly from the residue theorem. The angular integral yields

$$\int \frac{\mathrm{d}S_d}{S_d} \hbar^2 \mathbf{k}_\mathrm{F}^2 = \frac{\hbar^2 k_\mathrm{F}^2}{d} \delta_{\alpha\beta} = \frac{2m\varepsilon_\mathrm{F}}{d} \delta_{\alpha\beta} \tag{A.68}$$

and

$$\int_{-\infty}^{\infty} \mathrm{d}\omega' \frac{f(\hbar\omega' - \hbar\omega) - f(\hbar\omega')}{\hbar\omega} = \frac{1}{\hbar}. \tag{A.69}$$

Furthermore, the electron density is given by Eq. (A.60). We find the final result for the bare particle–hole propagator with impurity-dressed Green's functions,

$$\sigma_{\alpha\beta} = \frac{ne^2\tau_0}{m} \frac{1}{1 - i\omega\tau_0} \delta_{\alpha\beta}, \tag{A.70}$$

which is structure-wise identical with the Drude conductivity [281, 282].

In the next order of impurity perturbation, we take scattering events between particle and hole propagator into account, the so-called ladder diagrams. In the next section we will find a similar result than Eq. (A.70), only the isotropic elastic scattering time τ_0 will be replaced by an effective transport time, τ_tr.

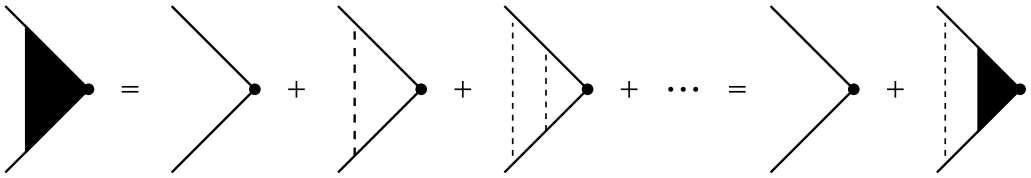

Figure A.7: *Ladder diagrams and dressed vertex.* The contribution from the ladder diagrams can be written in terms of a dressed vertex. This allows to formulate a Dyson equation for the dressed vertex and to calculate the contribution self-consistently. The bare verex contributes a factor $e\mathbf{v}$.

A.3 Boltzmann Conductivity: Taking the Ladder

To include disorder directly into the linear response evaluation, we consider an impurity vertex Γ in the current–current correlation function, see Fig. A.5. We neglect any diagrams that contain crossed impurity lines. Those contributions are smaller by a factor $\hbar/\varepsilon_F\tau$ and are discussed in Sec. 1.4. For the ladder diagrams, we can express the dressed vertex as (see Fig. A.7)

$$e v_\beta(\mathbf{k})\Gamma(i\omega_n, i\omega_n') = e v_\beta(\mathbf{k}) + \frac{n_{\text{imp}}}{\hbar^2}\int_{\mathbf{k}'} |V(\mathbf{k}-\mathbf{k}')|^2 \mathcal{G}(\mathbf{k}', i\omega_{n,+}')\mathcal{G}(\mathbf{k}', i\omega_{n,-}')\Gamma(i\omega_n, i\omega_n') e v_\beta(\mathbf{k}'), \tag{A.71}$$

where $\mathbf{v} = \hbar\mathbf{k}/m$. We multiply with $v_\beta(\mathbf{k})$ and assume that the scattering potential is only dependent on the angle ϕ, but not on the absolute value of $(\mathbf{k}-\mathbf{k}')$,

$$\Gamma(\omega, \omega') = 1 + \frac{n_{\text{imp}}}{\hbar^2}\int_{\mathbf{k}'} |V(\phi)|^2 G^{\text{ret}}(\mathbf{k}', \omega') G^{\text{adv}}(\mathbf{k}', \omega'-\omega)\Gamma\cos(\phi), \tag{A.72}$$

because we are only interested in the case where the poles lie in different complex half planes. Next we separate the angular and the absolute value part via

$$\Gamma(\omega, \omega') = 1 + \frac{n_{\text{imp}}}{\hbar^2}\Gamma\int \frac{\mathrm{d}S_d(\mathbf{k}')}{S_d}\cos(\phi)|V(\phi)|^2 \int \mathrm{d}k G^{\text{ret}}(\mathbf{k}', \omega') G^{\text{adv}}(\mathbf{k}', \omega'-\omega). \tag{A.73}$$

Note that for an isotropic scattering potential $\Gamma = 1$, and the Drude result is obtained. For general $V(\phi)$, the angular integration yields

$$\int \frac{\mathrm{d}S_d(\mathbf{k}')}{S_d}\cos(\phi)|V(\phi)|^2 = \int_{-1}^{1} \frac{\mathrm{d}\cos(\phi)}{2}\cos(\phi)|V(\phi)|^2 \equiv \overline{\cos(\phi)|V(\phi)|^2}, \tag{A.74}$$

and the integral over the Green's functions has been evaluated in Eq. (A.67). By defining

$$\frac{\hbar}{\tilde{\tau}} = 2\pi n_{\text{imp}} N_F \overline{\cos(\phi)|V(\phi)|^2}, \tag{A.75}$$

the Dyson equation yields

$$\Gamma = \frac{\tau_0^{-1} - i\omega}{\tau_0^{-1} - \tilde{\tau}^{-1} - i\omega}. \tag{A.76}$$

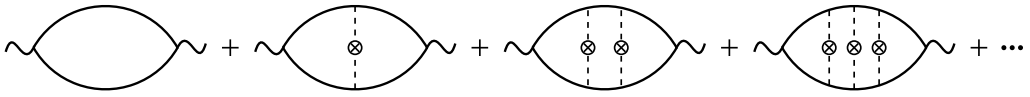

Figure A.8: *Ladder diagrams in the density–density correlation function.* Disorder in form of ladder diagrams evaluated in the density–density response results in the phenomenon of diffusion. The density vertex contributes a factor e.

Defining the transport time τ_{tr},

$$\frac{\hbar}{\tau_{\mathrm{tr}}} = \frac{\hbar}{\tau_0} - \frac{\hbar}{\tilde{\tau}} = 2\pi n_{\mathrm{imp}} N_{\mathrm{F}} \overline{[1-\cos(\phi)]\,|V(\phi)|^2}, \tag{A.77}$$

we find for the dressed vertex

$$\Gamma = \frac{\tau_{\mathrm{tr}}}{\tau_0} \frac{1 - i\omega\tau_0}{1 - i\omega\tau_{\mathrm{tr}}}. \tag{A.78}$$

The conductivity is therefore given by

$$\sigma_{\alpha\beta} = \frac{ne^2\tau_{\mathrm{tr}}}{m} \frac{1}{1 - i\omega\tau_{\mathrm{tr}}} \delta_{\alpha\beta}, \tag{A.79}$$

which has the same structure as the Drude conductivity Eq. (A.70), but with the elastic scattering time τ_0 replaced by the transport scattering time, τ_{tr}. Due to the angle dependence, low angle scattering does not contribute to the relaxation of the current, while back scattering dominates. This relates to the Boltzmann result for the conductivity of disordered Fermi systems. For isotropic scattering, the transport time becomes the elastic life time and the Drude result is obtained.

A.4 Electron Diffusion

Diffusion is phenomenon that is revealed by evaluation of the density–density correlation function. We derive the diffusion pole in this section for isotropic scattering but finite external momentum $\mathbf{q}$, because its calculation is directly related to the evaluation of the quantum corrections in the current–current correlation function.

We consider ladder diagrams between density vertices instead of current vertices, see Fig. A.8. Each density vertex contributes a factor e. We follow the notation and argumentation of Ref. [33] and Ref. [23]. In analogy to Eq. (A.41), the momentum dependent electron density is given by

$$n(\mathbf{q}) = e \sum_{\mathbf{k}} c^\dagger_{\mathbf{k}_-} c_{\mathbf{k}_+} \tag{A.80}$$

and the density–density correlation function, is similar to Eq. (A.42) given by

$$\chi(\mathbf{q}, i\omega_n) = -\frac{e^2}{\hbar L^d} \int_0^{\hbar\beta} \mathrm{d}\tau e^{i\omega_n\tau} \sum_{\sigma\sigma'} \sum_{\mathbf{k}\mathbf{k}'} \left\langle T_\tau c_{\mathbf{k}_+\sigma}(\tau) c^\dagger_{\mathbf{k}_-\sigma}(\tau) c_{\mathbf{k}'_-\sigma'}(0) c^\dagger_{\mathbf{k}'_+\sigma'}(0) \right\rangle. \tag{A.81}$$

By following the evaluation of the previous sections, we find

$$\chi(\mathbf{q}, i\omega_n) = \frac{2e^2}{\hbar} \frac{1}{\beta\hbar} \sum_{i\omega'_n} \int_{\mathbf{k}} \mathcal{G}(\mathbf{k}_+, i\omega'_{n,+}) \Gamma_{\mathrm{d}}(\mathbf{k}, \mathbf{q}, i\omega'_n) \mathcal{G}(\mathbf{k}_-, i\omega'_{n,-}), \tag{A.82}$$

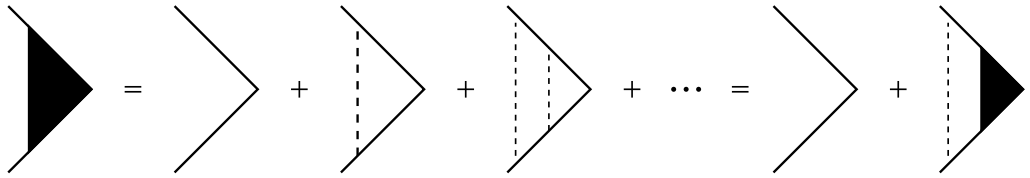

Figure A.9: *Dressed vertex for diffusion.* Again, the dressed vertex enables to calculate the contribution of disorder in the density–density response self-consistently.

where Γ_d denotes the ladder diagrams in the density–density propagator.

The Dyson equation for the dressed density vertex (see Fig. A.9) yields

$$e\Gamma_\mathrm{d}(\mathbf{k},\mathbf{q},i\omega_n,i\omega_n') = e + e\frac{n_\mathrm{imp}}{\hbar^2}\int\limits_{\mathbf{k}'} |V(\mathbf{k}-\mathbf{k}')|^2 \mathcal{G}(\mathbf{k}'_+,i\omega'_{n,+})\mathcal{G}(\mathbf{k}'_-,i\omega'_{n,-})\Gamma_\mathrm{d}(\mathbf{k}',\mathbf{q},i\omega_n'). \quad \text{(A.83)}$$

We assume that the scattering potential $V(\mathbf{k}-\mathbf{k}') = V$ does not depend on the momentum. Therefore, the left hand side cannot depend on $\mathbf{k}$. The momentum dependence of the dressed density vertex Γ_d is, regarding only the frequency dependence,

$$\begin{aligned}\Gamma_\mathrm{d}(\mathbf{q},i\omega_n') &= 1 + \frac{n_\mathrm{imp}V^2}{\hbar^2}\int\limits_{\mathbf{k}'} \mathcal{G}(\mathbf{k}'_+,i\omega'_{n,+})\mathcal{G}(\mathbf{k}'_-,i\omega'_{n,-})\Gamma_\mathrm{d}(\mathbf{q},i\omega_n') \\ &= 1 + \frac{n_\mathrm{imp}V^2}{\hbar^2}\Pi(\mathbf{q},i\omega_n,i\omega_n')\Gamma_\mathrm{d}(\mathbf{q},i\omega_n'),\end{aligned} \quad \text{(A.84)}$$

where the $i\omega_n$ dependence is lost, analog to Eq. (A.67). We find

$$\Gamma_\mathrm{d}(\mathbf{q},i\omega') = \frac{1}{1-\dfrac{n_\mathrm{imp}V^2}{\hbar^2}\Pi(\mathbf{q},i\omega_n,i\omega_n',)} \quad \text{(A.85)}$$

where the particle–hole propagator is given by

$$\Pi(\mathbf{q},i\omega_n,i\omega_n') = \int\limits_{\mathbf{k}'} \mathcal{G}(\mathbf{k}'_+,i\omega'_{n,+})\mathcal{G}(\mathbf{k}'_-,i\omega'_{n,-}) \quad \text{(A.86)}$$

To calculate the latter integral, we use again Eq. (A.65) and

$$\xi_{\mathbf{k}_\pm} = \xi_\mathbf{k} \pm \frac{\hbar^2}{2m}\mathbf{k}\cdot\mathbf{q} + O(q^2). \quad \text{(A.87)}$$

Note that it is essential for the result to keep the $\mathbf{q}$ dependence, in contrast to the evaluations of the current–current correlation functions. We neglect just the quadratic order in q in com-

parison with the Fermi momentum, where the integrand will yield its dominant contribution. For $\omega'_{n,+}\omega'_{n,-} < 0$ we solve

$$\begin{aligned}\Pi^{<}(\mathbf{q}, i\omega_n) &= N_\mathrm{F} \int \frac{\mathrm{d}S_d(\mathbf{k}')}{S_d} \int_{-\infty}^{\infty} \mathrm{d}\xi_{\mathbf{k}'} \frac{\hbar}{i\hbar\omega'_{n,+} - \xi_{\mathbf{k}} - \frac{\hbar^2}{2m}\mathbf{k}'\cdot\mathbf{q} + \frac{i\hbar}{2\tau_0}} \frac{\hbar}{i\hbar\omega'_{n,-} - \xi_{\mathbf{k}} + \frac{\hbar^2}{2m}\mathbf{k}'\cdot\mathbf{q} - \frac{i\hbar}{2\tau_0}} \\ &= N_\mathrm{F} \int \frac{\mathrm{d}S_d(\mathbf{k}')}{S_d} \frac{i2\pi\hbar^2}{i\hbar(\omega'_{n,+} - \omega'_{n,-}) - \hbar v_\mathrm{F}\hat{\mathbf{k}}'\cdot\mathbf{q} + \frac{i\hbar}{\tau_0}} \\ &= 2\pi\hbar N_\mathrm{F}\tau_0 \int \frac{\mathrm{d}S_d(\mathbf{k}')}{S_d} \frac{1}{1 + |\omega_n|\tau_0 + i\tau_0 v_\mathrm{F} q\cos(\phi)},\end{aligned} \tag{A.88}$$

where we find again that the particle–hole propagator is independent of $i\omega'_n$. Using the expression for the elastic scattering rate for each spin degree, Eq. (A.31), we find

$$\frac{n_\mathrm{imp}V^2}{\hbar^2}\Pi^{<}(\mathbf{q}, i\omega_n) = \int \frac{\mathrm{d}S_d(\mathbf{k}')}{S_d} \frac{1}{1 + |\omega_n|\tau_0 + ilq\cos(\phi)} \tag{A.89}$$

where the mean free path l is given by

$$v_\mathrm{F}\tau_0 = l. \tag{A.90}$$

In the diffusive limit, we assume $lq \ll 1$ as well as small frequencies, $|\omega_n|\tau_0 \ll 1$ and can expand Eq. (A.89) up to the first non-vanishing contribution, which comes with order l^2q^2. Note that this quadratic order in q gives a larger contribution as in the approximation Eq. (A.87) due to the l factor, which is proportional to the Fermi momentum:

$$\frac{1}{1 + |\omega_n|\tau_0 + ilq\cos(\phi)} \approx 1 - |\omega_n|\tau_0 - ilq\cos(\phi) - l^2q^2\cos^2(\phi) \tag{A.91}$$

and find that in the integration, the imaginary part vanishes and only the momentum squared contributes to the result

$$\frac{n_\mathrm{imp}V^2}{\hbar^2}\Pi^{<}(\mathbf{q}, i\omega_n) = \left(1 - |\omega_n|\tau_0 - Dq^2\tau_0\right), \tag{A.92}$$

where

$$D = \frac{v_\mathrm{F}^2\tau_0}{d} \tag{A.93}$$

is the diffusion constant. We find

$$\Gamma_\mathrm{d} = \begin{cases} \frac{\frac{1}{\tau_0}}{|\omega_n| + Dq^2} \\ 1 \end{cases}. \tag{A.94}$$

To calculate the charge susceptibility, we insert the calculated vertex into Eq. (A.82). Analog to Eq. (A.61) we find, if the poles are in the same half-plane, the static susceptibility

$$\chi(0,\omega)^{>} = -2e^2N_\mathrm{F}. \tag{A.95}$$

If the poles reside in different half-planes, we have to perform the integral

$$\chi(\mathbf{q}, i\omega_n)^< = \frac{2e^2}{\hbar}\frac{1}{\beta\hbar}\sum_{i\omega_n'}\int_{\mathbf{k}} \mathcal{G}(\mathbf{k}_+, i\omega_{n,+}')\mathcal{G}(\mathbf{k}_-, i\omega_{n,-}')\frac{1}{\tau_0|\omega_n| + \tau_0 Dq^2}. \tag{A.96}$$

However, as there is already the diffusion pole present, we can set $q = 0$ and $\omega_n \to 0$ in the Green's functions only, but keeping the two poles on different half planes. This results in

$$\begin{aligned}\chi(\mathbf{q}, i\omega_n)^< &\approx \frac{2e^2}{\hbar}\frac{1}{\beta\hbar}\sum_{i\omega_n'}\int_{\mathbf{k}} \frac{\hbar^2}{\left(i\hbar\omega_n' - \xi_{\mathbf{k}} + \frac{i\hbar}{2\tau_0}\right)\left(i\hbar\omega_n' - \xi_{\mathbf{k}} - \frac{i\hbar}{2\tau_0}\right)(\tau_0|\omega_n| + \tau_0 Dq^2)} \\ &= \frac{2e^2 N_\mathrm{F}}{\beta}\sum_{i\omega_n'}\frac{1}{\tau_0|\omega_n| + \tau_0 Dq^2}\int \mathrm{d}\xi \frac{1}{\left(\xi - i\hbar\omega_n' - \frac{i\hbar}{2\tau_0}\right)\left(\xi - i\hbar\omega_n' + \frac{i\hbar}{2\tau_0}\right)} \\ &= \frac{2e^2 N_\mathrm{F}}{\beta}\sum_{i\omega_n'}\frac{1}{\tau_0|\omega_n| + \tau_0 Dq^2}\frac{2\pi\tau_0}{\hbar},\end{aligned} \tag{A.97}$$

where the integral has been evaluated using the residuum theorem. The condition "<", which is $\Theta(-\omega_+\omega_-)$, yields the constraint

$$-\left|\frac{\omega_n}{2}\right| < \omega_n' < \left|\frac{\omega_n}{2}\right|, \tag{A.98}$$

and the sum over the fermionic Matsubara frequencies ω_n' results in $|n|$ equal contributions, while the bosonic frequencies are given by

$$\frac{2\pi|n|}{\hbar\beta} = |\omega_n|. \tag{A.99}$$

Therefore,

$$\chi(\mathbf{q}, i\omega_n)^< = 2e^2 N_\mathrm{F}\frac{|\omega_n|}{|\omega_n| + Dq^2}, \tag{A.100}$$

and the final result is

$$\chi(\mathbf{q}, i\omega_n) = -2e^2 N_\mathrm{F}\left(1 - \frac{|\omega_n|}{|\omega_n| + Dq^2}\right) = -2e^2 N_\mathrm{F}\frac{Dq^2}{|\omega_n| + Dq^2}. \tag{A.101}$$

For real frequencies, this defines the charge susceptibility,

$$\chi(\mathbf{q}, \omega) = -2e^2 N_\mathrm{F}\left(\frac{Dq^2}{Dq^2 - i\omega}\right). \tag{A.102}$$

This result can be used to derive the conductivity [23, 33]:

$$\sigma = \lim_{\omega\to 0}\lim_{q\to 0}\frac{i\omega}{q^2}\chi(\mathbf{q}, \omega), \tag{A.103}$$

where $2N_\mathrm{F}D = {}^{n\tau_0}/_m$ according to Eq. (A.60) and Eq. (A.93), and the Einstein relation is revealed:

$$\sigma = 2e^2 N_\mathrm{F} D = \frac{e^2 n\tau_0}{m}. \tag{A.104}$$

B Matrices for the Multiband Cooperon

For the spin-3/2 Dresselhaus Hamiltonian, Eq. (2.215), we list for each spin sector the corresponding matrices of the $\mathcal{L}$ operator. In addition, we list the determinants $\mathcal{D} = |\mathcal{L}/\kappa|$ of those matrices as well as the sum over diagonal minors, $\mathcal{M} = \sum_m |\mathcal{L}_{mm}/\kappa|$. The sum over inverse eigenvalues is given by $\mathcal{M}/\mathcal{D}$, and the magneto-conductivity can be calculated via Eq. (2.225).

Spin singlet $j = 0$ sector

The spin singlet is described by a one-level system without any internal structure. The solution is equal to the singlet contribution in the ILP calculation.

$$\frac{\mathcal{L}^{(0)}}{\kappa} = a_{n,0}, \tag{B.1}$$

where the sum over inverse eigenvalues is given by

$$-\sum_n \frac{\kappa}{E^{(0)}(n)} = -\sum_n \frac{1}{a_{n,0}}. \tag{B.2}$$

Spin triplet $j = 1$ sector

The spin triplet case is described by a three-level system; the solution is equivalent to the triplet contribution in the ILP calculation. The spin matrices are given by

$$J_+ = \begin{pmatrix} 0 & \sqrt{2} & 0 \\ 0 & 0 & \sqrt{2} \\ 0 & 0 & 0 \end{pmatrix}, \quad J_- = \begin{pmatrix} 0 & 0 & 0 \\ \sqrt{2} & 0 & 0 \\ 0 & \sqrt{2} & 0 \end{pmatrix}, \quad J_z = \begin{pmatrix} 1 & 0 & 0 \\ 0 & 0 & 0 \\ 0 & 0 & -1 \end{pmatrix}. \tag{B.3}$$

The corresponding $\mathcal{L}$ operators are identical to the ILP calculation,

$$\frac{\mathcal{L}^{(1)}(n \geq 1)}{\kappa} = \begin{pmatrix} a_{n-1,1} & -\sqrt{\frac{2nB'_{so}}{B}} & 0 \\ -\sqrt{\frac{2nB'_{so}}{B}} & a_{n,2} & -\sqrt{\frac{2(n+1)B'_{so}}{B}} \\ 0 & -\sqrt{\frac{2(n+1)B'_{so}}{B}} & a_{n+1,1} \end{pmatrix}, \tag{B.4}$$

and

$$\frac{\mathcal{L}^{(1)}(n=0, m=0)}{\kappa} = \begin{pmatrix} a_{0,2} & -\sqrt{\frac{2B'_{so}}{B}} \\ -\sqrt{\frac{2B'_{so}}{B}} & a_{1,1} \end{pmatrix}, \qquad \frac{\mathcal{L}^{(1)}(n=0, m=-1)}{\kappa} = a_{0,1}. \tag{B.5}$$

For the triplet sector, we find the ILP result,

$$\sum_{n,m} \frac{\kappa}{E_m(n)} = \frac{1}{a_{0,1}} + \frac{a_{1,1} + a_{0,2}}{a_{1,1}a_{0,2} - 2\frac{B'_{so}}{B}} + \sum_{n=1}^{n_{max}} \left(\frac{a_{n,1}^2 + 2a_{n,1}a_{n,2} - 1 - 2(2n+1)\frac{B'_{so}}{B}}{a_{n,2}\left(a_{n,1}^2 - 1\right) - 2\frac{B'_{so}}{B}\left[(2n+1)a_{n,1} - 1\right]} \right). \tag{B.6}$$

Spin quintet $j = 2$ sector

The spin quintet corresponds to a five level system where each Landau level splits into five sub-levels. The spin matrices are given by

$$J_+ = \begin{pmatrix} 0 & 2 & 0 & 0 & 0 \\ 0 & 0 & \sqrt{6} & 0 & 0 \\ 0 & 0 & 0 & \sqrt{6} & 0 \\ 0 & 0 & 0 & 0 & 2 \\ 0 & 0 & 0 & 0 & 0 \end{pmatrix}, \quad J_- = \begin{pmatrix} 0 & 0 & 0 & 0 & 0 \\ 2 & 0 & 0 & 0 & 0 \\ 0 & \sqrt{6} & 0 & 0 & 0 \\ 0 & 0 & \sqrt{6} & 0 & 0 \\ 0 & 0 & 0 & 2 & 0 \end{pmatrix}, \quad J_z = \begin{pmatrix} 2 & 0 & 0 & 0 & 0 \\ 0 & 1 & 0 & 0 & 0 \\ 0 & 0 & 0 & 0 & 0 \\ 0 & 0 & 0 & -1 & 0 \\ 0 & 0 & 0 & 0 & -2 \end{pmatrix}. \tag{B.7}$$

Due to the finite number of possible increments of the J_z quantum number, the $\mathcal{L}$ operator becomes block diagonal in a five-dimensional space of Landau levels with distinct level and magnetic quantum number,

$$\frac{\mathcal{L}^{(2)}(n \geq 2)}{\kappa} = \begin{pmatrix} a_{n-2,2} & -\sqrt{\frac{4(n-1)B'_{so}}{B}} & 0 & 0 & 0 \\ -\sqrt{\frac{4(n-1)B'_{so}}{B}} & a_{n-1,5} & -\sqrt{\frac{6nB'_{so}}{B}} & 0 & 0 \\ 0 & -\sqrt{\frac{6nB'_{so}}{B}} & a_{n,6} & -\sqrt{\frac{6(n+1)B'_{so}}{B}} & 0 \\ 0 & 0 & -\sqrt{\frac{6(n+1)B'_{so}}{B}} & a_{n+1,5} & -\sqrt{\frac{4(n+2)B'_{so}}{B}} \\ 0 & 0 & 0 & -\sqrt{\frac{4(n+2)B'_{so}}{B}} & a_{n+2,2} \end{pmatrix}, \tag{B.8}$$

$$\begin{aligned} \mathcal{D}(n \geq 2) = {} & a_{n-2,2}a_{n-1,5}a_{n,6}a_{n+1,5}a_{n+2,2} \\ & - 2\frac{B'_{so}}{B}\left[2(n+2)a_{n-2,2}a_{n-1,5}a_{n,6} + 3(n+1)a_{n-2,2}a_{n-1,5}a_{n+2,2}\right. \\ & \qquad \left. + 3na_{n-2,2}a_{n+1,5}a_{n+2,2} + 2(n-1)a_{n,6}a_{n+1,5}a_{n+2,2}\right] \\ & + 8\left(\frac{B'_{so}}{B}\right)^2\left[3n(n+2)a_{n-2,2} + 2(n-1)(n+2)a_{n,6} + 3(n-1)(n+1)a_{n+2,2}\right], \end{aligned} \tag{B.9}$$

$$\begin{aligned} \mathcal{M}(n \geq 2) = {} & a_{n-2,2}a_{n-1,5}a_{n,6}a_{n+1,5} + a_{n-2,2}a_{n-1,5}a_{n,6}a_{n+2,2} \\ & + a_{n-2,2}a_{n-1,5}a_{n+1,5}a_{n+2,2} + a_{n-2,2}a_{n,6}a_{n+1,5}a_{n+2,2} + a_{n-1,5}a_{n,6}a_{n+1,5}a_{n+2,2} \\ & - 2\frac{B'_{so}}{B}\left[2(n+2)a_{n-2,2}a_{n,6} + 3(2n+1)a_{n-2,2}a_{n+2,2} + 2(n-1)a_{n,6}a_{n+2,2}\right. \\ & \qquad + 2(n-1)a_{n,6}a_{n+1,5} + (5n+7)a_{n-2,2}a_{n-1,5} + (5n-2)a_{n+1,5}a_{n+2,2} \\ & \qquad \left. + 2(n+2)a_{n-1,5}a_{n,6} + 3(n+1)a_{n-1,5}a_{n+2,2} + 3na_{n-2,2}a_{n+1,5}\right] \\ & + 8\left(\frac{B'_{so}}{B}\right)^2\left(8n^2 + 8n - 7\right), \end{aligned} \tag{B.10}$$

and

$$\frac{\mathcal{L}^{(2)}(n=0,m=1)}{\kappa} = \begin{pmatrix} a_{0,5} & -\sqrt{\frac{6B'_{\rm so}}{B}} & 0 & 0 \\ -\sqrt{\frac{6B'_{\rm so}}{B}} & a_{1,6} & -\sqrt{\frac{12B'_{\rm so}}{B}} & 0 \\ 0 & -\sqrt{\frac{12B'_{\rm so}}{B}} & a_{2,5} & -\sqrt{\frac{12B'_{\rm so}}{B}} \\ 0 & 0 & -\sqrt{\frac{12B'_{\rm so}}{B}} & a_{3,2} \end{pmatrix}, \tag{B.11}$$

$$\mathcal{D} = a_{0,5}a_{1,6}a_{2,5}a_{3,2} - 6\frac{B'_{\rm so}}{B}\left(2a_{0,5}a_{1,6} + 2a_{0,5}a_{3,2} + a_{2,5}a_{3,2}\right) + 72\left(\frac{B'_{\rm so}}{B}\right)^2, \tag{B.12}$$

$$\mathcal{M} = a_{0,5}a_{1,6}a_{2,5} + a_{0,5}a_{1,6}a_{3,2} + a_{0,5}a_{2,5}a_{3,2} + a_{1,6}a_{2,5}a_{3,2} - 6\frac{B'_{\rm so}}{B}\left(4a_{0,5} + 2a_{1,6} + a_{2,5} + 3a_{3,2}\right), \tag{B.13}$$

and

$$\frac{\mathcal{L}^{(2)}(n=0,m=0)}{\kappa} = \begin{pmatrix} a_{0,6} & -\sqrt{\frac{6B'_{\rm so}}{B}} & 0 \\ -\sqrt{\frac{6B'_{\rm so}}{B}} & a_{1,5} & -\sqrt{\frac{8B'_{\rm so}}{B}} \\ 0 & -\sqrt{\frac{8B'_{\rm so}}{B}} & a_{2,2} \end{pmatrix}, \tag{B.14}$$

$$\mathcal{D} = a_{0,6}a_{1,5}a_{2,2} - 2\frac{B'_{\rm so}}{B}\left(4a_{0,6} + 3a_{2,2}\right), \tag{B.15}$$

$$\mathcal{M} = a_{0,6}a_{1,5} + a_{0,6}a_{2,2} + a_{1,5}a_{2,2} - 14\frac{B'_{\rm so}}{B}, \tag{B.16}$$

and

$$\frac{\mathcal{L}^{(2)}(n=0,m=-1)}{\kappa} = \begin{pmatrix} a_{0,5} & -\sqrt{\frac{4B'_{\rm so}}{B}} \\ -\sqrt{\frac{4B'_{\rm so}}{B}} & a_{1,2} \end{pmatrix}, \tag{B.17}$$

$$\mathcal{D} = a_{0,5}a_{1,2} - 4\frac{B'_{\rm so}}{B}, \tag{B.18}$$

$$\mathcal{M} = a_{0,5} + a_{1,2}, \tag{B.19}$$

and

$$\frac{\mathcal{L}^{(2)}(n=0,m=-2)}{\kappa} = a_{0,2}, \tag{B.20}$$

$$\mathcal{D} = a_{0,2}, \tag{B.21}$$

$$\mathcal{M} = 1. \tag{B.22}$$

Similar to the singlet channel, this contribution is assigned with a minus.

Spin septet $j = 3$ sector

The spin matrices for the septet sector are given by

$$J_+ = \begin{pmatrix} 0 & \sqrt{6} & 0 & 0 & 0 & 0 & 0 \\ 0 & 0 & \sqrt{10} & 0 & 0 & 0 & 0 \\ 0 & 0 & 0 & 2\sqrt{3} & 0 & 0 & 0 \\ 0 & 0 & 0 & 0 & 2\sqrt{3} & 0 & 0 \\ 0 & 0 & 0 & 0 & 0 & \sqrt{10} & 0 \\ 0 & 0 & 0 & 0 & 0 & 0 & \sqrt{6} \\ 0 & 0 & 0 & 0 & 0 & 0 & 0 \end{pmatrix}, \quad J_- = \begin{pmatrix} 0 & 0 & 0 & 0 & 0 & 0 & 0 \\ \sqrt{6} & 0 & 0 & 0 & 0 & 0 & 0 \\ 0 & \sqrt{10} & 0 & 0 & 0 & 0 & 0 \\ 0 & 0 & 2\sqrt{3} & 0 & 0 & 0 & 0 \\ 0 & 0 & 0 & 2\sqrt{3} & 0 & 0 & 0 \\ 0 & 0 & 0 & 0 & \sqrt{10} & 0 & 0 \\ 0 & 0 & 0 & 0 & 0 & \sqrt{6} & 0 \end{pmatrix},$$

$$J_z = \begin{pmatrix} 3 & 0 & 0 & 0 & 0 & 0 & 0 \\ 0 & 2 & 0 & 0 & 0 & 0 & 0 \\ 0 & 0 & 1 & 0 & 0 & 0 & 0 \\ 0 & 0 & 0 & 0 & 0 & 0 & 0 \\ 0 & 0 & 0 & 0 & -1 & 0 & 0 \\ 0 & 0 & 0 & 0 & 0 & -2 & 0 \\ 0 & 0 & 0 & 0 & 0 & 0 & -3 \end{pmatrix}, \tag{B.23}$$

and the $\mathcal{L}$ operator becomes block diagonal in a seven-dimensional subspace,

$$\frac{\mathcal{L}^{(3)}(n \geq 3)}{\kappa} =$$

$$\begin{pmatrix} a_{n-3,3} & -\sqrt{\frac{6(n-2)B'_{so}}{B}} & 0 & 0 & 0 & 0 & 0 \\ -\sqrt{\frac{6(n-2)B'_{so}}{B}} & a_{n-2,8} & -\sqrt{\frac{10(n-1)B'_{so}}{B}} & 0 & 0 & 0 & 0 \\ 0 & -\sqrt{\frac{10(n-1)B'_{so}}{B}} & a_{n-1,11} & -\sqrt{\frac{12nB'_{so}}{B}} & 0 & 0 & 0 \\ 0 & 0 & -\sqrt{\frac{12nB'_{so}}{B}} & a_{n,12} & -\sqrt{\frac{12(n+1)B'_{so}}{B}} & 0 & 0 \\ 0 & 0 & 0 & -\sqrt{\frac{12(n+1)B'_{so}}{B}} & a_{n+1,11} & -\sqrt{\frac{10(n+2)B'_{so}}{B}} & 0 \\ 0 & 0 & 0 & 0 & -\sqrt{\frac{10(n+2)B'_{so}}{B}} & a_{n+2,8} & -\sqrt{\frac{6(n+3)B'_{so}}{B}} \\ 0 & 0 & 0 & 0 & 0 & -\sqrt{\frac{6(n+3)B'_{so}}{B}} & a_{n+3,3} \end{pmatrix}, \tag{B.24}$$

$$
\begin{aligned}
\mathcal{D} = {} & a_{n-3,3}a_{n-2,8}a_{n-1,11}a_{n,12}a_{n+1,11}a_{n+2,8}a_{n+3,3} \\
& - 2\frac{B'_{\rm so}}{B}\Big[3(n+3)a_{n-3,3}a_{n-2,8}a_{n-1,11}a_{n,12}a_{n+1,11} + 5(n+2)a_{n-3,3}a_{n-2,8}a_{n-1,11}a_{n,12}a_{n+3,3} \\
& \quad + 6(n+1)a_{n-3,3}a_{n-2,8}a_{n-1,11}a_{n+2,8}a_{n+3,3} + 6na_{n-3,3}a_{n-2,8}a_{n+1,11}a_{n+2,8}a_{n+3,3} \\
& \quad + 5(n-1)a_{n-3,3}a_{n,12}a_{n+1,11}a_{n+2,8}a_{n+3,3} + 3(n-2)a_{n-1,11}a_{n,12}a_{n+1,11}a_{n+2,8}a_{n+3,3}\Big] \\
& + 4\left(\frac{B'_{\rm so}}{B}\right)^2\Big[18(n+3)(n+1)a_{n-3,3}a_{n-2,8}a_{n-1,11} + 18n(n+3)a_{n-3,3}a_{n-2,8}a_{n+1,11} \\
& \quad + 30n(n+2)a_{n-3,3}a_{n-2,8}a_{n+3,3} + 15(n-1)(n+3)a_{n-3,3}a_{n,12}a_{n+1,11} \\
& \quad + 25(n-1)(n+2)a_{n-3,3}a_{n,12}a_{n+3,3} + 30(n-1)(n+1)a_{n-3,3}a_{n+2,8}a_{n+3,3} \\
& \quad + 9(n-2)(n+3)a_{n-1,11}a_{n,12}a_{n+1,11} + 15(n-2)(n+2)a_{n-1,11}a_{n,12}a_{n+3,3} \\
& \quad + 18(n-2)(n+1)a_{n-1,11}a_{n+2,8}a_{n+3,3} + 18n(n-2)a_{n+1,11}a_{n+2,8}a_{n+3,3}\Big] \\
& - 144\left(\frac{B'_{\rm so}}{B}\right)^3\Big[5(n-1)(n+1)(n+3)a_{n-3,3} + 3(n-2)(n+1)(n+3)a_{n-1,11} \\
& \quad + 3(n-2)n(n+3)a_{n+1,11} + 5(n-2)n(n+2)a_{n+3,3}\Big],
\end{aligned}
\tag{B.25}
$$

$$
\begin{aligned}
\mathcal{M} = {} & a_{n-3,3}a_{n-2,8}a_{n-1,11}a_{n,12}a_{n+1,11}a_{n+2,8} + a_{n-3,3}a_{n-2,8}a_{n-1,11}a_{n,12}a_{n+1,11}a_{n+3,3} \\
& + a_{n-3,3}a_{n-2,8}a_{n-1,11}a_{n,12}a_{n+2,8}a_{n+3,3} + a_{n-3,3}a_{n-2,8}a_{n-1,11}a_{n+1,11}a_{n+2,8}a_{n+3,3} \\
& + a_{n-3,3}a_{n-2,8}a_{n,12}a_{n+1,11}a_{n+2,8}a_{n+3,3} + a_{n-3,3}a_{n-1,11}a_{n,12}a_{n+1,11}a_{n+2,8}a_{n+3,3} \\
& + a_{n-2,8}a_{n-1,11}a_{n,12}a_{n+1,11}a_{n+2,8}a_{n+3,3} \\
& - 2\frac{B'_{\rm so}}{B}\Big[(8n+19)a_{n-3,3}a_{n-2,8}a_{n-1,11}a_{n,12} + 3(n+3)a_{n-3,3}a_{n-2,8}a_{n-1,11}a_{n+1,11} \\
& \quad + 3(n+3)a_{n-3,3}a_{n-2,8}a_{n,12}a_{n+1,11} + 3(n+3)a_{n-3,3}a_{n-1,11}a_{n,12}a_{n+1,11} \\
& \quad + 3(n+3)a_{n-2,8}a_{n-1,11}a_{n,12}a_{n+1,11} + 6(n+1)a_{n-3,3}a_{n-2,8}a_{n-1,11}a_{n+2,8} \\
& \quad + 6na_{n-3,3}a_{n-2,8}a_{n+1,11}a_{n+2,8} + 5(n-1)a_{n-3,3}a_{n,12}a_{n+1,11}a_{n+2,8} \\
& \quad + 3(n-2)a_{n-1,11}a_{n,12}a_{n+1,11}a_{n+2,8} + (11n+16)a_{n-3,3}a_{n-2,8}a_{n-1,11}a_{n+3,3} \\
& \quad + 5(n+2)a_{n-3,3}a_{n-2,8}a_{n,12}a_{n+3,3} + 5(n+2)a_{n-3,3}a_{n-1,11}a_{n,12}a_{n+3,3} \\
& \quad + 5(n+2)a_{n-2,8}a_{n-1,11}a_{n,12}a_{n+3,3} + 6na_{n-3,3}a_{n-2,8}a_{n+1,11}a_{n+3,3} \\
& \quad + 5(n-1)a_{n-3,3}a_{n,12}a_{n+1,11}a_{n+3,3} + 3(n-2)a_{n-1,11}a_{n,12}a_{n+1,11}a_{n+3,3} \\
& \quad + 6(2n+1)a_{n-3,3}a_{n-2,8}a_{n+2,8}a_{n+3,3} + 5(n-1)a_{n-3,3}a_{n,12}a_{n+2,8}a_{n+3,3} \\
& \quad + 6(n+1)a_{n-3,3}a_{n-1,11}a_{n+2,8}a_{n+3,3} + 6(n+1)a_{n-2,8}a_{n-1,11}a_{n+2,8}a_{n+3,3} \\
& \quad + 3(n-2)a_{n-1,11}a_{n,12}a_{n+2,8}a_{n+3,3} + (11n-5)a_{n-3,3}a_{n+1,11}a_{n+2,8}a_{n+3,3} \\
& \quad + 6na_{n-2,8}a_{n+1,11}a_{n+2,8}a_{n+3,3} + 3(n-2)a_{n-1,11}a_{n+1,11}a_{n+2,8}a_{n+3,3} \\
& \quad + (8n-11)a_{n,12}a_{n+1,11}a_{n+2,8}a_{n+3,3}\Big] \\
& + 4\left(\frac{B'_{\rm so}}{B}\right)^2\Big[6(11n^2+31n+9)a_{n-3,3}a_{n-2,8} + 18(n+1)(n+3)a_{n-3,3}a_{n-1,11} \\
& \quad + 5(n-1)(8n+19)a_{n-3,3}a_{n,12} + 3(n+3)(11n-5)a_{n-3,3}a_{n+1,11} \\
& \quad + 30(n^2-1)a_{n-3,3}a_{n+2,8} + 5(17n^2+17n-16)a_{n-3,3}a_{n+3,3} \\
& \quad + 18(n+1)(n+3)a_{n-2,8}a_{n-1,11} + 18n(n+3)a_{n-2,8}a_{n+1,11} \\
& \quad + 30n(n+2)a_{n-2,8}a_{n+3,3} + 3(n-2)(8n+19)a_{n-1,11}a_{n,12} \\
& \quad + 9(n-2)(n+3)a_{n-1,11}a_{n+1,11} + 18(n-2)(n+1)a_{n-1,11}a_{n+2,8} \\
& \quad + 3(n-2)(11n+16)a_{n-1,11}a_{n+3,3} + 3(n+3)(8n-11)a_{n,12}a_{n+1,11} \\
& \quad + 5(n+2)(8n-11)a_{n,12}a_{n+3,3} + 18n(n-2)a_{n+1,11}a_{n+2,8} \\
& \quad + 18n(n-2)a_{n+1,11}a_{n+3,3} + 6(11n^2-9n-11)a_{n+2,8}a_{n+3,3}\Big] \\
& - 144\left(\frac{B'_{\rm so}}{B}\right)^3\Big[16n^3+24n^2-58n-33\Big],
\end{aligned}
\tag{B.26}
$$

and

$$\frac{\mathcal{L}^{(3)}(n=0,m=2)}{\kappa} = \begin{pmatrix} a_{0,8} & -\sqrt{\frac{10B'_{so}}{B}} & 0 & 0 & 0 & 0 \\ -\sqrt{\frac{10B'_{so}}{B}} & a_{1,11} & -\sqrt{\frac{24B'_{so}}{B}} & 0 & 0 & 0 \\ 0 & -\sqrt{\frac{24B'_{so}}{B}} & a_{2,12} & -\sqrt{\frac{36B'_{so}}{B}} & 0 & 0 \\ 0 & 0 & -\sqrt{\frac{36B'_{so}}{B}} & a_{3,11} & -\sqrt{\frac{40B'_{so}}{B}} & 0 \\ 0 & 0 & 0 & -\sqrt{\frac{40B'_{so}}{B}} & a_{4,8} & -\sqrt{\frac{30B'_{so}}{B}} \\ 0 & 0 & 0 & 0 & -\sqrt{\frac{30B'_{so}}{B}} & a_{5,3} \end{pmatrix}, \tag{B.27}$$

$$\begin{aligned} \mathcal{D} &= a_{0,8}a_{1,11}a_{2,12}a_{3,11}a_{4,8}a_{5,3} \\ &\quad - 2\frac{B'_{so}}{B}\left[15a_{0,8}a_{1,11}a_{2,12}a_{3,11} + 20a_{0,8}a_{1,11}a_{2,12}a_{5,3} + 18a_{0,8}a_{1,11}a_{4,8}a_{5,3}\right. \\ &\qquad \left. +12a_{0,8}a_{3,11}a_{4,8}a_{5,3} + 5a_{2,12}a_{3,11}a_{4,8}a_{5,3}\right] \\ &\quad + 20\left(\frac{B'_{so}}{B}\right)^2\left[54a_{0,8}a_{1,11} + 36a_{0,8}a_{3,11} + 48a_{0,8}a_{5,3} + 15a_{2,12}a_{3,11} + 20a_{2,12}a_{5,3} + 18a_{4,8}a_{5,3}\right] \\ &\quad - 10800\left(\frac{B'_{so}}{B}\right)^3, \end{aligned} \tag{B.28}$$

$$\begin{aligned} \mathcal{M} &= a_{0,8}a_{1,11}a_{2,12}a_{3,11}a_{4,8} + a_{0,8}a_{1,11}a_{2,12}a_{3,11}a_{5,3} + a_{0,8}a_{1,11}a_{2,12}a_{4,8}a_{5,3} \\ &\quad + a_{0,8}a_{1,11}a_{3,11}a_{4,8}a_{5,3} + a_{0,8}a_{2,12}a_{3,11}a_{4,8}a_{5,3} + a_{1,11}a_{2,12}a_{3,11}a_{4,8}a_{5,3} \\ &\quad - 2\frac{B'_{so}}{B}\left[35a_{0,8}a_{1,11}a_{2,12} + 15a_{0,8}a_{1,11}a_{3,11} + 18a_{0,8}a_{1,11}a_{4,8} + 38a_{0,8}a_{1,11}a_{5,3}\right. \\ &\qquad + 15a_{0,8}a_{2,12}a_{3,11} + 20a_{0,8}a_{2,12}a_{5,3} + 12a_{0,8}a_{3,11}a_{4,8} + 12a_{0,8}a_{3,11}a_{5,3} \\ &\qquad + 30a_{0,8}a_{4,8}a_{5,3} + 15a_{1,11}a_{2,12}a_{3,11} + 20a_{1,11}a_{2,12}a_{5,3} + 18a_{1,11}a_{4,8}a_{5,3} \\ &\qquad \left. +5a_{2,12}a_{3,11}a_{4,8} + 5a_{2,12}a_{3,11}a_{5,3} + 5a_{2,12}a_{4,8}a_{5,3} + 17a_{3,11}a_{4,8}a_{5,3}\right] \\ &\quad + 20\left(\frac{B'_{so}}{B}\right)^2\left[138a_{0,8} + 54a_{1,11} + 35a_{2,12} + 51a_{3,11} + 18a_{4,8} + 86a_{5,3}\right], \end{aligned} \tag{B.29}$$

and

$$\frac{\mathcal{L}^{(3)}(n=0,m=1)}{\kappa} = \begin{pmatrix} a_{0,11} & -\sqrt{\frac{12B'_{so}}{B}} & 0 & 0 & 0 \\ -\sqrt{\frac{12B'_{so}}{B}} & a_{1,12} & -\sqrt{\frac{24B'_{so}}{B}} & 0 & 0 \\ 0 & -\sqrt{\frac{24B'_{so}}{B}} & a_{2,11} & -\sqrt{\frac{30B'_{so}}{B}} & 0 \\ 0 & 0 & -\sqrt{\frac{30B'_{so}}{B}} & a_{3,8} & -\sqrt{\frac{24B'_{so}}{B}} \\ 0 & 0 & 0 & -\sqrt{\frac{24B'_{so}}{B}} & a_{4,3} \end{pmatrix}, \tag{B.30}$$

$$\begin{aligned} \mathcal{D} = {} & a_{0,11}a_{1,12}a_{2,11}a_{3,8}a_{4,3} \\ & - 6\frac{B'_{so}}{B}\left[4a_{0,11}a_{1,12}a_{2,11} + 5a_{0,11}a_{1,12}a_{4,3} + 4a_{0,11}a_{3,8}a_{4,3} + 2a_{2,11}a_{3,8}a_{4,3}\right], \\ & + 72\left(\frac{B'_{so}}{B}\right)^2\left[8a_{0,11} + 4a_{2,11} + 5a_{4,3}\right], \end{aligned} \tag{B.31}$$

$$\begin{aligned} \mathcal{M} = {} & a_{0,11}a_{1,12}a_{2,11}a_{3,8} + a_{0,11}a_{1,12}a_{2,11}a_{4,3} + a_{0,11}a_{1,12}a_{3,8}a_{4,3} \\ & + a_{0,11}a_{2,11}a_{3,8}a_{4,3} + a_{1,12}a_{2,11}a_{3,8}a_{4,3} \\ & - 6\frac{B'_{so}}{B}\left(9a_{0,11}a_{1,12} + 4a_{0,11}a_{2,11} + 4a_{0,11}a_{3,8} + 9a_{0,11}a_{4,3} + 4a_{1,12}a_{2,11}\right. \\ & \qquad \left. +5a_{1,12}a_{4,3} + 2a_{2,11}a_{3,8} + 2a_{2,11}a_{4,3} + 6a_{3,8}a_{4,3}\right) \\ & + 1224\left(\frac{B'_{so}}{B}\right)^2, \end{aligned} \tag{B.32}$$

and

$$\frac{\mathcal{L}^{(3)}(n=0,m=0)}{\kappa} = \begin{pmatrix} a_{0,12} & -\sqrt{\frac{12B'_{so}}{B}} & 0 & 0 \\ -\sqrt{\frac{12B'_{so}}{B}} & a_{1,11} & -\sqrt{\frac{20B'_{so}}{B}} & 0 \\ 0 & -\sqrt{\frac{20B'_{so}}{B}} & a_{2,8} & -\sqrt{\frac{18B'_{so}}{B}} \\ 0 & 0 & -\sqrt{\frac{18B'_{so}}{B}} & a_{3,3} \end{pmatrix}, \tag{B.33}$$

$$\mathcal{D} = a_{0,12}a_{1,11}a_{2,8}a_{3,3} - 2\frac{B'_{so}}{B}\left(9a_{0,12}a_{1,11} + 10a_{0,12}a_{3,3} + 6a_{2,8}a_{3,3}\right) + 216\left(\frac{B'_{so}}{B}\right)^2, \tag{B.34}$$

$$\begin{aligned} \mathcal{M} = {} & a_{0,12}a_{1,11}a_{2,8} + a_{0,12}a_{1,11}a_{3,3} + a_{0,12}a_{2,8}a_{3,3} + a_{1,11}a_{2,8}a_{3,3} \\ & - 2\frac{B'_{so}}{B}\left(19a_{0,12} + 9a_{1,11} + 6a_{2,8} + 16a_{3,3}\right), \end{aligned} \tag{B.35}$$

and

$$\frac{\mathcal{L}^{(3)}(n=0,m=-1)}{\kappa} = \begin{pmatrix} a_{0,11} & -\sqrt{\frac{10B'_{\mathrm{so}}}{B}} & 0 \\ -\sqrt{\frac{10B'_{\mathrm{so}}}{B}} & a_{1,8} & -\sqrt{\frac{12B'_{\mathrm{so}}}{B}} \\ 0 & -\sqrt{\frac{12B'_{\mathrm{so}}}{B}} & a_{2,3} \end{pmatrix}, \tag{B.36}$$

$$\mathcal{D} = a_{0,11}a_{1,8}a_{2,3} - 2\frac{B'_{\mathrm{so}}}{B}\left(6a_{0,11} + 5a_{2,3}\right), \tag{B.37}$$

$$\mathcal{M} = a_{0,11}a_{2,3} + a_{1,8}a_{2,3} + a_{0,11}a_{1,8} - 22\frac{B'_{\mathrm{so}}}{B}, \tag{B.38}$$

and

$$\frac{\mathcal{L}^{(3)}(n=0,m=-2)}{\kappa} = \begin{pmatrix} a_{0,8} & -\sqrt{\frac{6B'_{\mathrm{so}}}{B}} \\ -\sqrt{\frac{6B'_{\mathrm{so}}}{B}} & a_{1,3} \end{pmatrix}, \tag{B.39}$$

$$\mathcal{D} = a_{0,8}a_{1,3} - 6\frac{B'_{\mathrm{so}}}{B}, \tag{B.40}$$

$$\mathcal{M} = a_{0,8} + a_{1,3}, \tag{B.41}$$

and

$$\frac{\mathcal{L}^{(3)}(n=0,m=-3)}{\kappa} = a_{0,3}, \tag{B.42}$$

$$\mathcal{D} = a_{0,3}, \tag{B.43}$$

$$\mathcal{M} = 1. \tag{B.44}$$

C Fitting Multiband Data

Contents

For the theory of WL and WAL in magnetic fields, it is assumed that the mean free path of the particle is much smaller than the magnetic length, and that the all-dominant effect of the magnetic field is the quantization of the Cooperon momentum. However, this is not always the case in an experiment. Especially in multiband systems, the observed results might drastically deviate from the magneto-conductivity formulas in Chap. 2 due to the multiband Hall effect.

In this appendix, we construct a tool to explain magneto-transport data for experiments where the multiband Hall effect and the WL/WAL corrections have similar impact. We treat the electron quantum mechanically in terms of the corrections to the resistance, but semi-classical in terms of the Hall effect. In the data analysis we discuss in Sec. 3.2, we use the results of this appendix for the fitting procedure.

C.1 Disentangling Hall Effect and Quantum Corrections

C.1.1 One Charge Carrier Type

To determine the classical Hall effect, we first discuss the cyclotron motion of an electron in electric and magnetic fields. We use the Drude picture, where an electron with charge $(-e)$ in an electric field $\mathbf{E}$ gains a drift velocity

$$\mathbf{v}_\mathrm{d} = -e\mathbf{E}\frac{\tau}{m}, \tag{C.1}$$

where τ is the mean time between collisions. The current density is defined as

$$\mathbf{j} = -ne\mathbf{v}_\mathrm{d} = \sigma_0\mathbf{E}, \tag{C.2}$$

where

$$\sigma_0 = \frac{ne^2\tau}{m} = \frac{1}{\rho_0} \tag{C.3}$$

is the Drude conductivity and the zero index denotes the magnetic field independence. In addition, we consider a magnetic field $\mathbf{B}$, and the drift velocity is self-consistently replaced with[1]

$$\mathbf{v}_\mathrm{d} = -e\frac{\tau}{m}\left(\mathbf{E} + \mathbf{v}_\mathrm{d} \times \mathbf{B}\right), \tag{C.4}$$

which leads to a modified equation for the current density,[2]

$$\mathbf{j} = \sigma_0 \mathbf{E} - \frac{e\tau}{m}\mathbf{j} \times \mathbf{B}. \tag{C.5}$$

For a magnetic field perpendicular to the xy-plane, $\mathbf{B} = B\mathbf{e}_\mathrm{z}$, we find

$$\begin{pmatrix} E_\mathrm{x} \\ E_\mathrm{y} \end{pmatrix} = \rho_0 \begin{pmatrix} j_\mathrm{x} \\ j_\mathrm{y} \end{pmatrix} + \frac{B}{ne}\begin{pmatrix} j_\mathrm{y} \\ -j_\mathrm{x} \end{pmatrix} \tag{C.6}$$

which is, written in matrix form,

$$\begin{pmatrix} E_\mathrm{x} \\ E_\mathrm{y} \end{pmatrix} = \begin{pmatrix} \rho_0 & \frac{B}{en} \\ -\frac{B}{en} & \rho_0 \end{pmatrix}\begin{pmatrix} j_\mathrm{x} \\ j_\mathrm{y} \end{pmatrix}. \tag{C.7}$$

Equation (C.7) defines the resistivity tensor. Whereas the Hall effect manifests itself as a linear field dependence in the transversal component, the longitudinal component is not influenced by the field.

The conductivity tensor is given by inversion of the resistivity,

$$\sigma = \rho^{-1} = \frac{1}{\rho_0^2 + \left(\frac{B}{en}\right)^2}\begin{pmatrix} \rho_0 & -\frac{B}{en} \\ \frac{B}{en} & \rho_0 \end{pmatrix}. \tag{C.8}$$

Note that the longitudinal conductivity, contrary to the longitudinal resistivity, is dependent on the magnetic field due to the matrix inversion, $\sigma_{xx} = \sigma_0\left[1 - \sigma_0^2\,(B/en)^2\right] + O(B^4)$.

So far, we assumed electronic charge carriers. In the case of transport by holes, the formulas have to be adjusted. Formulas for both cases are summarized in Tab. C.1. The expressions of the current density are identical for both, electrons and holes. However, the drift velocities, which enter the Hall conductivity, have opposite sign. Therefore, a Hall measurement can determine the sign of the charge for the relevant charge carriers. In the fitting procedure, we keep the sign of the elementary charge e fixed and positive, but assign negative values for the case of the hole mobility μ_h as well as for the hole density n_h.[3]

[1] The drift velocity $\mathbf{v}_\mathrm{d}$ in this equation is considered to point in the direction of the external electric field that drives the current in the sample. This corresponds to a Hall setup with boundaries, where the current is allowed only in electric field direction. As a result, an additional electric field (perpendicular to the existing electric field) is produced, which is calculated via Eq. (C.4). This electric Hall field cancels exactly the effect of the Lorentz force, see Ref. [227].

[2] Note that the same equation can be derived from the Boltzmann equation under more general conditions [283].

[3] The Hall effect for Bloch electrons is in detailed considered in Ref. [227]. An electric field transports the electrons through the momentum quantum numbers of the band. Whereas only the charge carriers at the Fermi surface are relaxed by scattering events and contribute to the longitudinal transport, all electrons of the system contribute to the Hall effect, because the perpendicular motion is driven by the change of momentum quantum number. Whether the sign in the Hall effect is electron- or hole-like is decided by the closed orbits: electron-like closed orbits cause a electron-like Hall effect, hole-like closed orbits a hole-like Hall effect. However, if also open orbits contribute to the Hall effect, this picture changes drastically [227]. Still, for the relevant data obtained in $LaAlO_3/SrTiO_3$ heterostructures, we expect all orbits to be closed and electron-like.

	Electron-like carriers	Hole-like carriers
Charge	$q_\mathrm{e} = -e$	$q_\mathrm{h} = +e$
Drift velocity	$\mathbf{v}_\mathrm{e} = -e\mathbf{E}\frac{\tau}{m_\mathrm{e}}$	$\mathbf{v}_\mathrm{h} = e\mathbf{E}\frac{\tau}{m_\mathrm{h}}$
Current density	$\mathbf{j}_\mathrm{e} = -en_\mathrm{e}\mathbf{v}_\mathrm{e}$	$\mathbf{j}_\mathrm{h} = en_\mathrm{h}\mathbf{v}_\mathrm{h}$
Charge carrier mobility	$\mu_\mathrm{e} = \frac{e\tau}{m_\mathrm{e}}$	$\mu_\mathrm{h} = \frac{e\tau}{m_\mathrm{h}}$
Conductivity	$\sigma_\mathrm{e} = \frac{n_\mathrm{e}e^2\tau}{m_\mathrm{e}} = en_\mathrm{e}\mu_\mathrm{e}$	$\sigma_\mathrm{h} = \frac{n_\mathrm{h}e^2\tau}{m_\mathrm{h}} = en_\mathrm{h}\mu_\mathrm{h}$
Velocity (in **B**-field)	$\mathbf{v}_\mathrm{e} = -\frac{e\tau}{m_\mathrm{e}}(\mathbf{E} + \mathbf{v}_\mathrm{e} \times \mathbf{B})$	$\mathbf{v}_\mathrm{h} = \frac{e\tau}{m_\mathrm{h}}(\mathbf{E} + \mathbf{v}_\mathrm{h} \times \mathbf{B})$
Current density	$\mathbf{j}_\mathrm{e} = \frac{n_\mathrm{e}e^2\tau}{m_\mathrm{e}}(\mathbf{E} + \mathbf{v}_\mathrm{e} \times \mathbf{B})$	$\mathbf{j}_\mathrm{h} = \frac{n_\mathrm{h}e^2\tau}{m_\mathrm{h}}(\mathbf{E} + \mathbf{v}_\mathrm{h} \times \mathbf{B})$
In perp. **B**-field	$\begin{pmatrix}E_\mathrm{x}\\E_\mathrm{y}\end{pmatrix} = \frac{1}{\sigma_\mathrm{e}}\begin{pmatrix}j_\mathrm{e,x}\\j_\mathrm{e,y}\end{pmatrix} + \frac{B}{en_\mathrm{e}}\begin{pmatrix}j_\mathrm{e,y}\\-j_\mathrm{e,x}\end{pmatrix}$	$\begin{pmatrix}E_\mathrm{x}\\E_\mathrm{y}\end{pmatrix} = \frac{1}{\sigma_\mathrm{h}}\begin{pmatrix}j_\mathrm{h,x}\\j_\mathrm{h,y}\end{pmatrix} - \frac{B}{en_\mathrm{h}}\begin{pmatrix}j_\mathrm{h,y}\\-j_\mathrm{h,x}\end{pmatrix}$
Resistivity tensor	$\begin{pmatrix}E_\mathrm{x}\\E_\mathrm{y}\end{pmatrix} = \begin{pmatrix}\frac{1}{\sigma_\mathrm{e}} & \frac{B}{en_\mathrm{e}}\\-\frac{B}{en_\mathrm{e}} & \frac{1}{\sigma_\mathrm{e}}\end{pmatrix}\begin{pmatrix}j_\mathrm{e,x}\\j_\mathrm{e,y}\end{pmatrix}$	$\begin{pmatrix}E_\mathrm{x}\\E_\mathrm{y}\end{pmatrix} = \begin{pmatrix}\frac{1}{\sigma_\mathrm{h}} & -\frac{B}{en_\mathrm{h}}\\\frac{B}{en_\mathrm{h}} & \frac{1}{\sigma_\mathrm{h}}\end{pmatrix}\begin{pmatrix}j_\mathrm{h,x}\\j_\mathrm{h,y}\end{pmatrix}$

Table C.1: *Hall effect for electron- and hole-like charge carriers.* Formulas are given when the electric charge is assumed to be negative in case of electron-like charge carriers and positive in the case of hole-like charge carriers. Charge carrier densities and mobilities are all positive in this case; the current densities are parallel and the drift velocities anti-parallel. However, when the charge is fixed to be electron-like in both cases, the transversal resistivity enforces a sign in the hole density n_h, which becomes negative. In turn, the sign in the longitudinal resistivity has to be compensated, and mass m_h, as well as mobility μ_h, becomes negative.

We assume that both the WAL contribution and the Hall effect are additive in the conductivity. The full conductivity tensor consists of some part that is independent of the magnetic field, which we denote σ_0 in the following, and some part that is field dependent, $\delta\sigma(B)$. Localization effects will contribute to both. We write

$$\sigma(B) = \sigma_0 + \delta\sigma(B) = \sigma_0 + \delta\sigma(0) + \Delta\sigma(B), \tag{C.9}$$

where we defined the magneto-conductivity $\Delta\sigma(B) = \delta\sigma(B) - \delta\sigma(0)$.

The next step is crucial for our fitting approach. In magneto-transport, we can only detect the contributions to the quantum corrections that are magnetic field dependent. Any contributions to $\delta\sigma(B = 0)$, like the temperature dependence in Eq. (2.42) and Eq. (2.44), are captured by the Drude-like conductivity in form of effective parameters for the scattering time, density and mass. We replace

$$\sigma_0 = \frac{ne^2\tau}{m} \rightarrow \sigma_0 + \delta\sigma(0), \tag{C.10}$$

$$\frac{\sigma_0}{en} = \frac{e\tau}{m} \rightarrow \frac{\sigma_0 + \delta\sigma(0)}{en}, \tag{C.11}$$

which are only small quantum corrections. The second replacement, Eq. (C.11), enters in Eq. (C.4).[4] These replacements yield for Eq. (C.7):

$$\begin{pmatrix} E_\mathrm{x} \\ \\ E_\mathrm{y} \end{pmatrix} = \begin{pmatrix} \dfrac{1}{\sigma_0 + \delta\sigma(B)} & \dfrac{B}{en} \\ \\ -\dfrac{B}{en} & \dfrac{1}{\sigma_0 + \delta\sigma(B)} \end{pmatrix} \begin{pmatrix} j_\mathrm{x} \\ \\ j_\mathrm{y} \end{pmatrix}. \tag{C.12}$$

Finally,

$$\rho_{\mathrm{xx}} - \rho_0 = \frac{1}{\sigma_0 + \delta\sigma(B)} - \frac{1}{\sigma_0 + \delta\sigma(0)} \tag{C.13}$$

$$\frac{\rho_{\mathrm{xx}} - \rho_0}{\rho_0} = \frac{1}{1 + \rho_0\Delta\sigma(B)} - 1. \tag{C.14}$$

C.1.2 Two Charge Carrier Types

The Hall effect results in a non-trivial magneto-response when more than one charge carrier type is perceivable. In a multiple band situation, we consider a resistivity tensor as defined in Eq. (C.7), but for each band (or type of charge carrier), indexed by m, separately:

$$\rho_m = \begin{pmatrix} \rho_{0,m} & \dfrac{B}{en_m} \\ \\ -\dfrac{B}{en_m} & \rho_{0,m}. \end{pmatrix} \tag{C.15}$$

We restrict the calculation to the case of two bands in the following (this calculation is found e.g. in Refs. [227, 283]). For this calculation, we keep the charge fixed at the value of the

[4] The Hall constant $1/ne$ itself seems to be unaltered by WL [68, 284, 285] or spin–orbit coupling [286, 287].

electron charge. In case of hole-like charge carriers, the density and mobility of this band are defined by negative values, as explained above.

The different contributions to the conductivity can be treated additively, and we find the multiband resistivity tensor

$$\rho = \left(\rho_1^{-1} + \rho_2^{-1}\right)^{-1}. \tag{C.16}$$

Thus we have

$$\left(\rho_1^{-1} + \rho_2^{-1}\right)_{xx} = \frac{\rho_{0,1}\rho_{0,2}^2 + \rho_{0,1}^2\rho_{0,2} + \rho_{0,1}\left(\frac{B}{en_2}\right)^2 + \rho_{0,2}\left(\frac{B}{en_1}\right)^2}{\left[\rho_{0,1}^2 + \left(\frac{B}{en_1}\right)^2\right]\left[\rho_{0,2}^2 + \left(\frac{B}{en_2}\right)^2\right]}, \tag{C.17}$$

$$\left(\rho_1^{-1} + \rho_2^{-1}\right)_{xy} = -\frac{\frac{B}{en_1}\rho_{0,2}^2 + \frac{B}{en_2}\rho_{0,1}^2 + \left(\frac{B}{en_1}\right)^2\frac{B}{en_2} + \frac{B}{en_1}\left(\frac{B}{en_2}\right)^2}{\left[\rho_{0,1}^2 + \left(\frac{B}{en_1}\right)^2\right]\left[\rho_{0,2}^2 + \left(\frac{B}{en_2}\right)^2\right]}. \tag{C.18}$$

Inversion yields the components of the resistivity tensor

$$\rho_{xx} = \frac{\rho_{0,1}\rho_{0,2}\left(\rho_{0,1} + \rho_{0,2}\right) + \left(\rho_{0,1}\frac{1}{n_2^2} + \rho_{0,2}\frac{1}{n_1^2}\right)\frac{B^2}{e^2}}{\left(\rho_{0,1} + \rho_{0,2}\right)^2 + \left(\frac{1}{n_1} + \frac{1}{n_2}\right)^2\frac{B^2}{e^2}}, \tag{C.19}$$

$$\rho_{xy} = \frac{\left(\frac{\rho_{0,1}^2}{n_2} + \frac{\rho_{0,2}^2}{n_1}\right)\frac{B}{e} + \frac{1}{n_1 n_2}\left(\frac{1}{n_1} + \frac{1}{n_2}\right)\frac{B^3}{e^3}}{\left(\rho_{0,1} + \rho_{0,2}\right)^2 + \left(\frac{1}{n_1} + \frac{1}{n_2}\right)^2\frac{B^2}{e^2}}. \tag{C.20}$$

The magneto-resistivity is given by

$$\frac{\rho_{xx} - \rho_0}{\rho_0} = \frac{\rho_{0,1}\rho_{0,2}\left(\frac{1}{n_1\rho_{0,1}} - \frac{1}{n_2\rho_{0,2}}\right)^2\frac{B^2}{e^2}}{\left(\rho_{0,1} + \rho_{0,2}\right)^2 + \left(\frac{1}{n_1} + \frac{1}{n_2}\right)^2\frac{B^2}{e^2}}. \tag{C.21}$$

Note that for one electron and one hole band with the same charge carrier densities, $n_1 = -n_2$, the Hall resistivity is linear and the magneto-resistivity purely quadratic with no saturation for high fields [227].

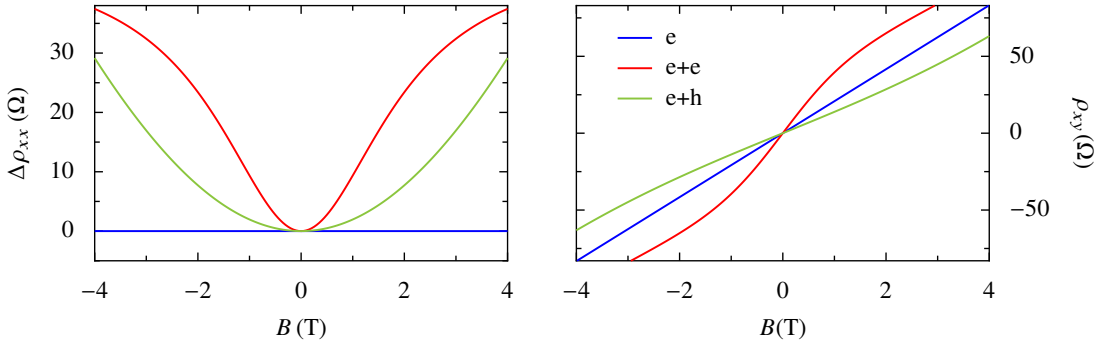

Figure C.1: *Multiband Hall effect.* Shown is the multiband Hall effect in the longitudinal resistivity $\Delta\rho_{xx}(B) = \rho_{xx}(B) - \rho_0$ and in the transversal resistivity $\rho_{xy}(B)$. For the single electron signal $n = 3 \times 10^{13}\ ^1/_{cm^2}$ and $\mu = 2 \times 10^3\ ^{cm^2}/_{Vs}$; there is no longitudinal signal and a linear Hall response. For the two electron signal we chose $n_1 = 1 \times 10^{13}\ ^1/_{cm^2}$, $n_2 = 2 \times 10^{13}\ ^1/_{cm^2}$, $\mu_1 = 2 \times 10^4\ ^{cm^2}/_{Vs}$ and $\mu_2 = 2 \times 10^3\ ^{cm^2}/_{Vs}$; a bell shaped curve appears in the longitudinal resistivity and the Hall signal features higher order terms. For the electron–hole picture, we chose $n_e = 4 \times 10^{13}\ ^1/_{cm^2}$, $n_h = 2.5 \times 10^{13}\ ^1/_{cm^2}$, $\mu_e = 2 \times 10^4\ ^{cm^2}/_{Vs}$ and $\mu_h = 2 \times 10^3\ ^{cm^2}/_{Vs}$; in that case both the linear and higher terms can have the same sign.

Written in terms of the mobility μ_m, where $\sigma_m = n_m e \mu_m$, we find

$$\rho_{xx} = \frac{1}{e\left(n_1\mu_1 + n_2\mu_2\right)} + \frac{\dfrac{n_1\mu_1 n_2\mu_2\left(\mu_1 - \mu_2\right)^2}{\left(n_1\mu_1 + n_2\mu_2\right)^3}\dfrac{B^2}{e}}{1 + \dfrac{\mu_1^2\mu_2^2\left(n_1 + n_2\right)^2}{\left(n_1\mu_1 + n_2\mu_2\right)^2}B^2}, \tag{C.22}$$

$$\rho_{xy} = \frac{\dfrac{n_1\mu_1^2 + n_2\mu_2^2}{\left(n_1\mu_1 + n_2\mu_2\right)^2}\dfrac{B}{e} + \dfrac{\mu_1^2\mu_2^2\left(n_1 + n_2\right)}{\left(n_1\mu_1 + n_2\mu_2\right)^2}\dfrac{B^3}{e}}{1 + \dfrac{\mu_1^2\mu_2^2\left(n_1 + n_2\right)^2}{\left(n_1\mu_1 + n_2\mu_2\right)^2}B^2}. \tag{C.23}$$

Plots are shown in Fig. C.1. For the magneto-resistance measurements in $LaAlO_3/SrTiO_3$, which we discuss in Sec. 3.2, it is useful to consider an expansion up to quartic order in the magnetic field,

$$\rho_{xx} = a_0 + a_2 B^2 + a_4 B^4 + O\left(B^6\right), \tag{C.24}$$

$$\rho_{xy} = a_1 B + a_3 B^3 + O\left(B^5\right), \tag{C.25}$$

where

$$a_0 = \frac{1}{e\left(n_1\mu_1 + n_2\mu_2\right)}, \tag{C.26}$$

$$a_1 = \frac{n_1\mu_1^2 + n_2\mu_2^2}{e\left(n_1\mu_1 + n_2\mu_2\right)^2}, \tag{C.27}$$

$$a_2 = \frac{n_1 n_2 \mu_1 \mu_2 \left(\mu_1 - \mu_2\right)^2}{e\left(n_1\mu_1 + n_2\mu_2\right)^3}, \tag{C.28}$$

$$a_3 = -\frac{n_1 n_2 \mu_1^2 \mu_2^2 \left(n_1 + n_2\right)\left(\mu_1 - \mu_2\right)^2}{e\left(n_1\mu_1 + n_2\mu_2\right)^4}, \tag{C.29}$$

$$a_4 = -\frac{n_1 \mu_1^3 n_2 \mu_2^3 \left(\mu_1 - \mu_2\right)^2 \left(n_1 + n_2\right)^2}{e\left(n_1\mu_1 + n_2\mu_2\right)^5}. \tag{C.30}$$

$$\tag{C.31}$$

Note that for two electron-like charge carriers generally $a_1 > 0$ and $a_3 < 0$.

In the following we discuss three special cases for two distinguished electron-like charge carriers:

- $\mu_1 \approx \mu_2 = \mu$: All terms beyond quadratic order in the magnetic field vanish, and we are left with the single-band case, but with total density $n_1 + n_2$:

$$\rho_{xx} \approx \rho_0 = \frac{1}{e\left(n_1 + n_2\right)\mu}, \tag{C.32}$$

$$\rho_{xy} \approx \frac{B}{e\left(n_1 + n_2\right)}. \tag{C.33}$$

  A fit to experimental data reveals the values for $n_1 + n_2$ as well as $\mu_1 = \mu_2$.

- $\mu_1 \gg \mu_2$ and $n_1 \sim n_2$:

$$\frac{\rho_{xx} - \rho_0}{\rho_0} \approx \frac{n_2\mu_1\mu_2}{n_1}B^2 - \frac{n_2\left(n_1 + n_2\right)^2\mu_1\mu_2^3}{n_1^3}B^4 \tag{C.34}$$

$$\rho_{xy} \approx \frac{B}{en_1} - \frac{n_2\left(n_1 + n_2\right)\mu_2^2}{n_1^3}\frac{B^3}{e} \tag{C.35}$$

  In this case, fits can determine all four values for n_1, μ_1, n_2, μ_2.

- $n_1\mu_1 \approx n_2\mu_2$ and $\mu_1 \gg \mu_2$ (and $n_1 \ll n_2$): Up to quartic order,

$$\frac{\rho_{xx} - \rho_0}{\rho_0} \approx \left(\mu_1 - \mu_2\right)^2\frac{B^2}{4} - \left(\mu_1^2 - \mu_2^2\right)^2\frac{B^4}{16} \approx \left(\frac{\mu_1 B}{2}\right)^2 - \left(\frac{\mu_1 B}{2}\right)^4, \tag{C.36}$$

$$\rho_{xy} \approx \frac{\mu_1 + \mu_2}{4n_1\mu_1}\frac{B}{e} - \frac{\left(\mu_1^2 - \mu_2^2\right)\left(\mu_1 + \mu_2\right)}{16n_1\mu_1}\frac{B^3}{e} \approx \frac{B}{4en_1} - \frac{\mu_1^2 B^3}{16en_1}. \tag{C.37}$$

  In this case, the parameters of the high mobility charge carriers, n_1 and μ_1, can be resolved separately, but only the product $n_2\mu_2$ can be determined by a fit.

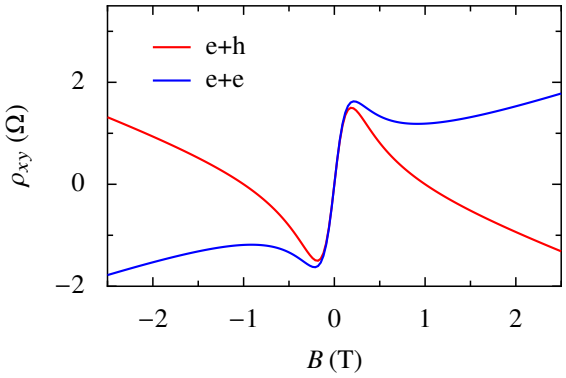

Figure C.2: *Non-monotonous Hall effect.* For this plot the rather extreme conditions $n_1 = 1 \times 10^{15}$ $^1/_{cm^2}$, $n_2 = 1 \times 10^{13}$ $^1/_{cm^2}$, $\mu_1 = 1 \times 10^3$ cm^2/Vs, $\mu_2 = 1 \times 10^5$ cm^2/Vs are chosen to illustrate the non-monotonous Hall effect. For two electron-like bands in low magnetic fields, the high mobility charge carriers control the low field signal, whereas the high density charge carriers control the high field regime, which results in a local maximum in the Hall signal. The same parameters are used for a hole-like low mobility band. In this case, the electrons control the low field behavior, whereas the holes dominate for higher fields, creating a global maximum in the Hall signal.

Note that under rather extreme conditions, a pronounced non-monotonous Hall signal can be found (see Fig. C.2).

It is useful to consider the high field limits of the general formulas Eq. (C.22) and Eq. (C.23):

$$\frac{\rho_{xx}(B \to \infty) - \rho_0}{\rho_0} = \frac{n_1 n_2 (\mu_1 - \mu_2)^2}{\mu_1 \mu_2 (n_1 + n_2)^2} = \text{constant}, \tag{C.38}$$

$$\rho_{xy}(B \to \infty) = \frac{B}{e(n_1 + n_2)}. \tag{C.39}$$

The high field Hall signal is generally dominated by the charge carriers with higher density.

Finally we compute the contribution of the WL correction to the multiband magneto-response. The resistivity tensor for each band is given by

$$\rho_m = \begin{pmatrix} \dfrac{1}{\sigma_{0,m} + \delta\sigma_m} & \dfrac{B}{en_m} \\ -\dfrac{B}{en_m} & \dfrac{1}{\sigma_{0,m} + \delta\sigma_m} \end{pmatrix} \tag{C.40}$$

and a two-band case yields

$$\rho_0 = \frac{1}{\sigma_{0,1} + \delta\sigma_1(0) + \sigma_{0,2} + \delta\sigma_2(0)} = \frac{1}{n_1\mu_1 + n_2\mu_2}. \tag{C.41}$$

Note that we absorb the part of the localization contribution that is independent of the magnetic field into effective values of density and mobility.

We further define $\Delta\sigma_m(B) = \delta\sigma_m(B) - \delta\sigma_m(0)$ and find

$$\frac{\rho_{xx}}{\rho_0} = \\ = \frac{\dfrac{1}{1+\rho_0(\Delta\sigma_1+\Delta\sigma_2)} + \dfrac{\rho_0(en_1\mu_1+\Delta\sigma_1)(en_2\mu_2+\Delta\sigma_2)}{[1+\rho_0(\Delta\sigma_1+\Delta\sigma_2)]^2}\left(\dfrac{en_1\mu_1+\Delta\sigma_1}{n_1^2}+\dfrac{en_2\mu_2+\Delta\sigma_2}{n_2^2}\right)\dfrac{B^2}{e^2}}{1+\dfrac{\rho_0^2(en_1\mu_1+\Delta\sigma_1)^2(en_2\mu_2+\Delta\sigma_2)^2}{[1+\rho_0(\Delta\sigma_1+\Delta\sigma_2)]^2}\left(\dfrac{1}{n_1}+\dfrac{1}{n_2}\right)^2\dfrac{B^2}{e^2}}, \tag{C.42}$$

$$\frac{\rho_{xy}}{\eta} = \frac{\left(\dfrac{(en_1\mu_1+\Delta\sigma_1)^2}{n_1}+\dfrac{(en_2\mu_2+\Delta\sigma_2)^2}{n_2}\right)\dfrac{B}{e}+\dfrac{(en_1\mu_1+\Delta\sigma_1)^2(en_2\mu_2+\Delta\sigma_2)^2(n_1+n_2)}{n_1^2n_2^2}\dfrac{B^3}{e^3}}{1+\dfrac{\rho_0^2(en_1\mu_1+\Delta\sigma_1)^2(en_2\mu_2+\Delta\sigma_2)^2}{[1+\rho_0(\Delta\sigma_1+\Delta\sigma_2)]^2}\left(\dfrac{1}{n_1}+\dfrac{1}{n_2}\right)^2\dfrac{B^2}{e^2}}, \tag{C.43}$$

$$\eta = \frac{\rho_0^2}{[1+\rho_0(\Delta\sigma_1+\Delta\sigma_2)]^2}, \tag{C.44}$$

where we drop the magnetic field dependence in $\Delta\sigma_m$ for a more compact notation. These are the full formulas for the case when a multiband magneto-response as well as quantum corrections to the conductivity are perceivable.

C.1.3 Three Charge Carrier Types

To close the section, we discuss the response when three kinds of charge carriers are relevant for transport. Following the same procedure as before, we find in this case

$$\rho_{xx} = \frac{1}{e(n_1\mu_1+n_2\mu_2+n_3\mu_3)}$$

$$+\frac{1}{(n_1\mu_1+n_2\mu_2+n_3\mu_3)^3}\left[\left(n_1\mu_1n_2\mu_2(\mu_1-\mu_2)^2+n_2\mu_2n_3\mu_3(\mu_2-\mu_3)^2+n_1\mu_1n_3\mu_3(\mu_1-\mu_3)^2\right)\frac{B^2}{e}\right.$$

$$\left.+\mu_1\mu_2\mu_3\left(n_1n_2\mu_3(\mu_1-\mu_2)^2+n_1\mu_2n_3(\mu_1-\mu_3)^2+\mu_1n_2n_3(\mu_2-\mu_3)^2\right)\frac{B^4}{e}\right]\times$$

$$\left[1+\frac{\mu_1^2\mu_2^2(n_1+n_2)^2+\mu_2^2\mu_3^2(n_2+n_3)^2+\mu_1^2\mu_3^2(n_1+n_3)^2+2\mu_1\mu_2\mu_3(\mu_1n_2n_3+n_1\mu_2n_3+n_1n_2\mu_3)}{(n_1\mu_1+n_2\mu_2+n_3\mu_3)^2}B^2\right.$$

$$\left.+\left(\frac{\mu_1\mu_2\mu_3(n_1+n_2+n_3)}{n_1\mu_1+n_2\mu_2+n_3\mu_3}\right)^2B^4\right]^{-1} \tag{C.45}$$

$$\rho_{xy} = \frac{1}{(n_1\mu_1 + n_2\mu_2 + n_3\mu_3)^2}\left[\left(n_1\mu_1^2 + n_2\mu_2^2 + n_3\mu_3^2\right)\frac{B}{e}\right.$$

$$\left. + \left[\mu_1^2\mu_2^2(n_1+n_2) + \mu_2^2\mu_3^2(n_2+n_3) + \mu_1^2\mu_3^2(n_1+n_3)\right]\frac{B^3}{e} + (n_1+n_2+n_3)\,\mu_1^2\mu_2^2\mu_3^2\frac{B^5}{e}\right] \times$$

$$\left[1 + \frac{\mu_1^2\mu_2^2(n_1+n_2)^2 + \mu_2^2\mu_3^2(n_2+n_3)^2 + \mu_1^2\mu_3^2(n_1+n_3)^2 + 2\mu_1\mu_2\mu_3(\mu_1 n_2 n_3 + n_1\mu_2 n_3 + n_1 n_2\mu_3)}{(n_1\mu_1 + n_2\mu_2 + n_3\mu_3)^2}B^2\right.$$

$$\left. + \left(\frac{\mu_1\mu_2\mu_3(n_1+n_2+n_3)}{n_1\mu_1 + n_2\mu_2 + n_3\mu_3}\right)^2 B^4\right]^{-1} \tag{C.46}$$

By setting $n_3 = 0$ and $\mu_3 = 0$ we regain the two-band result. Up to cubic order we find the following prefactors for the fitting procedure:

$$a_0 = \frac{1}{e(n_1\mu_1 + n_2\mu_2 + n_3\mu_3)} \tag{C.47}$$

$$a_1 = \frac{n_1\mu_1^2 + n_2\mu_2^2 + n_3\mu_3^2}{e(n_1\mu_1 + n_2\mu_2 + n_3\mu_3)^2} \tag{C.48}$$

$$a_2 = \frac{n_1 n_2\mu_1\mu_2(\mu_1-\mu_2)^2 + n_2 n_3\mu_2\mu_3(\mu_2-\mu_3)^2 + n_1 n_3\mu_1\mu_3(\mu_1-\mu_3)^2}{e(n_1\mu_1 + n_2\mu_2 + n_3\mu_3)^3} \tag{C.49}$$

$$\begin{aligned} a_3 = -\frac{1}{e(n_1\mu_1 + n_2\mu_2 + n_3\mu_3)^4}\Big\{ & n_1 n_2\mu_1^2\mu_2^2(n_1+n_2)(\mu_1-\mu_2)^2 \\ & + n_2 n_3\mu_2^2\mu_3^2(n_2+n_3)(\mu_2-\mu_3)^2 \\ & + n_1 n_3\mu_1^2\mu_3^2(n_1+n_3)(\mu_1-\mu_3)^2 \\ & + 2n_1\mu_1 n_2\mu_2 n_3\mu_3\left[\mu_1(\mu_1-\mu_2)(\mu_1-\mu_3) + \mu_2(\mu_2-\mu_3)(\mu_2-\mu_1) + \mu_3(\mu_3-\mu_1)(\mu_3-\mu_2)\right]\Big\}, \end{aligned} \tag{C.50}$$

Note that the parameters a_0–a_2 are extended by the third charge carrier type in a straightforward way, whereas in the cubic term a_3, there is a fundamentally new coupled term involved. For $n_3 \ll n_1, n_2$ and $\mu_3 \ll \mu_1, \mu_2$ we regain the two-band formulas. In the high field limit, the Hall conductivity gives, as expected,

$$\rho_{xy}(B \to \infty) = \frac{B}{e(n_1 + n_2 + n_3)}. \tag{C.51}$$

For two electron-like charge carriers, we have found that generally $a_1 > 0$ and $a_3 < 0$. In the following, we like to address the question whether the case $a_1 > 0$ as well as $a_3 > 0$ (which is the experimental finding in Sec. 3.2.2) can be explained in terms of a multiband Hall effect resulting from three electron-like charge carriers. For electrons, all n and μ are positive, and $a_1 > 0$ immediately. To check whether a_3 is negative, it is sufficient to proof the relation

$$f(\mu_1,\mu_2,\mu_3) = \mu_1(\mu_1-\mu_2)(\mu_1-\mu_3) + \mu_2(\mu_2-\mu_3)(\mu_2-\mu_1) + \mu_3(\mu_3-\mu_1)(\mu_3-\mu_2) > 0. \tag{C.52}$$

In the following we like to address the different possible cases:

- For the special case of equal mobilities $\mu_1 = \mu_2 = \mu_3$ we get directly $f = 0$ as well as $a_3 = 0$. This corresponds to the single band case with $n = n_1 + n_2 + n_3$.
- If two mobilities are equal, e.g. $\mu_2 = \mu_3 = \mu$, we get $f = \mu_1 (\mu_1 - \mu)^2 > 0$, which ensures $a_3 < 0$ (because in the electron case $\mu_1 > 0$). This corresponds to the two-band case with $n_\alpha = n_1$ and $n_\beta = n_2 + n_3$.
- Now let us consider without loss of generality the case $\mu_1 > \mu_2 > \mu_3 > 0$. Then we have

$$\frac{\mu_1}{\mu_2} > 1 > \frac{\mu_2 - \mu_3}{\mu_1 - \mu_3} \tag{C.53}$$

$$\Leftrightarrow \mu_1(\mu_1 - \mu_2)(\mu_1 - \mu_3) > \mu_2(\mu_1 - \mu_2)(\mu_2 - \mu_3) \tag{C.54}$$

$$\Leftrightarrow \mu_1(\mu_1 - \mu_2)(\mu_1 - \mu_3) + \mu_2(\mu_2 - \mu_3)(\mu_2 - \mu_1) > 0, \tag{C.55}$$

  and as $\mu_3 > 0$ as well as $(\mu_3 - \mu_1)(\mu_3 - \mu_2) > 0$, the condition Eq. (C.52) holds.

Therefore the experimental finding $a_1 > 0$ as well as $a_3 > 0$ cannot be explained by three distinguished electron-like charge carriers. Note that the different sign in the linear and cubic coefficient is a necessary but insufficient condition for electron–hole conductivity.

C.2 Self-Consistent Fitting Procedure

C.2.1 Quantum Corrections up to Order e^2/h

As the experimental data shown in Sec. 3.2.2 contain a multiband Hall dependence up to order B^3, we expand Eqs. (C.42)–(C.44) in the explicitly appearing magnetic field:

$$\begin{aligned}\frac{\rho_{xx} - \rho_0}{\rho_0} = {} & \frac{1}{1 + \rho_0 (\Delta\sigma_1 + \Delta\sigma_2)} - 1 \\ & + \frac{(en_1\mu_1 + \Delta\sigma_1)(en_2\mu_2 + \Delta\sigma_2)}{\rho_0 (en_1\mu_1 + \Delta\sigma_1 + en_2\mu_2 + \Delta\sigma_2)^3} \left(\frac{en_1\mu_1 + \Delta\sigma_1}{n_1} - \frac{en_2\mu_2 + \Delta\sigma_2}{n_2} \right)^2 \frac{B^2}{e^2}\end{aligned} \tag{C.56}$$

$$\begin{aligned}\rho_{xy} = {} & \frac{1}{(en_1\mu_1 + \Delta\sigma_1 + en_2\mu_2 + \Delta\sigma_2)^2} \left[\frac{(en_1\mu_1 + \Delta\sigma_1)^2}{n_1} + \frac{(en_2\mu_2 + \Delta\sigma_2)^2}{n_2} \right] \frac{B}{e} \\ & - \frac{n_1 + n_2}{n_1 n_2} \frac{(en_1\mu_1 + \Delta\sigma_1)^2 (en_2\mu_2 + \Delta\sigma_2)^2}{(en_1\mu_1 + \Delta\sigma_1 + en_2\mu_2 + \Delta\sigma_2)^4} \left(\frac{en_1\mu_1 + \Delta\sigma_1}{n_1} - \frac{en_2\mu_2 + \Delta\sigma_2}{n_2} \right)^2 \frac{B^3}{e^3}.\end{aligned} \tag{C.57}$$

For $\Delta\sigma_1 = \Delta\sigma_2 = 0$, the multiband case without localization corrections is revealed. Note that $\Delta\sigma$ is characterized by Eq. (2.170) and has a complicated magnetic field dependence. However, $\Delta\sigma$ is a quantum correction of order e^2/h and we expect $en\mu \gg \Delta\sigma$. Therefore, we find that the first term in the longitudinal resistivity, Eq. (C.56), is proportional to the correction in first order,

$$\frac{1}{1 + \rho_0 (\Delta\sigma_1 + \Delta\sigma_2)} - 1 \approx -\rho_0 (\Delta\sigma_1 + \Delta\sigma_2), \tag{C.58}$$

whereas the correction is negligible in other terms. We find for Eq. (C.56) and Eq. (C.57):

$$\rho_0 = \frac{1}{en_1\mu_1 + en_2\mu_2}, \tag{C.59}$$

$$\rho_{xx} \approx \frac{1}{en_1\mu_1 + en_2\mu_2 + \Delta\sigma_1 + \Delta\sigma_2} + \frac{n_1 n_2 \mu_1 \mu_2 \left(\mu_1 - \mu_2\right)^2}{\left(n_1\mu_1 + n_2\mu_2\right)^3} \frac{B^2}{e}, \tag{C.60}$$

$$\rho_{xy} \approx \frac{n_1\mu_1^2 + n_2\mu_2^2}{\left(n_1\mu_1 + n_2\mu_2\right)^2} \frac{B}{e} - \frac{n_1 n_2 \mu_1^2 \mu_2^2 \left(n_1 + n_2\right)\left(\mu_1 - \mu_2\right)^2}{\left(n_1\mu_1 + n_2\mu_2\right)^4} \frac{B^3}{e}, \tag{C.61}$$

where $\Delta\sigma(B)$ depends on the effective spin–orbit and inelastic fields. Altogether we end up with seven fitting parameters: n_1, n_2, μ_1, μ_2, B_{so}, B'_{so}, and B_i. Still, we aim to separate the multiband fitting from the WAL fitting. We define a_0–a_3 according to Eqs. (C.26)–(C.29) and the effective fitting formulas are given by

$$\rho_0 = a_0 \tag{C.62}$$

$$\rho_{xx} = \frac{a_0}{1 + a_0\Delta\sigma} + a_2 B^2 \tag{C.63}$$

$$\rho_{xy} = a_1 B + a_3 B^3. \tag{C.64}$$

To recalculate the parameters of the electron systems, we invert Eqs. (C.26)–(C.29) and find

$$0 = \mu_1^2 - \mu_1\left(\frac{a_1}{a_0} - \frac{a_3}{a_2}\right) - \frac{a_1 a_3}{a_0 a_2} - \frac{a_2}{a_0} \tag{C.65}$$

$$\mu_2 = \frac{a_2}{a_1 - a_0\mu_1} + \frac{a_1}{a_0} \tag{C.66}$$

$$en_1 = \frac{a_3 + a_2\mu_1}{a_0 a_2 \mu_1 \left(\mu_1 - \mu_2\right)} \tag{C.67}$$

$$en_2 = \frac{1 - ea_0 n_1 \mu_1}{a_0 \mu_2}. \tag{C.68}$$

The set of parameters seems not to be uniquely defined by the above equations Eqs. (C.65)–(C.68), but in fact (we denote the two solutions of the quadratic equation as "±")

$$\mu_{1,+} + \mu_{1,-} = \frac{a_1}{a_0} - \frac{a_3}{a_2} = \mu_1 + \mu_2. \tag{C.69}$$

The argument of the square root in the solution of the quadratic equation is always positive and two real solution exist. Therefore the choice of solutions is due to the symmetry of interchanging the indices $\{1, 2\}$. To sum up, we find the following formulas:

$$\mu_{1,2} = \left(\frac{a_1}{2a_0} - \frac{a_3}{2a_2}\right) \pm \sqrt{\left(\frac{a_1}{2a_0} + \frac{a_3}{2a_2}\right)^2 + \frac{a_2}{a_0}} \tag{C.70}$$

$$en_1 = \frac{a_3 + a_2\mu_1}{a_0 a_2 \mu_1 (\mu_1 - \mu_2)} \tag{C.71}$$

$$en_2 = \frac{1 - ea_0 n_1 \mu_1}{a_0 \mu_2}. \tag{C.72}$$

The allocation of the plus and minus solution of the mobility is tied to the choice of the densities.

The values for a_0 and a_2 in the longitudinal transport properties are naturally always positive, but the signs of a_1 and a_3 in the transversal transport properties depend on the nature of the charge carriers. We can decide between the following cases in the two-band scenario (e=electron band, h=hole band):

- e+e: $a_1 > 0$, $a_3 < 0$,
- h+h: $a_1 < 0$, $a_3 > 0$,
- e+h: $a_1 \gtrless 0$ for $n_\mathrm{e}\mu_\mathrm{e}^2 \gtrless n_\mathrm{h}\mu_\mathrm{h}^2$, $a_3 \gtrless 0$ for $n_\mathrm{e} \gtrless n_\mathrm{h}$,
- $\mathrm{sgn}(a_1) \neq \mathrm{sgn}(a_3) \Rightarrow$ e+h.

Therefore, the comparison of a_1 and a_3 can reveal a qualitative statement about the nature of charge carriers.

C.2.2 Quantum Corrections up to Order $B \times e^2/h$

To close this section, we discuss the case when we cannot neglect the localization contribution to the conductivities in higher order multiband signals (see Eq. (C.58) and the discussion there). We expand the original formulas Eq. (C.56) and Eq. (C.57) also in first order of $\Delta\sigma(B) \times B$ and find

$$\frac{\rho_{xx} - \rho_0}{\rho_0} = \frac{1}{1 + \rho_0 (\Delta\sigma_1 + \Delta\sigma_2)} - 1 + \frac{n_1\mu_1 n_2\mu_2 (\mu_1 - \mu_2)^2}{(n_1\mu_1 + n_2\mu_2)^2} B^2 + O\left(B^2 \Delta\sigma\right) \tag{C.73}$$

$$\begin{aligned} \rho_{xy} = {} & \frac{n_1\mu_1^2 + n_2\mu_2^2}{(n_1\mu_1 + n_2\mu_2)^2} \frac{B}{e} - \frac{n_1 n_2 \mu_1^2 \mu_2^2 (n_1 + n_2)(\mu_1 - \mu_2)^2}{(n_1\mu_1 + n_2\mu_2)^4} \frac{B^3}{e} \\ & + \frac{2(\mu_1 - \mu_2)(n_2\mu_2\Delta\sigma_1 - n_1\mu_1\Delta\sigma_2)}{(n_1\mu_1 + n_2\mu_2)^3} \frac{B}{e^2} + O\left[B(\Delta\sigma)^2 + B^3\Delta\sigma\right]. \end{aligned} \tag{C.74}$$

Besides the coefficients Eqs. (C.26)–(C.29), this introduces a coupling coefficient $a_\mathrm{c}(B)$ in the term $a_\mathrm{c}(B) \times B$, where

$$a_\mathrm{c} = \frac{2(\mu_1 - \mu_2)(n_2\mu_2\Delta\sigma_1 - n_1\mu_1\Delta\sigma_2)}{e^2 (n_1\mu_1 + n_2\mu_2)^3}. \tag{C.75}$$

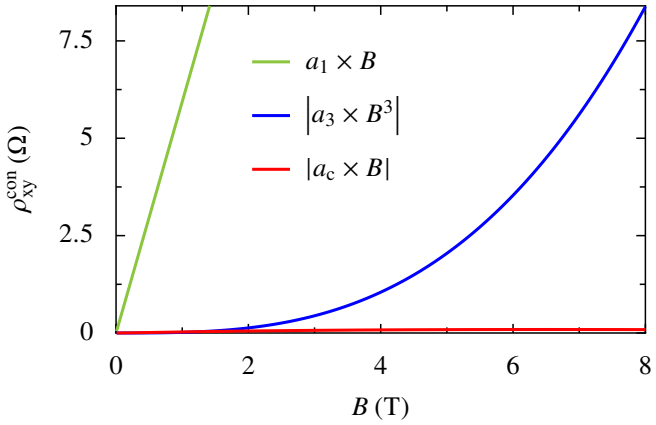

Figure C.3: *Comparison of the different contributions to the Hall resistivity.* We show the contributions ρ_{xy}^{con} to the Hall signal. We use parameters typical for the $LaAlO_3/SrTiO_3$ interface: $B_{so} = 0.25\,T$, $B_i = 0.005\,T$ (which corresponds to 2K), $n_e = 2.5 \times 10^{13}\,1/cm^2$, $n_h = 5 \times 10^{14}\,1/cm^2$, $\mu_e = 1000\,cm^2/Vs$, $\mu_h = 50\,cm^2/Vs$. The WAL is attributed to the high-mobility band in this plot. For the cubic and the WAL term, we plot the negative values for a better comparison with the linear term. A WAL correction to the Hall resistance exists in the multiband case, but it is negligible for the chosen parameters.

We find that neglecting the WAL contribution in the Hall response is a good approximation up to quadratic order in magnetic field. However, the linear Hall signal couples to a term linear in $\Delta\sigma(B)$. Although small, this term might make a difference in the fitting procedure.

In Fig. C.3, we plot for a comparison the different contributions to the Hall conductivity for typical values of the $LaAlO_3/SrTiO_3$ interface. The coupling term $a_c \times B$ is very small in comparison with the linear and cubic contribution to the Hall effect.

The complete fitting procedure can be treated self-consistently (see the diagrammatic plan on the right). Magneto-transport data for longitudinal and transversal resistivity has to be fed into the program. The parameter a_0 can be extracted directly. Arbitrary starting values for the effective fields B_i, B_{so}, and B'_{so} are chosen and the contribution of WAL is calculated for these values. We subtract the WAL correction from the longitudinal data and fit the remaining signal to obtain a_2 and a_4. The fitted curve $a_0 + a_2B^2 + a_4B^4$ can be subtracted from the original data to reveal the WAL correction. This procedure is solved in a self-consistent loop until we obtain a_2, B_i, B_{so}, and B'_{so}. In the next step, the Hall signal is fitted up to cubic order via $Ba_1 + B^3a_3$ and values for n_1, n_2, μ_1, and μ_2 are calculated. Optionally, the WAL correction can be considered (the densities and mobilities enter this term) and be subtracted from the Hall data. Again, this procedure can be solved in a second self-consistent loop. We find a_0 from the start, B_i, B_{so}, and B'_{so} from the first loop and n_1, n_2, μ_1, μ_2 from the second loop. The results for the experimental data on $LaAlO_3/SrTiO_3$ are discussed in detail in Chap. 3.

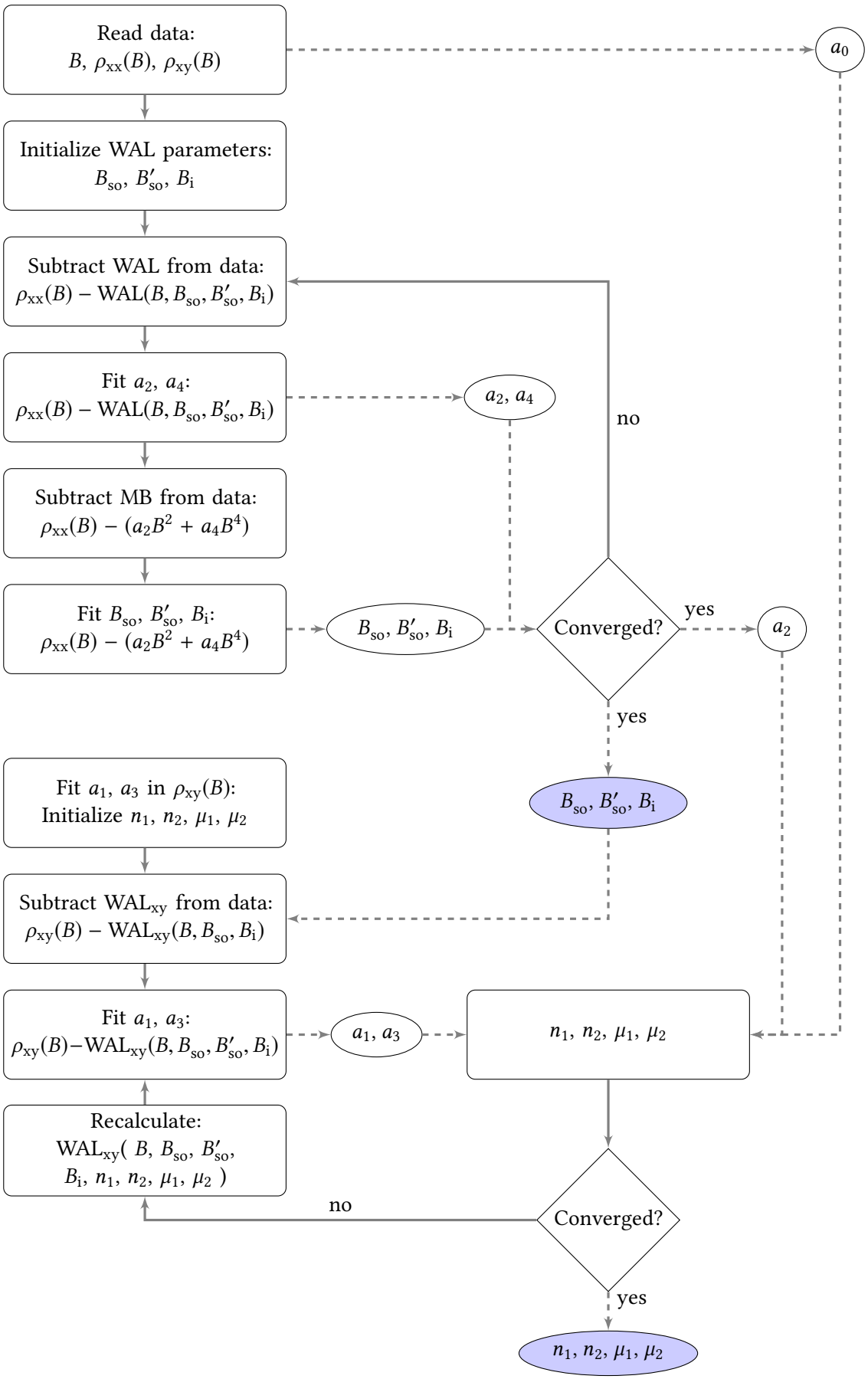
Read data:
B, $\rho_{xx}(B)$, $\rho_{xy}(B)$
a_0
Initialize WAL parameters:
B_{so}, B'_{so}, B_i
Subtract WAL from data:
$\rho_{xx}(B) - \mathrm{WAL}(B, B_{so}, B'_{so}, B_i)$
Fit a_2, a_4:
$\rho_{xx}(B) - \mathrm{WAL}(B, B_{so}, B'_{so}, B_i)$
a_2, a_4
no
Subtract MB from data:
$\rho_{xx}(B) - (a_2 B^2 + a_4 B^4)$
Fit B_{so}, B'_{so}, B_i:
$\rho_{xx}(B) - (a_2 B^2 + a_4 B^4)$
B_{so}, B'_{so}, B_i
Converged?
yes
a_2
yes
Fit a_1, a_3 in $\rho_{xy}(B)$:
Initialize n_1, n_2, μ_1, μ_2
B_{so}, B'_{so}, B_i
Subtract WAL_{xy} from data:
$\rho_{xy}(B) - \mathrm{WAL}_{xy}(B, B_{so}, B_i)$
Fit a_1, a_3:
$\rho_{xy}(B) - \mathrm{WAL}_{xy}(B, B_{so}, B'_{so}, B_i)$
a_1, a_3
n_1, n_2, μ_1, μ_2
Recalculate:
$\mathrm{WAL}_{xy}(B, B_{so}, B'_{so}, B_i, n_1, n_2, \mu_1, \mu_2)$
no
Converged?
yes
n_1, n_2, μ_1, μ_2

D Further Contributions to Magneto-Transport

Contents

Several quantum effects might appear in transport measurements of a disordered two-dimensional electron system, and it can be challenging to distinguish between all of those. There are contributions originating in Coulomb interaction, which can be related to both the particle–hole channel as well as the particle–particle channel of interaction processes. The vicinity of a superconducting state introduces Aslamazov–Larkin fluctuations (AL) and Maki–Thompson fluctuations (MT). Furthermore, the anomalous Hall effect (AHE) might enter in the transversal conductance. All these effects might overlay the observation of WL or WAL. In this appendix, we discuss these additional contributions to the conductivity tensor, as they are relevant for the data analysis in Chap. 3.

D.1 Superconducting Fluctuations

Quantum corrections in two-dimensional disordered materials due to superconducting fluctuations become important near a superconducting transition. For an overview concerning the consideration of WL and the different superconducting fluctuations, see Refs. [88, 288, 289]. In the literature, the corrections are often given in terms of magneto-conductance. Approximately, the following relation between $\Delta\sigma$ and $\Delta\rho$ holds:

$$\Delta\sigma = \sigma(B) - \sigma_0 = \frac{1}{\rho} - \frac{1}{\rho_0} = -\frac{\Delta\rho}{\rho\rho_0} \approx -\frac{\Delta\rho}{\rho_0^2}. \tag{D.1}$$

There are several contributions to the quantum conductivity due to the vicinity of a superconducting transition. A straightforward picture is drawn by AL diagrams: Fluctuations in

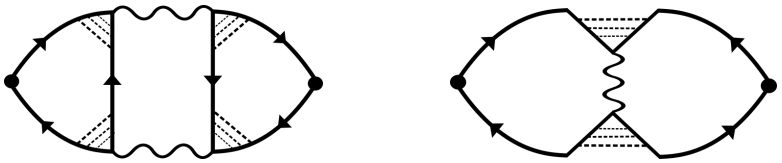

Figure D.1: *Feynman diagrams for the Aslamazov–Larkin and Maki–Thompson fluctuations.* Propagating electrons are represented by solid lines, the superconducting order parameter as wavy line, and disorder scattering by dashed lines. (a) The AL contribution can be described by two electrons forming a Cooper pair due to attractive electron–electron interaction. The disorder scattering contributes to the particle–particle channel. (b) The MT diagram also describes the formation of a Cooper pair and disorder scattering in the particle–particle channel. It can be considered as crossed ladder diagrams with an interim appearance of a Cooper pair.

the superconducting order parameter cause transport by electron pairs, see Fig. D.1 (a). MT fluctuations even have to be considered for temperatures an order of magnitude above the superconducting transition temperature. They can be visualized as a Cooper pair formation within the crossed diagrams [290], see Fig. D.1 (b). There is also a contribution due to a density of states effect, but this correction is rather small in comparison with the AL and MT fluctuation and is often omitted [242].

D.1.1 Aslamazov–Larkin Fluctuations

Although energetically unfavored, fluctuations of electron pairing contribute to the conductivity near the transition temperature T_c [291]. This correction describes a strong enhancement of the conductivity near the transition temperature and is given by

$$\delta\sigma^{\mathrm{AL}}(T) = \frac{e^2}{\pi h}\frac{\pi^2}{8\ln\left(\frac{T}{T_\mathrm{c}}\right)}. \tag{D.2}$$

The magneto-conductance near the transition temperature is given by [292, 293]

$$\Delta\sigma^{\mathrm{AL}}(B) = \frac{e^2}{\pi h}\frac{\pi^2}{4\ln\left(\frac{T}{T_\mathrm{c}}\right)}\left\{\left(\frac{2B^*}{B}\right)^2\left[\psi\left(\frac{1}{2}+\frac{B^*}{B}\right)-\psi\left(1+\frac{B^*}{B}\right)\right]+\frac{2B^*}{B}-\frac{1}{2}\right\}, \tag{D.3}$$

where the characteristic field B^* is

$$B^* = \frac{2k_\mathrm{B}T}{\pi eD}\ln\left(\frac{T}{T_\mathrm{c}}\right). \tag{D.4}$$

When the temperature of the measurement and the transition temperature is known, B^* is determined by the diffusion constant D.

D.1.2 Maki–Thompson Fluctuations

Another kind of fluctuations relates back to the work of Maki [294] and Thompson [295]. These fluctuations have their origin in the inelastic lifetime of the electrons, as pointed out

by Larkin [296]: If one electron of a pairing state is scattered into a new state of energy, this Cooper pair is broken [88]. Not too close to the transition temperature and for small magnetic fields, that is when both conditions

$$\ln\left(\frac{T}{T_\mathrm{c}}\right) \gg \frac{1}{k_\mathrm{B}T\tau_\mathrm{i}}, \tag{D.5}$$

$$4DeB \ll k_\mathrm{B}T\ln\left(\frac{T}{T_\mathrm{c}}\right), \tag{D.6}$$

are valid, this results in a magneto-conductance

$$\Delta\sigma^\mathrm{MT}(B) = -\beta_\mathrm{L}\frac{e^2}{\pi h}\left[\psi\left(\frac{1}{2}+\frac{B_\mathrm{i}}{B}\right) - \ln\left(\frac{B_\mathrm{i}}{B}\right)\right], \tag{D.7}$$

which has the same structure as the WL contribution except the different prefactor. This β_L factor is the Larkin electron–electron interaction strength.[1] In the vicinity of the transition temperature, the β_L function can be approximated,

$$\beta_\mathrm{L} \approx \frac{\pi^2}{4\ln\left(\frac{T}{T_\mathrm{c}}\right)}. \tag{D.8}$$

The above formulas have to be corrected very close to the transition temperature, that is when

$$\ln\left(\frac{T}{T_\mathrm{c}}\right) \ll 1, \tag{D.9}$$

$$4DeB < k_\mathrm{B}T\ln\left(\frac{T}{T_\mathrm{c}}\right). \tag{D.10}$$

In this case, more suitable formulas are given by [241]

$$\Delta\sigma^\mathrm{MT}(B) = -\beta_{\mathrm{LdS,\,A}}\frac{e^2}{\pi h}\left[\psi\left(\frac{1}{2}+\frac{B_\mathrm{i}}{B}\right) - \psi\left(\frac{1}{2}+\frac{B^*}{B}\right) + \ln\left(\frac{B^*}{B_\mathrm{i}}\right)\right], \tag{D.11}$$

where $\beta_{\mathrm{LdS,\,A}}$ differs only very near the transition temperature from the Larkin expression[2],

$$\beta_{\mathrm{LdS,\,A}}\left(\frac{T}{T_\mathrm{c}}, \delta_\mathrm{MT}\right) = \frac{\pi^2}{4}\left[\frac{1}{\ln\left(\frac{T}{T_\mathrm{c}}\right) - \delta_\mathrm{MT}}\right] \tag{D.12}$$

$$= \frac{\pi^2}{4}\frac{1}{1-\frac{B_\mathrm{i}}{B^*}}\frac{1}{\ln\left(\frac{T}{T_\mathrm{c}}\right)}, \tag{D.13}$$

where

$$\delta_\mathrm{MT} = \frac{\pi\hbar}{8k_\mathrm{B}T\tau_i} \tag{D.14}$$

[1] This Larkin electron–electron interaction strength seems to be independent of the spin–orbit coupling [296].
[2] Lopes dos Santos and Abrahams [241]

is the MT pair breaking parameter.

The temperature dependence in zero magnetic field not too close to the transition temperature, $2\pi k_B(T - T_c) \gg \hbar/\tau_i$, is described by (see Ref. [88])

$$\delta\sigma(T) = \frac{e^2}{\pi h}\frac{\pi^2}{4\ln\left(\frac{T}{T_c}\right)}\ln\left(\frac{\pi}{8\delta_{MT}}\right), \tag{D.15}$$

and close to the transition temperature [240],

$$\delta\sigma(T) = \frac{e^2}{\pi h}\frac{\pi^2}{4}\frac{1}{\ln\left(\frac{T}{T_c}\right) - \delta_{MT}}\ln\left(\frac{\ln\left(\frac{T}{T_c}\right)}{\delta_{MT}}\right). \tag{D.16}$$

D.1.3 Magnetotransport Well Above T_c

Generally, near the transition temperature where $\ln(T/T_c) \ll 1$, Eq. (D.3) and Eq. (D.11) are used along with the WL contribution, whereas far above T_c, for $\ln(T/T_c) \gtrsim 1$, the AL contributions can be neglected and only Eq. (D.7) is sufficient [289]. The crossover of the two regimes is expected for $T \approx 2.7 \times T_c$.

As the MT fluctuations can be noticeable even well above the superconducting transition temperature, we note that these contributions can result in a positive magneto-resistance. If also the localization contribution, Eq. (1.10), is important, the quantum correction is described by the magneto-conductance

$$\Delta\sigma(B) = (1 - \beta_L)\frac{e^2}{\pi h}\left[\psi\left(\frac{1}{2} + \frac{B_i}{B}\right) - \ln\left(\frac{B_i}{B}\right)\right]. \tag{D.17}$$

If the effect of the magnetic field on β_L can be neglected [296], there is no change expected in the slope of the magneto-resistance. Therefore the appearance of WAL, Eq. (2.46), can be clearly distinguished from the superconducting fluctuations. The interplay of MT fluctuations well above the transition temperature and the WL contribution is shown in Fig. D.2. The formula Eq. (D.17) is especially useful, because if the transition temperature (and the temperature of the measurement) is well known (for example by fitting the temperature dependence of the sheet resistance), there are no further fitting parameters needed except for the inelastic field.

D.1.4 Magneto-transport Very Near T_c

In the case $T \ll 2.7 \times T_c$, AL as well as MT fluctuations have to be considered in the magneto-transport. If we assume that the transition temperature and the temperature of the measurement are well known, we have to introduce one additional fitting parameter besides B_i and B_{so} (assumed that the elastic scattering field is large, $B_o \sim \infty$). This fitting parameter is the diffusion constant D in the effective field B^*, defined in Eq. (D.4). The full superconducting contribution is given by

$$\begin{aligned}\Delta\sigma^{SC}(B) = \frac{e^2}{\pi h}\frac{\pi^2}{4\ln\left(\frac{T}{T_c}\right)}\Bigg\{&\left(\frac{B^*}{B_i - B^*}\right)\left[\psi\left(\frac{1}{2} + \frac{B_i}{B}\right) - \psi\left(\frac{1}{2} + \frac{B^*}{B}\right) + \ln\left(\frac{B^*}{B_i}\right)\right] \\ &+ \left(\frac{2B^*}{B}\right)^2\left[\psi\left(\frac{1}{2} + \frac{B^*}{B}\right) - \psi\left(1 + \frac{B^*}{B}\right)\right] + \frac{2B^*}{B} - \frac{1}{2}\Bigg\}.\end{aligned} \tag{D.18}$$

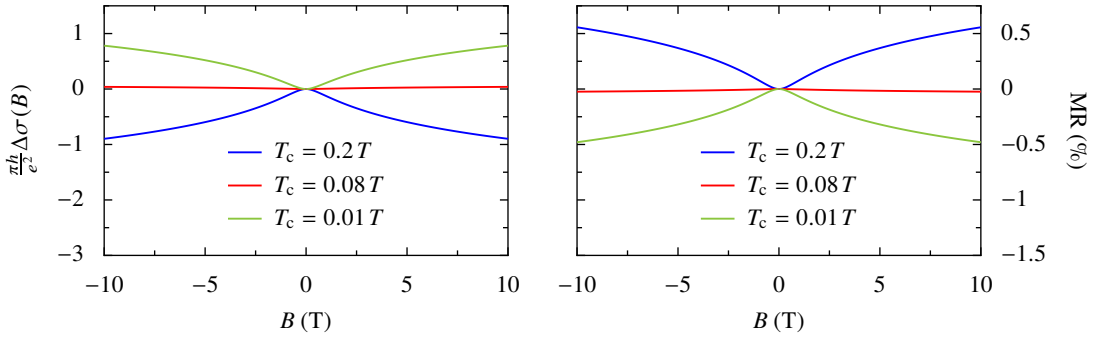

Figure D.2: *Interplay of weak localization and Maki–Thompson fluctuations.* The contribution by MT fluctuactions, Eq. (D.7), is noticable even at much higher temperatures than the superconducting transition temperature. As its sign is opposite to that of WL, the two effects cancel out for $T_c \approx 0.08T$. In this plot, the transition temperature T_c is varied whereas T (and $B_i = 0.3\,\mathrm{T}$) are kept constant. For the MR plot, the sheet resistance is chosen to be 500 Ω.

For known temperature, the diffusion constant can be extracted. This also allows to examine the scattering times instead of the effective magnetic fields via Eq. 2.36. The contributions of MT and AL fluctuations are compared in Fig. D.3.

It is important to keep in mind the limitation Eq. (D.10), which yields

$$B < \frac{\pi}{8} B^*(T). \tag{D.19}$$

Therefore, the temperature has to be chosen accordingly to the magnetic field range to remain in the valid regime of the above formula.

D.2 Electron–Electron Interaction

Electron–electron interaction in disordered Fermi systems can be taken into account perturbatively by considering diagrams in the Kubo evaluation that contain an additional interaction line in the ladder diagrams. For a detailed review of these contributions and diagrams, see Ref. [46]. In this section, we discuss briefly the different quantum contributions to the conductivity as they might become relevant for the evaluation in Chap. 3.

D.2.1 Particle–Hole Channel

Perturbation theory in the interaction strength reveals further corrections to the conductivity from the particle–hole channel of the Kubo conductivity (we show some relevant diagrams in Fig. D.4). The corrections to the magneto-conductance are given by [68, 297–299] (see [46] for the corrected version according to [300]):

$$\delta\sigma_I = \frac{e^2}{h} \begin{cases} -\frac{1}{A}\left(4 - \frac{3}{2}\widetilde{F}_\sigma\right)\sqrt{\frac{D}{2T}} & d = 1 \\ \frac{1}{2\pi}\left(2 - \frac{3}{2}\widetilde{F}_\sigma\right)\ln(T\tau) & d = 2 \\ \frac{1.3}{2\pi\sqrt{2}}\left(\frac{4}{3} - \frac{3}{2}\widetilde{F}_\sigma\right)\sqrt{\frac{T}{D}} & d = 3 \end{cases} \tag{D.20}$$

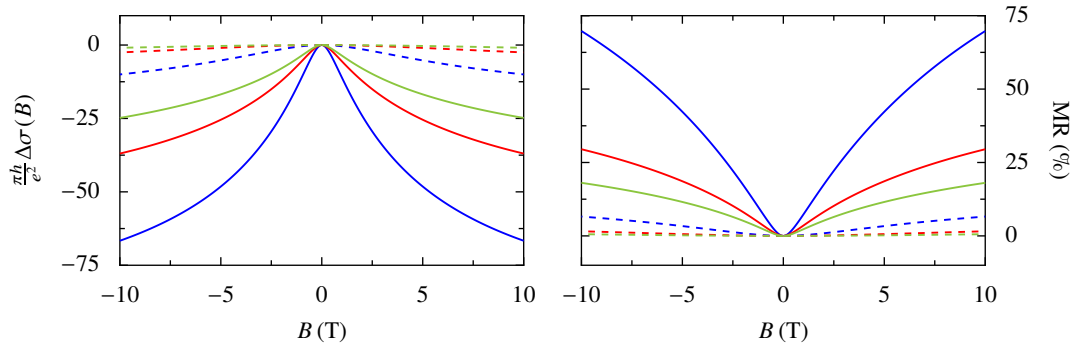

Figure D.3: *Maki–Thompson and Aslamazov–Larkin fluctuations near the superconducting transition.* MT (solid lines) and AL contributions (dashed lines) are shown for $T_c = 0.95T$ (blue curve), $T_c = 0.90T$ (red curve), and $T_c = 0.85T$ (green curve). Again, the MT fluctuations have a strong impact on the magneto-transport. The AL fluctuation are much weaker, but are noticeable nonetheless. The inelastic scattering field is chosen to be constant $B_i = 0.3\,\mathrm{T}$. The prefactor of the characteristic field B^* is chosen to be $2k_B T/\pi eD = 50\,\mathrm{T}$. In the plot, the transition temperature T_c is varied whereas T (and B_i) are kept constant. For the MR plot the sheet resistance is chosen to be $500\,\Omega$.

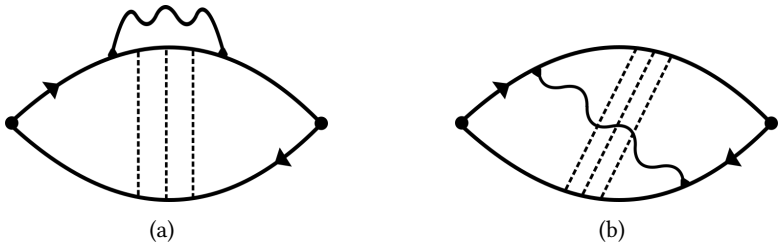

Figure D.4: *Relevant diagrams for the interaction in the particle–hole channel.* Propagating electrons are represented by solid lines, electron–electron interaction is represented as wavy line, and disorder scattering by dashed lines. The diagrams (a) and (b) contribute to the quantum conductivity. Together with Hartree terms, they lead to the corrections in Eq. (D.20). [46, 68]

where A is the wire cross-section area and

$$\widetilde{F}_\sigma = \begin{cases} \frac{8}{F}\left(1+\frac{F}{2}\right)\ln\left(1+\frac{F}{2}\right)-4 & d=2 \\ -\left[\frac{32F}{d(d-2)}\right]\left[1+\frac{dF}{4}-\left(1+\frac{F}{2}\right)^{\frac{d}{2}}\right] & d\neq 2 \end{cases} \tag{D.21}$$

where F is the screening factor, given by the angular average of the screened Coulomb interaction at the Fermi surface, which is in the range between zero and one [68]. The corresponding factor ${}^3\widetilde{F}_\sigma/2$ therefore is in the range between zero for no screening and ~ 1.3 for perfect screening.

Although the origin of these corrections are in the particle–hole channel, they are sensitive regarding an external magnetic field due to the splitting in spin-up and spin-down subbands. The pair propagators with anti-parallel spin are suppressed by magnetic field. The magneto-conductivity is given by [216, 301] (see again [46] for the corrected version)

$$\Delta\sigma(B,T) = -\frac{e^2}{\pi h}\frac{\widetilde{F}_\sigma}{2}\begin{cases} g_2\left(\frac{g\mu_B B}{k_B T}\right) & d=2 \\ \sqrt{\frac{T}{2D}}\,g_3\left(\frac{g\mu_B B}{k_B T}\right) & d=3 \end{cases}, \tag{D.22}$$

where the function g_2 is explicitly given by [216]

$$g_2(b) = \int_0^\infty \mathrm{d}\Omega \frac{\mathrm{d}^2}{\mathrm{d}\Omega^2}\left(\frac{\Omega}{e^\Omega-1}\right)\ln\left|1-\frac{b^2}{\Omega^2}\right|. \tag{D.23}$$

The limiting cases have been numerically calculated:

$$g_2(b) \approx \begin{cases} \ln\left(\frac{b}{1.3}\right) & b \gg 1 \\ 0.084 b^2 & b \ll 1 \end{cases} \tag{D.24}$$

and

$$g_3(b) \approx \begin{cases} \sqrt{b}-1.3 & b \gg 1 \\ 0.053 b^2 & b \ll 1 \end{cases}. \tag{D.25}$$

This causes a positive magneto-resistance, which has the same sign as WAL and the opposite of WL. However, the interaction induced positive magneto-resistance is specified by a monotonously growing function, which allows to distinguish it from WAL, where the slope changes. Furthermore, the interaction induced magneto-resistance is isotropic in the magnetic field direction, because its origin is not an orbital effect like the WL or WAL correction. Bergmann estimates a value in thin films of the order $\widetilde{F}_\sigma$ ~0.2–0.25 [302], but in MOSFETS, values much larger than 1 and up to even 4 have been reported, contradicting the above estimation for this value [303, 304]. In the above formulas, spin–orbit scattering has been neglected; spin–orbit coupling can change the formulas considerably [217, 305].

D.2.2 Particle–Particle Channel

Interaction corrections in the particle–particle channel [68] have been evaluated in Refs. [22, 298, 306]. These corrections have their origin in orbital effects and scale with the component of the magnetic field that is perpendicular to the two dimensional plane. They are given by [22]

$$\Delta\sigma(B,T) = -\frac{e^2}{\pi h} g(T) \begin{cases} \phi_2\left(\frac{2DeB}{\pi k_B T}\right) & d = 2 \\ \sqrt{\frac{eB}{\hbar}}\phi_3\left(\frac{2DeB}{\pi k_B T}\right) & d = 3 \end{cases}, \tag{D.26}$$

where $g(T)$ is the interaction strength, which can be positive (in case of Coulomb interaction) or negative (in case of superconducting fluctuations). The explicit expression for the two-dimensional case is given by

$$\phi_2(x) = \int_0^\infty \frac{t\mathrm{d}t}{\sinh^2(t)}\left(1 - \frac{xt}{\sinh(xt)}\right). \tag{D.27}$$

The functions can be calculated numerically and are give by the approximate terms

$$\phi_2(x) \approx \begin{cases} \ln(x) & x \gg 1 \\ \frac{\zeta(3)}{4}x^2 \approx 0.30x^2 & x \ll 1 \end{cases} \tag{D.28}$$

as well as

$$\phi_3(x) \approx \begin{cases} 1.90 & x \gg 1 \\ \frac{5\pi}{64}\zeta\left(\frac{5}{2}\right)x^{\frac{3}{2}} \approx 0.33x^{\frac{3}{2}} & x \ll 1 \end{cases}. \tag{D.29}$$

In presence of spin–orbit coupling, the above formulas have to be adapted [217]. The qualitative results are unchanged, but instead of the temperature cutoff, the spin–orbit scattering provides the cutoff in the particle–hole channel. A thorough calculation of interaction, both in the particle–particle as well as the particle–hole channel, in combination with spin–orbit coupling effects in the two dimensional case, is given in Refs. [305, 307]. Within the scope of this thesis, this effect is neglected.

D.3 Anomalous Hall Effect

The anomalous Hall effect (AHE) is an additional contribution to the original Hall effect that goes back to Hall himself [308]. It takes place in intrinsically time-reversal broken (like ferromagnetic) systems and has its origin in spin–orbit coupling [285]. In many materials, the AHE follows

$$\rho_{xy} = R_H B + R_{AHE} M_z(B), \tag{D.30}$$

where $R_H = 1/ne$ is the Hall constant, R_{AHE} the corresponding constant for the anomalous Hall effect, and $M_z(B)$ is the averaged magnetization of the sample. Several mechanisms can contribute to the value of R_{AHE}, where the most important originate from the Berry curvature (intrinsic AHE) and spin–orbit related scattering processes, as skew scattering and side jumps.

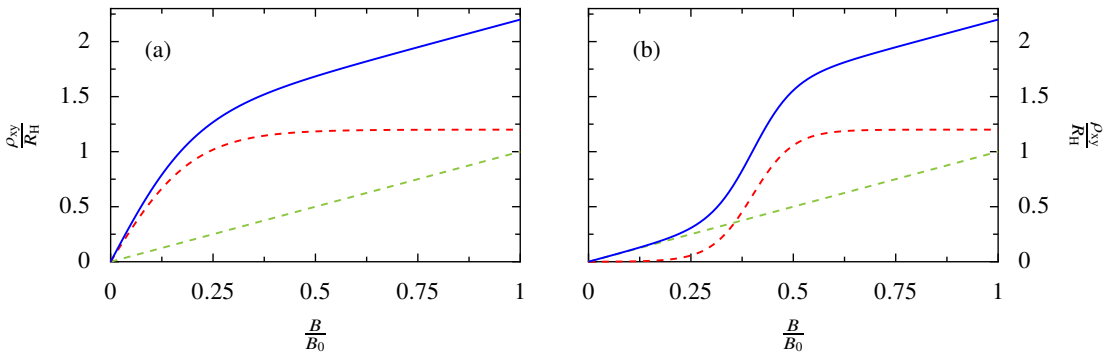

Figure D.5: *Signature of the anomalous Hall effect (AHE).* The linear Hall effect is shown as dashed green line; the AHE is shown as red dashed line. The resulting sum of these effects is shown in blue. The field B_0 denotes the scale for the saturation of the AHE. (a) For the typical AHE, as described by Eq. (D.31), two linear regimes in the Hall signal are expected, where the slope in the high field regime is smaller than in the low field regime. (b) AHE with low field magnetization $M \propto B^{\alpha}$ with $\alpha > 1$. The slope of the Hall signal is almost identical in the low and high magnetic field regime. Between these regimes, the curvature of the Hall signal changes.

For magnetic complex oxides, which show non-hysteretic behavior, the magnetization is often well described by [309]

$$M_z(B) = M_z^s \tanh\left(\frac{B}{B_c}\right), \tag{D.31}$$

where M_z^s is the saturation magnetization and B_c is some critical field. As this effect is relevant in many oxide heterostructures [309, 310], and especially discussed to appear in $LaAlO_3/SrTiO_3$ [164, 223, 225], this contribution has to be discussed within our analysis.

The typical signature of the AHE is the appearance of two linear regimes in the Hall signal, see Fig. D.5. This kind of signature can appear as a multiband Hall effect (see Fig. C.1) and it might be challenging to separate both contributions. The AHE found in $LaAlO_3/SrTiO_3$ still lacks an explanation.

List of Symbols and Acronyms

α, β, γ, δ	Spin indices
AHE	Anomalous Hall effect
AL	Aslamazov–Larkin fluctuations
β	β-function of renormalization group theory
β_{L}, $\beta_{\mathrm{LdS,\,A}}$	Interaction strength defined by Larkin / Lopes dos Santos and Abrahams
$\mathbf{B}$	Magnetic field
BKT	Berezinskiĭ–Kosterlitz–Thouless
B_{i}	Effective inelastic field
B_{m}	Effective spin scattering field
B_{o}	Effective elastic field
B_{so}	Effective spin-orbit field
B_{tr}	Effective transport field
C	Cooperon
d	Spatial dimension
δ_{ij}	Kronecker-Delta
δ_{MT}	Maki-Thomson pair breaking parameter
D	Diffusion constant
DMFT	Dynamical mean-field theory
DFT	Density functional theory
ε, ε_{F}	Energy, Fermi energy
ϵ	$d-2$
ϵ_{r}	Relative permittivity
$\mathbf{E}$	Electric field
$f(x)$	Fermi function
G	Conductance
g	Dimensionless conductance
$G^{\mathrm{ret/adv}}$	Retarded and Advanced Green's function
$\mathcal{G}$	Matsubara Green's function
g_{L}	Landé factor
γ_{EM}	Euler-Mascheroni constant
$\mathcal{H}$	Hamiltonian
HLN	Theory by Hikami, Larkin, and Nagaoka
ID	Interaction in the diffusion channel
ILP	Theory by Iordanskii, Lyanda-Geller, and Pikus
κ	$\frac{4eBD}{\hbar}$
L	System size

l	Mean free path
MR	Magneto-Resistivity or Magneto-Resistance, $\frac{\rho(B)-\rho(0)}{\rho(0)} = \frac{R(B)-R(0)}{R(0)}$
MIT	Metal–insulator transition
MOS(FET)	Metal–oxide–semiconductor (field-effect transistor)
MT	Maki–Thomson fluctuations
μ	Mobility
n	Charge carrier density
n_{imp}	Impurity density
N, N_{F}	Density of states at the Fermi level
ν	Critical exponent
ϕ	Angle
$\psi\left(\frac{1}{2}+x\right)$	Digamma function
$\Psi\left(\frac{1}{x}\right)$	$\psi\left(\frac{1}{2}+\frac{1}{x}\right)-\ln\left(\frac{1}{x}\right)$
R	Resistance
ρ	Resistivity
R_{sh}	Sheet resistance
σ	Conductivity
$\delta\sigma$	Quantum correction to the conductivity
$\Delta\sigma(B)$	$\delta\sigma(B)-\delta\sigma(0)$
$\boldsymbol{\sigma}$, $\boldsymbol{\rho}$	Vector of Pauli matrices
S_d	Unit sphere in d dimensions
sMIT	Symplectic metal-insulator transition
T, T_{c}	Temperature, critical temperature
τ	Life time
τ_0	Elastic life time
τ_{i}	Inelastic life time
τ_{m}	Magnetic (spin) life time
τ_{so}	Spin-orbit scattering or dephasing time
τ_{tr}	Transport time
$\Theta(x)$	Heaviside function
$\mathbf{v}$	(Group) Velocity
$\boldsymbol{\Omega}_{\mathrm{R/D},\,1/3}$	Bloch vector for Rashba/Dresselhaus single/triple spin winding
ω_n	Matsubara frequencies
$V_{\mathbf{k},\mathbf{k}'}$	Scattering potential
W	Disorder strength
WL	Weak localization
WAL	Weak anti-localization
ξ	Correlation lenght
$\xi_{\mathbf{k}}$	Kinetic Energy, $\frac{\hbar^2 k^2}{2m}$
z	Dynamical critical exponent
ζ	Riemannian ζ-function

Bibliography

[1] E. Abrahams, P. W. Anderson, D. C. Licciardello, and T. V. Ramakrishnan, "Scaling theory of localization: Absence of quantum diffusion in two dimensions," Phys. Rev. Lett. **42**, 673 (1979), URL http://link.aps.org/doi/10.1103/PhysRevLett.42.673.

[2] P. W. Anderson, "Absence of diffusion in certain random lattices," Phys. Rev. **109**, 1492 (1958), URL http://link.aps.org/doi/10.1103/PhysRev.109.1492.

[3] S. V. Kravchenko and M. P. Sarachik, "Metal-insulator transition in two-dimensional electron systems," Reports on Progress in Physics **67**, 1 (2004), URL http://stacks.iop.org/0034-4885/67/i=1/a=R01.

[4] S. V. Kravchenko and M. P. Sarachik, "A metal-insulator transition in 2D: Established facts and open questions," Physics Faculty Publications **5** (2010), URL http://www.worldscientific.com/doi/abs/10.1142/S021797921006454X.

[5] F. Wegner, "Four-loop-order β-function of nonlinear σ-models in symmetric spaces," Nuclear Physics B **316**, 663 (1989), ISSN 0550-3213, URL http://www.sciencedirect.com/science/article/pii/0550321389900631.

[6] S. Hikami, A. I. Larkin, and Y. Nagaoka, "Spin-orbit interaction and magnetoresistance in the two dimensional random system," Progress of Theoretical Physics **63**, 707 (1980), http://ptp.oxfordjournals.org/content/63/2/707.full.pdf+html, URL http://ptp.oxfordjournals.org/content/63/2/707.abstract.

[7] S. V. Iordanskii, Y. B. Lyanda-Geller, and G. E. Pikus, "Weak localization in quantum wells with spin-orbit interaction," Pis'ma Zh. Eksp. Teor. Fiz. **60**, 199 (1994), [JETP Lett. **60**, 206 (1994)], URL http://www.jetpletters.ac.ru/ps/1323/article_20010.shtml.

[8] P. Seiler, D. Braak, and T. Kopp, in preparation.

[9] P. Seiler, J. Zabaleta, R. Wanke, J. Mannhart, T. Kopp, and D. Braak, "Antilocalization at an oxide interface," Phys. Rev. B **97**, 075136 (2018), URL https://link.aps.org/doi/10.1103/PhysRevB.97.075136.

[10] M. Strößer, P. Seiler, T. Kopp, D. Braak, and G. Hammerl, in preparation.

[11] J. T. Edwards and D. J. Thouless, "Numerical studies of localization in disordered systems," Journal of Physics C: Solid State Physics **5**, 807 (1972), URL http://stacks.iop.org/0022-3719/5/i=8/a=007.

[12] F. Bloch, "Über die Quantenmechanik der Elektronen in Kristallgittern," Zeitschrift für Physik **52**, 555 (1929), ISSN 0044-3328, URL http://dx.doi.org/10.1007/BF01339455.

[13] X.-L. Qi and S.-C. Zhang, "Topological insulators and superconductors," Rev. Mod. Phys. **83**, 1057 (2011), URL https://link.aps.org/doi/10.1103/RevModPhys.83.1057.

[14] N. Mott, *Metal-Insulator Transitions* (Taylor & Francis, 1990), ISBN 9780850667837.

[15] J. Hubbard, "Electron correlations in narrow energy bands," Proceedings of the Royal Society of London A: Mathematical, Physical and Engineering Sciences **276**, 238 (1963), ISSN 0080-4630.

[16] P. Phillips, in *Advanced Solid State Physics* (Cambridge University Press, 2012), pp. 258–288, 2nd ed., ISBN 9781139031066, Cambridge Books Online, URL http://dx.doi.org/10.1017/CBO9781139031066.014.

[17] N. Mott, "Electrons in disordered structures," Advances in Physics **16**, 49 (1967), http://dx.doi.org/10.1080/00018736700101265, URL http://dx.doi.org/10.1080/00018736700101265.

[18] F. Evers and A. D. Mirlin, "Anderson transitions," Rev. Mod. Phys. **80**, 1355 (2008), URL http://link.aps.org/doi/10.1103/RevModPhys.80.1355.

[19] A. Abrikosov and I. Ryzhkin, "Conductivity of quasi-one-dimensional metal systems," Advances in Physics **27**, 147 (1978), https://doi.org/10.1080/00018737800101364, URL https://doi.org/10.1080/00018737800101364.

[20] A. M. Essin and J. E. Moore, "Topological insulators beyond the brillouin zone via chern parity," Phys. Rev. B **76**, 165307 (2007), URL https://link.aps.org/doi/10.1103/PhysRevB.76.165307.

[21] R. B. Laughlin, "Quantized Hall conductivity in two dimensions," Phys. Rev. B **23**, 5632 (1981), URL https://link.aps.org/doi/10.1103/PhysRevB.23.5632.

[22] B. L. Al'tshuler, A. G. Aronov, A. I. Larkin, and D. E. Khmel'nitskii, "Anomalous magnetoresistance in semiconductors," Zh. Eksp. Teor. Fiz. **81**, 768 (1981), [JETP **54**, 411 (1981)], URL http://www.jetp.ac.ru/cgi-bin/e/index/e/54/2/p411?a=list.

[23] P. Coleman, *Introduction to Many-Body Physics* (Cambridge University Press, 2015).

[24] K. Yakubo and S. Mizutaka, "Testing the order parameter of the Anderson transition," Journal of the Physical Society of Japan **81**, 104707 (2012), http://dx.doi.org/10.1143/JPSJ.81.104707, URL http://dx.doi.org/10.1143/JPSJ.81.104707.

[25] F. Wegner, "Electrons in disordered systems. Scaling near the mobility edge," Zeitschrift für Physik B Condensed Matter **25**, 327 (1976), ISSN 0722-3277, URL http://dx.doi.org/10.1007/BF01315248.

[26] L. P. Gor'kov, A. I. Larkin, and Khmel'nitskii, "Particle conductivity in a two-dimensional random potential," Pis'ma Zh. Eksp. Teor. Fiz. **30**, 248 (1979), [JETP Lett. **30**, 228 (1979)], URL http://www.jetpletters.ac.ru/ps/1364/article_20629.shtml.

[27] F. Wegner, "The mobility edge problem: Continuous symmetry and a conjecture," Zeitschrift für Physik B Condensed Matter **35**, 207 (1979), ISSN 0722-3277, URL http://dx.doi.org/10.1007/BF01319839.

[28] K. Efetov, A. Larkin, and D. Kheml'nitskii, "Interaction of diffusion modes in the theory of localization," Zh. Eksp. Teor. Fiz. **79**, 1120 (1980), [JETP **52**, 568 (1980)], URL http://www.jetp.ac.ru/cgi-bin/e/index/e/52/3/p568?a=list.

[29] W. Bernreuther and F. J. Wegner, "Four-loop-order β-function for two-dimensional nonlinear sigma models," Phys. Rev. Lett. **57**, 1383 (1986), URL http://link.aps.org/doi/10.1103/PhysRevLett.57.1383.

[30] S. Hikami, "Anderson localization in a nonlinear-σ-model representation," Phys. Rev. B **24**, 2671 (1981), URL http://link.aps.org/doi/10.1103/PhysRevB.24.2671.

[31] S. Hikami, "Anderson localization and nonlinear σ model," Progress of Theoretical Physics Supplement **84**, 120 (1985), /oup/backfile/content_public/journal/ptps/84/10.1143/ptps.84.120/2/84-120.pdf, URL http://dx.doi.org/10.1143/PTPS.84.120.

[32] Y. Imry, in *Introduction to mesoscopic physics* (Oxford University Press, 2008), pp. 9–31, 2nd ed., ISBN 9780199552696.

[33] C. D. Castro and R. Raimondi, *Statistical Mechanics and Applications in Condensed Matter* (Cambridge University Press, 2015).

[34] J. T. Chayes, L. Chayes, D. S. Fisher, and T. Spencer, "Finite-size scaling and correlation lengths for disordered systems," Phys. Rev. Lett. **57**, 2999 (1986), URL http://link.aps.org/doi/10.1103/PhysRevLett.57.2999.

[35] A. B. Harris, "Effect of random defects on the critical behaviour of Ising models," Journal of Physics C: Solid State Physics **7**, 1671 (1974), URL http://stacks.iop.org/0022-3719/7/i=9/a=009.

[36] D. Vollhardt and P. Wölfle, "Anderson localization in $d \leq 2$ dimensions: A self-consistent diagrammatic theory," Phys. Rev. Lett. **45**, 842 (1980), URL http://link.aps.org/doi/10.1103/PhysRevLett.45.842.

[37] D. Vollhardt and P. Wölfle, "Diagrammatic, self-consistent treatment of the Anderson localization problem in $d \leq 2$ dimensions," Phys. Rev. B **22**, 4666 (1980), URL http://link.aps.org/doi/10.1103/PhysRevB.22.4666.

[38] A. M. García-García, "Semiclassical theory of the Anderson transition," Phys. Rev. Lett. **100**, 076404 (2008), URL http://link.aps.org/doi/10.1103/PhysRevLett.100.076404.

[39] K. Slevin and T. Ohtsuki, "Corrections to scaling at the Anderson transition," Phys. Rev. Lett. **82**, 382 (1999), URL http://link.aps.org/doi/10.1103/PhysRevLett.82.382.

[40] K. Slevin and T. Ohtsuki, "Critical exponent for the Anderson transition in the three-dimensional orthogonal universality class," New Journal of Physics **16**, 015012 (2014), URL http://stacks.iop.org/1367-2630/16/i=1/a=015012.

[41] A. Rodriguez, L. J. Vasquez, K. Slevin, and R. A. Römer, "Critical parameters from a generalized multifractal analysis at the Anderson transition," Phys. Rev. Lett. **105**, 046403 (2010), URL http://link.aps.org/doi/10.1103/PhysRevLett.105.046403.

[42] A. Rodriguez, L. J. Vasquez, K. Slevin, and R. A. Römer, "Multifractal finite-size scaling and universality at the Anderson transition," Phys. Rev. B **84**, 134209 (2011), URL http://link.aps.org/doi/10.1103/PhysRevB.84.134209.

[43] M. Lopez, J.-F. m. c. Clément, P. Szriftgiser, J. C. Garreau, and D. Delande, "Experimental test of universality of the Anderson transition," Phys. Rev. Lett. **108**, 095701 (2012), URL http://link.aps.org/doi/10.1103/PhysRevLett.108.095701.

[44] T. Ying, Y. Gu, X. Chen, X. Wang, S. Jin, L. Zhao, W. Zhang, and X. Chen, "Anderson localization of electrons in single crystals: $Li_xFe_7Se_8$," Science Advances **2** (2016), http://advances.sciencemag.org/content/2/2/e1501283.full.pdf, URL http://advances.sciencemag.org/content/2/2/e1501283.

[45] G. Lemarié, J. Chabé, P. Szriftgiser, J. C. Garreau, B. Grémaud, and D. Delande, "Observation of the Anderson metal-insulator transition with atomic matter waves: Theory and experiment," Phys. Rev. A **80**, 043626 (2009), URL http://link.aps.org/doi/10.1103/PhysRevA.80.043626.

[46] P. A. Lee and T. V. Ramakrishnan, "Disordered electronic systems," Rev. Mod. Phys. **57**, 287 (1985), URL http://link.aps.org/doi/10.1103/RevModPhys.57.287.

[47] M. R. Zirnbauer, "Riemannian symmetric superspaces and their origin in random-matrix theory," Journal of Mathematical Physics **37**, 4986 (1996), URL http://scitation.aip.org/content/aip/journal/jmp/37/10/10.1063/1.531675.

[48] A. Altland and M. R. Zirnbauer, "Nonstandard symmetry classes in mesoscopic normal-superconducting hybrid structures," Phys. Rev. B **55**, 1142 (1997), URL http://link.aps.org/doi/10.1103/PhysRevB.55.1142.

[49] M. Caselle and U. Magnea, "Random matrix theory and symmetric spaces," Physics Reports **394**, 41 (2004), ISSN 0370-1573, URL http://www.sciencedirect.com/science/article/pii/S0370157304000092.

[50] P. Brouwer, Retrieval date: June 8, 2018, URL http://nbviewer.jupyter.org/github/topocm/topocm_content/blob/edx_2015/w9_disorder/scaling.ipynb#Metal-insulator-transition.

[51] P. Markoš and L. Schweitzer, "Critical regime of two-dimensional Ando model: relation between critical conductance and fractal dimension of electronic eigenstates," Journal of Physics A: Mathematical and General **39**, 3221 (2006), URL http://stacks.iop.org/0305-4470/39/i=13/a=003.

[52] T. Ando, "Numerical study of symmetry effects on localization in two dimensions," Phys. Rev. B **40**, 5325 (1989), URL http://link.aps.org/doi/10.1103/PhysRevB.40.5325.

[53] Y. Asada, K. Slevin, and T. Ohtsuki, "Anderson transition in two-dimensional systems with spin-orbit coupling," Phys. Rev. Lett. **89**, 256601 (2002), URL http://link.aps.org/doi/10.1103/PhysRevLett.89.256601.

[54] Y. Asada, K. Slevin, and T. Ohtsuki, "Numerical estimation of the β function in two-dimensional systems with spin-orbit coupling," Phys. Rev. B **70**, 035115 (2004), URL http://link.aps.org/doi/10.1103/PhysRevB.70.035115.

[55] P. W. Anderson, D. J. Thouless, E. Abrahams, and D. S. Fisher, "New method for a scaling theory of localization," Phys. Rev. B **22**, 3519 (1980), URL http://link.aps.org/doi/10.1103/PhysRevB.22.3519.

[56] K. Slevin, P. Markoš, and T. Ohtsuki, "Reconciling conductance fluctuations and the scaling theory of localization," Phys. Rev. Lett. **86**, 3594 (2001), URL http://link.aps.org/doi/10.1103/PhysRevLett.86.3594.

[57] T. Ohtsuki, K. Slevin, and B. Kramer, "Conductance distribution at two-dimensional Anderson transitions," Physica E: Low-dimensional Systems and Nanostructures **22**, 248 (2004), ISSN 1386-9477, 15th International Conference on Electronic Propreties of Two-Dimensional Systems (EP2DS-15), URL http://www.sciencedirect.com/science/article/pii/S1386947703008348.

[58] G. Orso, "Anderson transition of cold atoms with synthetic spin-orbit coupling in two-dimensional speckle potentials," Phys. Rev. Lett. **118**, 105301 (2017), URL https://link.aps.org/doi/10.1103/PhysRevLett.118.105301.

[59] L. Fu and C. L. Kane, "Topology, delocalization via average symmetry and the symplectic Anderson transition," Phys. Rev. Lett. **109**, 246605 (2012), URL http://link.aps.org/doi/10.1103/PhysRevLett.109.246605.

[60] H. Obuse, A. Furusaki, S. Ryu, and C. Mudry, "Two-dimensional spin-filtered chiral network model for the Z_2 quantum spin-Hall effect," Phys. Rev. B **76**, 075301 (2007), URL http://link.aps.org/doi/10.1103/PhysRevB.76.075301.

[61] K. Kobayashi, T. Ohtsuki, and K. Slevin, "Critical exponent for the quantum spin Hall transition in $\mathbb{Z}_2$ network model," International Journal of Modern Physics: Conference Series **11**, 114 (2012), http://www.worldscientific.com/doi/pdf/10.1142/S2010194512005995, URL http://www.worldscientific.com/doi/abs/10.1142/S2010194512005995.

[62] A. Yamakage, K. Nomura, K.-I. Imura, and Y. Kuramoto, "Criticality of the metal–topological insulator transition driven by disorder," Phys. Rev. B **87**, 205141 (2013), URL http://link.aps.org/doi/10.1103/PhysRevB.87.205141.

[63] M. Onoda, Y. Avishai, and N. Nagaosa, "Localization in a quantum spin Hall system," Phys. Rev. Lett. **98**, 076802 (2007), URL http://link.aps.org/doi/10.1103/PhysRevLett.98.076802.

[64] H. Obuse, A. Furusaki, S. Ryu, and C. Mudry, "Boundary criticality at the Anderson transition between a metal and a quantum spin Hall insulator in two dimensions," Phys. Rev. B **78**, 115301 (2008), URL http://link.aps.org/doi/10.1103/PhysRevB.78.115301.

[65] H. Obuse, A. R. Subramaniam, A. Furusaki, I. A. Gruzberg, and A. W. W. Ludwig, "Conformal invariance, multifractality, and finite-size scaling at Anderson localization transitions in two dimensions," Phys. Rev. B **82**, 035309 (2010), URL http://link.aps.org/doi/10.1103/PhysRevB.82.035309.

[66] J. S. Langer and T. Neal, "Breakdown of the concentration expansion for the impurity resistivity of metals," Phys. Rev. Lett. **16**, 984 (1966), URL http://link.aps.org/doi/10.1103/PhysRevLett.16.984.

[67] G. Bergmann, "Weak localization in thin films: A time-of-flight experiment with conduction electrons," Physics Reports **107**, 1 (1984), ISSN 0370-1573, URL http://www.sciencedirect.com/science/article/pii/0370157384901030.

[68] B. L. Al'tshuler, D. E. Khmel'nitzkii, A. I. Larkin, and P. A. Lee, "Magnetoresistance and Hall effect in a disordered two-dimensional electron gas," Phys. Rev. B **22**, 5142 (1980), URL http://link.aps.org/doi/10.1103/PhysRevB.22.5142.

[69] S. Maekawa and H. Fukuyama, "Magnetoresistance in two-dimensional disordered systems: Effects of Zeeman splitting and spin-orbit scattering," Journal of the Physical Society of Japan **50**, 2516 (1981), http://dx.doi.org/10.1143/JPSJ.50.2516, URL http://dx.doi.org/10.1143/JPSJ.50.2516.

[70] J. Rammer, *Quantum Transport Theory*, Frontiers in Physics Series (Westview Press, 2004), ISBN 9780813346229.

[71] J. Rammer, *Quantum Field Theory of Non-equilibrium States* (Cambridge University Press, 2007), ISBN 9781139465014, URL https://books.google.de/books?id=A7TbrAm5Wq0C.

[72] H. Fukuyama and E. Abrahams, "Inelastic scattering time in two-dimensional disordered metals," Phys. Rev. B **27**, 5976 (1983), URL https://link.aps.org/doi/10.1103/PhysRevB.27.5976.

[73] E. Abrahams, P. W. Anderson, P. A. Lee, and T. V. Ramakrishnan, "Quasiparticle lifetime in disordered two-dimensional metals," Phys. Rev. B **24**, 6783 (1981), URL https://link.aps.org/doi/10.1103/PhysRevB.24.6783.

[74] B. N. Narozhny, G. Zala, and I. L. Aleiner, "Interaction corrections at intermediate temperatures: Dephasing time," Phys. Rev. B **65**, 180202 (2002), URL https://link.aps.org/doi/10.1103/PhysRevB.65.180202.

[75] M. Eshkol, E. Eisenberg, M. Karpovski, and A. Palevski, "Dephasing time in a two-dimensional electron fermi liquid," Phys. Rev. B **73**, 115318 (2006), URL https://link.aps.org/doi/10.1103/PhysRevB.73.115318.

[76] B. Kramer and A. MacKinnon, "Localization: theory and experiment," Reports on Progress in Physics **56**, 1469 (1993), URL http://stacks.iop.org/0034-4885/56/i=12/a=001.

[77] Wolfram|Alpha, Retrieval date: May 29, 2018, URL http://www.wolframalpha.com/input/?i=digamma(1%2F2%2Bx+)+series.

[78] Wolfram|Alpha, Retrieval date: May 29, 2018, URL http://www.wolframalpha.com/input/?i=digamma(1%2F2).

[79] Wolfram|Alpha, Retrieval date: May 29, 2018, URL http://www.wolframalpha.com/input/?i=digamma(3%2F2).

[80] M. Wu, J. Jiang, and M. Weng, "Spin dynamics in semiconductors," Physics Reports **493**, 61 (2010), ISSN 0370-1573, URL http://www.sciencedirect.com/science/article/pii/S0370157310000955.

[81] R. J. Elliott, "Theory of the effect of spin-orbit coupling on magnetic resonance in some semiconductors," Phys. Rev. **96**, 266 (1954), URL http://link.aps.org/doi/10.1103/PhysRev.96.266.

[82] Y. Yafet, "Conduction electron spin relaxation in the superconducting state," Physics Letters A **98**, 287 (1983), ISSN 0375-9601, URL http://www.sciencedirect.com/science/article/pii/0375960183908745.

[83] P. Boross, B. Dóra, A. Kiss, and F. Simon, "A unified theory of spin-relaxation due to spin-orbit coupling in metals and semiconductors," Sci. Rep. **3**, 1 (2013), URL http://dx.doi.org/10.1038/srep03233.

[84] I. Žutić, J. Fabian, and S. Das Sarma, "Spintronics: Fundamentals and applications," Rev. Mod. Phys. **76**, 323 (2004), URL http://link.aps.org/doi/10.1103/RevModPhys.76.323.

[85] Y. Kawaguchi, H. Kitahara, and S. Kawaji, "Angular dependent negative magnetoresistance in Si-MOS (111) inversion layers," Solid State Communications **26**, 701 (1978), ISSN 0038-1098, URL http://www.sciencedirect.com/science/article/pii/0038109878907238.

[86] Y. Kawaguchi and S. Kawaji, "Negative magnetoresistance in silicon (100) MOS inversion layers," Journal of the Physical Society of Japan **48**, 699 (1980), http://dx.doi.org/10.1143/JPSJ.48.699, URL http://dx.doi.org/10.1143/JPSJ.48.699.

[87] Y. Kawaguchi, H. Kitahara, and S. Kawaji, "Negative magnetoresistance in a two-dimensional impurity band in cesiated p-Si(111) surface inversion layers," Surface Science **73**, 520 (1978), ISSN 0039-6028, URL http://www.sciencedirect.com/science/article/pii/0039602878905356.

[88] G. Bergmann, "Quantum corrections to the resistance in two-dimensional disordered superconductors above T_c: Al, Sn, and amorphous $Bi_{0.9}$ $Tl_{0.1}$ films," Phys. Rev. B **29**, 6114 (1984), URL https://link.aps.org/doi/10.1103/PhysRevB.29.6114.

[89] F. Komori, S. ichi Kobayashi, Y. Ootuka, and W. Sasaki, "Experimental study of electron localization in a two-dimensional metal," Journal of the Physical Society of Japan **50**, 1051 (1981), http://dx.doi.org/10.1143/JPSJ.50.1051, URL http://dx.doi.org/10.1143/JPSJ.50.1051.

[90] S. ichi Kobayashi, F. Komori, Y. Ootuka, and W. Sasaki, "ln T dependence of resistivity in two-dimensionally coupled fine particles of Cu," Journal of the Physical Society of Japan **49**, 1635 (1980), http://dx.doi.org/10.1143/JPSJ.49.1635, URL http://dx.doi.org/10.1143/JPSJ.49.1635.

[91] H. Mathur and A. D. Stone, "Quantum transport and the electronic Aharonov-Casher effect," Phys. Rev. Lett. **68**, 2964 (1992), URL http://link.aps.org/doi/10.1103/PhysRevLett.68.2964.

[92] P. D. Dresselhaus, C. M. A. Papavassiliou, R. G. Wheeler, and R. N. Sacks, "Observation of spin precession in GaAs inversion layers using antilocalization," Phys. Rev. Lett. **68**, 106 (1992), URL http://link.aps.org/doi/10.1103/PhysRevLett.68.106.

[93] M. D'yakonov and V. Perel, "Spin orientation of electrons associated with the interband absorption of light in semiconductors," Zh. Eksp. Teor. Fiz. **60**, 1954 (1971), [JETP **33**, 1053 (1971)], URL http://www.jetp.ac.ru/cgi-bin/e/index/e/33/5/p1053?a=list.

[94] A. H. Clark, R. D. Burnham, D. J. Chadi, and R. M. White, "Spin relaxation of conduction electrons in $Al_xGa_{1-x}As$," Phys. Rev. B **12**, 5758 (1975), URL http://link.aps.org/doi/10.1103/PhysRevB.12.5758.

[95] A. D. Caviglia, M. Gabay, S. Gariglio, N. Reyren, C. Cancellieri, and J.-M. Triscone, "Tunable Rashba spin-orbit interaction at oxide interfaces," Phys. Rev. Lett. **104**, 126803 (2010), URL http://link.aps.org/doi/10.1103/PhysRevLett.104.126803.

[96] T. Hernandez, C. W. Bark, D. A. Felker, C. B. Eom, and M. S. Rzchowski, "Localization of two-dimensional electron gas in $LaAlO_3/SrTiO_3$ heterostructures," Phys. Rev. B **85**, 161407 (2012), URL http://link.aps.org/doi/10.1103/PhysRevB.85.161407.

[97] D. Stornaiuolo, S. Gariglio, A. Fête, M. Gabay, D. Li, D. Massarotti, and J.-M. Triscone, "Weak localization and spin-orbit interaction in side-gate field effect devices at the $LaAlO_3/SrTiO_3$ interface," Phys. Rev. B **90**, 235426 (2014), URL http://link.aps.org/doi/10.1103/PhysRevB.90.235426.

[98] G. Dresselhaus, "Spin-orbit coupling effects in zinc blende structures," Phys. Rev. **100**, 580 (1955), URL http://link.aps.org/doi/10.1103/PhysRev.100.580.

[99] M. Glazov, E. Sherman, and V. Dugaev, "Two-dimensional electron gas with spin-orbit coupling disorder," Physica E: Low-dimensional Systems and Nanostructures **42**, 2157 (2010), ISSN 1386-9477, URL http://www.sciencedirect.com/science/article/pii/S1386947710002213.

[100] F. G. Pikus and G. E. Pikus, "Conduction-band spin splitting and negative magnetoresistance in A_3B_5 heterostructures," Phys. Rev. B **51**, 16928 (1995), URL http://link.aps.org/doi/10.1103/PhysRevB.51.16928.

[101] W. Knap, C. Skierbiszewski, A. Zduniak, E. Litwin-Staszewska, D. Bertho, F. Kobbi, J. L. Robert, G. E. Pikus, F. G. Pikus, S. V. Iordanskii, et al., "Weak anti-localization and spin precession in quantum wells," Phys. Rev. B **53**, 3912 (1996), URL http://link.aps.org/doi/10.1103/PhysRevB.53.3912.

[102] Y. A. Bychkov and E. I. Rashba, "Oscillatory effects and the magnetic susceptibility of carriers in inversion layers," Journal of Physics C: Solid State Physics **17**, 6039 (1984), URL http://stacks.iop.org/0022-3719/17/i=33/a=015.

[103] A. Manchon, H. C. Koo, J. Nitta, S. M. Frolov, and R. A. Duine, "New perspectives for Rashba spin-orbit coupling," Nat. Mater. **14**, 871 (2015), URL http://www.nature.com/nmat/journal/v14/n9/abs/nmat4360.html.

[104] G. Bihlmayer, O. Rader, and R. Winkler, "Focus on the Rashba effect," New Journal of Physics **17**, 050202 (2015), URL http://stacks.iop.org/1367-2630/17/i=5/a=050202.

[105] E. A. de Andrada e Silva, G. C. La Rocca, and F. Bassani, "Spin-orbit splitting of electronic states in semiconductor asymmetric quantum wells," Phys. Rev. B **55**, 16293 (1997), URL http://link.aps.org/doi/10.1103/PhysRevB.55.16293.

[106] L. Petersen and P. Hedegård, "A simple tight-binding model of spin–orbit splitting of sp-derived surface states," Surface Science **459**, 49 (2000), ISSN 0039-6028, URL http://www.sciencedirect.com/science/article/pii/S0039602800004416.

[107] R. Winkler, *Spin-orbit Coupling Effects in Two-Dimensional Electron and Hole Systems* (Springer-Verlag Berlin Heidelberg, 2003), 1st ed.

[108] Y. Kim, R. M. Lutchyn, and C. Nayak, "Origin and transport signatures of spin-orbit interactions in one- and two-dimensional $SrTiO_3$-based heterostructures," Phys. Rev. B **87**, 245121 (2013), URL http://link.aps.org/doi/10.1103/PhysRevB.87.245121.

[109] J. Zhou, W.-Y. Shan, and D. Xiao, "Spin responses and effective Hamiltonian for the two-dimensional electron gas at the oxide interface $LaAlO_3/SrTiO_3$," Phys. Rev. B **91**, 241302 (2015), URL http://link.aps.org/doi/10.1103/PhysRevB.91.241302.

[110] M. D'yakonov and V. Perel, "Spin relaxation of conduction electrons in noncentrosymmetric semiconductors," Soviet Physics Solid State, USSR **13**, 3023 (1972).

[111] T. Hassenkam, S. Pedersen, K. Baklanov, A. Kristensen, C. B. Sorensen, P. E. Lindelof, F. G. Pikus, and G. E. Pikus, "Spin splitting and weak localization in (110) $GaAs/Al_xGa_{1-x}As$ quantum wells," Phys. Rev. B **55**, 9298 (1997), URL http://link.aps.org/doi/10.1103/PhysRevB.55.9298.

[112] B. P. Brooks, "The coefficients of the characteristic polynomial in terms of the eigenvalues and the elements of an n×n matrix," Applied Mathematics Letters **19**, 511 (2006), ISSN 0893-9659, URL http://www.sciencedirect.com/science/article/pii/S0893965905002612.

[113] A. Punnoose, "Magnetoconductivity in the presence of Bychkov-Rashba spin-orbit interaction," Applied Physics Letters **88**, 252113 (2006), URL http://scitation.aip.org/content/aip/journal/apl/88/25/10.1063/1.2216027.

[114] D. Rainer and G. Bergmann, "Multiband effects in weak localization," Phys. Rev. B **32**, 3522 (1985), URL http://link.aps.org/doi/10.1103/PhysRevB.32.3522.

[115] S. G. Magalhães and A. Theumann, "Multiband and mass-anisotropy effects in the magnetoconductivity of a disordered electron gas," Phys. Rev. B **47**, 7572 (1993), URL http://link.aps.org/doi/10.1103/PhysRevB.47.7572.

[116] W. Nolting, *Grundkurs Theoretische Physik 5/2 - Quantenmechanik-Methoden und Anwendungen* (Springer Berlin Heidelberg, 2006).

[117] C. Cen, S. Thiel, J. Mannhart, and J. Levy, "Oxide nanoelectronics on demand," Science **323**, 1026 (2009), ISSN 0036-8075, http://science.sciencemag.org/content/323/5917/1026.full.pdf, URL http://science.sciencemag.org/content/323/5917/1026.

[118] J. Mannhart, D. Blank, H. Hwang, A. Millis, and J.-M. Triscone, "Two-dimensional electron gases at oxide interfaces," MRS Bulletin **33**, 1027 (2008), URL https://doi.org/10.1557/mrs2008.222.

[119] H. Hilgenkamp, "Novel transport phenomena at complex oxide interfaces," MRS Bulletin **38**, 1026 (2013), URL https://www.cambridge.org/core/journals/mrs-bulletin/article/novel-transport-phenomena-at-complex-oxide-interfaces/0144ECFD0CBE2AF21324BC3B0F3E91A5.

[120] J. Mannhart, H. Boschker, T. Kopp, and R. Valentí, "Artificial atoms based on correlated materials," Reports on Progress in Physics **79**, 084508 (2016), URL http://stacks.iop.org/0034-4885/79/i=8/a=084508.

[121] J. Ngai, F. Walker, and C. Ahn, "Correlated oxide physics and electronics," Annual Review of Materials Research **44**, 1 (2014), http://dx.doi.org/10.1146/annurev-matsci-070813-113248, URL http://dx.doi.org/10.1146/annurev-matsci-070813-113248.

[122] Y. Tokura and Y. Tomioka, "Colossal magnetoresistive manganites," Journal of Magnetism and Magnetic Materials **200**, 1 (1999), ISSN 0304-8853, URL http://www.sciencedirect.com/science/article/pii/S0304885399003522.

[123] P. Gegenwart and S. Trebst, "Spin-orbit physics: Kitaev matter," Nat. Phys. **11**, 444 (2015), URL http://dx.doi.org/10.1038/nphys3346.

[124] F. Loder, A. P. Kampf, and T. Kopp, "Route to topological superconductivity via magnetic field rotation," Scientific Reports **5**, 15302 (2015), URL http://www.ncbi.nlm.nih.gov/pmc/articles/PMC4609968/.

[125] A. Tsukazaki, A. Ohtomo, T. Kita, Y. Ohno, H. Ohno, and M. Kawasaki, "Quantum Hall effect in polar oxide heterostructures," Science **315**, 1388 (2007), ISSN 0036-8075, http://science.sciencemag.org/content/315/5817/1388.full.pdf, URL http://science.sciencemag.org/content/315/5817/1388.

[126] A. Tsukazaki, S. Akasaka, K. Nakahara, Y. Ohno, H. Ohno, D. Maryenko, A. Ohtomo, and M. Kawasaki, "Observation of the fractional quantum Hall effect in an oxide," Nat. Mater. **9**, 889 (2010), URL http://www.nature.com/nmat/journal/v9/n11/abs/nmat2874.html#supplementary-information.

[127] J. Mannhart and D. G. Schlom, "Oxide interfaces — An opportunity for electronics," Science **327**, 1607 (2010), ISSN 0036-8075, http://science.sciencemag.org/content/327/5973/1607.full.pdf, URL http://science.sciencemag.org/content/327/5973/1607.

[128] T. Ando, A. B. Fowler, and F. Stern, "Electronic properties of two-dimensional systems," Rev. Mod. Phys. **54**, 437 (1982), URL http://link.aps.org/doi/10.1103/RevModPhys.54.437.

[129] M. Breitschaft, V. Tinkl, N. Pavlenko, S. Paetel, C. Richter, J. R. Kirtley, Y. C. Liao, G. Hammerl, V. Eyert, T. Kopp, et al., "Two-dimensional electron liquid state at $LaAlO_3/SrTiO_3$ interfaces," Phys. Rev. B **81**, 153414 (2010), URL https://link.aps.org/doi/10.1103/PhysRevB.81.153414.

[130] P. Zubko, S. Gariglio, M. Gabay, P. Ghosez, and J.-M. Triscone, "Interface physics in complex oxide heterostructures," Annual Review of Condensed Matter Physics **2**, 141 (2011), http://dx.doi.org/10.1146/annurev-conmatphys-062910-140445, URL http://dx.doi.org/10.1146/annurev-conmatphys-062910-140445.

[131] J. A. Sulpizio, S. Ilani, P. Irvin, and J. Levy, "Nanoscale phenomena in oxide heterostructures," Annual Review of Materials Research **44**, 117 (2014), http://dx.doi.org/10.1146/annurev-matsci-070813-113437, URL http://dx.doi.org/10.1146/annurev-matsci-070813-113437.

[132] S. Stemmer and S. J. Allen, "Two-dimensional electron gases at complex oxide interfaces," Annual Review of Materials Research **44**, 151 (2014), http://dx.doi.org/10.1146/annurev-matsci-070813-113552, URL http://dx.doi.org/10.1146/annurev-matsci-070813-113552.

[133] B. Förg, C. Richter, and J. Mannhart, "Field-effect devices utilizing $LaAlO_3/SrTiO_3$ interfaces," Applied Physics Letters **100**, 053506 (2012), URL http://scitation.aip.org/content/aip/journal/apl/100/5/10.1063/1.3682102.

[134] D. Stornaiuolo, S. Gariglio, N. J. G. Couto, A. Fête, A. D. Caviglia, G. Seyfarth, D. Jaccard, A. F. Morpurgo, and J.-M. Triscone, "In-plane electronic confinement in superconducting $LaAlO_3/SrTiO_3$ nanostructures," Applied Physics Letters **101**, 222601 (2012), URL http://scitation.aip.org/content/aip/journal/apl/101/22/10.1063/1.4768936.

[135] J. Zabaleta, V. S. Borisov, R. Wanke, H. O. Jeschke, S. C. Parks, B. Baum, A. Teker, T. Harada, K. Syassen, T. Kopp, et al., "Hydrostatic pressure response of an oxide-based two-dimensional electron system," Phys. Rev. B **93**, 235117 (2016), URL http://link.aps.org/doi/10.1103/PhysRevB.93.235117.

[136] B. Meir, S. Gorol, T. Kopp, and G. Hammerl, "Observation of two-dimensional superconductivity in bilayers of $BaBiO_3$ and $BaPbO_3$," Phys. Rev. B **96**, 100507 (2017), URL https://link.aps.org/doi/10.1103/PhysRevB.96.100507.

[137] B. Meir, Dissertation, in preparation, Universität Augsburg (2018).

[138] H. Y. Hwang, Y. Iwasa, M. Kawasaki, B. Keimer, N. Nagaosa, and Y. Tokura, "Emergent phenomena at oxide interfaces," Nat. Mater. **11**, 103 (2012), URL http://www.nature.com/nmat/journal/v11/n2/abs/nmat3223.html.

[139] A. F. Santander-Syro, O. Copie, T. Kondo, F. Fortuna, S. Pailhes, R. Weht, X. G. Qiu, F. Bertran, A. Nicolaou, A. Taleb-Ibrahimi, et al., "Two-dimensional electron gas with universal subbands at the surface of $SrTiO_3$," Nature **469**, 189 (2011), URL http://www.nature.com/nature/journal/v469/n7329/full/nature09720.html.

[140] W. Meevasana, P. D. C. King, R. H. He, S.-K. Mo, M. Hashimoto, A. Tamai, P. Songsiriritthigul, F. Baumberger, and Z.-X. Shen, "Creation and control of a two-dimensional electron liquid at the bare $SrTiO_3$ surface," Nat. Mater. **10**, 114 (2011), URL http://www.nature.com/nmat/journal/v10/n2/full/nmat2943.html.

[141] J. Shen, H. Lee, R. Valentí, and H. O. Jeschke, "Ab initio study of the two-dimensional metallic state at the surface of $SrTiO_3$: Importance of oxygen vacancies," Phys. Rev. B **86**, 195119 (2012), URL https://link.aps.org/doi/10.1103/PhysRevB.86.195119.

[142] P. Delugas, V. Fiorentini, A. Mattoni, and A. Filippetti, "Intrinsic origin of two-dimensional electron gas at the (001) surface of $SrTiO_3$," Phys. Rev. B **91**, 115315 (2015), URL http://link.aps.org/doi/10.1103/PhysRevB.91.115315.

[143] A. Ohtomo and H. Y. Hwang, "A high-mobility electron gas at the $LaAlO_3/SrTiO_3$ heterointerface," Nature **427**, 423 (2004), URL http://dx.doi.org/10.1038/nature02308.

[144] M. Kawasaki, K. Takahashi, T. Maeda, R. Tsuchiya, M. Shinohara, O. Ishiyama, T. Yonezawa, M. Yoshimoto, and H. Koinuma, "Atomic control of the $SrTiO_3$ crystal surface," Science **266**, 1540 (1994), ISSN 0036-8075, http://science.sciencemag.org/content/266/5190/1540.full.pdf, URL http://science.sciencemag.org/content/266/5190/1540.

[145] G. Koster, B. L. Kropman, G. J. Rijnders, D. H. Blank, and H. Rogalla, "Influence of the surface treatment on the homoepitaxial growth of $SrTiO_3$," Materials Science and Engineering: B **56**, 209 (1998), ISSN 0921-5107, URL http://www.sciencedirect.com/science/article/pii/S0921510798002384.

[146] G. Herranz, M. Basletić, M. Bibes, C. Carrétéro, E. Tafra, E. Jacquet, K. Bouzehouane, C. Deranlot, A. Hamzić, J.-M. Broto, et al., "High mobility in $LaAlO_3/SrTiO_3$ heterostructures: Origin, dimensionality, and perspectives," Phys. Rev. Lett. **98**, 216803 (2007), URL http://link.aps.org/doi/10.1103/PhysRevLett.98.216803.

[147] H. P. R. Frederikse and W. R. Hosler, "Hall mobility in $SrTiO_3$," Phys. Rev. **161**, 822 (1967), URL http://link.aps.org/doi/10.1103/PhysRev.161.822.

[148] S. Thiel, G. Hammerl, A. Schmehl, C. W. Schneider, and J. Mannhart, "Tunable quasi-two-dimensional electron gases in oxide heterostructures," Science **313**, 1942 (2006), http://www.sciencemag.org/content/313/5795/1942.full.pdf, URL http://www.sciencemag.org/content/313/5795/1942.abstract.

[149] C. Cancellieri, M. L. Reinle-Schmitt, M. Kobayashi, V. N. Strocov, T. Schmitt, P. R. Willmott, S. Gariglio, and J.-M. Triscone, "Interface Fermi states of $LaAlO_3/SrTiO_3$ and related heterostructures," Phys. Rev. Lett. **110**, 137601 (2013), URL http://link.aps.org/doi/10.1103/PhysRevLett.110.137601.

[150] W. Liu, S. Gariglio, A. Fête, D. Li, M. Boselli, D. Stornaiuolo, and J.-M. Triscone, "Magneto-transport study of top- and back-gated $LaAlO_3/SrTiO_3$ heterostructures," APL Mater. **3**, 062805 (2015), URL http://scitation.aip.org/content/aip/journal/aplmater/3/6/10.1063/1.4921068.

[151] A. D. Caviglia, S. Gariglio, C. Cancellieri, B. Sacépé, A. Fête, N. Reyren, M. Gabay, A. F. Morpurgo, and J.-M. Triscone, "Two-dimensional quantum oscillations of the conductance at $LaAlO_3/SrTiO_3$ interfaces," Phys. Rev. Lett. **105**, 236802 (2010), URL http://link.aps.org/doi/10.1103/PhysRevLett.105.236802.

[152] N. Reyren, S. Thiel, A. D. Caviglia, L. F. Kourkoutis, G. Hammerl, C. Richter, C. W. Schneider, T. Kopp, A.-S. Rüetschi, D. Jaccard, et al., "Superconducting interfaces between insulating oxides," Science **317**, 1196 (2007), http://www.sciencemag.org/content/317/5842/1196.full.pdf, URL http://www.sciencemag.org/content/317/5842/1196.abstract.

[153] M. Basletic, J.-L. Maurice, C. Carretero, G. Herranz, O. Copie, M. Bibes, E. Jacquet, K. Bouzehouane, S. Fusil, and Barthelemy, "Mapping the spatial distribution of charge carriers in $LaAlO_3/SrTiO_3$ heterostructures," Nat. Mater. **7**, 621 (2008), URL http://dx.doi.org/10.1038/nmat2223.

[154] O. Copie, V. Garcia, C. Bödefeld, C. Carrétéro, M. Bibes, G. Herranz, E. Jacquet, J.-L. Maurice, B. Vinter, S. Fusil, et al., "Towards two-dimensional metallic behavior at $LaAlO_3/SrTiO_3$ interfaces," Phys. Rev. Lett. **102**, 216804 (2009), URL http://link.aps.org/doi/10.1103/PhysRevLett.102.216804.

[155] M. Sing, G. Berner, K. Goß, A. Müller, A. Ruff, A. Wetscherek, S. Thiel, J. Mannhart, S. A. Pauli, C. W. Schneider, et al., "Profiling the interface electron gas of $LaAlO_3/SrTiO_3$ heterostructures with hard x-ray photoelectron spectroscopy," Phys. Rev. Lett. **102**, 176805 (2009), URL https://link.aps.org/doi/10.1103/PhysRevLett.102.176805.

[156] A. Brinkman, M. Huijben, M. van Zalk, J. Huijben, U. Zeitler, J. C. Maan, W. G. van der Wiel, G. Rijnders, D. H. A. Blank, and H. Hilgenkamp, "Magnetic effects at the interface between non-magnetic oxides," Nat. Mater. **6**, 493 (2007), URL http://www.nature.com/nmat/journal/v6/n7/full/nmat1931.html.

[157] J. A. Bert, B. Kalisky, C. Bell, M. Kim, Y. Hikita, H. Y. Hwang, and K. A. Moler, "Direct imaging of the coexistence of ferromagnetism and superconductivity at the $LaAlO_3/SrTiO_3$ interface," Nat. Phys. **7**, 767 (2011), URL http://www.nature.com/nphys/journal/v7/n10/full/nphys2079.html.

[158] D. A. Dikin, M. Mehta, C. W. Bark, C. M. Folkman, C. B. Eom, and V. Chandrasekhar, "Coexistence of superconductivity and ferromagnetism in two dimensions," Phys. Rev. Lett. **107**, 056802 (2011), URL http://link.aps.org/doi/10.1103/PhysRevLett.107.056802.

[159] L. Li, C. Richter, J. Mannhart, and R. C. Ashoori, "Coexistence of magnetic order and two-dimensional superconductivity at $LaAlO_3/SrTiO_3$ interfaces," Nat. Phys. **7**, 762 (2011), URL http://www.nature.com/nphys/journal/v7/n10/abs/nphys2080.html.

[160] N. Pavlenko, T. Kopp, E. Y. Tsymbal, G. A. Sawatzky, and J. Mannhart, "Magnetic and superconducting phases at the $LaAlO_3/SrTiO_3$ interface: The role of interfacial Ti 3*d* electrons," Phys. Rev. B **85**, 020407 (2012), URL http://link.aps.org/doi/10.1103/PhysRevB.85.020407.

[161] J.-S. Lee, Y. W. Xie, H. K. Sato, C. Bell, Y. Hikita, H. Y. Hwang, and C.-C. Kao, "Titanium d_{xy} ferromagnetism at the $LaAlO_3/SrTiO_3$ interface," Nat. Mater. **12**, 703 (2013), URL http://dx.doi.org/10.1038/nmat3674.

[162] F. Bi, M. Huang, S. Ryu, H. Lee, C.-W. Bark, C.-B. Eom, P. Irvin, and J. Levy, "Room-temperature electronically-controlled ferromagnetism at the $LaAlO_3/SrTiO_3$ interface," Nat. Comm. **5** (2014), URL http://dx.doi.org/10.1038/ncomms6019.

[163] W. A. Atkinson, P. Lafleur, and A. Raslan, "Influence of the ferroelectric quantum critical point on $SrTiO_3$ interfaces," Phys. Rev. B **95**, 054107 (2017), URL https://link.aps.org/doi/10.1103/PhysRevB.95.054107.

[164] M. Ben Shalom, M. Sachs, D. Rakhmilevitch, A. Palevski, and Y. Dagan, "Tuning spin-orbit coupling and superconductivity at the $LaAlO_3/SrTiO_3$ interface: A magnetotransport study," Phys. Rev. Lett. **104**, 126802 (2010), URL http://link.aps.org/doi/10.1103/PhysRevLett.104.126802.

[165] K. Narayanapillai, K. Gopinadhan, X. Qiu, A. Annadi, Ariando, T. Venkatesan, and H. Yang, "Current-driven spin orbit field in $LaAlO_3/SrTiO_3$ heterostructures," Applied Physics Letters **105**, 162405 (2014), URL http://scitation.aip.org/content/aip/journal/apl/105/16/10.1063/1.4899122.

[166] S. Thiel, C. W. Schneider, L. F. Kourkoutis, D. A. Muller, N. Reyren, A. D. Caviglia, S. Gariglio, J.-M. Triscone, and J. Mannhart, "Electron scattering at dislocations in $LaAlO_3/SrTiO_3$ interfaces," Phys. Rev. Lett. **102**, 046809 (2009), URL http://link.aps.org/doi/10.1103/PhysRevLett.102.046809.

[167] N. Nakagawa, H. Y. Hwang, and D. A. Muller, "Why some interfaces cannot be sharp," Nat. Mater. **5**, 204 (2006), URL http://dx.doi.org/10.1038/nmat1569.

[168] S. Gariglio, A. Fête, and J.-M. Triscone, "Electron confinement at the $LaAlO_3/SrTiO_3$ interface," Journal of Physics: Condensed Matter **27**, 283201 (2015), URL http://stacks.iop.org/0953-8984/27/i=28/a=283201.

[169] S. Gariglio, M. Gabay, and J.-M. Triscone, "Research update: Conductivity and beyond at the $LaAlO_3/SrTiO_3$ interface," APL Materials **4**, 060701 (2016), https://doi.org/10.1063/1.4953822, URL https://doi.org/10.1063/1.4953822.

[170] Y.-Y. Pai, A. Tylan-Tyler, P. Irvin, and J. Levy, "Physics of $SrTiO_3$-based heterostructures and nanostructures: a review," Reports on Progress in Physics **81**, 036503 (2018), URL http://stacks.iop.org/0034-4885/81/i=3/a=036503.

[171] Y. Hotta, T. Susaki, and H. Y. Hwang, "Polar discontinuity doping of the $LaVO_3/SrTiO_3$ interface," Phys. Rev. Lett. **99**, 236805 (2007), URL http://link.aps.org/doi/10.1103/PhysRevLett.99.236805.

[172] M. Reinle-Schmitt, C. Cancellieri, D. Li, D. Fontaine, M. Medarde, E. Pomjakushina, C. Schneider, S. Gariglio, P. Ghosez, J.-M. Triscone, et al., "Tunable conductivity threshold at polar oxide interfaces," Nat. Comm. **3**, 932 (2012), URL http://dx.doi.org/10.1038/ncomms1936.

[173] M. Stengel, "First-principles modeling of electrostatically doped perovskite systems," Phys. Rev. Lett. **106**, 136803 (2011), URL https://link.aps.org/doi/10.1103/PhysRevLett.106.136803.

[174] C. Cancellieri, D. Fontaine, S. Gariglio, N. Reyren, A. D. Caviglia, A. Fête, S. J. Leake, S. A. Pauli, P. R. Willmott, M. Stengel, et al., "Electrostriction at the $LaAlO_3/SrTiO_3$ interface," Phys. Rev. Lett. **107**, 056102 (2011), URL https://link.aps.org/doi/10.1103/PhysRevLett.107.056102.

[175] H. Chen, A. M. Kolpak, and S. Ismail-Beigi, "Electronic and magnetic properties of $SrTiO_3/LaAlO_3$ interfaces from first principles," Advanced Materials **22**, 2881 (2010), ISSN 1521-4095, URL http://dx.doi.org/10.1002/adma.200903800.

[176] Y. Segal, J. H. Ngai, J. W. Reiner, F. J. Walker, and C. H. Ahn, "X-ray photoemission studies of the metal-insulator transition in $LaAlO_3/SrTiO_3$ structures grown by molecular beam epitaxy," Phys. Rev. B **80**, 241107 (2009), URL https://link.aps.org/doi/10.1103/PhysRevB.80.241107.

[177] M. Takizawa, S. Tsuda, T. Susaki, H. Y. Hwang, and A. Fujimori, "Electronic charges and electric potential at laalo$_3$/srtio$_3$ interfaces studied by core-level photoemission spectroscopy," Phys. Rev. B **84**, 245124 (2011), URL https://link.aps.org/doi/10.1103/PhysRevB.84.245124.

[178] Y. Chen, N. Pryds, J. E. Kleibeuker, G. Koster, J. Sun, E. Stamate, B. Shen, G. Rijnders, and S. Linderoth, "Metallic and insulating interfaces of amorphous $SrTiO_3$-based oxide heterostructures," Nano Letters **11**, 3774 (2011), pMID: 21823637, https://doi.org/10.1021/nl201821j, URL https://doi.org/10.1021/nl201821j.

[179] G. Herranz, F. Sánchez, N. Dix, M. Scigaj, and J. Fontcuberta, "High mobility conduction at (110) and (111) $LaAlO_3/SrTiO_3$ interfaces," Scientific Reports **2**, 758 (2012), URL http://dx.doi.org/10.1038/srep00758.

[180] S. S. A. Seo, Z. Marton, W. S. Choi, G. W. J. Hassink, D. H. A. Blank, H. Y. Hwang, T. W. Noh, T. Egami, and H. N. Lee, "Multiple conducting carriers generated in $LaAlO_3/SrTiO_3$ heterostructures," Applied Physics Letters **95**, 082107 (2009), URL http://scitation.aip.org/content/aip/journal/apl/95/8/10.1063/1.3213390.

[181] M. Ben Shalom, A. Ron, A. Palevski, and Y. Dagan, "Shubnikov-de Haas oscillations in $SrTiO_3/LaAlO_3$ interface," Phys. Rev. Lett. **105**, 206401 (2010), URL http://link.aps.org/doi/10.1103/PhysRevLett.105.206401.

[182] G. Berner, M. Sing, H. Fujiwara, A. Yasui, Y. Saitoh, A. Yamasaki, Y. Nishitani, A. Sekiyama, N. Pavlenko, T. Kopp, et al., "Direct k-space mapping of the electronic structure in an oxide-oxide interface," Phys. Rev. Lett. **110**, 247601 (2013), URL http://link.aps.org/doi/10.1103/PhysRevLett.110.247601.

[183] C. Cancellieri, M. L. Reinle-Schmitt, M. Kobayashi, V. N. Strocov, P. R. Willmott, D. Fontaine, P. Ghosez, A. Filippetti, P. Delugas, and V. Fiorentini, "Doping-dependent band structure of $LaAlO_3/SrTiO_3$ interfaces by soft x-ray polarization-controlled resonant angle-resolved photoemission," Phys. Rev. B **89**, 121412 (2014), URL http://link.aps.org/doi/10.1103/PhysRevB.89.121412.

[184] C. Cancellieri, A. S. Mishchenko, U. Aschauer, A. Filippetti, C. Faber, O. S. Barisic, V. A. Rogalev, T. Schmitt, N. Nagaosa, and V. N. Strocov, "Polaronic metal state at the $LaAlO_3/SrTiO_3$ interface," Nat. Comm. **7**, 10386 (2016), URL http://dx.doi.org/10.1038/ncomms10386.

[185] A. Dubroka, M. Rössle, K. W. Kim, V. K. Malik, L. Schultz, S. Thiel, C. W. Schneider, J. Mannhart, G. Herranz, O. Copie, et al., "Dynamical response and confinement of the electrons at the $LaAlO_3/SrTiO_3$ interface," Phys. Rev. Lett. **104**, 156807 (2010), URL http://link.aps.org/doi/10.1103/PhysRevLett.104.156807.

[186] P. Delugas, A. Filippetti, V. Fiorentini, D. I. Bilc, D. Fontaine, and P. Ghosez, "Spontaneous 2-dimensional carrier confinement at the n-type $SrTiO_3/LaAlO_3$ interface," Phys. Rev. Lett. **106**, 166807 (2011), URL http://link.aps.org/doi/10.1103/PhysRevLett.106.166807.

[187] R. Pentcheva and W. E. Pickett, "Avoiding the polarization catastrophe in $LaAlO_3$ overlayers on $SrTiO_3$(001) through polar distortion," Phys. Rev. Lett. **102**, 107602 (2009), URL https://link.aps.org/doi/10.1103/PhysRevLett.102.107602.

[188] R. Bistritzer, G. Khalsa, and A. H. MacDonald, "Electronic structure of doped d^0 perovskite semiconductors," Phys. Rev. B **83**, 115114 (2011), URL http://link.aps.org/doi/10.1103/PhysRevB.83.115114.

[189] N. Pavlenko and T. Kopp, "Structural relaxation and metal-insulator transition at the interface between $SrTiO_3$ and $LaAlO_3$," Surface Science **605**, 1114 (2011), ISSN 0039-6028, URL http://www.sciencedirect.com/science/article/pii/S003960281100118X.

[190] Z. Zhong, A. Tóth, and K. Held, "Theory of spin-orbit coupling at $LaAlO_3/SrTiO_3$ interfaces and $SrTiO_3$ surfaces," Phys. Rev. B **87**, 161102 (2013), URL http://link.aps.org/doi/10.1103/PhysRevB.87.161102.

[191] G. Khalsa, B. Lee, and A. H. MacDonald, "Theory of t_{2g} electron-gas Rashba interactions," Phys. Rev. B **88**, 041302 (2013), URL http://link.aps.org/doi/10.1103/PhysRevB.88.041302.

[192] F. Cossu, U. Schwingenschlögl, and V. Eyert, "Metal–insulator transition at the $LaAlO_3/SrTiO_3$ interface revisited: A hybrid functional study," Phys. Rev. B **88**, 045119 (2013), URL https://link.aps.org/doi/10.1103/PhysRevB.88.045119.

[193] A. Joshua, S. Pecker, J. Ruhman, E. Altman, and S. Ilani, "A universal critical density underlying the physics of electrons at the $LaAlO_3/SrTiO_3$ interface," Nat. Comm. **3**, 1129 (2012), URL http://dx.doi.org/10.1038/ncomms2116.

[194] M. Salluzzo, J. C. Cezar, N. B. Brookes, V. Bisogni, G. M. De Luca, C. Richter, S. Thiel, J. Mannhart, M. Huijben, A. Brinkman, et al., "Orbital reconstruction and the two-dimensional electron gas at the $LaAlO_3/SrTiO_3$ interface," Phys. Rev. Lett. **102**, 166804 (2009), URL http://link.aps.org/doi/10.1103/PhysRevLett.102.166804.

[195] Z. S. Popović, S. Satpathy, and R. M. Martin, "Origin of the two-dimensional electron gas carrier density at the $LaAlO_3$ on $SrTiO_3$ interface," Phys. Rev. Lett. **101**, 256801 (2008), URL http://link.aps.org/doi/10.1103/PhysRevLett.101.256801.

[196] H. Nakamura, T. Koga, and T. Kimura, "Experimental evidence of cubic Rashba effect in an inversion-symmetric oxide," Phys. Rev. Lett. **108**, 206601 (2012), URL https://link.aps.org/doi/10.1103/PhysRevLett.108.206601.

[197] N. Bovenzi and M. Diez, "Semiclassical theory of anisotropic transport at $laalo_3/srtio_3$ interfaces under an in-plane magnetic field," Phys. Rev. B **95**, 205430 (2017), URL https://link.aps.org/doi/10.1103/PhysRevB.95.205430.

[198] J. H. Haeni, P. Irvin, W. Chang, R. Uecker, P. Reiche, Y. L. Li, S. Choudhury, W. Tian, M. E. Hawley, B. Craigo, et al., "Room-temperature ferroelectricity in strained $SrTiO_3$," Nature **430**, 758 (2004), URL http://dx.doi.org/10.1038/nature02773.

[199] C. W. Bark, D. A. Felker, Y. Wang, Y. Zhang, H. W. Jang, C. M. Folkman, J. W. Park, S. H. Baek, H. Zhou, D. D. Fong, et al., "Tailoring a two-dimensional electron gas at the $LaAlO_3/SrTiO_3$ (001) interface by epitaxial strain," Proceedings of the National Academy of Sciences of the United States of America **108**, 4720 (2011), URL http://www.ncbi.nlm.nih.gov/pmc/articles/PMC3064336/.

[200] S. Nazir, M. Behtash, and K. Yang, "Enhancing interfacial conductivity and spatial charge confinement of $LaAlO_3/SrTiO_3$ heterostructures via strain engineering," Applied Physics Letters **105**, 141602 (2014), http://dx.doi.org/10.1063/1.4897626, URL http://dx.doi.org/10.1063/1.4897626.

[201] S. Nazir and K. Yang, "First-principles characterization of the critical thickness for forming metallic states in strained $LaAlO_3/SrTiO_3$(001) heterostructure," ACS Applied Materials & Interfaces **6**, 22351 (2014), pMID: 25486683, http://dx.doi.org/10.1021/am506336w, URL http://dx.doi.org/10.1021/am506336w.

[202] D. Fuchs, A. Sleem, R. Schäfer, A. G. Zaitsev, M. Meffert, D. Gerthsen, R. Schneider, and H. v. Löhneysen, "Incipient localization of charge carriers in the two-dimensional electron system in $LaAlO_3/SrTiO_3$ under hydrostatic pressure," Phys. Rev. B **92**, 155313 (2015), URL http://link.aps.org/doi/10.1103/PhysRevB.92.155313.

[203] X. Wang, W. M. Lü, A. Annadi, Z. Q. Liu, K. Gopinadhan, S. Dhar, T. Venkatesan, and Ariando, "Magnetoresistance of two-dimensional and three-dimensional electron gas in $LaAlO_3/SrTiO_3$ heterostructures: Influence of magnetic ordering, interface scattering, and dimensionality," Phys. Rev. B **84**, 075312 (2011), URL http://link.aps.org/doi/10.1103/PhysRevB.84.075312.

[204] A. Jost, V. K. Guduru, S. Wiedmann, J. C. Maan, U. Zeitler, S. Wenderich, A. Brinkman, and H. Hilgenkamp, "Transport and thermoelectric properties of the $LaAlO_3/SrTiO_3$ interface," Phys. Rev. B **91**, 045304 (2015), URL http://link.aps.org/doi/10.1103/PhysRevB.91.045304.

[205] S. Lerer, M. Ben Shalom, G. Deutscher, and Y. Dagan, "Low-temperature dependence of the thermomagnetic transport properties of the $SrTiO_3/LaAlO_3$ interface," Phys. Rev. B **84**, 075423 (2011), URL http://link.aps.org/doi/10.1103/PhysRevB.84.075423.

[206] D. Rakhmilevitch, I. Neder, M. B. Shalom, A. Tsukernik, M. Karpovski, Y. Dagan, and A. Palevski, "Anomalous response to gate voltage application in mesoscopic $LaAlO_3/SrTiO_3$ devices," Phys. Rev. B **87**, 125409 (2013), URL http://link.aps.org/doi/10.1103/PhysRevB.87.125409.

[207] M. Ben Shalom, I. Neder, A. Palevski, and Y. Dagan, "Phase Diagram of Micron-Size Bridges of $LaAlO_3/SrTiO_3$ Interface: Link Between Multiple Band Structure and Superconductivity," ArXiv e-prints (2014), 1402.4646, URL http://arxiv.org/abs/1402.4646v1.

[208] V. K. Guduru, A. McCollam, A. Jost, S. Wenderich, H. Hilgenkamp, J. C. Maan, A. Brinkman, and U. Zeitler, "Thermally excited multiband conduction in $LaAlO_3/SrTiO_3$ heterostructures exhibiting magnetic scattering," Phys. Rev. B **88**, 241301 (2013), URL http://link.aps.org/doi/10.1103/PhysRevB.88.241301.

[209] V. K. Guduru, A. Granados del Aguila, S. Wenderich, M. K. Kruize, A. McCollam, P. C. M. Christianen, U. Zeitler, A. Brinkman, G. Rijnders, H. Hilgenkamp, et al., "Optically excited multiband conduction in $LaAlO_3/SrTiO_3$ heterostructures," Applied Physics Letters **102**, 051604 (2013), URL http://scitation.aip.org/content/aip/journal/apl/102/5/10.1063/1.4790844.

[210] I. M. Lifshitz, "Anomalies of electron characteristics of a metal in the high pressure region," J. Exptl. Theoret. Phys. (U.S.S.R.) **38**, 1569 (1960), [JETP **11**, 1130 (1960)], URL http://www.jetp.ac.ru/cgi-bin/e/index/e/11/5/p1130?a=list.

[211] F. J. Wong, R. V. Chopdekar, and Y. Suzuki, "Disorder and localization at the $LaAlO_3/SrTiO_3$ heterointerface," Phys. Rev. B **82**, 165413 (2010), URL http://link.aps.org/doi/10.1103/PhysRevB.82.165413.

[212] Y. C. Liao, T. Kopp, C. Richter, A. Rosch, and J. Mannhart, "Metal-insulator transition of the $LaAlO_3$-$SrTiO_3$ interface electron system," Phys. Rev. B **83**, 075402 (2011), URL http://link.aps.org/doi/10.1103/PhysRevB.83.075402.

[213] A. Mawrie, T. Biswas, and T. K. Ghosh, "Magnetotransport properties of 2d fermionic systems with k -cubic Rashba spin-orbit interaction," Journal of Physics: Condensed Matter **26**, 405301 (2014), URL http://stacks.iop.org/0953-8984/26/i=40/a=405301.

[214] R. Moriya, K. Sawano, Y. Hoshi, S. Masubuchi, Y. Shiraki, A. Wild, C. Neumann, G. Abstreiter, D. Bougeard, T. Koga, et al., "Cubic Rashba spin-orbit interaction of a two-dimensional hole gas in a strained-Ge/SiGe quantum well," Phys. Rev. Lett. **113**, 086601 (2014), URL https://link.aps.org/doi/10.1103/PhysRevLett.113.086601.

[215] K. V. Shanavas, "Theoretical study of the cubic Rashba effect at the srtio$_3$(001) surfaces," Phys. Rev. B **93**, 045108 (2016), URL https://link.aps.org/doi/10.1103/PhysRevB.93.045108.

[216] P. A. Lee and T. V. Ramakrishnan, "Magnetoresistance of weakly disordered electrons," Phys. Rev. B **26**, 4009 (1982), URL http://link.aps.org/doi/10.1103/PhysRevB.26.4009.

[217] A. J. Millis and P. A. Lee, "Spin-orbit and paramagnon effects on magnetoconductance and tunneling," Phys. Rev. B **30**, 6170 (1984), URL http://link.aps.org/doi/10.1103/PhysRevB.30.6170.

[218] M. Diez, A. M. R. V. L. Monteiro, G. Mattoni, E. Cobanera, T. Hyart, E. Mulazimoglu, N. Bovenzi, C. W. J. Beenakker, and A. D. Caviglia, "Giant negative magnetoresistance driven by spin-orbit coupling at the $LaAlO_3/SrTiO_3$ interface," Phys. Rev. Lett. **115**, 016803 (2015), URL http://link.aps.org/doi/10.1103/PhysRevLett.115.016803.

[219] M. Ben Shalom, C. W. Tai, Y. Lereah, M. Sachs, E. Levy, D. Rakhmilevitch, A. Palevski, and Y. Dagan, "Anisotropic magnetotransport at the $SrTiO_3/LaAlO_3$ interface," Phys. Rev. B **80**, 140403 (2009), URL http://link.aps.org/doi/10.1103/PhysRevB.80.140403.

[220] M. Sachs, D. Rakhmilevitch, M. B. Shalom, S. Shefler, A. Palevski, and Y. Dagan, "Anomalous magneto-transport at the superconducting interface between $LaAlO_3$ and $SrTiO_3$," Physica C: Superconductivity **470, Supplement 1**, S746 (2010), ISSN 0921-4534, proceedings of the 9th International Conference on Materials and Mechanisms of Superconductivity, URL http://www.sciencedirect.com/science/article/pii/S0921453409008284.

[221] Ariando, X. Wang, G. Baskaran, Z. Q. Liu, J. Huijben, J. B. Yi, A. Annadi, A. R. Barman, A. Rusydi, S. Dhar, et al., "Electronic phase separation at the $LaAlO_3/SrTiO_3$ interface," Nat. Comm. **2**, 188 (2011), URL http://dx.doi.org/10.1038/ncomms1192.

[222] E. Flekser, M. Ben Shalom, M. Kim, C. Bell, Y. Hikita, H. Y. Hwang, and Y. Dagan, "Magnetotransport effects in polar versus non-polar $SrTiO_3$ based heterostructures," Phys. Rev. B **86**, 121104 (2012), URL http://link.aps.org/doi/10.1103/PhysRevB.86.121104.

[223] A. Joshua, J. Ruhman, S. Pecker, E. Altman, and S. Ilani, "Gate-tunable polarized phase of two-dimensional electrons at the $LaAlO_3/SrTiO_3$ interface," Proceedings of the National Academy of Sciences **110**, 9633 (2013), http://www.pnas.org/content/110/24/9633.full.pdf, URL http://www.pnas.org/content/110/24/9633.abstract.

[224] R. Pentcheva and W. E. Pickett, "Charge localization or itineracy at $LaAlO_3/SrTiO_3$ interfaces: Hole polarons, oxygen vacancies, and mobile electrons," Phys. Rev. B **74**, 035112 (2006), URL http://link.aps.org/doi/10.1103/PhysRevB.74.035112.

[225] J. Ruhman, A. Joshua, S. Ilani, and E. Altman, "Competition between Kondo screening and magnetism at the $LaAlO_3/SrTiO_3$ interface," Phys. Rev. B **90**, 125123 (2014), URL http://link.aps.org/doi/10.1103/PhysRevB.90.125123.

[226] W.-N. Lin, J.-F. Ding, S.-X. Wu, Y.-F. Li, J. Lourembam, S. Shannigrahi, S.-J. Wang, and T. Wu, "Electrostatic modulation of $LaAlO_3/SrTiO_3$ interface transport in an electric double-layer transistor," Advanced Materials Interfaces **1**, n/a (2014), ISSN 2196-7350, URL http://dx.doi.org/10.1002/admi.201300001.

[227] N. W. Ashcroft and N. D. Mermin, in *Solid State Physics* (Saunders College Publishing, 1976), Holt-Saunders International ed., ISBN 0-03-049346-3.

[228] R. Pentcheva, M. Huijben, K. Otte, W. E. Pickett, J. E. Kleibeuker, J. Huijben, H. Boschker, D. Kockmann, W. Siemons, G. Koster, et al., "Parallel electron-hole bilayer conductivity from electronic interface reconstruction," Phys. Rev. Lett. **104**, 166804 (2010), URL http://link.aps.org/doi/10.1103/PhysRevLett.104.166804.

[229] H. Lee, N. Campbell, J. Lee, T. J. Asel, T. R. Paudel, H. Zhou, J. W. Lee, B. Noesges, J. Seo, B. Park, et al., "Direct observation of a two-dimensional hole gas at oxide interfaces," Nat. Mater. p. 1476 (2018), URL https://doi.org/10.1038/s41563-017-0002-4.

[230] N. Pavlenko, T. Kopp, E. Y. Tsymbal, J. Mannhart, and G. A. Sawatzky, "Oxygen vacancies at titanate interfaces: Two-dimensional magnetism and orbital reconstruction," Phys. Rev. B **86**, 064431 (2012), URL https://link.aps.org/doi/10.1103/PhysRevB.86.064431.

[231] F. Lechermann, L. Boehnke, D. Grieger, and C. Piefke, "Electron correlation and magnetism at the $LaAlO_3/SrTiO_3$ interface: A DFT+DMFT investigation," Phys. Rev. B **90**, 085125 (2014), URL https://link.aps.org/doi/10.1103/PhysRevB.90.085125.

[232] H. Liang, L. Cheng, L. Wei, Z. Luo, G. Yu, C. Zeng, and Z. Zhang, "Nonmonotonically tunable rashba spin-orbit coupling by multiple-band filling control in $SrTiO_3$-based interfacial *d*-electron gases," Phys. Rev. B **92**, 075309 (2015), URL https://link.aps.org/doi/10.1103/PhysRevB.92.075309.

[233] B. Yan, M. Jansen, and C. Felser, "A large-energy-gap oxide topological insulator based on the superconductor $BaBiO_3$," Nat. Phys. **9**, 709 (2013), URL https://www.nature.com/articles/nphys2762.

[234] G. Li, B. Yan, R. Thomale, and W. Hanke, "Topological nature and the multiple dirac cones hidden in bismuth high-T_c superconductors," Scientific Reports **5**, 10435 (2015), URL http://dx.doi.org/10.1038/srep10435.

[235] L. F. Mattheiss, E. M. Gyorgy, and D. W. Johnson, "Superconductivity above 20 K in the Ba-K-Bi-O system," Phys. Rev. B **37**, 3745 (1988), URL https://link.aps.org/doi/10.1103/PhysRevB.37.3745.

[236] A. Sleight, J. Gillson, and P. Bierstedt, "High-temperature superconductivity in the $BaPb_{1-x}Bi_xO_3$ systems," Solid State Communications **17**, 27 (1975), ISSN 0038-1098, URL http://www.sciencedirect.com/science/article/pii/0038109875903270.

[237] R. Bartel, Dissertation, in preparation, Universität Augsburg.

[238] R. Bartel, P. Seiler, T. Kopp, and G. Hammerl, in preparation.

[239] T. I. Baturina, S. V. Postolova, A. Y. Mironov, A. Glatz, M. R. Baklanov, and V. M. Vinokur, "Superconducting phase transitions in ultrathin TiN films," EPL (Europhysics Letters) **97**, 17012 (2012), URL http://stacks.iop.org/0295-5075/97/i=1/a=17012.

[240] H. Ebisawa, S. Maekawa, and H. Fukuyama, "Pair breaking parameter of two-dimensional dirty superconductors," Solid State Communications **45**, 75 (1983), ISSN 0038-1098, URL http://www.sciencedirect.com/science/article/pii/0038109883903447.

[241] J. M. B. Lopes dos Santos and E. Abrahams, "Superconducting fluctuation conductivity in a magnetic field in two dimensions," Phys. Rev. B **31**, 172 (1985), URL https://link.aps.org/doi/10.1103/PhysRevB.31.172.

[242] A. Glatz, A. A. Varlamov, and V. M. Vinokur, "Fluctuation spectroscopy of disordered two-dimensional superconductors," Phys. Rev. B **84**, 104510 (2011), URL https://link.aps.org/doi/10.1103/PhysRevB.84.104510.

[243] Finkel'stein, "Influence of Coulomb interaction on the properties of disordered metals," Zh. Eksp. Teor. Fiz. **84**, 168 (1983), [JETP **57**, 97 (1983)], URL http://www.jetp.ac.ru/cgi-bin/e/index/e/57/1/p97?a=list.

[244] A. Finkel'stein, "Weak localization and Coulomb interaction in disordered systems," Zeitschrift für Physik B Condensed Matter **56**, 189 (1984), ISSN 0722-3277, URL http://dx.doi.org/10.1007/BF01304171.

[245] C. Castellani, C. Di Castro, P. A. Lee, and M. Ma, "Interaction-driven metal-insulator transitions in disordered fermion systems," Phys. Rev. B **30**, 527 (1984), URL http://link.aps.org/doi/10.1103/PhysRevB.30.527.

[246] D. Belitz and T. R. Kirkpatrick, "The Anderson-Mott transition," Rev. Mod. Phys. **66**, 261 (1994), URL http://link.aps.org/doi/10.1103/RevModPhys.66.261.

[247] S. V. Kravchenko, G. V. Kravchenko, J. E. Furneaux, V. M. Pudalov, and M. D'Iorio, "Possible metal-insulator transition at B =0 in two dimensions," Phys. Rev. B **50**, 8039 (1994), URL http://link.aps.org/doi/10.1103/PhysRevB.50.8039.

[248] S. V. Kravchenko, W. E. Mason, G. E. Bowker, J. E. Furneaux, V. M. Pudalov, and M. D'Iorio, "Scaling of an anomalous metal-insulator transition in a two-dimensional system in silicon at B =0," Phys. Rev. B **51**, 7038 (1995), URL http://link.aps.org/doi/10.1103/PhysRevB.51.7038.

[249] S. V. Kravchenko, D. Simonian, M. P. Sarachik, W. Mason, and J. E. Furneaux, "Electric field scaling at a $B = 0$ metal-insulator transition in two dimensions," Phys. Rev. Lett. **77**, 4938 (1996), URL http://link.aps.org/doi/10.1103/PhysRevLett.77.4938.

[250] A. Punnoose and A. M. Finkel'stein, "Dilute electron gas near the metal-insulator transition: Role of valleys in silicon inversion layers," Phys. Rev. Lett. **88**, 016802 (2001), URL http://link.aps.org/doi/10.1103/PhysRevLett.88.016802.

[251] A. Punnoose and A. M. Finkel'stein, "Metal-insulator transition in disordered two-dimensional electron systems," Science **310**, 289 (2005), http://www.sciencemag.org/content/310/5746/289.full.pdf, URL http://www.sciencemag.org/content/310/5746/289.abstract.

[252] S. Anissimova, S. V. Kravchenko, A. Punnoose, A. M. Finkel'stein, and T. M. Klapwijk, "Flow diagram of the metal-insulator transition in two dimensions," Nat. Phys. **3**, 707 (2007), URL http://dx.doi.org/10.1038/nphys685.

[253] D. A. Knyazev, O. E. Omel'yanovskii, V. M. Pudalov, and I. S. Burmistrov, "Metal-insulator transition in two dimensions: Experimental test of the two-parameter scaling," Phys. Rev. Lett. **100**, 046405 (2008), URL http://link.aps.org/doi/10.1103/PhysRevLett.100.046405.

[254] D. Simonian, S. V. Kravchenko, M. P. Sarachik, and V. M. Pudalov, "Magnetic field suppression of the conducting phase in two dimensions," Phys. Rev. Lett. **79**, 2304 (1997), URL http://link.aps.org/doi/10.1103/PhysRevLett.79.2304.

[255] S. A. Vitkalov, H. Zheng, K. M. Mertes, M. P. Sarachik, and T. M. Klapwijk, "Small-angle Shubnikov–de Haas measurements in a 2d electron system: The effect of a strong in-plane magnetic field," Phys. Rev. Lett. **85**, 2164 (2000), URL http://link.aps.org/doi/10.1103/PhysRevLett.85.2164.

[256] S. A. Vitkalov, M. P. Sarachik, and T. M. Klapwijk, "Spin polarization of two-dimensional electrons determined from Shubnikov–de Haas oscillations as a function of angle," Phys. Rev. B **64**, 073101 (2001), URL http://link.aps.org/doi/10.1103/PhysRevB.64.073101.

[257] K. M. Mertes, H. Zheng, S. A. Vitkalov, M. P. Sarachik, and T. M. Klapwijk, "Temperature dependence of the resistivity of a dilute two-dimensional electron system in high parallel magnetic field," Phys. Rev. B **63**, 041101 (2001), URL http://link.aps.org/doi/10.1103/PhysRevB.63.041101.

[258] Y. Tsui, S. A. Vitkalov, M. P. Sarachik, and T. M. Klapwijk, "Conductivity of silicon inversion layers: Comparison with and without an in-plane magnetic field," Phys. Rev. B **71**, 113308 (2005), URL http://link.aps.org/doi/10.1103/PhysRevB.71.113308.

[259] A. A. Shashkin, S. V. Kravchenko, V. T. Dolgopolov, and T. M. Klapwijk, "Sharp increase of the effective mass near the critical density in a metallic two-dimensional electron system," Phys. Rev. B **66**, 073303 (2002), URL http://link.aps.org/doi/10.1103/PhysRevB.66.073303.

[260] A. A. Shashkin, M. Rahimi, S. Anissimova, S. V. Kravchenko, V. T. Dolgopolov, and T. M. Klapwijk, "Spin-independent origin of the strongly enhanced effective mass in a dilute 2d electron system," Phys. Rev. Lett. **91**, 046403 (2003), URL http://link.aps.org/doi/10.1103/PhysRevLett.91.046403.

[261] S. Anissimova, A. Venkatesan, A. A. Shashkin, M. R. Sakr, S. V. Kravchenko, and T. M. Klapwijk, "Magnetization of a strongly interacting two-dimensional electron system in perpendicular magnetic fields," Phys. Rev. Lett. **96**, 046409 (2006), URL http://link.aps.org/doi/10.1103/PhysRevLett.96.046409.

[262] A. A. Shashkin, A. A. Kapustin, E. V. Deviatov, V. T. Dolgopolov, and Z. D. Kvon, "Strongly enhanced effective mass in dilute two-dimensional electron systems: System-independent origin," Phys. Rev. B **76**, 241302 (2007), URL http://link.aps.org/doi/10.1103/PhysRevB.76.241302.

[263] C. Cen, S. Thiel, G. Hammerl, C. W. Schneider, K. E. Andersen, C. S. Hellberg, J. Mannhart, and J. Levy, "Nanoscale control of an interfacial metal-insulator transition at room temperature," Nat. Mater. **7**, 298 (2008), URL http://www.nature.com/nmat/journal/v7/n4/suppinfo/nmat2136_S1.html.

[264] L. E. Golub, "Weak antilocalization in high-mobility two-dimensional systems," Phys. Rev. B **71**, 235310 (2005), URL http://link.aps.org/doi/10.1103/PhysRevB.71.235310.

[265] M. M. Glazov and L. E. Golub, "Spin splitting and weak localization in 2d heterostructures," Physica E: Low-dimensional Systems and Nanostructures **40**, 1490 (2008), ISSN 1386-9477, 17th International Conference on Electronic Properties of Two-Dimensional Systems, URL http://www.sciencedirect.com/science/article/pii/S1386947707005152.

[266] M. M. Glazov and L. E. Golub, "Spin-orbit interaction and weak localization in heterostructures," Semiconductor Science and Technology **24**, 064007 (2009), URL http://stacks.iop.org/0268-1242/24/i=6/a=064007.

[267] V. A. Guzenko, M. Akabori, T. Schäpers, S. Cabañas, T. Sato, T. Suzuki, and S. Yamada, "Weak antilocalization measurements on a 2-dimensional electron gas in an InGaSb/InAlSb heterostructure," physica status solidi (c) **3**, 4227 (2006), ISSN 1610-1642, URL http://dx.doi.org/10.1002/pssc.200672848.

[268] L. Sun, W. Zhou, G. Yu, L. Shang, K. Gao, Y. Zhou, T. Lin, L. Cui, Y. Zeng, and J. Chu, "Strong spin-orbit interactions in an InAlAs/InGaAs/InAlAs two-dimensional electron gas by weak antilocalization analysis," Japanese Journal of Applied Physics **48**, 063004 (2009), URL http://stacks.iop.org/1347-4065/48/i=6R/a=063004.

[269] D. Spirito, L. Di Gaspare, F. Evangelisti, A. Di Gaspare, E. Giovine, and A. Notargiacomo, "Weak antilocalization and spin-orbit interaction in a two-dimensional electron gas," Phys. Rev. B **85**, 235314 (2012), URL http://link.aps.org/doi/10.1103/PhysRevB.85.235314.

[270] V. A. Guzenko, T. Schäpers, and H. Hardtdegen, "Weak antilocalization in high mobility Ga_x In_{1-x} As / In P two-dimensional electron gases with strong spin-orbit coupling," Phys. Rev. B **76**, 165301 (2007), URL http://link.aps.org/doi/10.1103/PhysRevB.76.165301.

[271] A. Sawada and T. Koga, "Universal modeling of weak antilocalization corrections in quasi-two-dimensional electron systems using predetermined return orbitals," Phys. Rev. E **95**, 023309 (2017), URL https://link.aps.org/doi/10.1103/PhysRevE.95.023309.

[272] E. Lettl, P. Seiler, and T. Kopp, in preparation.

[273] M. Schreiber, S. S. Hodgman, P. Bordia, H. P. Lüschen, M. H. Fischer, R. Vosk, E. Altman, U. Schneider, and I. Bloch, "Observation of many-body localization of interacting fermions in a quasirandom optical lattice," Science **349**, 842 (2015), ISSN 0036-8075, http://science.sciencemag.org/content/349/6250/842.full.pdf, URL http://science.sciencemag.org/content/349/6250/842.

[274] J.-y. Choi, S. Hild, J. Zeiher, P. Schauß, A. Rubio-Abadal, T. Yefsah, V. Khemani, D. A. Huse, I. Bloch, and C. Gross, "Exploring the many-body localization transition in two dimensions," Science **352**, 1547 (2016), ISSN 0036-8075, http://science.sciencemag.org/content/352/6293/1547.full.pdf, URL http://science.sciencemag.org/content/352/6293/1547.

[275] D. A. Abanin and Z. Papić, "Recent progress in many-body localization," Annalen der Physik **529**, 1700169 (2017), ISSN 1521-3889, 1700169, URL http://dx.doi.org/10.1002/andp.201700169.

[276] G. Mahan, *Many-Particle physics* (Plenum Press, New York, 1993), 2nd ed.

[277] W. Nolting, *Grundkurs Theoretische Physik 7 - Viel-Teilchen-Theorie* (Springer Berlin Heidelberg, 2005).

[278] A. L. Fetter and J. D. Walecka, *Quantum Theory of Many-Particle Systems* (Dover Publications, inc., New York, 2003).

[279] R. Kubo, "Statistical-Mechanical Theory of Irreversible Processes. I.," J. Phys. Soc. Jpn. **12**, 570 (1957), URL http://jpsj.ipap.jp/link?JPSJ/12/570/.

[280] T. Matsubara, "A new approach to quantum-statistical mechanics," Progress of Theoretical Physics **14**, 351 (1955), http://ptp.oxfordjournals.org/content/14/4/351.full.pdf+html, URL http://ptp.oxfordjournals.org/content/14/4/351.abstract.

[281] P. Drude, "Zur Elektronentheorie der Metalle," Annalen der Physik **306**, 566 (1900), URL http://adsabs.harvard.edu/abs/1900AnP...306..566D.

[282] P. Drude, "Zur Elektronentheorie der Metalle; II. Teil. Galvanomagnetische und thermomagnetische Effecte," Annalen der Physik **308**, 369 (1900), URL http://adsabs.harvard.edu/abs/1900AnP...308..369D.

[283] J. M. Ziman, *Principles of the Theory of Solids:* (Cambridge University Press, Cambridge, 1972), 2nd ed., ISBN 9781139644075, URL https://www.cambridge.org/core/books/principles-of-the-theory-of-solids/F9E87699164B7094168277D4867EE4FC.

[284] H. Fukuyama, "Hall effect in two-dimensional disorderd systems," Journal of the Physical Society of Japan **49**, 644 (1980), http://dx.doi.org/10.1143/JPSJ.49.644, URL http://dx.doi.org/10.1143/JPSJ.49.644.

[285] N. Nagaosa, J. Sinova, S. Onoda, A. H. MacDonald, and N. P. Ong, "Anomalous Hall effect," Rev. Mod. Phys. **82**, 1539 (2010), URL https://link.aps.org/doi/10.1103/RevModPhys.82.1539.

[286] H. Fukuyama, "Effects of strong spin-orbit scattering on Hall effect in weakly localized regime," Journal of the Physical Society of Japan **52**, 18 (1983), http://dx.doi.org/10.1143/JPSJ.52.18, URL http://dx.doi.org/10.1143/JPSJ.52.18.

[287] H. Fukuyama, "Theory of weakly localized regime of the Anderson localizaton in two dimensions," Surface Science **113**, 489 (1982), ISSN 0039-6028, URL http://www.sciencedirect.com/science/article/pii/0039602882906380.

[288] P. Santhanam, S. Wind, and D. E. Prober, "Localization, superconducting fluctuations, and superconductivity in thin films and narrow wires of aluminum," Phys. Rev. B **35**, 3188 (1987), URL http://link.aps.org/doi/10.1103/PhysRevB.35.3188.

[289] M. Giannouri, E. Rocofyllou, C. Papastaikoudis, and W. Schilling, "Weak-localization, Aslamazov-Larkin, and Maki-Thompson superconducting fluctuation effects in disordered Zr_{1-x} Rh_x films above T_c," Phys. Rev. B **56**, 6148 (1997), URL https://link.aps.org/doi/10.1103/PhysRevB.56.6148.

[290] A. Levchenko, "Transport theory of superconductors with singular interaction corrections," Phys. Rev. B **81**, 012507 (2010), URL https://link.aps.org/doi/10.1103/PhysRevB.81.012507.

[291] L. G. Aslamasov and A. I. Larkin, "The influence of fluctuation pairing of electrons on the conductivity of normal metal," Physics Letters A **26**, 238 (1968), URL http://www.sciencedirect.com/science/article/pii/0375960168906233?via%3Dihub.

[292] E. Abrahams, R. Prange, and M. Stephen, "Effect of a magnetic field on fluctuations above T_c," Physica **55**, 230 (1971), ISSN 0031-8914, URL http://www.sciencedirect.com/science/article/pii/0031891471902552.

[293] M. H. Redi, "Two-dimensional fluctuation-induced conductivity above the critical temperature," Phys. Rev. B **16**, 2027 (1977), URL https://link.aps.org/doi/10.1103/PhysRevB.16.2027.

[294] K. Maki, "Critical fluctuation of the order parameter in a superconductor. I," Progress of Theoretical Physics **40**, 193 (1968), URL http://dx.doi.org/10.1143/PTP.40.193.

[295] R. S. Thompson, "Microwave, flux flow, and fluctuation resistance of dirty type-II superconductors," Phys. Rev. B **1**, 327 (1970), URL https://link.aps.org/doi/10.1103/PhysRevB.1.327.

[296] A. I. Larkin, "Reluctance of two-dimensional systems," Pis'ma Zh. Eksp. Teor. Fiz. **31**, 239 (1980), [JETP Lett. **31**, 219 (1980)], URL http://www.jetpletters.ac.ru/ps/1343/article_20284.shtml.

[297] B. L. Al'tshuler and A. G. Aronov, "Damping of one-electron excitations in metals," Pis'ma Zh. Eksp. Teor. Fiz. **30**, 514 (1979), [JETP Lett. **30**, 482 (1979)], URL http://www.jetpletters.ac.ru/ps/1367/article_20683.shtml.

[298] H. Fukuyama, "Effects of interactions on non-metallic behaviors in two-dimensional disordered systems," Journal of the Physical Society of Japan **48**, 2169 (1980), http://dx.doi.org/10.1143/JPSJ.48.2169, URL http://dx.doi.org/10.1143/JPSJ.48.2169.

[299] B. L. Altshuler, A. G. Aronov, and P. A. Lee, "Interaction effects in disordered Fermi systems in two dimensions," Phys. Rev. Lett. **44**, 1288 (1980), URL http://link.aps.org/doi/10.1103/PhysRevLett.44.1288.

[300] B. Altshuler and A. Aronov, "Fermi-liquid theory of the electron-electron interaction effects in disordered metals," Solid State Communications **46**, 429 (1983), ISSN 0038-1098, URL http://www.sciencedirect.com/science/article/pii/0038109883905707.

[301] A. Kawabata, "Positive magnetoresistance induced by Zeeman splitting in two-dimensional systems," Journal of the Physical Society of Japan **50**, 2461 (1981), http://dx.doi.org/10.1143/JPSJ.50.2461, URL http://dx.doi.org/10.1143/JPSJ.50.2461.

[302] G. Bergmann, "Coulomb-anomaly of the Hall-effect in thin disordered Au-films," Solid State Communications **49**, 775 (1984), ISSN 0038-1098, URL http://www.sciencedirect.com/science/article/pii/0038109884900784.

[303] D. J. Bishop, R. C. Dynes, and D. C. Tsui, "Magnetoresistance in Si metal-oxide-semiconductor field-effect transitors: Evidence of weak localization and correlation," Phys. Rev. B **26**, 773 (1982), URL http://link.aps.org/doi/10.1103/PhysRevB.26.773.

[304] E. Abrahams, S. V. Kravchenko, and M. P. Sarachik, "Metallic behavior and related phenomena in two dimensions," Rev. Mod. Phys. **73**, 251 (2001), URL http://link.aps.org/doi/10.1103/RevModPhys.73.251.

[305] H. Fukuyama, "Effects of mutual interactions in weakly localized regime of disordered two-dimensional systems. iii. Spin-orbit scattering," Journal of the Physical Society of Japan **51**, 1105 (1982), http://dx.doi.org/10.1143/JPSJ.51.1105, URL http://dx.doi.org/10.1143/JPSJ.51.1105.

[306] H. Fukuyama, "Effects of mutual interactions in weakly localized regime of disordered two-dimensional systems. i. Magnetoresistance and spin-susceptibility," Journal of the Physical Society of Japan **50**, 3407 (1981), http://dx.doi.org/10.1143/JPSJ.50.3407, URL http://dx.doi.org/10.1143/JPSJ.50.3407.

[307] G. Deutscher and H. Fukuyama, "Anomalous magnetoresistance of thin metallic films," Phys. Rev. B **25**, 4298 (1982), URL http://link.aps.org/doi/10.1103/PhysRevB.25.4298.

[308] E. H. Hall, "XVIII. On the "Rotational Coefficient" in nickel and cobalt," The London, Edinburgh, and Dublin Philosophical Magazine and Journal of Science **12**, 157 (1881), http://dx.doi.org/10.1080/14786448108627086, URL http://dx.doi.org/10.1080/14786448108627086.

[309] F. Gunkel, C. Bell, H. Inoue, B. Kim, A. G. Swartz, T. A. Merz, Y. Hikita, S. Harashima, H. K. Sato, M. Minohara, et al., "Defect control of conventional and anomalous electron transport at complex oxide interfaces," Phys. Rev. X **6**, 031035 (2016), URL https://link.aps.org/doi/10.1103/PhysRevX.6.031035.

[310] D. Stornaiuolo, C. Cantoni, G. M. De Luca, R. Di Capua, E. Di. Gennaro, G. Ghiringhelli, B. Jouault, D. Marrè, D. Massarotti, F. Miletto Granozio, et al., "Tunable spin polarization and superconductivity in engineered oxide interfaces," Nat. Mater. **15**, 278 (2015), URL http://dx.doi.org/10.1038/nmat4491.

Acknowledgements

Nini, danke für deine Unterstützung in allen Lebenslagen!

Thilo, danke für all die schönen Jahre am Lehrstuhl. In deiner Gruppe hatte ich das beispiellose Gefühl, stets Raum für eigene Ideen und gleichzeitig eine starke Unterstützung zu haben.

Daniel, deine Scharfsinnigkeit auch im komplexesten mathematischen Gefilde (und nicht nur dort!) sind legendär – deine Sichtweise hat mich vorangebracht und viel zu dieser Arbeit beigetragen.

Jone und Betina, es war mir eine Freude als Theoretiker mit euch Experimentatorinnen arbeiten zu dürfen! Ich habe nicht nur wahnsinnig viel von euch gelernt, sondern ihr habt auch unglaublich viel Arbeit in die Daten gesteckt, die ich in dieser Arbeit zeige!

German, danke für die vielen schönen Diskussionen in all den Jahren, sei es über die Stolpersteine der Programmierung oder der Quantengravitation. Außerdem war dein Sinn für Zeichensetzung von unschätzbarem Wert für diese Arbeit.

Prof. Eckern, Ihnen danke ich herzlich dafür, dass Sie sich als Gutachter und Prüfer zur Verfügung gestellt haben – und darüber hinaus für viele Jahre der Unterstützung während meines Studiums, angefangen von meiner ersten Lehrtätigkeit bis zum Mentoring in der Graduiertenschule.

Prof. Ingold, ich danke Ihnen, dass Sie sich als mündlicher Prüfer zur Verfügung gestellt haben – und auch, dass Sie mir die Welt der relativistischen Quantenfeldtheorie gezeigt haben!

I thank Prof. Piet Brouwer for taking the time to provide the external report.

Priv.-Doz. Dr. Krug von Nidda, ich danke Ihnen dafür, dass Sie den Vorsitz für die mündliche Prüfung übernommen haben.

Klaus, dank dir ist das Institut zu mehr geworden ist als einem Arbeitsplatz. Es lebe der Jazz!

Elias, du hast mich mit Kuchen, Obst und apulischen Zitronen versorgt, auch wenn am Abend sonst schon alle nach Hause gegangen waren. Danke auch, dass ich dich immer zu allem um wissenschaftlichen Rat fragen konnte.

Alex, ohne dich als treuen Mittagsgefährten hätte ich oft allein in der Mensa gesessen. Danke auch, dass du immer wieder einen neuen kulinarischen Rat zur Stelle hattest!

Kevin und Stefan, ich danke euch für die schöne Büroatmosphäre. Selten kann man in einem Raum mit vier Personen in vollständiger Ruhe arbeiten, wenn es darauf ankommt – und trotzdem verfechtete Diskussionen über Grundlagenphysik führen, wenn einem danach ist!

Christine und Lore, ihr hält den Lehrstuhl zusammen – danke für eure unermüdliche (vor allem auch moralische!) Unterstützung im Auf und Ab der Promotion.

Butschi, Andi, Chris, mit euch waren die TRR80 Workshops einfach grandios. Michi, auch wenn unser Kaffeeseminar nicht bis ganz zum Ende durchgehalten hat, wird es uns sicher mit seinen ausufernden Diskussionen allen gut in Erinnerung bleiben. Es war mir eine besondere Freude, mit euch gemeinsam die Promotion zu bestreiten!

Ich danke all den guten Freunden, Verwandten, Kollegen und allen anderen, die zum Gelingen dieser Arbeit beigetragen haben, auch wenn sie hier nicht namentlich erwähnt wurden!

Schließlich danke ich der DFG und dem TRR80 Projekt, welche für die finanzielle Unterstützung dieses Projekts gesorgt haben.